Dissertation

submitted to the

Combined Faculty of Natural Sciences and Mathematics
of Heidelberg University, Germany

for the degree of

Doctor of Natural Sciences

put forward by

Linda Shen

born in

Greven, Germany

Oral examination on

July 23rd, 2020

Universal dynamics and thermalization in isolated quantum systems

Referees: Prof. Dr. Jürgen Berges
Prof. Dr. Matthias Bartelmann

Universal dynamics and thermalization in isolated quantum systems

The goal of this work is to explore the relaxation dynamics of isolated quantum systems driven out of equilibrium, focusing on nonequilibrium phenomena emerging on the way to thermal equilibrium. We study close-to-equilibrium states relaxing to thermal equilibrium directly as well as far-from-equilibrium states approaching a transient regime characterized by a self-similar time evolution.

One of the most persistent challenges concerns the thermalization process of the quark-gluon plasma in heavy-ion collisions. We address this issue by investigating the equilibration process of the quark-meson model, an effective low-energy theory of quantum chromodynamics (QCD) that captures important features of QCD including the chiral phase transition. Our simulations probe the approach of quantum thermal equilibrium, characterized by the emergence of Bose-Einstein and Fermi-Dirac distribution functions, in different regions of the phase diagram. We find additional light fermionic degrees of freedom in the crossover region of the quasiparticle excitation spectrum.

A remarkable feature of isolated quantum systems is that far-from-equilibrium states can approach nonthermal fixed points, where the dynamics becomes self-similar and universal across disparate physical systems. We study the infrared nonthermal fixed point by investigating the scaling properties of distribution functions in a relativistic scalar field theory as well as a spin-1 Bose gas. For the scalar field theory we also compute the effective four-vertex and unequal-time two-point correlation functions entailing the nonthermal properties of the system in terms of a strongly violated fluctuation-dissipation theorem. In the spin-1 Bose gas quickly emerging long-range correlations indicate the formation of a condensate out of equilibrium.

Universelle Dynamik und Thermalisierung in isolierten Quantensystemen

Das Ziel dieser Arbeit ist es, die Relaxationsdynamik von aus dem Gleichgewicht gebrachten isolierten Quantensystemen besser zu verstehen. Dabei liegt der Fokus auf Nichtgleichgewichtsphänomenen auf dem Weg zum thermischen Gleichgewicht. Wir betrachten Zustände nahe des Gleichgewichts, die direkt zum thermischen Gleichgewicht relaxieren, sowie Zustände fern des Gleichgewichts, welche zwischenzeitlich ein Regime mit selbstähnlicher Zeitevolution erreichen.

Der Thermalisierungsprozess des Quark-Gluon-Plasmas stellt eine der langanhaltenden Herausforderungen dar. Wir befassen uns mit diesem Problem, indem wir den Thermalisierungsprozess des Quark-Meson-Modells, einer effektiven Niedrigenergietheorie der Quantenchromodynamik (QCD), die wichtige Eigenschaften der QCD wie den chiralen Phasenübergang enthält, untersuchen. In unseren Simulationen erreicht das System den Quantengleichgewichtszustand, welcher sich durch Bose-Einstein und Fermi-Dirac Verteilungsfunktionen auszeichnet, in verschiedenen Regionen des Phasendiagrams. Wir beobachten im Quasiteilchenspektrum des Systems zusätzliche leichte fermionische Freiheitsgrade im Bereich des Crossover-Übergangs.

Eine besondere Eigenschaft von isolieren Quantensystemen ist, dass sie sich fern des Gleichgewichts nichtthermischen Fixpunkten nähern können, an denen die Dynamik selbstähnlich und über verschiedene physikalische Systeme hinweg universell wird. Wir untersuchen den nichtthermischen Fixpunkt im Infrarotbereich anhand der Skalierungseigenschaften von Verteilungsfunktionen einer relativistischen Skalarfeldtheorie sowie eines Spin-1 Bosegases. Für die Skalarfeldtheorie berechnen wir zudem den effektiven Viervertex und Zweipunktkorrelationsfunktionen zu ungleichen Zeiten, welche die nichtthermischen Eigenschaften des Systems in Form eines gebrochenen Fluktuations-Dissipations-Theorems aufzeigen. Beim Spin-1 Bosegas signalisiert der schnelle Aufbau von langreichweitigen Korrelationen die Formierung eines Kondensats fern des Gleichgewichts.

Contents

Chapter 1

Introduction

The approach to thermal equilibrium in isolated quantum systems is a challenging subject that plays an important role in various fields of physics such as cosmology [1–4], high-energy [5–7] and condensed matter physics [8–11]. The question of whether, and how, closed quantum systems equilibrate, once they are driven out of equilibrium, addresses fundamental relationships between the macroscopic description of statistical physics and the microscopic quantum world. While the description of thermal states has been established within the framework of quantum statistical physics, there remain open questions about how thermodynamic properties emerge from local dynamics following microscopic laws [12, 13].

The current interest in this topic is in particular triggered by recent experimental advances in atomic, molecular, optical, and condensed matter physics, which now allow one to build, control, and study various assemblies of isolated quantum systems in the laboratory [14]. The availability of these experimental platforms provides an unprecedented opportunity to explore the nonequilibrium dynamics of closed interacting quantum systems [15]. One guiding question of intensive experimental and theoretical efforts is: How does an isolated quantum many-body system that is prepared in a nonthermal initial state relax to thermal equilibrium? The two research areas heavy-ion physics and ultracold atoms, where this question is currently addressed, serve as the main motivation for the work in this thesis and are briefly outlined in the following.

In the field of heavy-ion physics, understanding nonequilibrium dynamics and thermalization is a major challenge. Ultrarelativistic heavy-ion collisions create a medium with very high energy density, where atomic nuclei break up into quarks and gluons. The early stages of a highly energetic heavy-ion collision constitute a far-from-equilibrium environment with the subsequent thermalization process posing one of the central and challenging problems. After rapidly thermalizing, the quarks and gluons form a hot and dense state of matter known as the quark-gluon plasma (QGP). As the system further expands and cools down, quarks and gluons combine to hadrons.

One goal of current research programs on heavy ions is to explore the different states of strongly interacting matter and establish a connection to the corresponding phase diagram [7, 16, 17]. While in particular the transition from the QGP to the hadronic states is of interest, most experimental observables can only provide information about the integrated time evolution of the system. Disentangling the different stages of the thermalization process is challenging both experimentally and theoretically. Currently, the time evolution of the deconfined medium produced in heavy-ion collisions can be analyzed using a combination of real-time lattice simulation techniques at early times [18, 19], effective

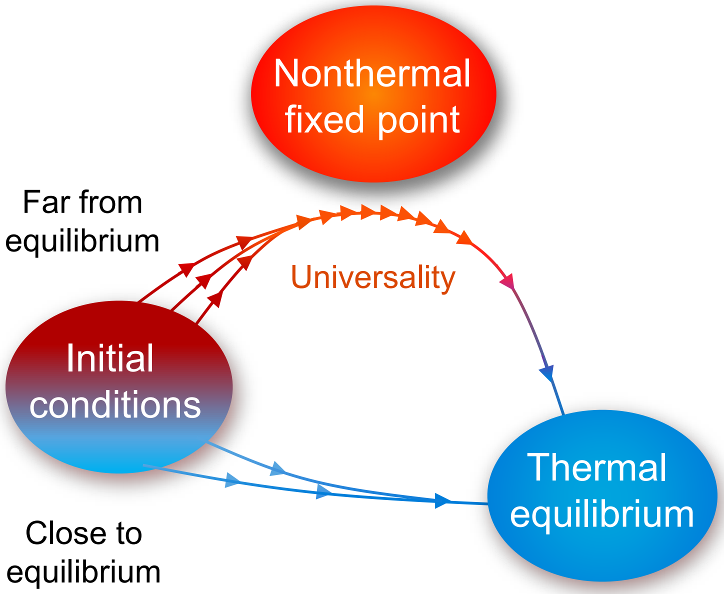

Figure 1.1: Visualization of different ways to approach thermal equilibrium. Initial conditions close to equilibrium may lead a system directly to the thermal state. For far-from-equilibrium initial conditions a system can approach a nonthermal fixed point before relaxing to thermal equilibrium. In the vicinity of such a nonthermal fixed point, the time evolution becomes self-similar and is characterized by universal scaling functions and universal scaling exponents. This figure was first used in the preprint version of [27] and later appeared in [28]; it is based on many works concerning nonthermal fixed points, inter alia [27–38].

kinetic theory at intermediate times [20, 21], and hydrodynamics at late times [22, 23]. Thereby kinetic theory entails how the preequilibrium system evolves into a state of quasilocal equilibrium well accounted for by viscous hydrodynamics.

The relaxation to thermal equilibrium also plays a role in ongoing research activities with ultracold atoms, which contribute to our current understanding of nonequilibrium dynamics in quantum many-body systems. A plethora of atomic species can by now be cooled to ultracold temperatures, reaching down to the nanokelvin scale, by applying a sequence of different cooling techniques, where the gas is confined by magnetic or optical fields [24, 25]. At such low temperatures, the quantum mechanical nature of atoms leads to a plethora of interesting phenomena such as Bose-Einstein condensation. The created clouds of ultracold atoms are well isolated from the environment and accessible for experimental studies. Since ultracold quantum gas experiments can be used to realize generic models of quantum field theory, they open the door to study fundamental aspects of thermalization processes in isolated quantum systems [26].

With the impetus from heavy-ion collisions and ultracold atomic gases, this thesis aims to contribute to our understanding of far-from-equilibrium dynamics and thermalization in isolated quantum systems. While there exist many nonequilibrium phenomena in nature, here the focus is put on two kinds of relaxation dynamics, as sketched in Figure 1.1. If the system is prepared in an initial state close to equilibrium, it can quickly thermalize. Reaching the state of thermal equilibrium, the system effectively looses all memory about the details of the initial state. In contrast, for far-from-equilibrium initial conditions the system can take a trajectory where it approaches a nonthermal fixed point before relaxing to thermal equilibrium [27–38]. At a nonthermal fixed point, an effective loss of memory occurs and the dynamics of the system becomes self-similar. The correlation functions can be described in terms of scaling functions and scaling exponents, which results in an enormous reduction of the sensitivity to details of the underlying microscopic theory and initial conditions. Various field theories or physical systems can exhibit the same *universal* scaling properties such that systems can be grouped into universality classes. The existence of universal regimes leads to the observation of qualitative and even quantitative agreements between different physical systems. Using the concept of universality, one can employ simple model systems to learn more about systems that belong to the same universality class but are otherwise difficult to access.

The first main topic of this thesis concerns the trajectory of direct thermalization. We employ the quark-meson model as an effective low-energy approach to quantum chromodynamics (QCD). Starting from different nonequilibrium initial states, our simulations capture the whole time evolution. In particular, we compute spectral properties. An effective loss of memory of the initial state occurs as the system approaches quantum thermal equilibrium characterized by Bose-Einstein and Fermi-Dirac statistics. The system thermalizes in different regions of the phase diagram of the model, with final states only depending on the energy of the initial state and not on microscopic details. We find additional light fermionic degrees of freedom in the crossover region of the excitation spectrum.

Universal dynamics at a nonthermal fixed point is the second main topic analyzed in this thesis. Universality classes occurring far from equilibrium provide exciting new links between different physical systems such as deconfined nuclear matter and cold atomic gases. Here we study the dynamics in the vicinity of nonthermal fixed points by means of two different physical systems.

On the one hand, we consider (massless) relativistic scalar fields interacting via a quartic self-interaction. Since the infrared scaling exponents and functions of this model belong to the same universality class as the nonrelativistic scalar field theory [32], it can be used to study universal properties of dilute Bose gases. Based on the universality between highly occupied scalar and gauge field theories at weak couplings [27], one may also use this model to learn more about the highly occupied gluon fields created in the initial stages of heavy-ion collisions. In our analysis we employ an effective action approach that includes quantum effects from first principles. A systematic expansion in the number of field components allows us to study nonperturbatively large couplings. Our approach provides direct access to the nonequilibrium dynamics of unequal-time two-point correlation functions, which carry information about the excitation spectrum of the system. A comparison of spectral functions and statistical correlations allows us to study the fluctuation-dissipation relation, where a strong violation in the infrared regime is observed. Moreover, we show that the effective four-vertex function also reveals self-similar scaling behavior.

One the other hand, we investigate a spin-1 Bose gas subject to strong spin-dependent interactions. Present-day experiments can realize ultracold atomic gases forming spin-1 Bose-Einstein condensates. We employ classical-statistical simulations to study the far-from-equilibrium time evolution starting from different initial conditions. While we can probe certain scaling properties, the system does not approach the self-similar scaling regime associated to nonthermal fixed points. We observe the quick emergence of long-range correlations in the system which signals the formation of a condensate far from equilibrium.

1.1 Outline of the thesis

This thesis covers three parts. The first part discusses the far-from-equilibrium dynamics of relativistic scalar field theories. The main objective is to gain a better understanding of equal-time and unequal-time quantities in the nonequilibrium evolution. The second part deals with the thermalization dynamics of the quark-meson model, where scalar fields are coupled to fermion fields. Here, the main interest is to study spectral properties of the system undergoing a thermalization process. The third part explores the far-from-equilibrium dynamics in a spin-1 Bose gas. The aim is to study the time evolution of systems including spin-dependent interactions in order to gain a better understanding of ongoing experimental efforts.

The theoretical foundation for the first two parts is laid out in Chapter 2 introducing the treatment of nonequilibrium quantum field theory in terms of the two-particle irreducible (2PI) effective action. We discuss functional methods in detail before presenting self-consistent nonequilibrium evolution equations. Analytical expressions for systematic expansion schemes are provided. The analyses in Chapters 3 and 4 employ this 2PI effective action framework for the investigation of nonequilibrium real-time dynamics.

In Chapter 3 we study the far-from-equilibrium dynamics of a relativistic N-component scalar field theory close to a nonthermal fixed point. We study both equal-time as well as unequal-time correlation functions. Universal scaling properties and correlation functions are determined in momentum and time in the self-similar regime. Comparing the spectral and statistical components of two-point correlation functions reveals strong violations of the fluctuation-dissipation relation in the nonperturbative infrared regime.

Chapter 4 deals with the thermalization process of a low-energy effective theory for QCD, the so-called quark-meson model. We show that the time evolution starting from nonequilibrium initial conditions leads to late-time states in quantum thermal equilibrium characterized by the fluctuation-dissipation relation. Our simulations provide insight into the emergent degrees of freedom during the time evolution as spectral functions encode the quasiparticle content of the system. Computing different order parameters of the model allows us to distinguish final states in the chirally broken, crossover, and chirally symmetric regions of the phase diagram.

The theoretical background for the third part is given in Chapter 5 where we introduce spin-1 Bose-Einstein condensates and their interactions. The mean-field and Bogoliubov approximations provide insight into the mean-field phase diagram and the excitation spectrum of the system.

Chapter 6 discusses the nonequilibrium dynamics of a spin-1 Bose gas subject to strong spin-dependent interactions. Although the particle distribution functions become self-similar for a wide range of times, the system does approach a universal self-similar scaling regime. We observe a significant deceleration of the dynamics that is accompanied with a fast buildup of long-range correlations indicating the formation of a nonthermal condensate.

Finally, Chapter 7 summarizes the main results of this thesis and gives an outlook onto future prospects of this work.

We note that the main results of the conducted research are contained in Chapters 3, 4 and 6. In addition, substantial information allowing prospective students or coworkers to work on these topics is provided in the appendices for each of these chapters.

Chapter 2

Quantum field theory out of equilibrium

This chapter provides background knowledge for the description of quantum fields out of equilibrium using functional integrals. We present the treatment of nonequilibrium quantum field theory in terms of the so-called *two-particle irreducible* (2PI) *effective action*, including relevant expressions and commonly used approximation schemes for the relativistic scalar field theory as well as the quark-meson model. Readers acquainted with 2PI effective action techniques can continue with Chapter 3, where the required theoretical basics are pointed out briefly.

In nonequilibrium quantum field theory one is concerned with a real-time description of quantum processes out of equilibrium using techniques from quantum field theory. There is a broad range of applications, including relativistic heavy-ion collision experiments, early universe cosmology as well as collective phenomena in condensed matter physics. For introductory texts, see for instance [39–43].

Nonequilibrium dynamics can be studied through the time evolution of correlation functions since in quantum field theory the complete physical information is contained in the set of all n-point correlation functions. For example, two-point functions provide basic information about field excitations, which we interpret as particles, and can be used to define occupation numbers.

This chapter is organized as follows. In Section 2.1 we recall the functional methods that are used in quantum field theory to calculate correlation functions. Subsequently, Section 2.2 outlines the theoretical framework needed to obtain information about systems out of equilibrium. The building blocks for studying the nonequilibrium evolution of a real scalar field theory are presented in Section 2.3. Finally, the quark-meson model and its description within the 2PI framework are outlined in Section 2.4.

The discussion of this chapter provides the theoretical basics for Chapters 3 and 4. The theoretical background for Chapter 6 is presented in Chapter 5.

2.1 The functional integral representation of quantum field theory

The path integral formalism is one way to describe a quantum field theory. Details on the functional approach to quantum field theory can be found in standard textbooks, e.g. [44–46]. The basic object of the path integral approach is the *generating functional* $Z[J]$, from which all n-point correlation functions can be computed. A particular theory is solved in its entirety if an exact closed-form expression for $Z[J]$ of that theory is found. In this section, we present functional methods for a vacuum quantum field theory using the example of a single scalar quantum field φ. In later sections, the results are carried forward to the N-component scalar field theory as well as the quark-meson model.

2.1.1 The generating functional

Time-ordered correlation functions in quantum field theory are the expectation values of time-ordered products of field operators. In the path integral representation of quantum field theory, such an expectation value is expressed in terms of a functional integral. For a scalar field φ with classical action $S[\varphi]$, the n-point correlation function is given by

$$\langle T\varphi(x_1)\ldots\varphi(x_n)\rangle = \frac{\int \mathcal{D}\varphi\ \varphi(x_1)\ldots\varphi(x_n)\ e^{iS[\varphi]}}{\int \mathcal{D}\varphi\ e^{iS[\varphi]}}\ , \tag{2.1}$$

where the time-ordering operator T orders the field operators from right to left in time. Note that this n-point correlation function does not include vacuum bubble contributions as they are canceled out by the denominator. In terms of Feynman diagrams, this means that (2.1) contains both fully connected as well as partially connected diagrams with n external points, but no vacuum bubble diagrams that are not connected to any of the external points. We define the so-called *generating functional*

$$Z[J] \equiv \int \mathcal{D}\varphi\ e^{iS[\varphi]+iJ\cdot\varphi}\,, \tag{2.2}$$

which depends on an external source term $J(x)$. Here, we use the dot as a shorthand notation for one spacetime integration, i.e. $J\cdot\varphi = \int \mathrm{d}^4x\ J(x)\varphi(x)$. Equivalently, the generating functional can be expressed in terms of the expectation value

$$\frac{Z[J]}{Z[0]} = \langle T e^{iJ\cdot\varphi}\rangle\ , \tag{2.3}$$

which corresponds to the canonical quantization formulation of quantum field theory [44]. One can compute any time-ordered n-point correlation function from the generating functional by taking n functional derivatives with respect to the source term,

$$\langle T\varphi(x_1)\ldots\varphi(x_n)\rangle = \frac{1}{Z[0]}\ \frac{\delta}{i\delta J(x_1)}\ \cdots\ \frac{\delta}{i\delta J(x_n)} Z[J]\bigg|_{J=0}\ . \tag{2.4}$$

The equations of motion for all n-point correlation functions are encoded in the generating functional $Z[J]$, for which different representations in terms of effective actions exist. In the upcoming sections, we discuss the effective action, the one-particle irreducible (1PI) and the two-particle irreducible (2PI) effective action, where the latter is used later to derive the nonequilibrium equations of motion for one- and two-point correlation functions.

2.1.2 The effective action

We are particularly interested in computing fully connected correlation functions since they carry the relevant information, while all disconnected diagrams can be constructed from connected ones. The *effective action*, defined as

$$iW[J] = \ln \frac{Z[J]}{Z[0]}\,, \tag{2.5}$$

provides the generating functional for these fully connected correlation functions. By taking derivatives with respect to the source J one obtains the fully connected correlation functions

$$G(x_1, ...x_n) = \frac{\delta}{i\delta J(x_1)} \cdots \frac{\delta}{i\delta J(x_n)}\, iW[J] \bigg|_{J=0}\,, \tag{2.6}$$

where diagrammatically all n external points are connected to each other.

For later purposes, we explicitly state expressions for one-point and two-point functions. The connected one-point function in the presence of sources is given by

$$\phi_J(x) \equiv \frac{\delta W[J]}{\delta J(x)}\,, \tag{2.7}$$

where the subscript J stresses the dependence on the source J. The connected one-point function, also known as the field expectation value or the *macroscopic field*, follows directly as

$$\phi(x) = \phi_J(x)\Big|_{J=0} = G(x) = \frac{\delta W[J]}{\delta J(x)}\bigg|_{J=0}\,. \tag{2.8}$$

The connected two-point function can be computed according to

$$\begin{aligned} G(x,y) &= \frac{\delta}{i\delta J(x)}\frac{\delta}{i\delta J(y)}\, iW[J]\bigg|_{J=0} = \frac{\delta}{i\delta J(x)}\left(\frac{1}{Z[J]}\frac{\delta}{i\delta J(y)}\, Z[J]\right)\bigg|_{J=0} \\ &= \frac{1}{Z[0]}\frac{\delta}{i\delta J(x)}\frac{\delta}{i\delta J(y)}Z[J]\bigg|_{J=0} - \frac{1}{Z[0]}\frac{\delta}{i\delta J(x)}Z[J]\bigg|_{J=0}\frac{1}{Z[0]}\frac{\delta}{i\delta J(y)}Z[J]\bigg|_{J=0} \\ &= \langle T\varphi(x)\varphi(y)\rangle - \phi(x)\phi(y)\,, \end{aligned} \tag{2.9}$$

where it becomes clear that the fully connected two-point function is just the full two-point function deducting the disconnected pieces, which are phrased in terms of the macroscopic field.

Once all connected correlation functions are found, the theory is completely solved since the generating functional $Z[J]$ can be recovered by exponentiation of $iW[J]$.

2.1.3 The 1PI effective action

In this section, we consider an important subclass of the fully connected correlation functions: the *one-particle irreducible* (1PI) n-point correlation functions. These are fully connected correlation functions represented by Feynman diagrams that cannot be separated into two nontrivial diagrams by cutting a single line. They are of particular interest since the renormalizability of a theory can be determined from these 1PI correlation functions. If there are only finitely many divergent 1PI n-point functions $\Gamma^{(n)}$, all divergences can be removed by a finite number of local counterterms. Furthermore, 1PI diagrams can be used to describe quantum corrections to a two-point function, which are phrased in terms of the *self-energy*.

The generating functional for 1PI connected diagrams is called the 1PI effective action, which we here denote by Γ_{1PI}, and is obtained from the effective action $W[J]$ by performing a Legendre transform with respect to the macroscopic field. Assume that (2.7) can be inverted such that there exists a unique $J_\phi(x)$ being an x-dependent functional of ϕ. Then the 1PI effective action can be written as

$$\Gamma_{\text{1PI}}[\phi] \equiv W[J_\phi] - \int_y \frac{\delta W[J]}{\delta J(y)} J_\phi(y) = W[J_\phi] - \int_y \phi(y) J_\phi(y) \tag{2.10}$$

where ϕ is the field in the presence of the source J. Consequently, the first functional derivative of the 1PI effective action with respect to the field gives back the current,

$$\begin{aligned} \frac{\delta\Gamma_{\text{1PI}}[\phi]}{\delta\phi(x)} &= \frac{\delta W[J_\phi]}{\delta\phi(x)} - \int_y \phi(y) \frac{\delta J_\phi(y)}{\delta\phi(x)} - J_\phi(x) \\ &= \int_y \underbrace{\frac{\delta W[J_\phi]}{\delta J_\phi(y)}}_{\phi(y)} \frac{\delta J_\phi(y)}{\delta\phi(x)} - \int_y \phi(y) \frac{\delta J_\phi(y)}{\delta\phi(x)} - J_\phi(x) = -J_\phi(x)\,, \end{aligned}$$

which vanishes in the absence of sources, meaning that the 1PI effective action has an extremum at $J = 0$. Using $\bar{\phi} = \phi_{J=0}$ to denote the one-point function for vanishing external sources, this can be phrased in terms of the stationary condition

$$\left.\frac{\delta\Gamma_{\text{1PI}}[\phi]}{\delta\phi(x)}\right|_{\phi=\bar{\phi}} = 0\,. \tag{2.11}$$

Since $\bar{\phi}$ is the field that extremizes the 1PI effective action, it is called the physical or stationary solution. In other words, in the absence of external sources the 1PI effective action is extremal on its physical field expectation value $\phi = \bar{\phi}$ and the equation of motion for $\bar{\phi}$ is determined by (2.11). If ϕ is not an extremum of $\Gamma_{\text{1PI}}[\phi]$, i.e. $\phi \neq \bar{\phi}$, it represents the expectation value of the field in the presence of a nonzero background source [45]. Because $\bar{\phi}$ must be constant in translation-invariant theories, it is often referred to as *vacuum* in the literature. At the stationary solution, the 1PI effective action coincides with the sourceless generating functional, i.e.

$$\Gamma_{\text{1PI}}[\phi = \bar{\phi}] = W[J = 0]\,, \tag{2.12}$$

which reflects the fact that the 1PI effective action provides just another formulation containing all information about the quantum field theory [47]. In contrast to the generating functional and the effective action, the 1PI effective action (2.10) is a functional of the field only and does not depend on the source J. The 1PI correlation functions are computed by taking functional derivatives with respect to the field,

$$\Gamma^{(n)}(x_1, ..., x_n) = \left.\frac{\delta^n \Gamma_{\text{1PI}}[\phi]}{\delta\phi(x_1)...\delta\phi(x_n)}\right|_{\phi=\bar{\phi}}\,. \tag{2.13}$$

The 1PI two-point function $\Gamma^{(2)}(x, y)$ is also referred to as the *proper* two-point function [48].

Another related concept in quantum field theory is the 1PI *effective potential* defined as

$$V_{\mathrm{1PI}}(\phi_{\mathrm{const}}) = -\frac{1}{(2\pi)^4\delta^4(0)}\,\Gamma_{\mathrm{1PI}}[\phi = \phi_{\mathrm{const}}], \tag{2.14}$$

where ϕ_{const} is a constant field such that $V_{\mathrm{1PI}}(\phi_{\mathrm{const}})$ is a function and not a functional [44]. When the field is set constant in the effective action, kinetic terms vanish and all remaining terms can be pulled out of the spacetime integral. The prefactor in (2.14) is introduced in order to cancel the resulting spacetime volume factor $\int_x = (2\pi)^4\delta^4(0)$. We shall refer to the minimum of this effective potential as ϕ_{min}, which is specified by

$$\left.\frac{\mathrm{d}V_{\mathrm{1PI}}(\phi_{\mathrm{const}})}{\mathrm{d}\phi_{\mathrm{const}}}\right|_{\phi_{\mathrm{const}}=\phi_{\mathrm{min}}} = 0\,. \tag{2.15}$$

In general, the minimum of an effective potential and the field expectation value are not equal, i.e. $\phi_{\mathrm{min}} \neq \bar{\phi}(x)$. However, in translational invariant theories $\bar{\phi}$ must be constant in spacetime implying that $\bar{\phi} = \phi_{\mathrm{min}}$ such that the minimum of the 1PI effective potential and the stationary solution to the 1PI effective action coincide.

2.1.4 The 2PI effective action

An equivalent description of the physics can be phrased in terms of the *two-particle irreducible* (2PI) effective action Γ_{2PI} which is parametrized in terms of the one-point and two-point functions. The 2PI effective action is convenient for studying nonequilibrium initial-value problems and it allows for systematic approximation schemes. A review can be found in [48].

To construct the 2PI effective action, we consider the effective action for (fully) connected Greens functions again,

$$Z[J,R] = e^{iW[J,R]} = \int \mathcal{D}\varphi\; e^{iS[\varphi]+iJ\cdot\varphi+\frac{i}{2}\varphi\cdot R\cdot\varphi}, \tag{2.16}$$

where not only a linear source $J(x)$ but also a bilinear source $R(x,y)$ is added such that both Z and W now depend on two source terms. A variation of the effective action with respect to the source terms yields the following relations to the one-point and two-point functions,

$$\left.\frac{\delta W[J,R]}{\delta J(x)}\right|_{J=0,R=0} = \phi(x)\,, \tag{2.17a}$$

$$\left.\frac{\delta W[J,R]}{\delta R(x,y)}\right|_{J=0,R=0} = \frac{1}{2}\,\langle T\varphi(x)\varphi(y)\rangle = \frac{1}{2}\Big(G(x,y) + \phi(x)\phi(y)\Big)\,, \tag{2.17b}$$

which follows straightforwardly from (2.5) and (2.16). The 2PI effective action is obtained from $iW[J,R]$ by performing two Legendre transformations, one with respect to the linear source J related to the field ϕ and one with respect to the bilinear source R related to the connected propagator G,

$$\begin{aligned}\Gamma_{\mathrm{2PI}}[\phi,G] &= W[J,R] - \int_x \frac{\delta W[J,R]}{\delta J(x)}J(x) - \int_{x,y}\frac{\delta W[J,R]}{\delta R(x,y)}R(y,x)\\ &= W[J,R] - \int_x \phi(x)J(x) - \frac{1}{2}\int_{x,y} G(x,y)R(x,y) - \frac{1}{2}\int_{x,y}\phi(x)R(x,y)\phi(y)\,,\end{aligned} \tag{2.18}$$

where J and R become functionals of ϕ and G by inverting (2.17) in the presence of sources. In contrast to the generating functionals Z and W, the 2PI effective action is a functional of the one- and two-point functions ϕ and G. From the expression (2.18) one can easily deduce the stationary conditions

$$\frac{\delta\Gamma_{\mathrm{2PI}}[\phi,G]}{\delta\phi(x)} = -J(x) - \int_y R(x,y)\phi(y)\,, \qquad \frac{\delta\Gamma_{\mathrm{2PI}}[\phi,G]}{\delta G(x,y)} = -\frac{1}{2}R(x,y)\,. \tag{2.19}$$

In the absence of sources, these yield the equations of motion for ϕ and G. Thus, the physical one-point and two-point functions are determined by the stationary solutions $\bar{\phi}$ and $\bar{G}$ of the following two conditions,

$$\left.\frac{\delta\Gamma_{\mathrm{2PI}}[\phi,G]}{\delta\phi(x)}\right|_{\phi=\bar{\phi},G=\bar{G}(\phi)} = 0\,, \tag{2.20a}$$

$$\left.\frac{\delta\Gamma_{\mathrm{2PI}}[\phi,G]}{\delta G(x,y)}\right|_{\phi,G=\bar{G}(\phi)} = 0\,. \tag{2.20b}$$

Here, the physical two-point function $\bar{G}(\phi)$ is an implicit function of the field. Because it is obtained by a variation of the 2PI effective action, it is also called the *variational propagator*. Note that the stationary solutions are not necessarily equal to the vacuum expectation values minimizing the effective potential [49].

In the absence of sources, the 2PI effective action evaluated at the stationary solution $\bar{G}(\phi)$ is equal to the 1PI effective action,

$$\Gamma_{\mathrm{1PI}}[\phi] = \Gamma_{\mathrm{2PI}}[\phi, G = \bar{G}(\phi)]\,. \tag{2.21}$$

This relation can be extended to higher functional representations, the so-called nPI effective actions $\Gamma_{n\mathrm{PI}}[\phi, G, V_3, ..., V_n]$, which are constructed accordingly and include the higher-order correlation functions V_3, ... , V_n. For vanishing sources, these formulations are equivalent to the exact theory according to

$$\Gamma_{\mathrm{1PI}}[\phi] = \Gamma_{\mathrm{2PI}}[\phi, G = \bar{G}(\phi)] = ... = \Gamma_{n\mathrm{PI}}[\phi, G = \bar{G}(\phi), ..., V_n = \bar{V}_n(\phi)]\,. \tag{2.22}$$

We note that this relation also holds in certain approximation schemes and allows us to calculate 1PI correlation functions using the 2PI effective action or approximations of the 2PI effective action. This is interesting because a crucial feature of 2PI-derivable approximations is that the derived equations of motion conserve global symmetries and associated Noether currents in time. In particular, the energy is conserved, which is very useful when studying out-of-equilibrium processes where most other quantities, such as particle distribution functions, evolve in a complicated way. The conservation of energy applies not only to the full 2PI effective action but to to any level of truncation. We emphasize that truncations of the 2PI effective action can lead to differences between the variational propagator $\bar{G}(x,y)$ and the proper two-point function $\Gamma^{(2)}(x,y)$ [48].

Since most of the time the exact form of the 2PI effective action is not known, it is convenient to decompose it into tree-level, one-loop and higher order contributions [50],

$$\Gamma_{\mathrm{2PI}}[\phi,G] = S[\phi] + \Gamma_1[\phi,G] + \Gamma_2[\phi,G] + \text{const.}\ , \tag{2.23}$$

where the tree-level contribution is given by the classical action S as a functional of the macroscopic field ϕ, the one-loop terms are denoted by Γ_1, and all higher order contributions are included in $\Gamma_2[\phi, G]$. In this framework $\Gamma_2[\phi, G]$ only contains contributions from 2PI vacuum diagrams with interactions given by the classical action of the theory and propagator lines set equal to the fully connected propagator $G(x, y)$ in (2.17b). A diagram is called 2PI if it does not separate into two nontrivial diagrams when cutting two propagator lines.

2.2 Nonequilibrium quantum field theory

In standard vacuum quantum field theory, one primarily considers the scattering of free particles coming in from infinity and flying off to infinity after some interaction, a process that can be described as a boundary value problem. In contrast, nonequilibrium quantum field theory deals with the time evolution of a quantum system that is specified by an out-of-equilibrium state at some particular initial time. Therefore, one now has to address an initial value problem where the initial state can be determined by initial conditions for the correlation functions.

In this section, we describe the closed time path formalism and introduce the generating functional for nonequilibrium setups. For more extensive discussions on nonequilibrium quantum field theory we refer to [40–42, 51].

2.2.1 The nonequilibrium problem

Before coming to the closed time path, we briefly point out in what sense nonequilibrium quantum field theory is challenging by contrasting with the equilibrium case. In equilibrium quantum field theory, n-point correlation functions can be computed in the canonical quantization formalism using the interaction picture, where the correlator is related to the vacuum as well as the creation and annihilation operators of the free theory. Consider a quantum many-body system that is governed by a time-dependent Hamiltonian $H(t)$. We assume that the time-dependence of H is such that the particles in the system are noninteracting in the distant past $t = -\infty$ as well as the distant future $t = +\infty$. The interactions are adiabatically switched on, reaching their actual physical strength at some time before the observation time t, and adiabatically switched off, such that the system becomes noninteracting again at some time after t.

At $t = \pm\infty$, the ground state of the system corresponds to the simple ground state of the noninteracting system $|0\rangle$. According to the *Gell-Mann and Low theorem* [52], the ground state $|0\rangle$ is related to the ground state of the interacting many-body system $|\Omega\rangle$ via the relation

$$|\Omega\rangle = U_\varepsilon(t, -\infty)\,|0\rangle\ , \tag{2.24}$$

where U_ε is the adiabatic evolution operator with subscript ε indicating that the interactions are turned on and off adiabatically. In the adiabatic case, turning interactions on and off brings the noninteracting ground state of a system back to the same state up to a possible phase factor, i.e.

$$U_\varepsilon(-\infty, \infty)\,|0\rangle = e^{i\theta}\,|0\rangle\ , \tag{2.25}$$

which implies that the phase factor is determined by $e^{i\theta} = \langle 0|\,U_\varepsilon(\infty, -\infty)\,|0\rangle$. As a consequence, the expectation value of an operator $\mathcal{O}$ with respect to the interacting ground state $|\Omega\rangle$ can be computed as follows:

$$\begin{aligned}\langle\Omega|\,\mathcal{O}\,|\Omega\rangle &= \langle 0|U_\varepsilon(-\infty,t)\,\mathcal{O}\,U_\varepsilon(t,-\infty)|0\rangle \\ &= e^{-i\theta}\,\underbrace{\langle 0|\,e^{i\theta}}_{\langle 0|U_\varepsilon(\infty,-\infty)}\,U_\varepsilon(-\infty,t)\mathcal{O}U_\varepsilon(t,-\infty)\,|0\rangle \\ &= \frac{\langle 0|U_\varepsilon(\infty,t)\,\mathcal{O}\,U_\varepsilon(t,-\infty)|0\rangle}{\langle 0|\,U_\varepsilon(\infty,-\infty)\,|0\rangle}\,. \end{aligned} \tag{2.26}$$

From the numerator of this equation we see that the ground state $|0\rangle$ is first evolved from the distant past to the observation time, where the observable operator $\mathcal{O}$ acts, and then to the distant future, where the overlap with the known state $\langle 0|$ is computed. Thus, in this procedure one only needs to consider the forward time evolution. Thereby, the denominator in (2.26) takes care of subtracting the vacuum loop contributions, i.e. all diagrams that are not connected to any external points.

Unfortunately, equation (2.26) does not hold in a general nonequilibrium situation. If the Hamiltonian contains some nonadiabatic time dependence, the system is driven away from equilibrium during the time evolution and there is no guarantee that the system returns to its ground state [40, 42]. The restriction to adiabatically switching interactions on and off is not needed when using the closed time path formulation which we introduce in the next section.

2.2.2 The closed time path

The closed time path formalism, also known as the Schwinger-Keldysh formalism [53, 54], has been widely used in the literature, in as well as out of equilibrium, to study initial value problems using the path integral formulation of quantum field theory.

The state of an arbitrary physical system can be described in terms of its density matrix $\rho(t)$. Knowing the density matrix at all times t is equivalent to knowing the whole time evolution of the system. The time evolution of the density matrix $\rho(t)$ is governed by the von Neumann equation according to

$$i\frac{\partial}{\partial t}\rho(t) = [H(t),\rho(t)]\,, \tag{2.27}$$

with $H(t)$ being the Hamiltonian of the system. A formal solution to the von Neumann equation can be written as

$$\rho(t) = U(t,t_0)\rho(t_0)U^{-1}(t,t_0)\,, \tag{2.28}$$

where the unitary time evolution operator $U(t,t_0)$ evolves the density matrix from the initial time t_0 to the time t. Since Hamiltonian operators at different times generally do not commute with each other, the time evolution operator is understood to be given by

$$U(t,t') = Te^{-i\int_{t'}^{t} H(t)\,\mathrm{d}t}\,, \tag{2.29}$$

with T being the time-ordering operator. If the Hamiltonian is time-independent, such as in isolated

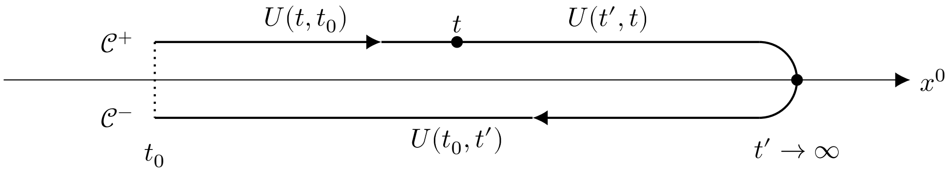

Figure 2.1: Sketch of the closed time path or Schwinger-Keldysh contour $\mathcal{C}$. Note that the forward and backward parts of the curve, $\mathcal{C}^+$ and $\mathcal{C}^-$, are shifted away from the real axis only to make them better visible.

quantum systems, the evolution operator simplifies to

$$U(t,t') = e^{-iH(t-t')} . \tag{2.30}$$

Since we aim to compute n-point correlation functions, we are interested in finding the expectation value of an observable $\mathcal{O}$ at some given time t. In the Schrödinger picture, this can be expressed in terms of the density matrix according to

$$\langle \mathcal{O}(t) \rangle = \mathrm{Tr}[\rho(t)\mathcal{O}] \tag{2.31}$$

where the trace is performed in the state space of the physical system under consideration. Using (2.28) and the cyclicity of the trace, this can be rewritten as

$$\langle \mathcal{O}(t) \rangle = \mathrm{Tr}[\rho(t_0)U(t_0,t')U(t',t)\,\mathcal{O}\,U(t,t_0)] , \tag{2.32}$$

where we notice that the time evolution operator suffices $U(t,t'') = U(t,t')U(t',t'')$. Read from right to left, this expression reflects the evolution from time t_0 to t, where the observable is evaluated, toward an intermediate time t' and then back to initial time t_0. The calculation of an observable therefore requires an evolution of the initial state both forward and backward. This is the origin of the closed time path shown in Figure 2.1. We have seen in the previous section how this forward-backward evolution can be avoided in equilibrium, where the backward time evolution can be eliminated. In a general nonequilibrium setup, however, there is no guarantee that the system returns to the same vacuum state. In terms of Heisenberg operators, (2.32) can be expressed as

$$\langle \mathcal{O}(t) \rangle = \mathrm{Tr}[\rho(t_0)\,\mathcal{O}(t)] , \tag{2.33}$$

which essentially defines expectation values for nonequilibrium settings.

Time evolution along the closed time path is the central subject in nonequilibrium field theory. The nonequilibrium formulation of a quantum field theory can be constructed using time-ordering along the closed time path $\mathcal{C}$. Thereby, time-ordering is defined as usual along the forward contour $\mathcal{C}^+$ and as reversed time-ordering along the backward contour $\mathcal{C}^-$. Once the initial density matrix is specified, (2.32) enables us to calculate the expectation values of an operator at any time t. For the calculation of arbitrary correlation functions, however, it is practical switch from the operator language back to the path integral formalism [42, 55].

Thereby it is conventional to write $\varphi(x) = \varphi^{\pm}(x)$ for $x^0 \in \mathcal{C}^{\pm}$ in order to distinguish whether the field belongs to the forward or the backward branch of the closed time path. In this notation the classical action follows as

$$S[\varphi^+,\varphi^-] = \int_{t_0}^{\infty} \mathrm{d}x^0 \int \mathrm{d}^d x \left(\mathscr{L}[\varphi^+] - \mathscr{L}[\varphi^-]\right), \tag{2.34}$$

with Lagrangian $\mathscr{L}$ and spatial dimensionality d. The minus sign in front of the second term accounts for the reversed time integration on the backward branch. In the limit $t_0 \to -\infty$ all spacetime integrations run from $-\infty$ to ∞ such that all calculations can be performed in the standard $(d+1)$-dimensional Minkowski spacetime. The corresponding generating functional for correlation functions then reads

$$Z[J] = \int \mathcal{D}\varphi^+ \mathcal{D}\varphi^- e^{iS[\varphi^+,\varphi^-] + iJ^+\cdot\varphi^+ - iJ^-\cdot\varphi^-}, \tag{2.35}$$

where we introduced the linear source terms $J^\pm(x)$ with x^0 on $\mathcal{C}^\pm$. Bilinear sources are taken into account by adding the term

$$\frac{1}{2}\int_{x,y} \begin{pmatrix} \varphi^+(x) & \varphi^-(x) \end{pmatrix} \begin{pmatrix} R^{++}(x,y) & -R^{+-}(x,y) \\ -R^{-+}(x,y) & R^{--}(x,y) \end{pmatrix} \begin{pmatrix} \varphi^+(y) \\ \varphi^-(y) \end{pmatrix}, \tag{2.36}$$

where again the superscripts indicate whether the respective time arguments of the sources are on the forward or backward branch of the closed time path. For instance, the source term $R^{+-}(x,y)$ refers to $R(x,y)$ with $x^0 \in \mathcal{C}^+$ and $y^0 \in \mathcal{C}^-$.

2.2.3 The nonequilibrium generating functional

The closed time path introduced in the previous section provides us with a basic ingredient for the computation of nonequilibrium correlation functions using a generating functional. We treat nonequilibrium dynamics as an initial value problem and specify the initial conditions in terms of an initial density matrix. Then the functional methods presented in Section 2.1 with time variables considered to be on the closed time path can be used to describe the dynamics out of equilibrium.

Again, we would like to make use of a generating functional that contains all information about the correlation functions. The nonequilibrium state of a system is described by a nonthermal density matrix, which is used in order to compute expectation values according to to (2.33). Using the expression of the generating functional given in (2.3), the nonequilibrium generating functional containing all information about the nonequilibrium dynamics is defined as

$$Z_{\mathrm{NE}}[J,R;\rho] = \mathrm{Tr}\left[\rho(t_0)\, T_{\mathcal{C}}\; e^{iJ\cdot\varphi + \frac{i}{2}\varphi\cdot R\cdot\varphi}\right], \tag{2.37}$$

where $\rho(t_0)$ is the initial density matrix describing some nonequilibrium initial state, $T_{\mathcal{C}}$ ensures the time-ordering along the Schwinger-Keldysh contour, and dot products represent spacetime integrals with time integrations along the closed time path, i.e.

$$J\cdot\varphi = \int_{\mathcal{C}} \mathrm{d}x^0 \int \mathrm{d}^d x\; J(x)\varphi(x). \tag{2.38}$$

Analogously to the equilibrium case, we include two source terms for the construction of the corresponding nonequilibrium 2PI effective action. The nonequilibrium n-point correlation functions can be computed from the nonequilibrium generating functional,

$$\begin{aligned}\langle T_{\mathcal{C}}\, \varphi(x_1)\ ...\ \varphi(x_n)\rangle &= \mathrm{Tr}\left[\, \rho(t_0)\ T_{\mathcal{C}}\, \varphi(x_1)\ ...\ \varphi(x_n)\right] \\ &= \frac{\delta}{i\delta J(x_1)}\ ...\ \frac{\delta}{i\delta J(x_n)}\ Z_{\mathrm{NE}}[J,R;\rho]\,\bigg|_{J=0,R=0}\ , \end{aligned} \tag{2.39}$$

with fields ordered in time along the closed time contour. The trace can be evaluated in terms of eigenstates of the Heisenberg field operator at initial time,

$$\hat{\varphi}(t_0 = 0^{\pm}, \mathbf{x})\, |\varphi^{\pm}\rangle = \varphi(0^{\pm}, \mathbf{x})\, |\varphi^{\pm}\rangle\ , \tag{2.40}$$

where we choose $t_0 = 0^+$ as the starting point and $t_0 = 0^-$ as the end point of the closed time path. For notational convenience, we write $\varphi^{\pm} \equiv \varphi(0^{\pm}, \mathbf{x})$ in the following. Employing these sets of eigenstates, the generating functional can be written as

$$\begin{aligned} Z_{\mathrm{NE}}[J,R;\rho] &= \int \mathrm{d}\varphi^+\ \langle\varphi^+|\, \rho(t_0)\ T_{\mathcal{C}}\ e^{iJ\cdot\varphi+\frac{i}{2}\varphi\cdot R\cdot\varphi}\, |\varphi^+\rangle \\ &= \int \mathrm{d}\varphi^+ \int \mathrm{d}\varphi^-\ \langle\varphi^+|\, \rho(t_0)\, |\varphi^-\rangle\, \langle\varphi^-|\, T_{\mathcal{C}}\ e^{iJ\cdot\varphi+\frac{i}{2}\varphi\cdot R\cdot\varphi}\, |\varphi^+\rangle\ , \end{aligned} \tag{2.41}$$

where the transition amplitude matrix element $\langle\varphi^-|...|\varphi^+\rangle$ can be written in terms of a path integral over classical fields $\varphi(x)$ sufficing boundary conditions,

$$\langle\varphi^-|\, T_{\mathcal{C}}\ e^{iJ\cdot\varphi+\frac{i}{2}\varphi\cdot R\cdot\varphi}\, |\varphi^+\rangle = \int_{\varphi=\varphi^+}^{\varphi=\varphi^-} \mathcal{D}'\varphi\ e^{iS[\varphi]+iJ\cdot\varphi+\frac{i}{2}\varphi\cdot R\cdot\varphi}\, . \tag{2.42}$$

The time integration along $\mathcal{C}$ ensures that the fields are ordered along the closed time path. The path integral considers all configurations $\varphi = \varphi(x^0, \mathbf{x})$ depending on space and times $x^0 \in \mathcal{C}$ that satisfy the boundary conditions $\varphi = \varphi(0^{\pm}, \mathbf{x})$. The prime in the functional measure $\mathcal{D}'\varphi$ indicates that the integration over fields at time $x^0 = t_0$ is excluded. Using (2.42), the generating functional can be written as

$$Z_{\mathrm{NE}}[J,R;\rho] = \underbrace{\int \mathrm{d}\varphi^+\, \mathrm{d}\varphi^-\ \langle\varphi^+|\rho(t_0)|\varphi^-\rangle}_{\text{intial conditions}}\ \underbrace{\int_{\varphi^+}^{\varphi^-} \mathcal{D}'\varphi\ e^{iS[\varphi]+iJ\cdot\varphi+\frac{i}{2}\varphi\cdot R(x,y)\cdot\varphi}}_{\text{quantum dynamics}}\ , \tag{2.43}$$

with $\varphi^{\pm} = \varphi(0^{\pm}, \mathbf{x})$ being the field at initial time on the forward and backward contour, respectively. This formula reflects the two important ingredients entering a nonequilibrium quantum field theory. Firstly, the statistical fluctuations are encoded in the averaging procedure by the matrix elements of the initial density operator $\rho(t_0)$. Secondly, the quantum fluctuations are included in terms of the functional integral with classical action $S[\varphi]$ [41]. In the following, we discuss how we can specify the initial density operator and deduce the corresponding nonequilibrium evolution equations.

2.2.4 Gaussian initial conditions

Nonequilibrium dynamics poses an initial value problem that requires the specification of an initial state at some time t_0. Since the specification of the initial density operator is equivalent to the knowledge of all correlation functions at initial time t_0, it is convenient to consider a Gaussian initial density matrix that is fully determined by one-point and two-point functions.

The initial conditions in the nonequilibrium generating functional (2.43) are specified in terms of the initial density matrix element $\langle\varphi^+|\rho(t_0)|\varphi^-\rangle$. In thermal equilibrium, the density matrix is determined by $\rho_{\text{eq}} \sim e^{-\beta H}$, with inverse temperature β, and can be interpreted as the evolution operator $\exp(-i\tau H)$ in imaginary time $\tau = -i\beta$. Nonequilibrium density matrices do not have this special form.

The most general density matrix can be parametrized as

$$\langle\varphi^+|\rho(t_0)|\varphi^-\rangle = \mathcal{N} e^{ih_{\mathcal{C}}[\varphi]}\,, \tag{2.44}$$

with $\mathcal{N}$ being a normalization factor and $h_{\mathcal{C}}[\varphi]$ an expansion in powers of the field,

$$\begin{aligned} h_{\mathcal{C}}[\varphi] = \alpha_0 &+ \int\limits_{x_1} \alpha_1(x_1)\varphi(x_1) + \frac{1}{2}\int\limits_{x_1,x_2} \alpha_2(x_1,x_2)\varphi(x_1)\varphi(x_2) \\ &+ \frac{1}{3!}\int\limits_{x_1,x_2,x_3} \alpha_3(x_1,x_2,x_3)\varphi(x_1)\varphi(x_2)\varphi(x_3) + \ldots\,, \end{aligned}$$

where the subscript $\mathcal{C}$ indicates that time integrals are taken along the closed time path as always in nonequilibrium setups. Because the density matrix is only specified at the initial time t_0, the time integrals can only contribute at $t = t_0$ implying that the (complex) coefficients $\alpha_1(x_1)$, $\alpha_2(x_1,x_2)$, $\alpha_3(x_1,x_2,x_3)$, ... vanish for $x_1^0, x_2^0, x_3^0, \ldots \neq t_0$. We further note that the fields satisfy the boundary conditions $\varphi(x) = \varphi(0^\pm, \mathbf{x})$ at initial time as determined by $\langle\varphi^+|...|\varphi^-\rangle$.

A density matrix is said to be *Gaussian*, if $h_{\mathcal{C}}[\varphi]$ is at most quadratic in the field with all higher order terms vanishing, i.e. $\alpha_3 = \alpha_4 = \ldots = 0$. In this case, the coefficient functions α_0, α_1 and α_2 constitute five (real) parameter functions. Hence, the most general Gaussian density matrix is described by five parameters and can be written as

$$\begin{aligned} \langle\varphi^+|\rho_{\text{Gauss}}(t_0)|\varphi^-\rangle = \frac{1}{\sqrt{2\pi\xi^2}} \exp\Big\{ i\dot{\phi}(\varphi^+ - \varphi^-) - \frac{\sigma^2+1}{8\xi^2}\left[(\varphi^+ - \phi)^2 + (\varphi^- - \phi)^2\right] \\ + i\frac{\eta}{2\xi}\left[(\varphi^+ - \phi)^2 - (\varphi^- - \phi)^2\right] + \frac{\sigma^2-1}{4\xi^2}(\varphi^+ - \phi)(\varphi^- - \phi)\Big\}\,, \end{aligned} \tag{2.45}$$

where the spatial dependence has been omitted. Specifying the five parameter functions ϕ, $\dot{\phi}$, ξ, η and σ is equivalent to a set of initial conditions for the one-point and two-point functions. For (2.45), they can be related to each other by

$$\phi = \text{Tr}\left[\rho\ \varphi(t)\right]\Big|_{t=0}\,, \tag{2.46a}$$

$$\dot{\phi} = \text{Tr}\left[\rho\ \partial_t\varphi(t)\right]\Big|_{t=0}\,, \tag{2.46b}$$

$$\xi^2 = \text{Tr}\left[\rho\ \varphi(t)\varphi(t')\right]\Big|_{t=t'=0} - \phi\phi\,, \tag{2.46c}$$

$$\xi\eta = \text{Tr}\left[\rho\ \left(\partial_t\varphi(t)\varphi(t') + \varphi(t)\partial_{t'}\varphi(t')\right)\right]\Big|_{t=t'=0} - \dot{\phi}\phi\,, \tag{2.46d}$$

$$\eta^2 + \frac{\sigma^2}{4\xi^2} = \mathrm{Tr}\left[\rho\ \partial_t\varphi(t)\partial_{t'}\varphi(t')\right]\Big|_{t=t'=0} - \dot{\phi}\dot{\phi}\,, \tag{2.46e}$$

where spatial arguments have been suppressed and the density matrix ρ denotes the Gaussian density matrix in (2.45), i.e. $\rho = \rho_{\mathrm{Gauss}}(t_0)$. The equivalence can be shown explicitly, for instance by computing

$$\mathrm{Tr}[\rho_{\mathrm{Gauss}}(t_0)\varphi(t_0)] = \frac{1}{\sqrt{2\pi\xi^2}}\int_{-\infty}^{\infty}\mathrm{d}\varphi\ e^{-\frac{1}{2\xi^2}(\varphi-\phi)^2}\varphi(t_0)\ = \phi\,, \tag{2.47}$$

where the Gaussian integral can be evaluated by shifting $\varphi \to \varphi + \phi$. One can check that all higher order n-point functions vanish at initial time for the Gaussian density matrix (2.45). Consequently, a Gaussian initial state can be specified in terms of initial conditions for the one-point and two-point functions of the field.

2.2.5 The nonequilibrium 2PI effective action

If we compare our expansion of the initial density matrix (2.44) with the nonequilibrium generating functional (2.37), we see that α_0 becomes an irrelevant normalization constant while α_1 and α_2 can be absorbed into the sources J and R, respectively. Since no higher order coefficient functions appear in Gaussian density matrices, the nonequilibrium generating functional with a Gaussian density matrix is equivalent to a generating functional including linear and bilinear source terms,

$$Z_{\mathrm{NE}}[J, R; \rho_{\mathrm{Gauss}}] = Z_{\mathrm{NE}}[J', R'], \tag{2.48}$$

where the right-hand side corresponds to the generating functional (2.16) with time integrations along the closed time path and shifted source terms as indicated by the primes. Consequently, the nonequilibrium 2PI effective action with Gaussian initial conditions is equivalent to the 2PI effective action introduced in (2.18) with time integrations along the closed time path $\mathcal{C}$ and shifted source terms. The discussion of Section 2.1.4 is directly carried over to nonequilibrium settings by taking time integrations with respect to the closed time path.

It is important to note that although the initial density matrix $\rho(t_0)$ is chosen to be Gaussian, the density matrix can evolve to non-Gaussian states at later times $t > t_0$ due to interactions. Therefore, the consideration of Gaussian initial states does not restrict the quantum dynamics but merely the choice of initial values for the correlation functions to states where only one-point and two-point functions are nonvanishing [41].

Up to this point we considered the description of a quantum field theory out of equilibrium using the example of a scalar field. In the subsequent sections we discuss the N-component real scalar field theory and the quark-meson model, which are studied in Chapters 3 and 4, respectively.

2.3 The relativistic scalar field theory

In this section we present the two-particle irreducible (2PI) effective action framework for the $O(N)$-symmetric real scalar field theory studied in Chapter 3. The exact evolution equations are derived and an expansion in $1/N$, with N being the number of fields components, is introduced. This expansion provides a systematic approximation scheme to study the nonequilibrium time evolution of the theory.

We consider N real scalar fields with bare mass m interacting via a quartic self-coupling λ. The classical action is given by

$$S[\varphi] = \int_x \left[\frac{1}{2}\partial^\mu \varphi_a(x)\partial_\mu \varphi_a(x) - \frac{1}{2}m^2 \varphi_a(x)\varphi_a(x) - \frac{\lambda}{4!\,N}\Big(\varphi_a(x)\varphi_a(x)\Big)^2 \right] , \tag{2.49}$$

where φ_a denotes the classical field. A summation over field space indices $a = 1, \dots, N$ and Lorentz indices $\mu = 0, 1, 2, 3$ is implied. We use the shorthand integral notation $\int_x \equiv \int_{\mathcal{C}} \mathrm{d}x^0 \int \mathrm{d}^3x$ with $x = (x^0, \mathbf{x})$, where for the nonequilibrium settings considered the time path $\mathcal{C}$ is given by the Schwinger-Keldysh contour, see Section 2.2.2. The action is invariant under $O(N)$ transformations in field space. If at least one scalar field component acquires a nonvanishing expectation value, i.e. $\phi_a = \langle \varphi_a \rangle \neq 0$, the $O(N)$-symmetry is spontaneously broken.

We use 2PI effective action techniques in order to deduce the evolution equations for the one-point and two-point functions of the scalar field theory, which in the following are denoted by ϕ and G, respectively. The construction of the 2PI effective action for a single scalar field is described in Section 2.1.4 and can be generalized to a N-component scalar field, see [41] for a detailed derivation.

From now on, we neglect the subscript and write $\Gamma = \Gamma_{\mathrm{2PI}}$ for the 2PI effective action. For the scalar field theory defined in (2.49) one obtains

$$\Gamma[\phi, G] = S[\phi] + \frac{i}{2}\,\mathrm{Tr}\left[\ln\left(G^{-1}\right) + G_{\mathrm{cl}}^{-1}(\phi)G\right] + \Gamma_2[\phi, G] + \mathrm{const.}\,, \tag{2.50}$$

where the second term describes the one-loop contribution with G_{cl}^{-1} being the classical inverse propagator specified below. In direct analogy to (2.20), the stationary conditions for the N-component scalar field theory read

$$\left.\frac{\delta \Gamma[\phi, G]}{\delta \phi_a(x)}\right|_{\phi=\bar{\phi}, G=\bar{G}(\phi)} = 0\,, \tag{2.51a}$$

$$\left.\frac{\delta \Gamma[\phi, G]}{\delta G_{ab}(x, y)}\right|_{\phi, G=\bar{G}(\phi)} = 0\,, \tag{2.51b}$$

with physical solutions $\bar{\phi}$ and $G = \bar{G}$. The equation of motion for the variational propagator is obtained from (2.51b). Variation of the 2PI effective action with respect to the propagator includes the computation of the following two terms

$$\begin{aligned}
\frac{\delta}{\delta G_{ab}(x, y)}\Big(\mathrm{Tr}\left[\ln(G^{-1})\right]\Big) &= \frac{\delta}{\delta G_{ab}(x, y)}\Big(\ln\left[\det(G)^{-1}\right]\Big) \\
&= -\frac{1}{\det(G)}\,\frac{\delta}{\delta G_{ab}(x, y)}\Big(\det(G)\Big) \\
&= -G^{-1}_{ba}(y, x)\,,
\end{aligned} \tag{2.52a}$$

$$\begin{aligned}
\frac{\delta}{\delta G_{ab}(x, y)}\Big(\mathrm{Tr}\left[G_{\mathrm{cl}}^{-1}(\phi)G\right]\Big) &= \frac{\delta}{\delta G_{ab}(x, y)}\left(\int_{u,v} G^{-1}_{\mathrm{cl},cd}(u, v; \phi)G_{dc}(v, u)\right) \\
&= \int_{u,v} G^{-1}_{\mathrm{cl},cd}(u, v; \phi)\,\delta_{ad}\delta_{bc}\delta(v - x)\delta(u - y) \\
&= G^{-1}_{\mathrm{cl},ba}(y, x; \phi)\,,
\end{aligned} \tag{2.52b}$$

for which we use the standard matrix identities

$$\mathrm{Tr}\ln M = \ln\det M\,, \qquad\qquad \frac{\partial\det(M)}{\partial M_{ab}} = \det(M)\ \left(M^{-1}\right)^T_{ab}\,,$$

with M denoting an arbitrary matrix [56]. We further note that the time-ordered connected propagator is symmetric in the exchange of both spacetime arguments and field space indices,

$$G_{ab}(x,y) = \langle T_{\mathcal{C}}\varphi_a(x)\varphi_b(y)\rangle - \phi_a(x)\phi_b(y) = \langle T_{\mathcal{C}}\varphi_b(y)\varphi_a(x)\rangle - \phi_b(y)\phi_a(x) = G_{ba}(y,x)\,,$$

since the fields obey the bosonic commutation relation $[\varphi_a(x),\varphi_b(y)] = 0$ while $T_{\mathcal{C}}$ takes care of the time-ordering. Using (2.52) one obtains the equation of motion for the variational propagator,

$$i\bar{G}^{-1}_{ab}(x,y;\phi) = iG^{-1}_{\mathrm{cl},ab}(x,y;\phi) - i\Sigma_{ab}(x,y;\phi,G)\Big|_{G=\bar{G}(\phi)}\,, \tag{2.53}$$

with classical inverse propagator and self-energy defined as

$$iG^{-1}_{\mathrm{cl},ab}(x,y;\phi) \equiv \frac{\delta^2 S[\phi]}{\delta\phi_a(x)\delta\phi_b(y)}\,, \tag{2.54}$$

$$i\Sigma_{ab}(x,y;\phi,G) \equiv -2\,\frac{\delta\Gamma_2[\phi,G]}{\delta G_{ab}(x,y)}\,. \tag{2.55}$$

In the N-component scalar field theory discussed here, the classical inverse propagator is given by

$$iG^{-1}_{\mathrm{cl},ab}(x,y;\phi) = -\left[\partial_\mu\partial^\mu\delta_{ab} + M^2_{\mathrm{cl},ab}(x;\phi)\right]\delta_{\mathcal{C}}(x-y)\,, \tag{2.56}$$

where the δ-function is evaluated along the closed time path $\mathcal{C}$ for the temporal coordinate and the classical effective mass squared can be written as

$$M^2_{\mathrm{cl},ab}(x;\phi) = m^2\delta_{ab} + \frac{\lambda}{6N}\phi_c(x)\phi_c(x)\delta_{ab} + \frac{\lambda}{3N}\phi_a(x)\phi_b(x)\,. \tag{2.57}$$

In the subsequent sections we show how the equation of motion (2.53) can be phrased in terms of integro-differential equations. In the course of the derivation, we decompose the propagator into spectral and statistical components, assume translational and rotational invariance in space, and truncate the effective action using the systematic large-N expansion scheme.

2.3.1 Spectral and statistical components

In this section we introduce a decomposition of the two-point function G into spectral and statistical components that have a simple physical interpretation. The spectral function represents the spectrum of the theory, i.e. it encodes which states are available. On the other hand, the statistical propagator contains information about occupation numbers, i.e. how the available states are occupied. This section summarizes introductory parts of [41, 57–59].

In the following, we consider a single component scalar field, for which we derive a number of useful relations. The relevant expressions for a scalar field with N components are stated at the end. Let us first define the Wightman functions

$$G^{>}(x,y) = \langle \varphi(x)\varphi(y) \rangle - \phi(x)\phi(y)\,, \tag{2.58a}$$

$$G^{<}(x,y) = \langle \varphi(y)\varphi(x) \rangle - \phi(x)\phi(y) = G^{>}(y,x)\,, \tag{2.58b}$$

where $\langle\,\cdot\,\rangle = \mathrm{Tr}[\rho_0\,\cdot\,]$ denotes the expectation value as the average over an initial density matrix ρ_0. These correlation functions satisfy the hermiticity properties

$$[G^{>}(y,x)]^* = G^{>}(x,y)\,, \qquad\qquad [G^{<}(y,x)]^* = G^{<}(x,y)\,, \tag{2.59}$$

which can be easily verified, e.g. by computing

$$[G^{>}(y,x)]^* = \left(\mathrm{Tr}\left[\rho\,\varphi(y)\varphi(x)\right]\right)^* = \mathrm{Tr}\left[\left(\rho\,\varphi(y)\varphi(x)\right)^\dagger\right] = \mathrm{Tr}\left[\varphi(x)\varphi(y)\rho\right] = G^{>}(x,y)\,,$$

under usage of the cyclicity of the trace and the hermiticity of the field ϕ. One can represent the time-ordered connected two-point function in terms of the Wightman functions (2.58),

$$\begin{aligned} G(x,y) &= \langle T_{\mathcal{C}}\varphi(x)\varphi(y)\rangle - \phi(x)\phi(y) \\ &= \Theta_{\mathcal{C}}(x^0-y^0)G^{>}(x,y) + \Theta_{\mathcal{C}}(y^0-x^0)G^{<}(x,y), \end{aligned} \tag{2.60}$$

with contour step function $\Theta_{\mathcal{C}}$ defined along the closed time path $\mathcal{C}$. One can also construct the retarded and the advanced propagators from (2.58),

$$G_R(x,y) = i\Theta_{\mathcal{C}}(x^0-y^0)\Big[G^{>}(x,y) - G^{<}(x,y)\Big]\,, \tag{2.61a}$$

$$G_A(x,y) = -i\Theta_{\mathcal{C}}(y^0-x^0)\Big[G^{>}(x,y) - G^{<}(x,y)\Big]\,, \tag{2.61b}$$

where the retarded propagator characterizes the response of a system to small external perturbations. If the hermiticity properties (2.59) are fulfilled, the retarded and advanced propagators are related by

$$G_A(y,x) = G_R^*(x,y)\,. \tag{2.62}$$

In a real scalar field theory, the symmetry condition $G^{>}(x,y) = G^{<}(y,x)$ ensures that $G_R(x,y)$ and $G_A(x,y)$ are real functions with $G_A(x,y) = G_R(y,x)$. Computing

$$G^{>}(x,y) - G^{<}(x,y) = G^{>}(x,y) - G^{>}(y,x) = G^{>}(x,y) - [G^{<}(x,y)]^* = 2i\,\mathrm{Im}\,G^{>}(x,y)$$

shows that the right-hand sides of (2.61) are real.

The hermiticity properties (2.59) imply that the propagator $G(x,y)$ can be described by one complex function. Equivalently, it can be parametrized in terms of the two real-valued functions

$$F(x,y) = \frac{1}{2}\left[G^{>}(x,y) + G^{<}(x,y)\right]\,, \tag{2.63a}$$

$$\rho(x,y) = \;i\;\left[G^{>}(x,y) - G^{<}(x,y)\right]\,, \tag{2.63b}$$

corresponding to the statistical and the spectral components mentioned above. We write $G^{>}(x,y) = F(x,y) - \frac{i}{2}\rho(x,y)$ and $G^{<}(x,y) = F(x,y) + \frac{i}{2}\rho(x,y)$, and insert these expressions into (2.60) to obtain a formula for the decomposition of any two-point function into statistical and spectral components,

$$G(x,y) = F(x,y) - \frac{i}{2}\rho(x,y)\,\mathrm{sgn}_{\mathcal{C}}(x^0 - y^0). \tag{2.64}$$

In contrast to the case of thermal equilibrium, where F and ρ are related to each other by the fluctuation-dissipation theorem, out of equilibrium the statistical and spectral functions are independent from each other.

In the case of bosonic fields, the statistical and spectral functions can be expressed in terms of the anticommutator, denoted by curly brackets, and the commutator, denoted by squared brackets,

$$F(x,y) = \frac{1}{2}\left\langle \{\varphi(x), \varphi(y)\}\right\rangle - \phi(x)\phi(y)\,, \tag{2.65a}$$

$$\rho(x,y) = i\ \left\langle [\varphi(x), \varphi(y)]\right\rangle, \tag{2.65b}$$

satisfying the symmetry properties $F(x,y) = F(y,x)$ and $\rho(x,y) = -\rho(y,x)$. The spectral function encodes the bosonic commutation relations,

$$\rho(x,y)\Big|_{x^0=y^0} = 0\,, \qquad\qquad \partial_{x^0}\rho(x,y)\Big|_{x^0=y^0} = \delta(\mathbf{x}-\mathbf{y})\,, \tag{2.66}$$

and is directly related to the retarded propagator $G_R(x,y) = \theta_{\mathcal{C}}(x^0 - y^0)\rho(x,y)$ and the advanced propagator $G_A(x,y) = -\theta_{\mathcal{C}}(y^0 - x^0)\rho(x,y)$, which can be seen from (2.61). Using the hermiticity properties (2.59) one can write $\rho(x,y) = G_R(x,y) - G_A(x,y) = -2\,\mathrm{Im}\,G^{>}(x,y)$ to express the spectral function in terms of the retarded and advanced propagators.

For the N-component scalar field with field space indices $a, b = 1, ..., N$, the decomposition of the propagator and the self-energy into statistical and spectral components reads

$$G_{ab}(x,y) = F_{ab}(x,y) - \frac{i}{2}\rho_{ab}(x,y)\,\mathrm{sgn}_{\mathcal{C}}(x^0 - y^0)\,, \tag{2.67}$$

$$\Sigma_{ab}(x,y) = C_{ab}(x,y) - \frac{i}{2}A_{ab}(x,y)\,\mathrm{sgn}_{\mathcal{C}}(x^0 - y^0) - i\Sigma^{\mathrm{local}}_{ab}(x)\delta(x-y)\,, \tag{2.68}$$

where we use C and A to denote the symmetric and antisymmetric parts of the self-energy, respectively. In the self-energy, we additionally single out the local term $\Sigma^{\mathrm{local}}_{ab}$ that contributes to the effective mass.

2.3.2 Symmetries

Spatial translation and rotation invariance

In this thesis we consider spatially homogeneous systems where one-point functions only depends on one time coordinate and two-point functions only depend on two temporal coordinates and a relative spatial coordinate. Consequently, any two-point function can be spatially Fourier transformed according to

$$G(x,y) \equiv G(t,t',\mathbf{x}-\mathbf{y}) = \int_{\mathbf{p}} G(t,t',\mathbf{p})\ e^{i\mathbf{p}(\mathbf{x}-\mathbf{y})}\,, \tag{2.69}$$

where we use $t = x^0$, $t' = y^0$, and the shorthand notation $\int_{\mathbf{p}} = \int \mathrm{d}^3p/(2\pi)^3$. By construction, the two-point functions $F(x,y)$ and $\rho(x,y)$ are symmetric and antisymmetric under the exchange of the spacetime coordinates x and y, respectively, such that $F(t,t',\mathbf{p}) = +F(t',t,-\mathbf{p})$ and $\rho(t,t',\mathbf{p}) =$

$-\rho(t',t,-\mathbf{p})$. The commutation relations (2.66) can be phrased in Fourier space as

$$\rho(t,t',\mathbf{p})\Big|_{t=t'} = 0\,, \qquad \partial_t\,\rho(t,t',\mathbf{p})\Big|_{t=t'} = 1\,, \qquad \partial_t\partial_{t'}\,\rho(t,t',\mathbf{p})\Big|_{t=t'} = 0\,, \tag{2.70}$$

which holds for spatially translation invariant systems.

In addition, we assume spatial isotropy such that the momentum dependence of the two-point functions reduces to $G(t,t',\mathbf{p}) = G(t,t',|\mathbf{p}|)$. Consequently, the symmetry properties of the statistical and spectral functions are only reflected in their temporal arguments, i.e. $F(t,t',|\mathbf{p}|) = +F(t',t,|\mathbf{p}|)$ and $\rho(t,t',|\mathbf{p}|) = -\rho(t',t,|\mathbf{p}|)$.

We note that the time-dependence of the two-point functions can be expressed in terms of the central time $\tau = (t+t')/2$ and the relative time $\Delta t = t - t'$. This notation allows us to perform an additional Fourier transformation with respect to Δt,

$$G(\tau,p^0,\mathbf{p}) = \int_{\Delta t = t-t'} G(\tau,t-t',\mathbf{p})\; e^{-ip^0(t-t')}\,, \tag{2.71}$$

where p^0 is the Fourier mode corresponding to Δt. This yields the two-point function as a function of the four-momentum $p = (p^0,\mathbf{p})$ and the central time τ. In spacetime translation invariant settings, such as thermal equilibrium, there is no dependence on the central time τ. Since the real-valued statistical function is symmetric in coordinate space, the Fourier-space statistical function $F(\tau,p)$ is symmetric in p, i.e. $F^*(\tau,p) = F(\tau,p) = F(\tau,-p)$. In contrast, the antisymmetric spectral function suffices $\rho^*(\tau,p) = -\rho(\tau,p) = \rho(\tau,-p)$.

Spontaneous symmetry breaking

We consider the general case where the expectation value of the macroscopic field can be nonzero. By virtue of the $O(N)$ symmetry, it is possible to rotate the system such that all but one field component vanish. If we single out one particular field direction, the $O(N)$ symmetry is spontaneously broken to an $O(N-1)$ symmetry. Without loss of generality, we choose $\phi_a \neq 0$ with $a = 1$ and refer to the 1-direction in field index space as the longitudinal direction. The other field directions are called transverse directions, where $\phi_\alpha = 0$ for $\alpha = 2,...,N$. In this convention, each field component can be expressed as

$$\phi_a = \phi_1\delta_{a1} + \phi_\alpha\delta_{a\alpha}\,, \tag{2.72}$$

with field space indices $a = 1,...,N$ and $\alpha = 2,...,N$. The remaining $O(N-1)$ symmetry allows us to rotate the propagator to be diagonal in the transverse directions, $G_{\alpha\beta}(x,y) = G_\perp(x,y)\delta_{\alpha\beta}$, implying $G_{\alpha\alpha}(x,y) = (N-1)G_\perp(x,y)$. Hence, we can take the two-point functions to be diagonal with one longitudinal and $N-1$ transverse entries,

$$G_{ab}(x,y) = \mathrm{diag}\left(G_\parallel(x,y), G_\perp(x,y),\; \dots\;, G_\perp(x,y)\right). \tag{2.73}$$

In the symmetric regime, where $\phi = 0$, the two-point functions further simplify to $G = G_\parallel = G_\perp$.

2.3.3 Exact evolution equations

In this section we present the exact evolution equations obtained from the 2PI effective action. We first discuss the macroscopic field and subsequently come to the statistical and spectral functions introduced above. For a detailed derivation of the expressions we refer to [58, 60].

The equation of motion for the macroscopic field is determined by the stationary condition (2.51a). Since the expectation values of the transverse field directions are zero, the only relevant equation is the one for $\phi_1(t) \equiv \langle\sigma(t)\rangle$, where the label σ is motivated from the quark-meson model where the scalar field is identified as the sigma meson. Making use of the decomposition into spectral and statistical functions, the field equation can be written as

$$\left[\partial_t^2 + m^2 + \frac{\lambda}{6N}\langle\sigma(t)\rangle^2 + \frac{\lambda}{6N}\left(3\int_{\mathbf{p}} F_{\parallel}(t,t,\mathbf{p}) + (N-1)\int_{\mathbf{p}} F_{\perp}(t,t,\mathbf{p})\right)\right]\langle\sigma(t)\rangle = \frac{\delta\Gamma_2[\phi,G]}{\delta\langle\sigma(t)\rangle}\,. \quad (2.74)$$

The tadpole terms with $F_{\parallel}$ and $F_{\perp}$ originate from the $G_{\mathrm{cl}}^{-1}(\phi)G$-term in (2.50) and are therefore independent of any truncation of the 2PI effective action.

After finding the evolution equation for the field, we now turn to the equations of motion for the two-point functions. Since the evolution equation (2.53) is not suitable for the numerical evaluation of the initial value problems that appear in nonequilibrium settings, we rewrite the equation by convoluting it with the two-point function, i.e.

$$\int_z G_{\mathrm{cl}}^{-1}(x,z;\phi)G(z,y) - \int_z \left[\Sigma(x,z;\phi,G,\Delta)\right]G(z,y) = \delta(x-y), \quad (2.75)$$

where we suppress field indices for notational convenience. This yields an evolution equation for the time-ordered connected propagator of the form

$$\left[\Box_x + M^2(x;\phi)\right]G(x,y) + i\int_z \left[\Sigma(x,z;\phi,G,\Delta)\right]G(z,y) = -i\delta(x-y)\,, \quad (2.76)$$

with some effective mass M^2. Corresponding expressions can be found for the statistical and spectral two-point functions. Since our numerical simulations are performed in spatial momentum space, we present the formulas in terms of Fourier modes and refer to [55] for details on the calculation.

The complete set of evolution equations reads

$$\begin{aligned}\left[\partial_t^2 + \mathbf{p}^2 + M_{\parallel}^2(t)\right]F_{\parallel}(t,t',|\mathbf{p}|) = &-\int_{t_0}^{t} \mathrm{d}t'' A_{\parallel}(t,t'',|\mathbf{p}|)F_{\parallel}(t'',t',|\mathbf{p}|)\\ &+\int_{t_0}^{t'} \mathrm{d}t'' C_{\parallel}(t,t'',|\mathbf{p}|)\rho_{\parallel}(t'',t',|\mathbf{p}|)\,,\end{aligned} \quad (2.77a)$$

$$\begin{aligned}\left[\partial_t^2 + \mathbf{p}^2 + M_{\perp}^2(t)\right]F_{\perp}(t,t',|\mathbf{p}|) = &-\int_{t_0}^{t} \mathrm{d}t'' A_{\perp}(t,t'',|\mathbf{p}|)F_{\perp}(t'',t',|\mathbf{p}|)\\ &+\int_{t_0}^{t'} \mathrm{d}t'' C_{\perp}(t,t'',|\mathbf{p}|)\rho_{\perp}(t'',t',|\mathbf{p}|)\,,\end{aligned} \quad (2.77b)$$

$$\left[\partial_t^2 + \mathbf{p}^2 + M_\parallel^2(t)\right] \rho_\parallel(t,t',|\mathbf{p}|) = -\int_t^{t'} \mathrm{d}t'' A_\parallel(t,t'',|\mathbf{p}|)\rho_\parallel(t'',t',|\mathbf{p}|)\,, \tag{2.77c}$$

$$\left[\partial_t^2 + \mathbf{p}^2 + M_\perp^2(t)\right] \rho_\perp(t,t',|\mathbf{p}|) = -\int_t^{t'} \mathrm{d}t'' A_\perp(t,t'',|\mathbf{p}|)\rho_\perp(t'',t',|\mathbf{p}|)\,, \tag{2.77d}$$

where C and A are the symmetric and antisymmetric self-energy components, and the time-dependent effective masses are given by the expressions

$$M_\parallel^2(t) = m^2 + \frac{\lambda}{2N}\left\langle\sigma(t)\right\rangle^2 + \Sigma_\parallel^{\mathrm{local}}(t)\,, \tag{2.78a}$$

$$M_\perp^2(t) = m^2 + \frac{\lambda}{6N}\left\langle\sigma(t)\right\rangle^2 + \Sigma_\perp^{\mathrm{local}}(t)\,, \tag{2.78b}$$

which are also referred to as *gap equations*. The coupling between longitudinal and transverse components of the bosonic two-point functions occurs solely via the self-energies. The evolution equations are causal since they only depend on times prior to the evaluation. The history of the time evolution is contained in the *memory integrals* on the right-hand side of the equations in (2.77) [41].

In this section we presented the full set of evolution equations without any approximations but including the assumption of spatial translation and rotation invariance. The equations are derived from first principles and capture the whole quantum evolution. Since they are in general too complicated to be solved analytically without approximations, we elaborate on a systematic nonperturbative approximation scheme in the following section.

2.3.4 The large-N expansion

In this section we discuss the large-N expansion, also known as $1/N$ expansion, where one applies a systematic expansion in $1/N$ with N being the number of scalar field components. Truncations of the 2PI effective action build on the large-N expansion provide practicable approximations to study the dynamics of nonperturbative quantum field theories.

Various approximation schemes of the 2PI effective action have been used in the literature. While in [50] a loop expansion of the 2PI effective action was studied, the systematic expansion in $1/N$ is advantageous for theories with large occupancies and/or strong couplings. The large-N expansion has been studied for $O(N)$-symmetric scalar field theories in the symmetric phase where $\phi = 0$ [60], as well as the broken phase where $\phi \neq 0$ [58]. Additional fermion contributions were considered in [61]. For a more detailed discussion we refer to [41].

If the quartic coupling λ of the $O(N)$ symmetric scalar field theory under consideration is large, diagrams of any loop order can become equally important such that a truncation at finite loop order would fail. The large-N expansion classifies diagrams according to their scaling with the number of field components N and organizes contributions to the 2PI effective action accordingly,

$$\Gamma_2[\phi,G] = \underbrace{\Gamma_2^{\mathrm{LO}}[\phi,G]}_{\sim N^1} + \underbrace{\Gamma_2^{\mathrm{NLO}}[\phi,G]}_{\sim N^0} + \underbrace{\Gamma_2^{\mathrm{NNLO}}[\phi,G]}_{\sim N^{-1}} + \,...\;, \tag{2.79}$$

where the expansion in powers of $1/N$ provides a controlled expansion parameter that does not rely on weak couplings.

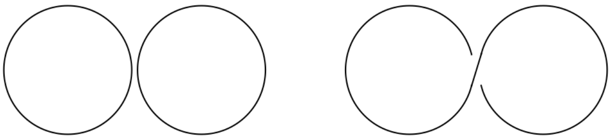

Figure 2.2: The (only) LO diagram is shown on the left, the two-loop NLO diagram on the right. Closed lines indicate traces in $O(N)$ space contributing with a factor of N. The left diagram is of order N^1 in the large N expansion while the right one is of order N^0, although both are of order λ in a perturbative coupling expansion.

We present a classification scheme for the N-component scalar field theory that is based on $O(N)$-invariants, for instance scalars in field space. Using the fields ϕ_a one can only construct one independent invariant under $O(N)$ rotations,

$$\phi_a\phi_a = \phi_1\phi_1 + \phi_2\phi_2 + \ \dots\ + \phi_N\phi_N \sim N\,, \tag{2.80}$$

which corresponds to a trace with respect to the field indices and therefore scales with the number of field components N. Clearly, the kinetic term and the mass term in the classical action scale with N according to this scheme. The self-interaction term is written such that it also scales proportional to N, implying that the interaction vertex carries a factor of $1/N$.

The 2PI effective action is an $O(N)$-invariant scalar in field space that is constructed by the two functions ϕ_a and G_{ab}. All possible $O(N)$-invariants that can be constructed from these two functions are build from the irreducible invariants,

$$\phi_a\phi_a\,, \qquad\qquad (G^n)_{aa}\,, \qquad\qquad \phi_a\phi_b(G^n)_{ab}\,, \qquad\qquad (n \leq N)$$

which constitute the invariants that are not factorizable in field-index space. These irreducible invariants correspond to traces in field space. They contribute with a factor of N in the power counting scheme while every vertex provides a factor of $1/N$. Each term in $\Gamma[\phi, G]$ is an $O(N)$-singlet that can be represented by a closed loop diagram (vacuum bubble).

In the course of this work, we consider the expansion (2.79) at *next-to-leading order* (NLO) in $1/N$. The obtained approximation of the 2PI effective action is used to derive expressions for the self-energies appearing in the equations of motion presented in Section 2.3.3. The 2PI diagrams relevant for our approximation are contained in $\Gamma_2^{\mathrm{LO}}[G]$ and $\Gamma_2^{\mathrm{NLO}}[\phi, G]$, where G is the variational propagator at NLO in the large N expansion.

The leading-order (LO) contribution to the effective action is independent of the macroscopic field ϕ and can be written as [41]

$$\Gamma_2^{\mathrm{LO}}[\phi, G] = -\frac{\lambda}{4!\,N}\int_x G_{aa}(x,x)G_{bb}(x,x)\,, \tag{2.81}$$

which scales with N^1 since $G_{aa} = \delta_{aa}G = NG$. This term corresponds to the two-loop vacuum diagram shown on the left in Figure 2.2. The LO correction contributes with a tadpole term to the propagator, which corresponds to a local self-energy contribution describing a mass shift. It cannot account for scattering interactions. Hence, the LO spectral function is given by the same δ-peak as for the free-field case since no broadening of the spectrum occurs. We note that the Boltzmann equation at NLO deploys this LO spectral function.

One has to distinguish the LO two-loop diagram (2.81) from the two-loop diagram at NLO,

$$-\frac{\lambda}{4!\,N}\int_x G_{ab}(x,x)G_{ab}(x,x), \tag{2.82}$$

shown on the right in Figure 2.2. As this term only contains one trace in field space, it scales with N^0 and hence constitutes a diagram at NLO.

The full NLO contribution comprises an infinite series of closed loop diagrams that can be expressed as [41]

$$\Gamma_2^{\mathrm{NLO}}[\phi,G] = \frac{i}{2}\operatorname{Tr}\ln B(G) - \frac{i\lambda}{6N}\int_{x,y} I(x,y;G)H(x,y;G), \tag{2.83}$$

where the trace is taken in spacetime and we make use of the following expressions:

$$B(x,y;G) = \delta(x-y) + i\frac{\lambda}{6N}G_{ab}(x,y)G_{ab}(x,y), \tag{2.84}$$

$$I(x,y;G) = \frac{\lambda}{6N}G_{ab}(x,y)G_{ab}(x,y) - i\frac{\lambda}{6N}\int_z I(x,z;G)G_{ab}(z,y)G_{ab}(z,y), \tag{2.85}$$

$$H(x,y;G) = -\phi_a(x)G_{ab}(x,y)\phi_b(y). \tag{2.86}$$

The functions B and I scale with N^0 whereas H scales with N^1, ensuring that all terms in Γ_2^{NLO} are proportional to N^0. We note that the functions B and I are related to each other by $B^{-1}(x,y;G) = \delta(x-y) - iI(x,y;G)$, which is a helpful relation in calculations.

The first term in (2.83) describes an infinite series of diagrams without macroscopic field insertions, depicted in the first and second lines of Figure 2.3. The explicit expressions for these diagrams are obtained by expanding the logarithm as an infinite sum,

$$\ln\left[\mathbb{1} + M\right] = \sum_{n=1}^{\infty}\frac{(-1)^{n-1}M^n}{n} = M - \frac{M^2}{2} + \ldots\,,$$

where we use convolutions for multiplications and evaluate traces with respect to spacetime coordinates, e.g.

$$M^2(x,z) = \int_y M(x,y)M(y,z)\,, \qquad \operatorname{Tr} M^2(x,z) = \int_x\int_y M(x,y)M(y,x)\,.$$

The second term in (2.83) encodes an infinite sum of diagrams with macroscopic field insertions coming from the H-term. The associated diagrams are shown in the bottom row of Figure 2.3.

The self-energy is obtained by taking the functional derivative of Γ_2 with respect to G, see (2.55), which diagrammatically corresponds to opening one propagator line. Since Γ_2 only contains 2PI diagrams, cutting one line yields 1PI diagrams, which are exactly the diagrams that contribute to the self-energy of the propagator.

Having specified the approximation of the 2PI effective action, we can now derive the resulting expressions for the self-energies that enter the equations of motion. In the course of this, we make use

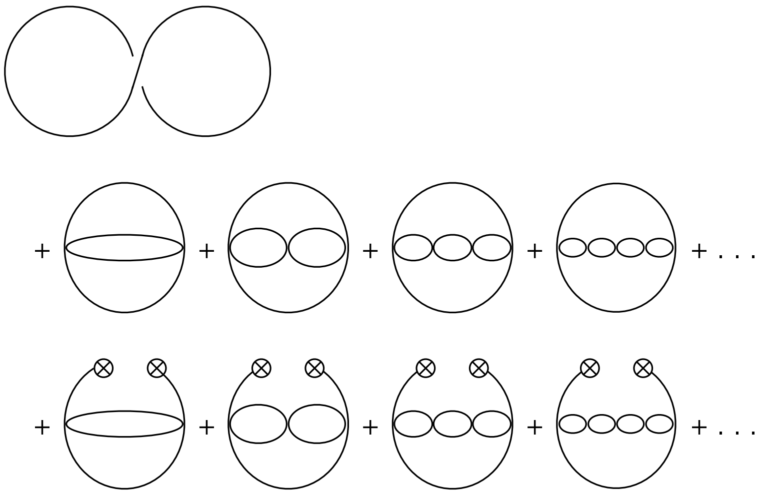

Figure 2.3: Diagrams contributing at NLO in the large-N expansion. The closed propagator loops correspond to $G_{ab}G_{ab}$, while the loops with insertion of two macroscopic fields (indicated by the crossed circles) represent $\phi_a G_{ab} \phi_b$. Since the number of loops equals the number of vertices in each diagram, all diagrams are of order N^0.

of the decomposition of the propagators into spectral and statistical components (F and ρ) introduced in Section 2.3.1 and the symmetries discussed in Section 2.3.2.

The field equation

The equation of motion for the macroscopic field in the NLO approximation of the 2PI effective action is determined by

$$\frac{\delta \Gamma_2[\phi, G]}{\delta \langle \sigma(t) \rangle} = \frac{\lambda}{3N} \int_{t_0}^{t} \mathrm{d}t' \int_{\mathbf{p}} \Big[I_\rho(t,t',|\mathbf{p}|) F_\parallel(t,t',|\mathbf{p}|) + I_F(t,t',|\mathbf{p}|) \rho_\parallel(t,t',|\mathbf{p}|) \Big] \, \langle \sigma(t') \rangle \,, \tag{2.87}$$

where $F_\parallel$ and $\rho_\parallel$ are the statistical and spectral components of $G_\parallel$. The functions I_F and I_ρ represent the respective components of I, for which explicit expressions are presented below.

The self-energies

The self-energy is defined as the functional derivative of Γ_2 with respect to the variational propagator,

$$\Sigma_{ab}(x,y;\phi,G) \equiv 2i \frac{\delta \Gamma_2[\phi, G, \Delta]}{\delta G_{ab}(x,y)} \,, \tag{2.88}$$

and can be decomposed into a local, a statistical and a spectral component according to (2.68). The local part of the self-energy is given by

$$\Sigma^{\mathrm{local}}_{ab}(t;F) = \frac{\lambda}{6N} \int_{\mathbf{q}} \Big[F_{cc}(t,t,|\mathbf{q}|) \delta_{ab} + F_{ab}(t,t,|\mathbf{q}|) \Big] \,, \tag{2.89}$$

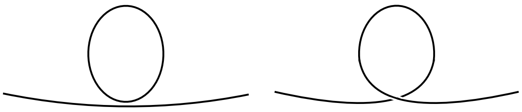

Figure 2.4: LO and NLO tadpole contribution to the self-energy of the variational propagator G as given in (2.89). The left (right) diagram derives from the LO (NLO) two-loop diagram in Figure 2.2 and scales with N^0 (N^{-1}).

which only depends on F since ρ is antisymmetric and vanishes at equal times. The two terms correspond to the two two-loop diagrams shown in Figure 2.2 and describe the tadpole contribution to the self-energy. The associated diagrams for the propagator are depicted in Figure 2.4. For the longitudinal and transverse directions they read

$$\Sigma_{\parallel}^{\text{local}}(t;F) = \frac{\lambda}{6N}\int_{\mathbf{q}}\Big[3F_{\parallel}(t,t,|\mathbf{q}|) + (N-1)F_{\perp}(t,t,|\mathbf{q}|)\Big], \tag{2.90a}$$

$$\Sigma_{\perp}^{\text{local}}(t;F) = \frac{\lambda}{6N}\int_{\mathbf{q}}\Big[\ F_{\parallel}(t,t,|\mathbf{q}|) + (N+1)F_{\perp}(t,t,|\mathbf{q}|)\Big]. \tag{2.90b}$$

Since the nonlocal self-energy contributions form convolutions in momentum space, it is easier to evaluate them in coordinate space where they can be calculated as direct products. The relevant coordinate-space expressions for the self-energy are

$$\begin{aligned} C_{ab}(x,y) = -\frac{\lambda}{3N}\Bigg\{ & I_F(x,y)\Big[\phi_a(t)\phi_b(t') + F_{ab}(x,y)\Big] - \frac{1}{4}I_\rho(x,y)\rho_{ab}(x,y) \\ & + P_F(x,y)F_{ab}(x,y) - \frac{1}{4}P_\rho(x,y)\rho_{ab}(x,y)\Bigg\} \end{aligned} \tag{2.91a}$$

$$\begin{aligned} A_{ab}(x,y) = -\frac{\lambda}{3N}\Bigg\{ & I_\rho(x,y)\Big[\phi_a(t)\phi_b(t') + F_{ab}(x,y)\Big] + I_F(x,y)\rho_{ab}(x,y) \\ & + P_\rho(x,y)F_{ab}(x,y) + P_F(x,y)\rho_{ab}(x,y)\Bigg\}, \end{aligned} \tag{2.91b}$$

where the spacetime dependence of the two-point functions is $(x,y) = (t,t',|\mathbf{x}-\mathbf{y}|)$ under the considered symmetries. Furthermore, we provide expressions for the statistical and spectral components of (2.85), which in spatial Fourier space can be written as

$$\begin{aligned} I_F(t,t',|\mathbf{p}|) = \Pi_F(t,t',|\mathbf{p}|) & - \int_0^t \mathrm{d}t''\ I_\rho(t,t'',|\mathbf{p}|)\Pi_F(t'',t',|\mathbf{p}|) \\ & + \int_0^{t'} \mathrm{d}t''\ I_F(t,t'',|\mathbf{p}|)\Pi_\rho(t'',t',|\mathbf{p}|), \end{aligned} \tag{2.92a}$$

$$I_\rho(t,t',|\mathbf{p}|) = \Pi_\rho(t,t',|\mathbf{p}|) - \int_{t'}^t \mathrm{d}t''\ I_\rho(t,t'',|\mathbf{p}|)\Pi_\rho(t'',t',|\mathbf{p}|), \tag{2.92b}$$

using the one-loop self-energy contributions

$$\Pi_F(t,t',|\mathbf{p}|) = \frac{\lambda}{6N}\int_{\mathbf{q}}\Big[F_{ab}(t,t',|\mathbf{p}-\mathbf{q}|)F_{ab}(t,t',|\mathbf{q}|) - \frac{1}{4}\rho_{ab}(t,t',|\mathbf{p}-\mathbf{q}|)\rho_{ab}(t,t',|\mathbf{q}|)\Big], \tag{2.93a}$$

$$\Pi_\rho(t,t',|\mathbf{p}|) = \frac{\lambda}{3N}\int_{\mathbf{q}} F_{ab}(t,t',|\mathbf{p}-\mathbf{q}|)\rho_{ab}(t,t',|\mathbf{q}|), \tag{2.93b}$$

that can be expressed as direct products in coordinate space, and are symmetric and antisymmetric, respectively.

The functions P_F and P_ρ describe the interactions of the fluctuations with the macroscopic field. Since the macroscopic field only depends on time, we can directly write down the spatial Fourier transformed H-terms as

$$H_F(t,t',|\mathbf{p}|) = -\left\langle\sigma(t)\right\rangle\; F_{\|}(t,t',|\mathbf{p}|)\;\left\langle\sigma(t')\right\rangle, \tag{2.94a}$$

$$H_\rho(t,t',|\mathbf{p}|) = -\left\langle\sigma(t)\right\rangle\; \rho_{\|}(t,t',|\mathbf{p}|)\;\left\langle\sigma(t')\right\rangle, \tag{2.94b}$$

where we use that only the 1-component of the macroscopic field is nonzero. The expressions for P_F and P_ρ in momentum space are

$$\begin{aligned}P_F(t,t',|\mathbf{p}|) = -\frac{\lambda}{3N}\Bigg\{&H_F(t,t',|\mathbf{p}|)\\ &-\int_{t_0}^{t}\mathrm{d}t''\Big[H_\rho(t,t'',|\mathbf{p}|)I_F(t'',t',|\mathbf{p}|)\\ &\qquad + I_\rho(t,t'',|\mathbf{p}|)\Big(H_F(t'',t',|\mathbf{p}|) + J_F(t'',t'',|\mathbf{p}|)\Big)\Big]\\ &+\int_{t_0}^{t'}\mathrm{d}t''\Big[H_F(t,t'',|\mathbf{p}|)I_\rho(t'',t',|\mathbf{p}|)\\ &\qquad + I_F(t,t'',|\mathbf{p}|)\Big(H_\rho(t'',t',|\mathbf{p}|) + J_\rho(t'',t',|\mathbf{p}|)\Big)\Big]\Bigg\},\end{aligned} \tag{2.95a}$$

$$\begin{aligned}P_\rho(t,t',|\mathbf{p}|) = -\frac{\lambda}{3N}\Bigg\{&H_\rho(t,t',|\mathbf{p}|)\\ &-\int_{t'}^{t}\mathrm{d}t''\Big[H_\rho(t,t'',|\mathbf{p}|)I_\rho(t'',t',|\mathbf{p}|)\\ &\qquad + I_\rho(t,t'',|\mathbf{p}|)\Big(H_\rho(t'',t',|\mathbf{p}|) + J_\rho(t'',t'',|\mathbf{p}|)\Big)\Big]\Bigg\},\end{aligned} \tag{2.95b}$$

using the nested integrals

$$J_F(t'',t',|\mathbf{p}|) = \int_{t_0}^{t'}\mathrm{d}s\; H_F(t'',s,|\mathbf{p}|)I_\rho(s,t',|\mathbf{p}|) - \int_{t_0}^{t''}\mathrm{d}s\; H_\rho(t'',s,|\mathbf{p}|)I_F(s,t',|\mathbf{p}|), \tag{2.96a}$$

$$J_\rho(t'',t',|\mathbf{p}|) = \int_{t''}^{t'}\mathrm{d}s\; H_\rho(t'',s,|\mathbf{p}|)I_\rho(s,t',|\mathbf{p}|). \tag{2.96b}$$

These are all expressions needed in order to compute the self-energies at NLO in the large-N expansion.

The energy-momentum tensor

Since the dynamics deduced from an effective action automatically guarantee that the energy of the system is conserved, an important observable to compute is the energy density. We obtain the energy density from the energy-momentum tensor, which is defined as the variation of the effective action with respect to the metric $g_{\mu\nu}(x)$,

$$T_{\mu\nu}(x) = \frac{2}{\sqrt{-g(x)}} \frac{\delta\Gamma[\phi, G, g^{\mu\nu}]}{\delta g^{\mu\nu}}\bigg|_{g_{\mu\nu}=\eta_{\mu\nu}} , \tag{2.97}$$

with $-g(x) \equiv \det g_{\mu\nu}(x)$ and spacetime coordinate x. While doing so, the metric is assumed to be a general spacetime dependent metric. The result is evaluated at $g_{\mu\nu}$ equal to the Minkowski metric $\eta_{\mu\nu} = \mathrm{diag}(+1, -1, -1, -1)$.

For an explicit calculation of the energy-momentum tensor at NLO in the large N expansion we refer to Appendix C in [62]. Here, we only summarize the results for the energy density, which is obtained from T_{00}. The energy density consists of a contribution from the classical action,

$$\varepsilon^{\mathrm{cl}}(t) = \left[\frac{1}{2}\partial_t\phi_a(t)\partial_t\phi_a(t) + \frac{1}{2}m^2\phi_a(t)\phi_a(t) + \frac{\lambda}{4!\,N}\Big(\phi_a(t)\phi_a(t)\Big)^2\right] , \tag{2.98}$$

and contributions from the bosonic mode energy,

$$\begin{aligned}\varepsilon^{\phi}(t, |\mathbf{p}|) = \frac{1}{2}&\left[\partial_t\partial_{t'}F_{aa}(t, t', |\mathbf{p}|)\Big|_{t=t'} + |\mathbf{p}|^2 F_{aa}(t, t, |\mathbf{p}|) + M^2_{\mathrm{cl},ab}(t)F_{ba}(t, t, |\mathbf{p}|)\right]\\ &+ \frac{\lambda}{4!\,N}F_{aa}(t, t, |\mathbf{p}|)\int_{\mathbf{q}} F_{aa}(t, t, |\mathbf{q}|)\\ &+ \frac{1}{2}\left[I_F(t, t, |\mathbf{p}|) + P_F(t, t, |\mathbf{p}|) + \frac{\lambda}{3N}H_F(t, t, |\mathbf{p}|)\right] .\end{aligned} \tag{2.99}$$

Together, they sum up to the total energy density according to

$$\varepsilon(t) = \varepsilon^{\mathrm{cl}}(t) + \int_{\mathbf{p}} \varepsilon^{\phi}(t, |\mathbf{p}|) . \tag{2.100}$$

We note that the energy density is an equal-time quantity.

2.4 The quark-meson model

This section outlines the two-particle irreducible (2PI) effective action framework for the quark-meson model. The exact evolution equations are presented and the approximations relevant for our analysis in Chapter 4 are introduced.

The quark-meson model is an effective low-energy theory for quantum chromodynamics (QCD) that incorporates the physics of chiral symmetry breaking of the two lightest quark flavors while integrating out the explicit dynamics of gluons, see e.g. [63]. More details about the physics of this model are provided in Section 4.2.

We consider the $N_f = 2$ light quark flavors up and down with an identical current quark mass $m_{u/d} = m_\psi$, coupled to a scalar mesonic field and a triplet of pseudoscalar pion fields. The classical action reads

$$S[\bar{\psi},\psi,\sigma,\pi] = \int \mathrm{d}^4x \Big[\bar{\psi}\left(i\gamma^\mu\partial_\mu - m_\psi\right)\psi - \frac{g}{N_f}\bar{\psi}\left(\sigma + i\gamma_5\tau^\alpha\pi^\alpha\right)\psi + \frac{1}{2}\left(\partial_\mu\sigma\partial^\mu\sigma + \partial_\mu\pi^\alpha\partial^\mu\pi^\alpha\right)$$

$$- \frac{1}{2}m^2\left(\sigma^2 + \pi^\alpha\pi^\alpha\right) - \frac{\lambda}{4!\,N}\left(\sigma^2+\pi^\alpha\pi^\alpha\right)^2 \Big], \tag{2.101}$$

with τ^α $(\alpha = 1,2,3)$ denoting the Pauli and γ^μ $(\mu = 0,1,2,3)$ the Dirac matrices, while spinor and flavor indices are suppressed. In (2.101), m_ψ is the current quark mass and m^2 the mesonic mass parameter. The lowest mass states of the mesonic scalar-pseudoscalar multiplet, σ and $\vec{\pi}$, are given by the $N = 4$ scalar components of the bosonic field $\varphi_a(x) = \{\sigma(x), \pi^1(x), \pi^2(x), \pi^3(x)\}$ interacting via a quartic self-coupling λ. The boson fields φ_a are coupled to the fermion fields ψ and $\bar{\psi} = \psi^\dagger\gamma^0$ via the Yukawa interaction g, which is expressed in terms of $h = g/N_f$ in the following.

The π mesons play the role of the light Goldstone bosons in the chirally broken phase whereas the σ meson represents the heavy mode. Assigning these roles to the components of the scalar field is achieved by choosing a coordinate system in field space where the field expectation value has a single component defining the σ direction, i.e. $\phi_a(x) = \langle\varphi_a(x)\rangle = \{\langle\sigma(x)\rangle\,,\, 0,\, 0,\, 0\,\}$.

The purely bosonic sector of the quark-meson model corresponds to a relativistic scalar field theory as discussed in Section 2.3, with $N = 4$ and nonvanishing field expectation value given by $\langle\sigma\rangle$. For the quark-meson model, the mesonic two-point function can be written as $G = \mathrm{diag}(G_\sigma, G_\pi, G_\pi, G_\pi)$, interpreting the longitudinal and transverse components as the sigma meson and pion propagators, respectively. The corresponding exact evolution equations are obtained by replacing $\parallel$ and $\perp$ by σ and π in (2.77). In the following, we discuss the quark sector and all additional contributions originating from it.

The construction of the 2PI effective action can be generalized to fermionic fields, see [41] for a derivation. We assume that the time-ordered fermionic two-point function $\Delta = \langle T_{\mathcal{C}}\psi(x)\bar{\psi}(y)\rangle$, with $\mathcal{C}$ denoting the closed time path, is diagonal in flavor space. The 2PI effective action of the quark-meson model can be written as [41]

$$\Gamma[\phi,G,\Delta] = S[\phi] + \frac{i}{2}\,\mathrm{Tr}\ln\left[G^{-1}\right] + \frac{i}{2}\,\mathrm{Tr}\left[G_{\mathrm{cl}}^{-1}(\phi)G\right]$$

$$- i\,\mathrm{Tr}\ln\left[\Delta^{-1}\right] - i\,\mathrm{Tr}\left[\Delta_{\mathrm{cl}}^{-1}(\phi)\Delta\right] + \Gamma_2[\phi,G,\Delta] + \mathrm{const.}\,, \tag{2.102}$$

where S is the classical action given by (2.101), and G_{cl}^{-1} and $\Delta_{\mathrm{cl}}^{-1}$ are the classical meson and quark propagators derived from it. As before, traces, logarithms and products have to be evaluated in the functional sense. Since the expectation values of fermionic fields vanish, i.e. $\langle\psi(x)\rangle = \langle\bar{\psi}(x)\rangle = 0$, fermions do not contribute to the classical action term in Γ. In the quark-meson model, the 2PI diagrams contained in $\Gamma_2[\phi,G,\Delta]$ can depend on the macroscopic field as well as the meson and quark propagator lines denoted by G and Δ, respectively. In addition to the stationary conditions (2.51), one needs to take into account the stationary condition

$$\left.\frac{\delta\Gamma[\phi,G,\Delta]}{\delta\Delta(x,y)}\right|_{\phi,\Delta=\bar{\Delta}(\phi)} = 0\,,$$

which leads to the equation of motion for the quark propagator. In direct analogy to (2.53), the evolution equation of the quark propagator can be written as

$$i\bar{\Delta}^{-1}(x,y;\phi) = i\Delta^{-1}_{\mathrm{cl},ij}(x,y;\phi) - i\Sigma^{\psi}(x,y;\phi,G,\Delta)\Big|_{\Delta=\bar{\Delta}(\phi)}, \tag{2.103}$$

where the classical inverse propagator and the self-energy are defined as

$$i\Delta^{-1}_{\mathrm{cl}}(x,y;\phi) \equiv \frac{\delta^2 S[\psi]}{\delta\bar{\psi}(x)\delta\psi(y)}, \tag{2.104}$$

$$i\Sigma^{\psi}(x,y;\phi,G,\Delta) \equiv +1\frac{\delta\Gamma_2[\phi,G,\Delta]}{\delta\Delta(x,y)}, \tag{2.105}$$

with a plus sign on the right-hand side of (2.105) for fermionic fields. The classical inverse propagator obtained from the classical action (2.101) reads

$$i\Delta^{-1}_{\mathrm{cl}}(x,y;\phi) = \left[i\gamma^{\mu}\partial_{\mu} - M_{\psi}(x;\phi)\right]\delta_{\mathcal{C}}(x-y), \tag{2.106}$$

where the δ-function is evaluated along the closed time path $\mathcal{C}$ for the temporal coordinate, and the classical effective mass is given by $M_{\psi}(x;\phi) = m_{\psi} + h\langle\sigma(x)\rangle$ since (2.106) is evaluated at the field expectation value $\phi_a(x) = \{\langle\sigma(x)\rangle, 0, 0, 0\}$.

2.4.1 Spectral and statistical components

As in the relativistic scalar field theory, we decompose all two-point functions into spectral and statistical components. The decomposition of the quark propagator and the quark self-energy can be written as

$$\Delta^{\psi}(x,y) = F^{\psi}(x,y) - \frac{i}{2}\rho^{\psi}(x,y)\,\mathrm{sgn}_{\mathcal{C}}(x^0-y^0), \tag{2.107}$$

$$\Sigma^{\psi}(x,y) = C^{\psi}(x,y) - \frac{i}{2}A^{\psi}(x,y)\,\mathrm{sgn}_{\mathcal{C}}(x^0-y^0), \tag{2.108}$$

where the sign functions are taken along the closed time path $\mathcal{C}$. The components C^{ψ} and A^{ψ} represent the symmetric and antisymmetric parts of the quark self-energy.

The fermionic statistical and spectral functions are defined as the commutator, denoted by squared brackets, and the anticommutator, denoted by curly brackets,

$$F^{\psi}_{AB}(x,y) = \frac{1}{2}\left\langle[\psi_A(x),\bar{\psi}_B(y)]\right\rangle, \tag{2.109a}$$

$$\rho^{\psi}_{AB}(x,y) = i\left\langle\{\psi_A(x),\bar{\psi}_B(y)\}\right\rangle, \tag{2.109b}$$

where the Dirac spinor indices $A,B = 1,2,3,4$ are written explicitly. They obey the hermiticity properties $\left[\rho^{\psi}(y,x)\right]^{\dagger} = -\gamma^0\rho^{\psi}(x,y)\gamma^0$ and $\left[F^{\psi}(y,x)\right]^{\dagger} = \gamma^0F^{\psi}(x,y)\gamma^0$.

2.4.2 Symmetries

The quark two-point functions constitute 4 × 4 matrices in spinor space. Although fermionic two-point functions have 16 Dirac components, the number of independent components can be reduced by symmetry arguments. It is convenient to apply the Lorentz decomposition, according to which any quantity $M = M(x, y)$ with two indices in Dirac space can be decomposed as

$$M = M_S + i\gamma_5 M_P + \gamma_\mu M_V^\mu + \gamma_\mu \gamma_5 M_A^\mu + \frac{1}{2}\sigma_{\mu\nu} M_T^{\mu\nu} \,, \tag{2.110}$$

with $\sigma_{\mu\nu} = \frac{i}{2}\left[\gamma_\mu, \gamma_\nu\right]$ and $\gamma_5 = i\gamma^0\gamma^1\gamma^2\gamma^3$. In this basis, the scalar, pseudo-scalar, vector, axial vector, and tensor components are given by

$$\begin{aligned}
M_S &= \frac{1}{4}\,\mathrm{Tr}\,[M] \,, \\
M_P &= \frac{1}{4}\,\mathrm{Tr}\,[-i\gamma_5 M] \,, \\
M_V^\mu &= \frac{1}{4}\,\mathrm{Tr}\,[\gamma^\mu M] \,, \\
M_A^\mu &= \frac{1}{4}\,\mathrm{Tr}\,[\gamma_5\gamma^\mu M] \,, \\
M_T^{\mu\nu} &= \frac{1}{4}\,\mathrm{Tr}\,[\sigma^{\mu\nu} M] \,,
\end{aligned}$$

where the trace acts in Dirac space.

Assuming that the system is homogeneous and isotropic in space, and that parity as well as CP invariance hold, the only nonvanishing components of the fermionic two-point functions are the scalar, vector and $0i$-tensor components. We note that if one additionally requires invariance under chiral symmetry transformations, only the vector part remains [61]. As a consequence of isotropy, the momentum dependence of the various components can be further simplified to

$$M_S(x^0, y^0, \mathbf{p}) = M_S(x^0, y^0, |\mathbf{p}|) \,, \qquad M_V^0(x^0, y^0, \mathbf{p}) = M_0(x^0, y^0, |\mathbf{p}|) \,, \tag{2.111a}$$

$$M_V^i(x^0, y^0, \mathbf{p}) = \frac{p^i}{p} M_V(x^0, y^0, |\mathbf{p}|) \,, \qquad M_T^{0i}(x^0, y^0, \mathbf{p}) = \frac{p^i}{p} M_T(x^0, y^0, |\mathbf{p}|) \,. \tag{2.111b}$$

In this work we refer to the functions M_S, M_0, M_V and M_T on the right-hand sides of (2.111) as the scalar, vector, vector-zero and tensor components, respectively. These components are deployed to analyze the quark sector. Applying the Lorentz decomposition to the statistical and spectral quark propagators and self-energies, one can derive evolution equations for these four components.

2.4.3 Exact evolution equations

In this section we present the exact evolution equations for the quark-meson model. The stationary conditions of the 2PI effective action lead to the equations of motion of the macroscopic field, the meson and the quark two-point functions. We refer to [55, 61] for a derivation of the fermionic evolution equations.

In comparison to (2.74) the equation of motion for the field expectation value $\langle\sigma\rangle$ obtains an additional term due to the quark sector. The field equation of the quark-meson model reads

$$\left[\partial_t^2 + M^2(t)\right]\langle\sigma(t)\rangle = 4g\int_{\mathbf{p}} F_S(t, t, \mathbf{p}) + \frac{\delta\Gamma_2[G, \Delta, \phi]}{\delta\,\langle\sigma(t)\rangle} \,, \tag{2.112}$$

with

$$M^2(t) = m^2 + \frac{\lambda}{6N}\left\langle \sigma(t)\right\rangle^2 + \frac{\lambda}{6N}\left(3\int_{\mathbf{p}} F_\sigma(t,t,\mathbf{p}) + (N-1)\int_{\mathbf{p}} F_\pi(t,t,\mathbf{p})\right) . \tag{2.113}$$

The additional F_S-term arises in the chirally broken case and describes the fermion backreaction on the field. It pushes the field to nonzero field expectation values even in the case where $\langle\sigma(t)\rangle = \partial_t \langle\sigma(t)\rangle = 0$ at initial time. The functional $\Gamma_2[G,\Delta,\phi]$ contains all contributions from two-particle irreducible vacuum diagrams implying that the Γ_2-term in (2.112) contains all nonlocal contributions to the interactions of the spectral and statistical functions with the macroscopic field.

The exact evolution equations for the mesons are given by (2.77), where longitudinal and transverse components are interpreted as the sigma and pi mesons in the quark-meson model. Additional contributions due to the quarks only enter in the self-energy terms, for which we provide expressions in Section 2.4.4, where the considered approximation is discussed.

In the quark sector we take into account the four components introduced in (2.111): scalar, vector-zero, vector and tensor. The evolution equations for the quark statistical functions are

$$\begin{aligned}
i\partial_t F_S(t,t',|\mathbf{p}|) &= -i|\mathbf{p}|\; F_T(t,t',|\mathbf{p}|) + M_\psi(t) F_0(t,t',|\mathbf{p}|) \\
&\quad + \int_{t_0}^{t} \mathrm{d}t'' \Big[A_S(t,t'',|\mathbf{p}|)\; F_0(t'',t',|\mathbf{p}|) + A_0(t,t'',|\mathbf{p}|)\; F_S(t'',t',|\mathbf{p}|) \\
&\qquad\qquad + iA_V(t,t'',|\mathbf{p}|)\; F_T(t'',t',|\mathbf{p}|) - iA_T(t,t'',|\mathbf{p}|)\; F_V(t'',t',|\mathbf{p}|) \Big] \\
&\quad + \int_{t_0}^{t'} \mathrm{d}t'' \Big[- C_S(t,t'',|\mathbf{p}|)\; \rho_0(t'',t',|\mathbf{p}|) - C_0(t,t'',|\mathbf{p}|)\; \rho_S(t'',t',|\mathbf{p}|) \\
&\qquad\qquad - iC_V(t,t'',|\mathbf{p}|)\; \rho_T(t'',t',|\mathbf{p}|) + iC_T(t,t'',|\mathbf{p}|)\; \rho_V(t'',t',|\mathbf{p}|) \Big],
\end{aligned} \tag{2.114a}$$

$$\begin{aligned}
i\partial_t F_0(t,t',|\mathbf{p}|) &= |\mathbf{p}| F_V(t,t',|\mathbf{p}|) + M_\psi(t) F_S(t,t',|\mathbf{p}|) \\
&\quad + \int_{t_0}^{t} \mathrm{d}t'' \Big[A_S(t,t'',|\mathbf{p}|)\; F_S(t'',t',|\mathbf{p}|) - A_T(t,t'',|\mathbf{p}|)\; F_T(t'',t',|\mathbf{p}|) \\
&\qquad\qquad + A_0(t,t'',|\mathbf{p}|)\; F_0(t'',t',|\mathbf{p}|) - A_V(t,t'',|\mathbf{p}|)\; F_V(t'',t',|\mathbf{p}|) \Big] \\
&\quad + \int_{t_0}^{t'} \mathrm{d}t'' \Big[- C_S(t,t'',|\mathbf{p}|)\; \rho_S(t'',t',|\mathbf{p}|) + C_T(t,t'',|\mathbf{p}|)\; \rho_T(t'',t',|\mathbf{p}|) \\
&\qquad\qquad - C_0(t,t'',|\mathbf{p}|)\; \rho_0(t'',t',|\mathbf{p}|) + C_V(t,t'',|\mathbf{p}|)\; \rho_V(t'',t',|\mathbf{p}|) \Big],
\end{aligned} \tag{2.114b}$$

$$\begin{aligned}
\partial_t F_V(t,t',|\mathbf{p}|) &= -i|\mathbf{p}| F_0(t,t',|\mathbf{p}|) + M_\psi(t) F_T(t,t',|\mathbf{p}|) \\
&\quad + \int_{t_0}^{t} \mathrm{d}t'' \Big[- iA_0(t,t'',|\mathbf{p}|)\; F_V(t'',t',|\mathbf{p}|) + iA_V(t,t'',|\mathbf{p}|)\; F_0(t'',t',|\mathbf{p}|) \\
&\qquad\qquad + A_S(t,t'',|\mathbf{p}|)\; F_T(t'',t',|\mathbf{p}|) + A_T(t,t'',|\mathbf{p}|)\; F_S(t'',t',|\mathbf{p}|) \Big] \\
&\quad + \int_{t_0}^{t'} \mathrm{d}t'' \Big[+ iC_0(t,t'',|\mathbf{p}|)\; \rho_V(t'',t',|\mathbf{p}|) - iC_V(t,t'',|\mathbf{p}|)\; \rho_0(t'',t',|\mathbf{p}|)
\end{aligned}$$

$$- C_S(t,t'',|\mathbf{p}|)\;\rho_T(t'',t',|\mathbf{p}|) - C_T(t,t'',|\mathbf{p}|)\;\rho_S(t'',t',|\mathbf{p}|)\Big], \qquad (2.114\text{c})$$

$$\begin{aligned}\partial_t F_T(t,t',|\mathbf{p}|) = {} & |\mathbf{p}| F_S(t,t',|\mathbf{p}|) - M_\psi(t) F_V(t,t',|\mathbf{p}|)\\ & + \int_{t_0}^{t} \mathrm{d}t''\Big[- A_S(t,t'',|\mathbf{p}|)\;F_V(t'',t',|\mathbf{p}|) - A_V(t,t'',|\mathbf{p}|)\;F_S(t'',t',|\mathbf{p}|)\\ & \qquad - iA_0(t,t'',|\mathbf{p}|)\;F_T(t'',t',|\mathbf{p}|) + iA_T(t,t'',|\mathbf{p}|)\;F_0(t'',t',|\mathbf{p}|)\Big]\\ & + \int_{t_0}^{t'} \mathrm{d}t''\Big[+ C_S(t,t'',|\mathbf{p}|)\;\rho_V(t'',t',|\mathbf{p}|) + C_V(t,t'',|\mathbf{p}|)\;\rho_S(t'',t',|\mathbf{p}|)\\ & \qquad + iC_0(t,t'',|\mathbf{p}|)\;\rho_T(t'',t',|\mathbf{p}|) - iC_T(t,t'',|\mathbf{p}|)\;\rho_0(t'',t',|\mathbf{p}|)\Big], \end{aligned} \qquad (2.114\text{d})$$

and for the quark spectral functions

$$\begin{aligned} i\partial_t \rho_S(t,t',|\mathbf{p}|) = {} & -i|\mathbf{p}|\;\rho_T(t,t',|\mathbf{p}|) + M_\psi(t)\rho_0(t,t',|\mathbf{p}|)\\ & + \int_{t'}^{t} \mathrm{d}t''\Big[A_S(t,t'',|\mathbf{p}|)\;\rho_0(t'',t',|\mathbf{p}|) + A_0(t,t'',|\mathbf{p}|)\;\rho_S(t'',t',|\mathbf{p}|)\\ & \qquad + iA_V(t,t'',|\mathbf{p}|)\;\rho_T(t'',t',|\mathbf{p}|) - iA_T(t,t'',|\mathbf{p}|)\;\rho_V(t'',t',|\mathbf{p}|)\Big], \end{aligned} \qquad (2.115\text{a})$$

$$\begin{aligned} i\partial_t \rho_0(t,t',|\mathbf{p}|) = {} & |\mathbf{p}|\rho_V(t,t',|\mathbf{p}|) + M_\psi(t)\rho_S(t,t',|\mathbf{p}|)\\ & + \int_{t'}^{t} \mathrm{d}t''\Big[A_S(t,t'',|\mathbf{p}|)\;\rho_S(t'',t',|\mathbf{p}|) - A_T(t,t'',|\mathbf{p}|)\;\rho_T(t'',t',|\mathbf{p}|)\\ & \qquad + A_0(t,t'',|\mathbf{p}|)\;\rho_0(t'',t',|\mathbf{p}|) - A_V(t,t'',|\mathbf{p}|)\;\rho_V(t'',t',|\mathbf{p}|)\Big], \end{aligned} \qquad (2.115\text{b})$$

$$\begin{aligned} \partial_t \rho_V(t,t',|\mathbf{p}|) = {} & -i|\mathbf{p}|\rho_0(t,t',|\mathbf{p}|) + M_\psi(t)\rho_T(t,t',|\mathbf{p}|)\\ & + \int_{t'}^{t} \mathrm{d}t''\Big[- iA_0(t,t'',|\mathbf{p}|)\;\rho_V(t'',t',|\mathbf{p}|) + iA_V(t,t'',|\mathbf{p}|)\;\rho_0(t'',t',|\mathbf{p}|)\\ & \qquad + A_S(t,t'',|\mathbf{p}|)\;\rho_T(t'',t',|\mathbf{p}|) + A_T(t,t'',|\mathbf{p}|)\;\rho_S(t'',t',|\mathbf{p}|)\Big], \end{aligned} \qquad (2.115\text{c})$$

$$\begin{aligned} \partial_t \rho_T(t,t',|\mathbf{p}|) = {} & |\mathbf{p}|\rho_S(t,t',|\mathbf{p}|) - M_\psi(t)\rho_V(t,t',|\mathbf{p}|)\\ & + \int_{t'}^{t} \mathrm{d}t''\Big[- A_S(t,t'',|\mathbf{p}|)\;\rho_V(t'',t',|\mathbf{p}|) - A_V(t,t'',|\mathbf{p}|)\;\rho_S(t'',t',|\mathbf{p}|)\\ & \qquad - iA_0(t,t'',|\mathbf{p}|)\;\rho_T(t'',t',|\mathbf{p}|) + iA_T(t,t'',|\mathbf{p}|)\;\rho_0(t'',t',|\mathbf{p}|)\Big], \end{aligned} \qquad (2.115\text{d})$$

where the effective fermion mass is given by $M_\psi(x) = m_\psi + h\,\langle\sigma(x)\rangle$, which also appears in (2.106). We note that the factors of i are necessary because the vector-zero component is imaginary while all other components are real.

2.4.4 Approximations at NLO

In order to carry out explicit computations, it is necessary to approximate the 2PI effective action. A truncation of the quantum fluctuations contained in the 2PI effective action allows us to derive

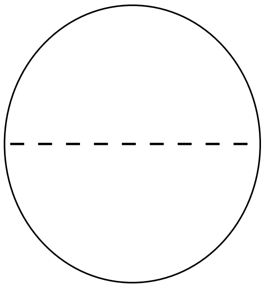

Figure 2.5: The fermion-boson-loop diagram. A full line indicates a fermion propagator while a dashed line denotes a boson propagator.

expressions for the self-energies entering the evolution equations. In this section we introduce our approximation scheme and present the therefrom derived self-energy terms.

Our work deploys an expansion to next-to-leading order (NLO) in $1/N$ and g, where $N = 4$ is the number of scalar field components and g the Yukawa coupling. In the meson sector, we employ the large-N expansion discussed in Section 2.3.4, which provides a controlled nonperturbative approximation scheme. Taking into account quantum fluctuations up to NLO includes scattering as well as off-shell and memory effects, and is capable of handling relatively large couplings [60]. In the quark sector, a loop expansion in g to NLO contributes in form of the fermion-boson-loop originally discussed in [61], which can be represented by the diagram shown in Figure 2.5.

The 2PI diagrams relevant for our approximation can be structured according to

$$\Gamma_2[\phi, G, \Delta] = \Gamma_2^{\mathrm{LO}}[\phi, G] + \Gamma_2^{\mathrm{NLO}}[\phi, G] + \Gamma_2[\Delta, G]\,, \tag{2.116}$$

with the first two terms describing the LO and NLO contributions of the bosonic sector given by (2.81) and (2.83), while the last term contains the fermion-boson-loop,

$$\Gamma_2[\Delta, G] = -ih^2 \frac{N_f}{2} \int_{x,y} \mathrm{Tr}\left[\Delta(x,y)\Delta(y,x)\right] G_{aa}(x,y)\,, \tag{2.117}$$

with the trace acting in Dirac space.

The self-energy terms for the chirally symmetric case of $m_\psi = 0$ have been derived in [61, 64] while a computation of the self-energy contributions for nonvanishing fermion bare mass m_ψ can be found in [55]. In the following, we provide a summary of the relevant expressions in this approximation.

The field equation

Apart from the additional term in the field equation (2.112), no further changes arise from the presence of quarks. One finds that

$$\frac{\delta\Gamma_2[\phi, G, \Delta]}{\delta\left\langle\sigma(t)\right\rangle} = \frac{\delta\Gamma_2[\phi, G]}{\delta\left\langle\sigma(t)\right\rangle} \tag{2.118}$$

with the right-hand side given by (2.87).

The self-energies

We first provide expressions for the meson and subsequently for the quark self-energies. All terms are presented in coordinate space where the self-energies can be written as direct products. Thereby the quark two-point functions are expressed in terms of the Lorentz components introduced in (2.110), assuming that they suffice the symmetry properties (2.111) in momentum space.

While the local parts of the bosonic self-energies are the same as in the scalar field theory, the nonlocal self-energy terms obtain additional contributions from the fermion-boson-loop (2.117). In coordinate space the relevant expressions for the meson self-energies read

$$\begin{aligned} C^{\phi}_{ab}(x,y) &= C_{ab}(x,y) \\ &\quad - 4h^2 N_f \delta_{ab} \Bigg\{ F^{\mu}_V(x,y) F_{V,\mu}(x,y) - F_S(x,y) F_S(x,y) - F^{0i}_T(x,y) F^{0i}_T(x,y) \\ &\qquad - \frac{1}{4}\Big[\rho^{\mu}_V(x,y)\rho_{V,\mu}(x,y) - \rho_S(x,y)\rho_S(x,y) - \rho^{0i}_T(x,y)\rho^{0i}_T(x,y)\Big]\Bigg\}, \end{aligned} \tag{2.119a}$$

$$\begin{aligned} A^{\phi}_{ab}(x,y) &= A_{ab}(x,y) \\ &\quad - 8h^2 N_f \delta_{ab} \Bigg\{ \rho^{\mu}_V(x,y) F_{V,\mu}(x,y) - \rho_S(x,y) F_S(x,y) - \rho^{0i}_T(x,y) F^{0i}_T(x,y) \Bigg\}, \end{aligned} \tag{2.119b}$$

where A^{ϕ} and C^{ϕ} are the bosonic self-energy expressions for the quark-meson model while A and C correspond to the self-energies of the real scalar field theory with expressions given by (2.91). We note that spatial isotropy and homogeneity imply that the spacetime dependence is $(x,y) = (x^0, y^0, |\mathbf{x}-\mathbf{y}|)$.

The statistical and spectral parts of the quark self-energy are written in terms of the relevant Lorentz components. The statistical fermion self-energy can be expressed in terms of

$$\begin{aligned} C_S(x,y) = -h^2 \Bigg\{ & F_S(x,y)\Big[F_{\sigma}(x,y) + (N-1)F_{\pi}(x,y)\Big] \\ & - \frac{1}{4}\rho_S(x,y)\Big[\rho_{\sigma}(x,y) + (N-1)\rho_{\pi}(x,y)\Big]\Bigg\}, \end{aligned} \tag{2.120a}$$

$$\begin{aligned} C^{\mu}_V(x,y) = -h^2 \Bigg\{ & F^{\mu}_V(x,y)\Big[F_{\sigma}(x,y) + (N-1)F_{\pi}(x,y)\Big] \\ & - \frac{1}{4}\rho^{\mu}_V(x,y)\Big[\rho_{\sigma}(x,y) + (N-1)\rho_{\pi}(x,y)\Big]\Bigg\}, \end{aligned} \tag{2.120b}$$

$$\begin{aligned} C^{0i}_T(x,y) = -h^2 \Bigg\{ & F^{0i}_T(x,y)\Big[F_{\sigma}(x,y) + (N-1)F_{\pi}(x,y)\Big] \\ & - \frac{1}{4}\rho^{0i}_T(x,y)\Big[\rho_{\sigma}(x,y) + (N-1)\rho_{\pi}(x,y)\Big]\Bigg\}, \end{aligned} \tag{2.120c}$$

while the spectral part is given by

$$A_S(x,y) = -h^2 \Bigg\{ F_S(x,y)\Big[\rho_{\sigma}(x,y) + (N-1)\rho_{\pi}(x,y)\Big]$$

$$+ \rho_S(x,y)\Big[F_\sigma(x,y) + (N-1)F_\pi(x,y)\Big]\Bigg\}, \tag{2.121a}$$

$$\begin{aligned} A_V^\mu(x,y) = -h^2\Bigg\{ & F_V^\mu(x,y)\Big[\rho_\sigma(x,y) + (N-1)\rho_\pi(x,y)\Big] \\ & + \rho_V^\mu(x,y)\Big[F_\sigma(x,y) + (N-1)F_\pi(x,y)\Big]\Bigg\}, \end{aligned} \tag{2.121b}$$

$$\begin{aligned} A_T^{0i}(x,y) = -h^2\Bigg\{ & F_T^{0i}(x,y)\Big[\rho_\sigma(x,y) + (N-1)\rho_\pi(x,y)\Big] \\ & + \rho_T^{0i}(x,y)\Big[F_\sigma(x,y) + (N-1)F_\pi(x,y)\Big]\Bigg\}, \end{aligned} \tag{2.121c}$$

where again spatial isotropy and homogeneity are implied.

The energy-momentum tensor

In the quark-meson model, the energy density receives contributions from the bosonic as well as the fermionic sectors. Hence, the total energy density can be written as

$$\frac{E(t)}{V} = \varepsilon^{\mathrm{cl}}(t) + \int_{\mathbf{p}} \left[\ \varepsilon^{\phi}(t,|\mathbf{p}|) + \varepsilon^{\psi}(t,|\mathbf{p}|)\ \right] , \tag{2.122}$$

where the classical energy density $\varepsilon^{\mathrm{cl}}$ is given by (2.98), the bosonic mode energy density ε^{ϕ} by (2.99) and the fermionic mode energy density ε^{ψ} by

$$\varepsilon^{\psi}(t,|\mathbf{p}|) = -16\Big[|\mathbf{p}|F_V(t,t,|\mathbf{p}|) + M_\psi(x)F_S(t,t,|\mathbf{p}|) + R(t,|\mathbf{p}|)\Big], \tag{2.123}$$

with

$$\begin{aligned} R(x^0,|\mathbf{p}|) = \ & \int_0^{x^0} \mathrm{d}y^0 \Big[+ A_S(x^0,y^0,|\mathbf{p}|)\ F_S(y^0,x^0,|\mathbf{p}|) - A_T(x^0,y^0,|\mathbf{p}|)\ F_T(y^0,x^0,|\mathbf{p}|) \\ & \qquad + A_0(x^0,y^0,|\mathbf{p}|)\ F_0(y^0,x^0,|\mathbf{p}|) - A_V(x^0,y^0,|\mathbf{p}|)\ F_V(y^0,x^0,|\mathbf{p}|)\Big] \\ + & \int_0^{x^0} \mathrm{d}y^0 \Big[- C_S(x^0,y^0,|\mathbf{p}|)\ \rho_S(y^0,x^0,|\mathbf{p}|) + C_T(x^0,y^0,|\mathbf{p}|)\ \rho_T(y^0,x^0,|\mathbf{p}|) \\ & \qquad - C_0(x^0,y^0,|\mathbf{p}|)\ \rho_0(y^0,x^0,|\mathbf{p}|) + C_V(x^0,y^0,|\mathbf{p}|)\ \rho_V(y^0,x^0,|\mathbf{p}|)\Big], \end{aligned} \tag{2.124}$$

which corresponds to memory integrals of the evolution equation for F_0 evaluated at $x^0 = t = t'$.

Chapter 3

Universal dynamics of relativistic scalar fields

This chapter aims to explore the far-from-equilibrium dynamics of an isolated quantum many-body system described by a relativistic scalar field theory. It is based on "*Spectral, statistical and vertex functions in scalar quantum field theory far from equilibrium*" by L. Shen and J. Berges, published in Phys. Rev. D **101**, 056009 (2020) [65], where figures and large parts of the text are taken from. While J. Berges guided the project and participated in writing the text, I performed the numerical simulations, carried out the data analysis and contributed significantly to the text. The employed code was developed by A. Rothkopf and is publicly accessible via the Zenodo repository under [66].

Our analysis builds on the computation of the nonequilibrium dynamics of a relativistic scalar field theory starting from overoccupied initial conditions, for which we deploy the two-particle irreducible (2PI) effective action techniques introduced in the previous chapter. As the system approaches the infrared nonthermal fixed point characterized by self-similar scaling, universal properties of the particle distribution function as well as the effective four-vertex can be studied. In addition, we investigate the evolution of the unequal-time two-point correlation functions, which contain information about the quasiparticle content of the system. Our analysis shows that the fluctuation-dissipation relation is violated in the nonperturbative infrared regime.

This chapter is organized as follows: We begin with a short motivation for our work in Section 3.1. In Section 3.2 we introduce the model and specify the class of far-from-equilibrium initial conditions that we consider. The results for the equal-time two-point correlation functions and the effective four-vertex are presented in Section 3.3. We extract self-similar scaling properties for a wide range of couplings, and compare the numerical results to analytical estimates. Section 3.4 shows our results for the unequal-time two-point correlation functions, where spectral as well as statistical functions are analyzed. We identify three characteristic momentum regimes and investigate the role of the fluctuation-dissipation relation in each of these regimes. Finally, we conclude in Section 3.5.

The discussion is supplemented by a number of appendices containing more details about the work of this chapter. In Appendix 3.A we present analytical results for the free scalar field theory, from which one can gain more intuition for the quantities deployed within the 2PI framework. Appendix 3.B provides a detailed description of the numerical methods, including discretization, initial conditions, and numerical stability checks. How we numerically compute scaling exponents and Wigner transformations is outlined in Appendices 3.C and 3.D, respectively. A calculation of the vertex functions can be found in Appendix 3.E.

3.1 Introduction

The nonequilibrium dynamics of relativistic scalar quantum fields form an important cornerstone in our understanding of the evolution of the early universe. According to the theory of inflation, the early universe undergoes an epoch of accelerated expansion for a short time after the big bang. The inflationary paradigm provides an excellent way to solve flatness and horizon problems that appear in the standard hot big bang model, see e.g. [67] for a review. In many inflationary models the expansion of the universe is caused by the quantum fluctuations of a scalar field called the *inflaton* field, which after the inflationary phase stores the whole energy density of the universe. The subsequent evolution, known as *reheating*, involves a nonperturbatively fast decay of the inflaton field, accompanied by an explosive particle production due to dynamical instabilities [2, 68]. In general, these instabilities create highly occupied excitations at some characteristic momentum scale Q_0, which differs significantly from the temperature of a thermally equilibrated system with the same energy density and particle number.

The overoccupied system relaxes in terms of self-similar cascades, transporting particles toward low momentum scales [30, 32] and energy to higher momenta [69, 70]. Similar phenomena are predicted to characterize the dynamics of the highly excited quark-gluon plasma during the early stages of a heavy-ion collision [71–74]. Recently, self-similar scaling phenomena have been experimentally discovered in ultracold quantum gases far from equilibrium, showing remarkable universal properties in the nonperturbative infrared regime at sufficiently low momenta [28, 29, 75]. Theoretical descriptions of the underlying nonthermal infrared fixed points typically involve effective kinetic theory [31, 32, 36, 76–78] or classical-statistical approximations [32, 79–84] in the weak coupling limit.

In this chapter, we study the time evolution of relativistic scalar quantum fields starting from overoccupied initial conditions. The nonequilibrium evolution is addressed from first principles by solving the equations of motion obtained from the 2PI effective action. We consider a self-interacting N-component field theory often employed in the context of scalar inflaton models, which can also be taken to describe the Higgs sector of the standard model of particle physics for $N = 4$. A self-consistent expansion in powers of $1/N$ to next-to-leading order (NLO) provides a nonperturbative account of the dynamics, such that we may analyze the highly occupied infrared for a wide range of interaction strengths. This has been previously employed to study the far-from-equilibrium dynamics of this model, focusing on the role of a symmetry breaking field expectation value for its evolution [62]. Here, we analyze for the first time the self-similar scaling properties of two-point correlators and the effective four-vertex in quantum field theory at NLO without further approximations by numerically extracting the universal dynamical exponents and scaling functions. We compare our results to previous weak-coupling estimates for *equal-time* two-point correlators using effective kinetic theory or classical-statistical field theory [32].

A further important focus of our work is the computation of *unequal-time* correlation functions far from equilibrium, namely the commutator expectation value of two field operators and the respective anticommutator at different times. The former gives the spectral function, which provides essential information about the nature of the excitations, such as the possible existence or absence of long-lived quasiparticles far from equilibrium. In contrast, the anticommutator expectation value captures quantum-statistical aspects, such as the occupation number of modes. While in thermal equilibrium the spectral (commutator) and statistical (anticommutator) correlation functions are related by the fluctuation-dissipation relation, this is in general violated out of equilibrium. Here we compute both spectral and statistical correlation functions directly based on the underlying quantum field. While at sufficiently high momenta we recover the expected quasiparticle structure with a generalized fluctuation-dissipation relation, we demonstrate that significant violations occur in the nonperturbative infrared regime.

3.2 Scalar quantum field theory far from equilibrium

We consider the relativistic N-component scalar quantum field theory discussed in Section 2.3 for massless fields interacting via a quartic self-coupling λ. The $O(N)$-symmetric classical action is given by

$$S = \int \mathrm{d}^4x \left[\frac{1}{2}\partial^{\mu}\varphi_a(x)\partial_{\mu}\varphi_a(x) - \frac{\lambda}{4!\,N}\Big(\varphi_a(x)\varphi_a(x)\Big)^2 \right] , \tag{3.1}$$

which corresponds to (2.49) with $m = 0$. As before, the a summation over field indices $a = 1, \dots, N$ and Lorentz indices $\mu = 0, 1, 2, 3$ is implied, and we use the four-vector $x = (x^0, \mathbf{x})$.

Quantum corrections are taken into account using the large-N expansion at next-to-leading order (NLO) of the two-particle irreducible (2PI) effective action [58, 60], which we outlined in Section 2.3.4. This self-consistent expansion scheme is uniform in time, resumming secular terms such that it can be applied also to study late-time dynamics [41].

A full description of general out-of-equilibrium dynamics can be based on the time-ordered two-point correlation function. Equivalently, one can deploy both commutator and anticommutator expectation values of products of field operators. These correspond to the statistical function F and the spectral function ρ introduced in Section 2.3.1, see (2.65). They are given by

$$F_{ab}(x,y) = \frac{1}{2}\left\langle \{\varphi_a(x), \varphi_b(y)\} \right\rangle - \left\langle \varphi_a(x) \right\rangle \left\langle \varphi_b(y) \right\rangle , \tag{3.2a}$$

$$\rho_{ab}(x,y) = i \left\langle [\varphi_a(x), \varphi_b(y)] \right\rangle , \tag{3.2b}$$

where the operator nature of the fields is implied. $\{.,.\}$ denotes the anticommutator and $[.,.]$ the commutator that is applied to the field operators $\varphi_a(x)$.

At NLO in the large-N expansion, the evolution equations for F and ρ are given by (2.77) with the self-energy terms provided in Section 2.3.4. For their solution we have to supply initial conditions at time $x^0 = t = 0$. Here we employ initial conditions for the spatially homogeneous system with a vanishing macroscopic field, i.e. $\langle \varphi_a(t) \rangle = \partial_t \langle \varphi_a(t) \rangle = 0$ at $t = 0$ for all field components. By virtue of the $O(N)$ symmetry, the field expectation value then remains zero at all times. This allows us to write

$$F_{ab}(x,y) = F(x,y)\delta_{ab} , \quad \rho_{ab}(x,y) = \rho(x,y)\delta_{ab}, \tag{3.3}$$

such that we only need to consider the diagonal elements $F(x,y)$ and $\rho(x,y)$.

We deploy Gaussian initial conditions that can be fully determined in terms of the spectral and statistical two-point functions. The initial conditions at $t = 0$ for the spectral function are fixed by its antisymmetry, $\rho(t, t, \mathbf{x}, \mathbf{y}) = 0$, and the equal-time commutation relations of the bosonic quantum theory (2.70). For the statistical function at initial time we consider free-field correlations, see Appendix 3.A for details about the free theory, which in spatial Fourier space with momentum $\mathbf{p}$ are parametrized as

$$F(t,t',|\mathbf{p}|)\Big|_{t=t'=0} = \frac{f_{\mathbf{p}}+1/2}{\omega_{\mathbf{p}}}\cos\left[\omega_{\mathbf{p}}(t-t')\right]\Big|_{t=t'=0}. \tag{3.4}$$

Here $f_{\mathbf{p}}$ denotes an initial particle number distribution with dispersion $\omega_{\mathbf{p}}$. The latter is set at initial time by $\omega_{\mathbf{p}} = \sqrt{|\mathbf{p}|^2 + m_{\text{init}}^2}$ in the limit of a vanishing initial mass $m_{\text{init}} \to 0^+$. Following [62], we consider the initial condition of a highly occupied system of particles with distribution function

$$f_{\mathbf{p}} = \frac{n_0}{\lambda}\,\Theta(Q_0 - |\mathbf{p}|)\,, \tag{3.5}$$

where the characteristic momentum Q_0 sets the initial scale, n_0 is an occupancy parameter, and Θ denotes the Heaviside step function. Because the initial occupancy is inversely proportional to the coupling, this represents a nonperturbative problem even for $\lambda \ll 1$. Since the NLO approximation for the dynamics is non-Gaussian, higher correlations build up during the time evolution. Details about the specification of the initial conditions in our simulations are outlined in Appendix 3.B.2.

Starting from this overoccupied initial situation, we compute the time evolution of the system by numerically solving the coupled NLO evolution equations for the statistical and spectral correlation functions. The NLO approximation for the statistical and spectral components of the self-energies, which we denote by $C(x,y)$ and $A(x,y)$ according to the decomposition (2.68), entails a geometric series summation of the correlation functions $F(x,y)$ and $\rho(x,y)$, which can be conveniently expressed in terms of the summation functions $I_F(x,y)$ and $I_\rho(x,y)$. For vanishing macroscopic field, the self-energy expressions (2.91) simplify to

$$C(x,y) = -\frac{\lambda}{3N}\Big(F(x,y)I_F(x,y) - \frac{1}{4}\rho(x,y)I_\rho(x,y)\Big)\,, \tag{3.6a}$$

$$A(x,y) = -\frac{\lambda}{3N}\Big(F(x,y)I_\rho(x,y) + \rho(x,y)I_F(x,y)\Big)\,, \tag{3.6b}$$

where the summation functions I_F and I_ρ given by (2.92) contain as building blocks the 'one-loop' self-energies $\Pi_F(x,y)$ and $\Pi_\rho(x,y)$ in (2.93). The spectral component of the one-loop self-energy is directly related to the retarded one-loop self-energy,

$$\Pi_R(x,y) = \Theta(x^0 - y^0)\Pi_\rho(x,y)\,. \tag{3.7}$$

We emphasize that the large-N approximation only involves a systematic power counting of factors of $1/N$. As a consequence, the terms neglected are suppressed by an additional power of $1/N$. Since this is not an expansion in powers of the coupling λ, even nonperturbative situations far from equilibrium such as the overoccupied initial conditions specified by (3.5) can be addressed. Moreover, the NLO contributions are essential: at LO ($N \to \infty$) the right-hand side of the evolution equations (2.77) would vanish since the self-energies (3.6) are zero at that order.

The numerical results presented in this work employ $N = 4$ and occupation parameter $n_0 = 100$. We study a wide range of coupling parameters $\lambda = 0.01, 0.10, 1.0, 2.0$. If not stated otherwise, $\lambda = 1.0$ is used. In the following, all quantities are given in units of the characteristic initial scale Q_0 and are stated as dimensionless numbers, see Appendix 3.B.3 for details about mass dimensions. The equations of motion are discretized on a lattice with temporal step a_t and spatial lattice spacing a_s. The results shown are obtained from computations using $N_s = 500$ points on a spatial grid with $a_s = 0.75$, corresponding to an ultraviolet (UV) momentum cutoff of $\Lambda_{\text{UV}} = 4.19$ and an infrared (IR) cutoff of

$\Lambda_{\mathrm{IR}} = 0.0084$. We checked that all relevant results are insensitive to both IR and UV cutoffs. In order to efficiently approach late times, the time step a_t is tuned to be as large as possible while checking numerical convergence to runs with smaller time steps. For the presented numerical results a time step of $a_t = 0.3$ is used. Details about the numerical computations are explained in Appendix 3.B.

3.3 Universal scaling dynamics of equal-time correlations

We first consider the time nonequilibrium evolution of the statistical correlation function (3.2a) at equal times, for which the spectral function (3.2b) vanishes because of its antisymmetry. A similar calculation for a larger class of initial conditions (with nonzero initial field expectation value) has been done in [62] pointing out the independence of rescaled results on system parameters, such as the value of the coupling λ or details of the initial conditions, in an emergent universal regime associated to a nonthermal fixed point [30, 32]. Exploiting this insensitivity to initial condition details, we restrict ourselves to the symmetric regime with initial conditions described in Section 3.2. This reduces the numerical efforts and we do not have to employ an adaptive grid size as done in [62], which allows us for the first time to accurately extract the universal self-similar scaling exponents and scaling function from the complete NLO evolution equations (2.77) with (2.91) — (2.93) by numerical computations. A calculation of the far-from-equilibrium scaling exponents and function has so far only been done using additional assumptions, such as a quasiparticle ansatz for an effective kinetic description at the nonthermal fixed point in [32, 76, 77], or based on classical-statistical field theory approximations in [32] in the weak-coupling limit. We emphasize that our approach is not restricted to weak couplings and includes genuine quantum effects at NLO in the large-N expansion.

3.3.1 Particle distribution

So far, the phenomenon of scaling has mainly been discussed in terms of a particle number distribution function, whose time-dependence we extract from the two-point correlation function as [41, 60]

$$f(t, |\mathbf{p}|) + \frac{1}{2} = \sqrt{F(t, t', |\mathbf{p}|)\partial_t \partial_{t'} F(t, t', |\mathbf{p}|)}\,\Big|_{t=t'} . \tag{3.8}$$

Similarly, one may define a time-dependent effective dispersion

$$\omega(t, |\mathbf{p}|) = \sqrt{\frac{\partial_t \partial_{t'} F(t, t', |\mathbf{p}|)}{F(t, t', |\mathbf{p}|)}}\,\Bigg|_{t=t'} , \tag{3.9}$$

such that we have at initial time $f(t = 0, |\mathbf{p}|) = f_{\mathbf{p}}$ and $\omega(t = 0, |\mathbf{p}|) = \omega_{\mathbf{p}}$ in accordance with (3.4). These quasiparticle expressions comply with the free theory, as shown in Appendix 3.A.

Starting from the overoccupied initial state at $t = 0$, the nonequilibrium evolution leads to a redistribution of both particle number and mode energy. In the upper plot of Figure 3.1, we show the time evolution of the distribution function $f(t, \mathbf{p})$. The effective mass m_{eff}, which is given by the approximately time-independent value of the dispersion at zero momentum as analyzed in Section 3.4.2, is also indicated. For $t \gtrsim 1500$, the dynamics slows down considerably and we analyze in the following whether the system becomes self-similar. We concentrate on the nonperturbative behavior for sufficiently low momenta, and refer to [62, 70] for the analysis of the perturbative high-momentum properties .

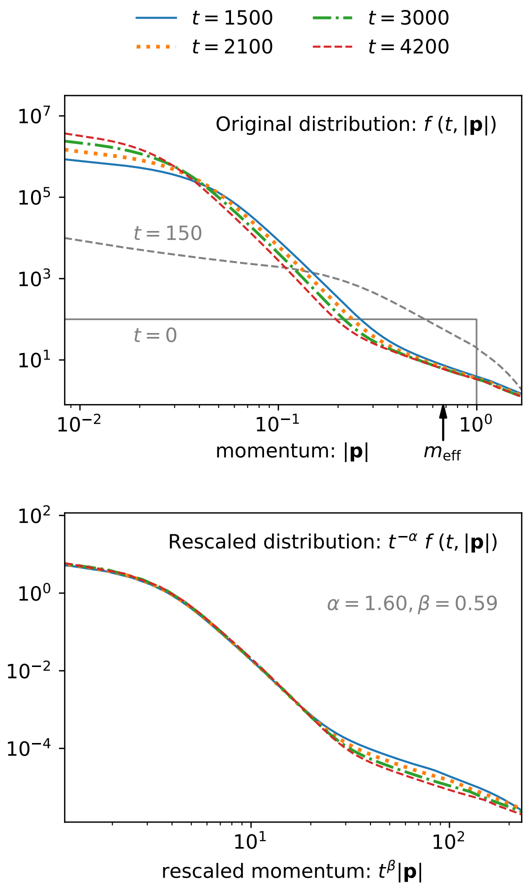

Figure 3.1: The upper graph shows the distribution function as a function of momentum at different times. In the lower plot, the rescaled distribution versus rescaled momentum is given.

For a self-similar time evolution the distribution obeys the scaling property

$$f(t, |\mathbf{p}|) = t^{\alpha} f_S(t^{\beta}|\mathbf{p}|)\,, \tag{3.10}$$

with scaling exponents α, β and time-independent scaling function f_S. Therefore, in the scaling regime $t^{-\alpha} f(t, |\mathbf{p}|)$ does not depend on time and momentum separately but only on the product $t^{\beta}|\mathbf{p}|$ for a set of exponents α and β. Universality implies that the shape of the distribution function and the values of the exponents do not depend on the microscopic model parameters, such as the value of the coupling λ, which is discussed in the following.

As shown in the lower plot of Figure 3.1, the distribution function at different times can be rescaled such that the curves of $t^{-\alpha} f(t, |\mathbf{p}|)$ as a function of $t^{\beta}|\mathbf{p}|$ lie on top of each other for lower momenta. Numerically, the scaling exponents are obtained by comparing the distribution function at some reference time t_{ref} with several earlier times t, where we perform comparisons within a time window of $\Delta t_{\mathrm{w}} = 720$. For details on the method and the employed error estimation we refer to Appendix 3.C. In Figure 3.2 we show our results for the scaling exponents α and β for different couplings where the data points are binned for the plots. Both exponents approach approximately constant values given in Table 3.1. For later comparison, we also present values for the exponent α_{λ} as defined in the table caption.

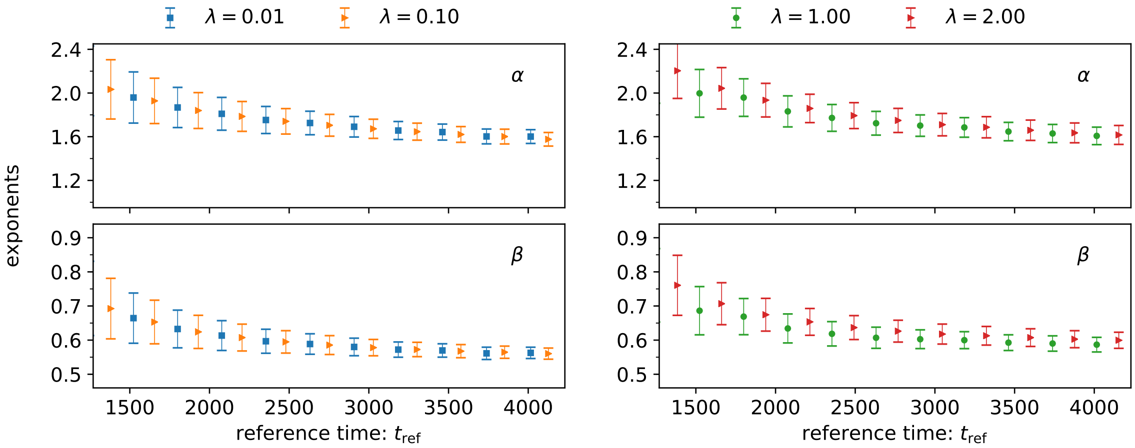

Figure 3.2: The scaling exponents α and β for the self-similar behavior of the distribution function $f(t,|\mathbf{p}|)$ extracted at reference times t_{ref}, shown for different values of the coupling parameter λ.

λ	α	β	$2(\beta-\alpha)$
0.01	1.59 ± 0.06	0.56 ± 0.02	-2.06 ± 0.13
0.10	1.60 ± 0.06	0.57 ± 0.02	-2.06 ± 0.13
1.00	1.60 ± 0.08	0.59 ± 0.02	-2.02 ± 0.17
2.00	1.61 ± 0.09	0.60 ± 0.02	-2.02 ± 0.19

Table 3.1: Exponents α and β obtained from the scaling analysis of the particle distribution $f(t,|\mathbf{p}|)$. Using these values we also give $\alpha_\lambda = 2(\beta-\alpha)$ for later comparison, which is the expected scaling exponent of the four-vertex introduced in Section 3.3.3. Our results are shown for different values of the coupling parameter λ.

The exponents for all couplings studied here agree within errors with each other. Furthermore, they are consistent with the results found in [32] using classical-statistical lattice simulations, confirming that statistical fluctuations dominate over genuine quantum fluctuations in this highly occupied regime. As pointed out in [32, 76, 77], the values of these exponents coincide with those of the corresponding nonrelativistic scalar model, since infrared momenta below m_{eff} of the relativistic theory behave nonrelativistically. Within errors, we also find $\alpha = d\beta$ for $d = 3$ spatial dimensions such that $\int_{\mathbf{p}} f(t,|\mathbf{p}|) = t^{\alpha-d\beta}\int_{\mathbf{q}} f_S(|\mathbf{q}|)$ is approximately conserved, reflecting a transport of particles toward lower momenta for the $\beta > 0$ observed.

3.3.2 Mode energy

In addition, we consider the time-dependent mode energy $\varepsilon(t,|\mathbf{p}|)$ given by (2.99), which in the $O(N)$-symmetric case becomes

$$\frac{\varepsilon(t,|\mathbf{p}|)}{N} = \left[\frac{\partial_t\partial_{t'}}{2} + \frac{\mathbf{p}^2}{2} + \frac{\lambda}{4!}\int_{\mathbf{q}} F(t,t,|\mathbf{q}|)\right] F(t,t',|\mathbf{p}|)\Big|_{t=t'} + \frac{1}{2N} I_F(t,t,|\mathbf{p}|) \tag{3.11}$$

$$\simeq \omega(t,\mathbf{p})\left[f(t,|\mathbf{p}|) + \frac{1}{2}\right], \tag{3.12}$$

where the approximation employed for the last line is only used here to analyze the quasiparticle content of the dynamics. As shown by (3.40) in Appendix 3.A, the relation is exact in the free theory.

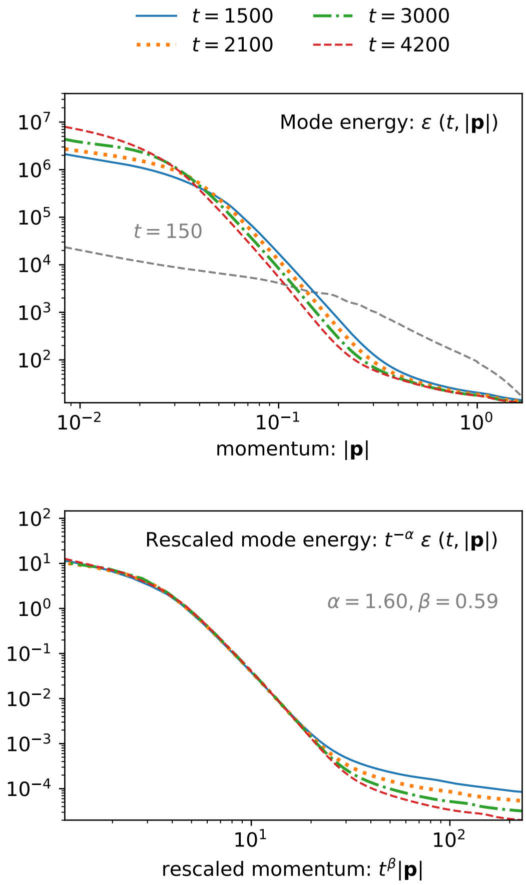

Figure 3.3: The original and rescaled mode energies at different times. The same exponents as obtained from the scaling analysis of the distribution function f are used.

The momentum sum of the mode energy (3.11) is equal to the conserved total energy density at NLO, $\varepsilon(t) = \int \mathrm{d}^3\mathbf{p}/(2\pi)^3 \varepsilon(t, |\mathbf{p}|)$. In our simulations $\varepsilon(t)$ is conserved at the level of $1\,\%$ accuracy for the times under consideration.

The scaling analysis for the mode energy density employs

$$\varepsilon(t, |\mathbf{p}|) = t^\alpha\, \varepsilon_S(t^\beta |\mathbf{p}|)\,, \tag{3.13}$$

where we anticipate that the scaling exponents are the same as for the distribution function, and ε_S denotes the energy scaling function. The upper graph of Figure 3.3 shows the time evolution of $\varepsilon(t, |\mathbf{p}|)$, while the lower one displays the rescaled quantity $t^{-\alpha}\varepsilon(t, |\mathbf{p}|)$ as a function of $t^\beta|\mathbf{p}|$ employing the same values for the exponents as obtained from the particle number distribution. One observes that in the scaling regime all curves collapse to a single one in the infrared to very good accuracy.

In order to illustrate this agreement, we analyze the approximate quasiparticle energy density given by (3.12). In Figure 3.4 the mode energy at NLO (3.11) is compared to the quasiparticle expression (3.12). One observes rather good agreement, in particular in terms of the scaling properties.

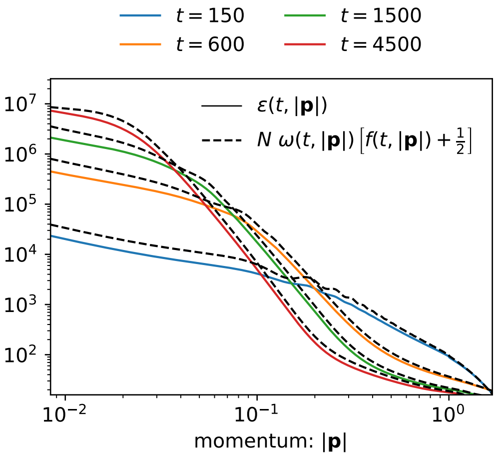

Figure 3.4: Comparison of the mode energy at NLO (3.11) and the quasiparticle expression (3.12) as a function of momentum for different times.

3.3.3 Scaling of the effective coupling

In this section we analyze the scaling properties of the four-vertex in an approximation based on the large-N expansion to NLO. Since we are interested in a slowly evolving self-similar scaling regime, we may simplify the computation considerably by relying on a derivative expansion in time. More precisely, at lowest order in derivatives it is convenient to consider the (on-shell) effective coupling in Fourier space given by [31–33]

$$\lambda_{\text{eff}}(t, |\mathbf{p}|) = \frac{\lambda}{|1 + \Pi_R(t, |\mathbf{p}|)|^2} . \tag{3.14}$$

This effective coupling approximates the full four-vertex, which at this order receives its momentum dependence from the resummed geometric series underlying the NLO approximation [58, 60]. Moreover, the effective coupling is directly related to the summation functions (2.92) according to [31–33]

$$\frac{\lambda_{\text{eff}}(t, |\mathbf{p}|)}{\lambda} = \frac{I_F(t, |\mathbf{p}|)}{\Pi_F(t, |\mathbf{p}|)} . \tag{3.15}$$

In the following this is used to numerically compute the time-dependent effective coupling, where $I_F(t, |\mathbf{p}|)$ and $\Pi_F(t, |\mathbf{p}|)$ are obtained from the expressions (2.92) and (2.93) in spatial Fourier space evaluated at equal times.

Using the scaling property (3.10) of the distribution function in the expression for the self-energies (2.93) in the nonrelativistic regime, one expects [32, 76, 77]

$$\lambda_{\text{eff}}(t, |\mathbf{p}|) = t^{\alpha_\lambda} \lambda_{\text{eff},S}(t^\beta |\mathbf{p}|) , \tag{3.16}$$

with scaling function $\lambda_{\text{eff},S}$ and coupling scaling exponent

$$\alpha_\lambda = -2 \left[(2 - d)\beta + \alpha \right] , \tag{3.17}$$

directly related to the occupation number exponents α and β in d spatial dimensions. A derivation of this relation is presented in Appendix 3.E.

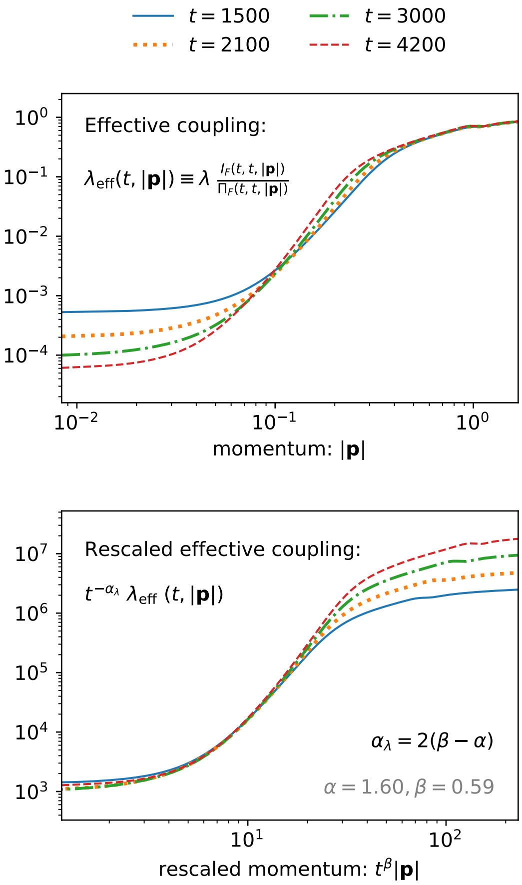

Figure 3.5: The original and rescaled effective coupling for different times.

The upper panel of Figure 3.5 shows the momentum dependence of the effective coupling at different times. Remarkably, the effective coupling drops over several orders of magnitude in the nonperturbative infrared regime, where the occupation number grows larger with time. This nonequilibrium phenomenon of a dynamically reduced four-vertex counteracts the dramatic Bose enhancement from the very high occupancies in the infrared, which would otherwise lead to faster and faster dynamics for growing occupancies. The corresponding phenomenon has recently also been experimentally observed in an atomic Bose gas far from equilibrium [75].

The lower graph of Figure 3.5 demonstrates that the numerical data for the effective coupling collapses rather well to a common curve in the infrared momentum range when rescaled accordingly. As a check, we also determine the scaling exponents α_λ and β defined by (3.16) directly from our numerical data without assuming the scaling relation (3.17), see Appendix 3.C for details on the method. The binned data obtained for α_λ in this way is plotted in Figure 3.6, where we also show the results for the exponent if computed according to (3.17) using the scaling exponents α and β. We observe a good agreement of the data although the errors for the analysis using λ_{eff} are larger and fluctuate stronger, which is reflected in enhanced statistical errors as discussed in Appendix 3.C. The asymptotic values approached are presented in Table 3.2.

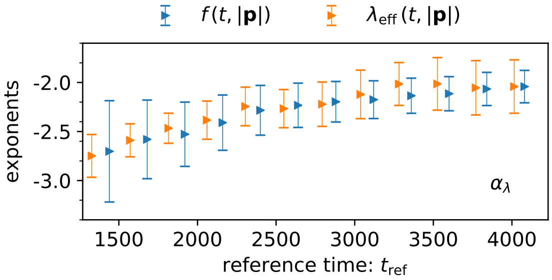

Figure 3.6: The scaling exponents α_λ obtained from the analysis of the distribution function f as well as the effective coupling λ_{eff} for quartic self-interaction $\lambda = 1.0$.

λ	α_λ	β	$\beta - \alpha_\lambda/2$
0.01	-2.00 ± 0.42	0.60 ± 0.02	1.60 ± 0.25
1.00	-2.01 ± 0.42	0.67 ± 0.02	1.68 ± 0.25

Table 3.2: Scaling exponents for the relativistic scalar field theory. The exponents α_λ and β are obtained from the analysis of the effective coupling $\lambda_{\text{eff}}(t,|\mathbf{p}|)$. The last column shows the computed values for $\alpha = \beta - \alpha_\lambda/2$.

3.4 Spectral and statistical correlations at unequal times

For the study of correlation functions at different times t and t' it is convenient to rephrase the time-dependence in terms of Wigner coordinates, employing the central time $\tau = (t+t')/2$ and the relative time $\Delta t = t - t'$. For the spatially homogeneous and isotropic system, we then denote the two-point functions using the new temporal coordinates as $F(\tau, \Delta t, |\mathbf{p}|)$ and $\rho(\tau, \Delta t, |\mathbf{p}|)$.

In order to study the frequency spectrum of these statistical and spectral functions, we consider a finite-range Fourier transformation of the Wigner space propagators with respect to the relative time Δt,

$$F(\tau,\omega,|\mathbf{p}|) = \int_{-2\tau}^{2\tau} \mathrm{d}\Delta t \; e^{i\omega\Delta t} F\left(\tau, \Delta t, |\mathbf{p}|\right), \tag{3.18a}$$

$$i\tilde{\rho}(\tau,\omega,|\mathbf{p}|) = \int_{-2\tau}^{2\tau} \mathrm{d}\Delta t \; e^{i\omega\Delta t} \rho\left(\tau, \Delta t, |\mathbf{p}|\right), \tag{3.18b}$$

where the factor of i is introduced such that both $\tilde{\rho}(\tau,\omega,|\mathbf{p}|)$ and $F(\tau,\omega,|\mathbf{p}|)$ are real. To ease the notation, we neglect the tilde for the real spectral function in frequency space, $\tilde{\rho}(\tau,\omega,|\mathbf{p}|)$, in the following, having in mind the extra factor of i in its definition.

The integrals with respect to the relative times in (3.18) are fundamentally restricted by $\pm 2\tau$ for the initial value problems with $t, t' \geq 0$. Moreover, it is sufficient to present the propagators for positive Δt or ω, since the statistical (spectral) function is (anti)symmetric in Δt and hence ω. Effects resulting from the finite-time boundary vanish in the limit $\tau \to \infty$ and are discussed further in Section 3.4.1. Details on the numerical treatment are presented in Appendix 3.D.

Using (3.18), the momentum-space representation of the equal-time commutation relation (2.70) can be written as the sum rule

$$\int_0^\infty \frac{\mathrm{d}\omega}{\pi} \; \omega \; \rho(\tau,\omega,\mathbf{p}) = 1\,, \tag{3.19}$$

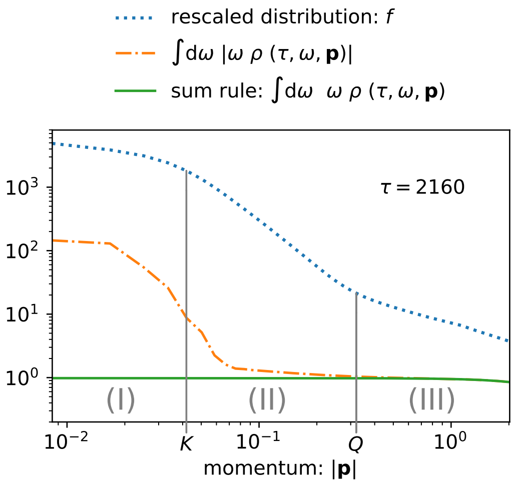

Figure 3.7: Comparison of the sum rule for the spectral function (3.19) and the modified expression (3.20) with the absolute value of the integrand as a function of momentum. The significant deviations at low momenta result from negative values of $\rho(\tau, \omega, \mathbf{p})$. Shown is also the particle distribution function from which we identify the time-dependent scales $K(t)$ and $Q(t)$.

where the factor ω in the integrand appears due to the second-order time derivatives in the relativistic theory and is absent in the corresponding nonrelativistic model. We emphasize that in the interacting quantum field theory the spectral function $\rho(\tau, \omega, |\mathbf{p}|)$ is, in general, not positive for $\omega > 0$. In contrast, simple quasiparticle descriptions typically rely on positivity, such as the free-field spectral function with a positive particle peak at the frequency that is equal to the mass of the particle. We can check whether positivity is approximately realized by comparing to the corresponding expression with the absolute value of the integrand of (3.19),

$$\int_0^\infty \frac{\mathrm{d}\omega}{\pi}\, |\omega\ \rho(\tau, \omega, \mathbf{p})|\,. \tag{3.20}$$

Figure 3.7 compares this modified expression to the sum rule as a function of spatial momentum. Here the data for the Fourier transformed spectral function is computed using a discrete Fourier transformation, see Appendix 3.D for details. For sufficiently large momenta, we indeed observe agreement as expected based on the validity of perturbation theory in this regime. However, at low momenta significant deviations are seen, indicating that there is no simple quasiparticle spectral function in the deep infrared.

To further analyze this behavior, we distinguish three momentum regimes which we identify with the help of the particle distribution function defined in (3.8), as shown in Figure 3.7. There we indicate a characteristic time-dependent momentum scale $K(t)$, where the distribution function shows maximum positive curvature in the scaling regime, along with $Q(t)$ defined by the scale of maximum negative curvature. These two scales are used to identify the

(I) infrared “plateau” regime, $|\mathbf{p}| \ll K(t)$,

(II) infrared “power-law” regime, $K(t) \ll |\mathbf{p}| \ll Q(t)$,

(III) high-momentum perturbative regime, $|\mathbf{p}| \gg Q(t)$.

We emphasize that both momentum regimes (I) and (II) constitute the inverse particle cascade and

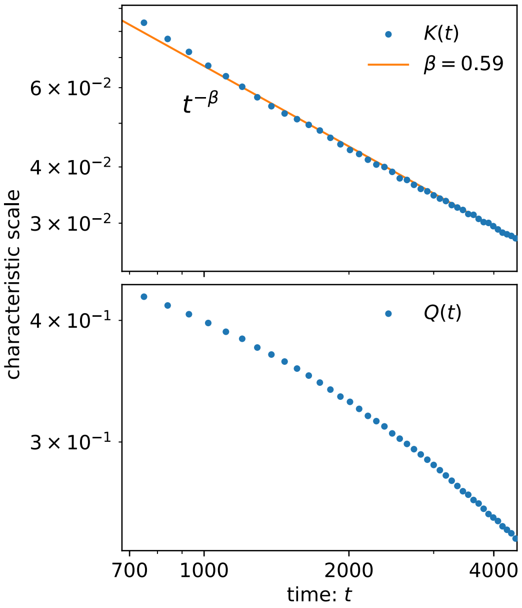

Figure 3.8: Time evolution of the characteristic infrared momentum scale $K(t)$ (upper plot) and the scale $Q(t)$ separating the infrared and the high-momentum regime (lower plot). The time evolution of the infrared scale becomes $K(t) \sim t^{-\beta}$, while $Q(t)$ evolves somewhat faster than a simple power-law.

are characterized by the same universal scaling exponents. In particular, $K(t) \sim t^{-\beta}$, which can be inferred from the upper graph of Figure 3.8. The scale $Q(t)$ also evolves toward the infrared as can be seen in lower plot of Figure 3.8. It appears not to be described by a simple power law, as the evolution becomes faster with time.

In the following, we discuss the differences of the unequal-time two-point functions in the three momentum regimes in detail.

3.4.1 Violations of the fluctuation-dissipation relation

In contrast to our nonequilibrium situation considered, thermal equilibrium is time-translation invariant, such that correlation functions only depend on relative coordinates and there is no τ-dependence. Moreover, the statistical and spectral functions in thermal equilibrium, $F^{(\mathrm{eq})}$ and $\rho^{(\mathrm{eq})}$, are related by the fluctuation-dissipation theorem, see e.g. [41], according to

$$F^{(\mathrm{eq})}(\omega, \mathbf{p}) = \Big(f_{\mathrm{BE}}(\omega) + \frac{1}{2}\Big)\rho^{(\mathrm{eq})}(\omega, \mathbf{p})\,. \tag{3.21}$$

This implies that the ratio $F^{(\mathrm{eq})}(\omega, \mathbf{p})/\rho^{(\mathrm{eq})}(\omega, \mathbf{p})$ is independent of spatial momentum $\mathbf{p}$ and determined by the frequency-dependent Bose-Einstein distribution $f_{\mathrm{BE}}(\omega) = (e^{\beta\omega} - 1)^{-1}$ with inverse temperature β in the absence of conserved charges.

Out of equilibrium, the statistical and spectral correlation functions are linearly independent in general, but one may hope to find some generalized fluctuation-dissipation relation where the Bose-Einstein distribution is replaced by a time-dependent distribution function. Such a generalized relation provides, for instance, the basis for standard kinetic descriptions.

In order to study the nonequilibrium frequency-space two-point functions, we consider the Fourier Wigner space propagators $F(\tau, \omega, |\mathbf{p}|)$ and $\rho(\tau, \omega, |\mathbf{p}|)$ for times τ at which the system has reached

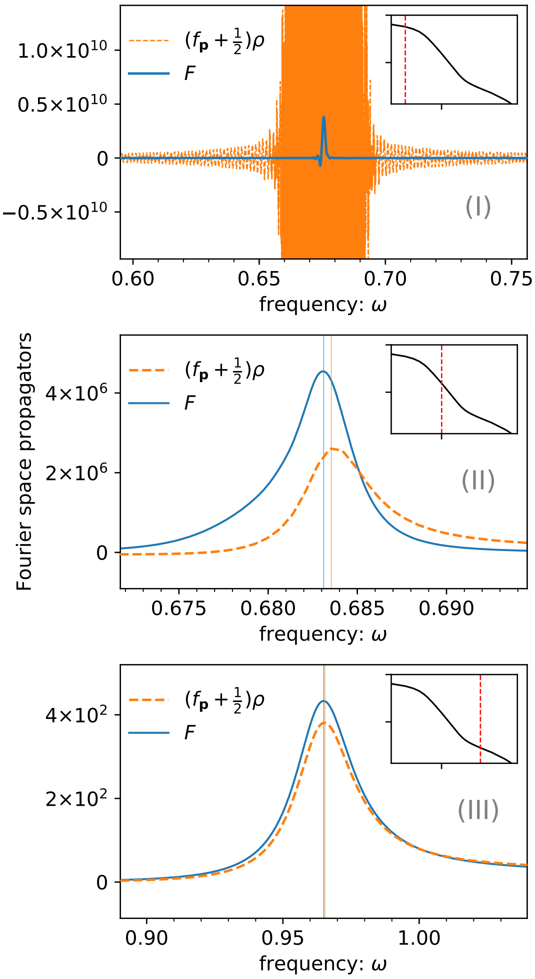

Figure 3.9: Comparison of $(f(t=\tau,|\mathbf{p}|)+1/2)\,\rho(\tau,\omega,|\mathbf{p}|)$ and $F(\tau,\omega,|\mathbf{p}|)$ as a function of frequency ω at time $\tau=2250$ for given momenta in the three regimes (I), (II) and (III) from top to bottom. Here $p_{(\mathrm{I})}=0.017$, $p_{(\mathrm{II})}=0.101$ and $p_{(\mathrm{III})}=0.679$ are marked in the inset (red dashed line), where the distribution function f is plotted as a function of $|\mathbf{p}|$ (black line) on a double logarithmic scale.

the scaling regime. Details on the numerical computation of the frequency-space propagators can be found in Appendix 3.D. As discussed above, we expect the spectral function to describe a quasiparticle excitation spectrum for sufficiently large momenta of regime (III) and maybe (II).

Figure 3.9 shows the numerical results for $[f(t=\tau,|\mathbf{p}|)+1/2]\rho(\tau,\omega,|\mathbf{p}|)$ and $F(\tau,\omega,|\mathbf{p}|)$ as a function of ω at some time $\tau=2250$ in the scaling regime for three different momenta in the ranges (I), (II), and (III) as indicated in the inset. As anticipated, from the upper graph one observes that both expressions are clearly different in the deep infrared regime (I). The middle graph shows that in regime (II) both quantities become similar in shape, however, the respective peaks are shifted relative to each other and the height is not the same. In contrast, F and $(f+1/2)\rho$ have the same Breit-Wigner shape for the considered momentum in regime (III) although the amplitudes do not fully agree yet. As the momenta become larger, we checked that this agreement gets more accurate. This establishes a well-defined generalized fluctuation-dissipation relation in terms of the nonequilibrium distribution function $f(\tau,|\mathbf{p}|)$ in the high-momentum regime.

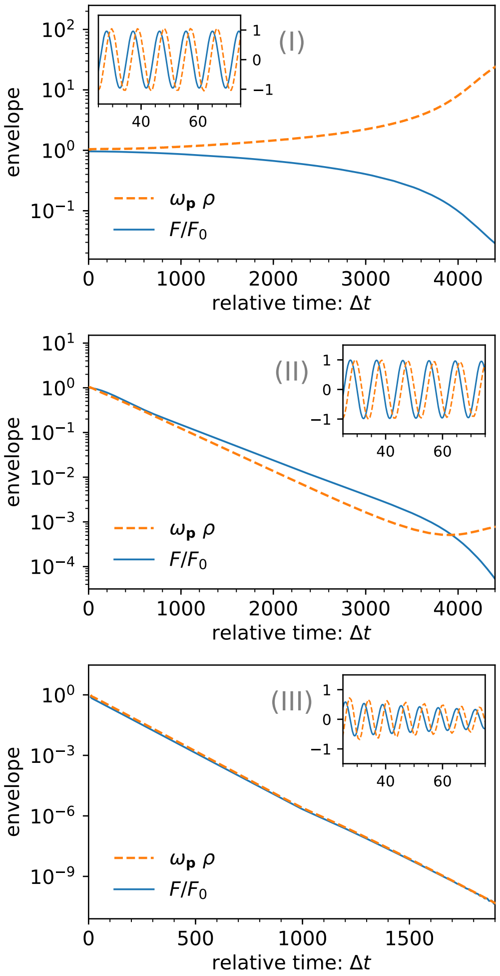

Figure 3.10: Envelopes of the spectral and statistical functions as a function of relative time Δt at $\tau = 2250$, shown for the same momenta as in Figure 3.9. The spectral function is rescaled by the oscillation frequency $\omega_\mathbf{p}$ and the statistical function by its maximum $F_0 = F(\tau, \Delta t = 0, |\mathbf{p}|)$ The inset displays the oscillation in Δt at shorter times on a linear scale. The time axis of the bottom plot shows a smaller time range since numerical uncertainties arise for envelopes becoming smaller than $\mathcal{O}(10^{-9})$.

We now analyze the behavior of the spectral function in regime (I) in more detail. The upper graph of Figure 3.9 reveals that the spectral function has the shape of an enveloped oscillation in this regime. We emphasize that this behavior is insensitive to the numerical discretization, i.e. to changes of the time-step size, the spatial grid spacing or the volume size. Instead, it is related to the initial time boundaries at $t \geq 0$ and $t' \geq 0$, which enter the integration boundaries in (3.18). In order to understand this effect better, it is helpful to consider the Wigner space propagators $F(\tau, \Delta t, |\mathbf{p}|)$ and $\rho(\tau, \Delta t, |\mathbf{p}|)$, i.e. without the Fourier transformation with respect to relative time Δt. Both functions oscillate in Δt with a frequency that in general can depend on both τ and $|\mathbf{p}|$. The envelopes of these oscillations are plotted in Figure 3.10, where the insets show the actual oscillations. The oscillation frequency can be used to define a dispersion relation $\omega(\tau, |\mathbf{p}|)$, which we call *Wigner dispersion* in order to distinguish it from the effective dispersion defined in (3.9). Since the oscillation frequencies observed are practically constant during the self-similar time evolution, the Wigner dispersion is quasi-stationary.

In principle, one could obtain Wigner dispersions for the statistical and spectral functions separately. This seems necessary at first sight, since the behavior of F and ρ is clearly different in the infrared, as seen in Figure 3.9. However, we find that the relative difference $(\omega_F - \omega_\rho)/\omega_F$ is smaller than 0.1 % such that for all practical purposes the Wigner dispersions of the statistical and spectral functions are treated as being equal.

While the oscillation frequencies of $F(\tau, \Delta t, |\mathbf{p}|)$ and $\rho(\tau, \Delta t, |\mathbf{p}|)$ are practically equal, the envelopes of the oscillations can differ significantly from each other in the infrared. Figure 3.10 compares the envelopes of F and ρ, which are plotted on a logarithmic scale against the relative time Δt, in the different momentum regimes. In (II) and (III), one observes that both F and ρ decay exponentially in Δt, which leads to well-defined quasiparticle peaks in frequency space as seen in Figure 3.9. In regime (I), however, the spectral function grows toward the initial-time boundaries whereas the statistical function is damped stronger than exponentially (upper plot of Figure 3.10).

To analyze this further, it is helpful to consider the simplified case of strictly exponentially damped oscillations. Omitting the τ-dependence for the moment, we approximately write

$$F(\Delta t, |\mathbf{p}|) \simeq e^{-\gamma_{\mathbf{p}}|\Delta t|} \cos(\omega_{\mathbf{p}} \Delta t)\ F_0\,, \tag{3.22a}$$

$$\rho(\Delta t, |\mathbf{p}|) \simeq e^{-\gamma_{\mathbf{p}}|\Delta t|} \sin(\omega_{\mathbf{p}} \Delta t)\ \omega_{\mathbf{p}}^{-1}\,, \tag{3.22b}$$

where $\gamma_{\mathbf{p}}$ is the damping constant, F_0 denotes the amplitude of the statistical function at $\Delta t = 0$, and the factor $\omega_{\mathbf{p}}^{-1}$ in (3.22b) ensures that the spectral function suffices the commutation relation (2.70). For this ansatz, calculating the Fourier transform with respect to the relative time Δt analytically yields the frequency-space propagators

$$F(\omega, |\mathbf{p}|) = F_0\ \frac{2\gamma_{\mathbf{p}}\ \left(\omega^2 + \omega_{\mathbf{p}}^2\right)}{(\omega^2 - \omega_{\mathbf{p}}^2)^2 + (2\omega\gamma_{\mathbf{p}})^2}, \tag{3.23a}$$

$$\rho(\omega, |\mathbf{p}|) = \frac{4\gamma_{\mathbf{p}}\ \omega}{(\omega^2 - \omega_{\mathbf{p}}^2)^2 + (2\omega\gamma_{\mathbf{p}})^2}, \tag{3.23b}$$

where the latter corresponds to the relativistic Breit-Wigner function [85]. On-shell, where $(\omega^2 + \omega_{\mathbf{p}}^2) \approx 2\omega^2$, the statistical function is also described by a Breit-Wigner shape. The damping constant $\gamma_{\mathbf{p}}$ determines the width of the quasiparticle peak.

In regime (III), F and ρ decay with the same damping constant and consequently have the same Breit-Wigner shape in Fourier space, see Figure 3.9. We can determine the parameters $\gamma_{\mathbf{p}}$, $\omega_{\mathbf{p}}$ and F_0 by fitting our data to either (3.22) or (3.23). Since the Fourier Wigner space propagators are numerically obtained by a discrete Fourier transformation of the Wigner propagators, both methods are equivalent up to numerical uncertainties.

When looking at regime (II) the statistical function has a slightly larger damping constant than the spectral function. The main difference, however, appears at large relative times Δt, i.e. at the temporal boundaries $t = 0$ and $t' = 0$, where the spectral function grows somewhat while the statistical function decays even faster. This means that spectral correlations at large time-separations are enhanced whereas statistical correlations are suppressed. As a consequence, the Fourier Wigner propagators shown in Figure 3.9 reveal different shapes.

For exponentially decaying Wigner space propagators, the effects from finite integration bounds are negligible at sufficiently late times, where τ is large. However, in regime (I) the spectral function does not decay toward the initial-time boundaries whereas the statistical function drops very quickly. Consequently, only the statistical function is described by a peak in Fourier Wigner space. However,

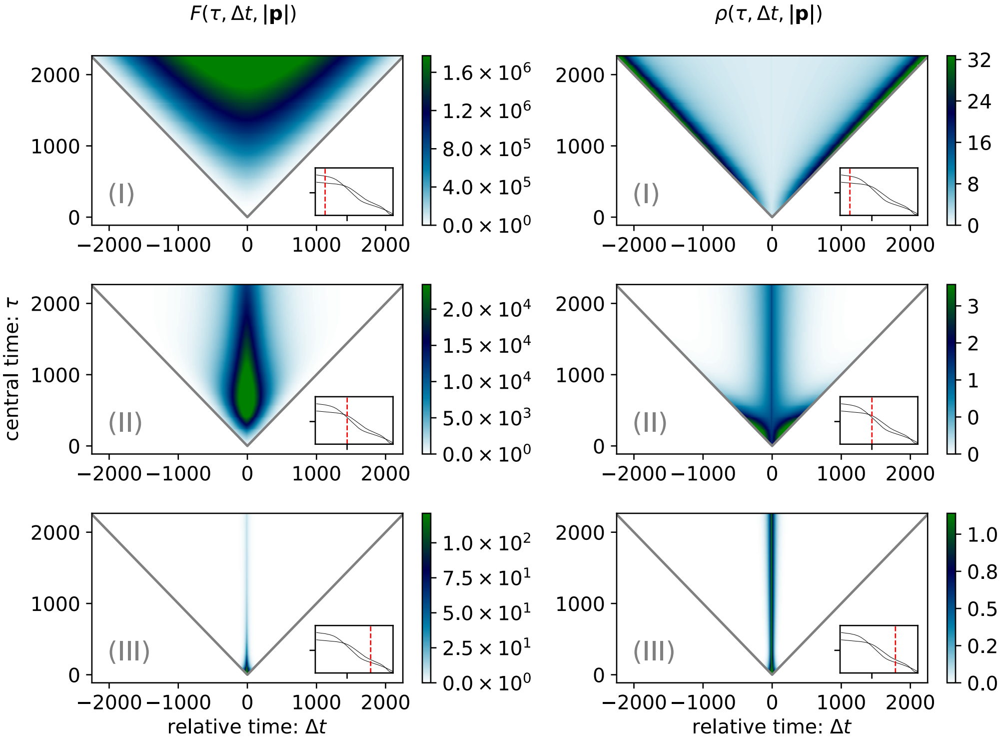

Figure 3.11: The spectral and statistical functions as a function of central time τ and relative time $\Delta\tau$ for the three different momenta as indicated by the dashed line in the insets. The latter show the distribution functions as a function of momentum for two different times.

the peak cannot be described by a Breit-Wigner function since no exponential decay is involved. In contrast, the growth of the spectral function at large relative times is sharply cut off by the time boundary $|\Delta t| \leq 2\tau$ appearing in initial value problems. Hence, the Wigner transformation gives rise to fast oscillations of the spectral propagator in frequency space, as seen in the upper plot of Figure 3.9. The oscillation frequency is determined by the integration range. The spectral propagator $\rho(\tau, \omega, |\mathbf{p}|)$ oscillates in ω with frequency 2τ and has an envelope that is peaked around $\omega = \omega_{\mathbf{p}}$.

The differences of the Wigner space propagators between the three momentum regimes can be visualized more clearly when looking at the contour plots shown in Figure 3.11, where the relative time Δt labels the horizontal axis, the central time τ the vertical axis, and the envelopes of $F(\tau, \Delta t, |\mathbf{p}|)$ and $\rho(\tau, \Delta t, |\mathbf{p}|)$ are encoded in the color scheme. The initial time bounds $t, t' \geq 0$, equivalent to $-2\tau \leq \Delta t \leq 2\tau$, are marked by the gray lines. Each horizontal slice corresponds to a fixed central τ and can be Wigner-transformed with respect to Δt in order to obtain the corresponding Fourier Wigner space propagators. The propagators shown in Figure 3.9 correspond to the latest available time slices at $\tau = 2250$.

In accordance with the behavior of the particle distribution function discussed above, the amplitude of F decreases by several orders of magnitude when going from low to high momenta (left plots of Figure 3.11 from top to bottom). In contrast, the spectral function ρ does not differ much in amplitude since it is normalized according to the sum rule (3.19).

The contour plots in Figure 3.11 visualize how the envelopes of F and ρ evolve with time τ. Due to the self-similar time evolution, going toward later times τ is equivalent to moving to larger momenta $|\mathbf{p}|$. In the infrared momentum regime, the increase of the amplitude of the spectral function toward

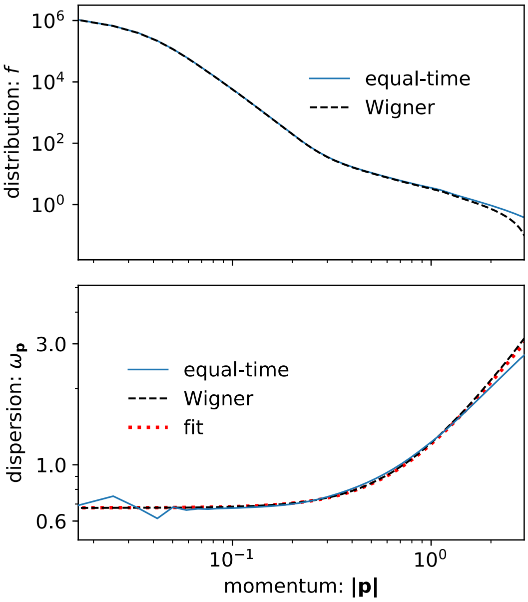

Figure 3.12: The distribution function f and the dispersion relation ω at time $t = \tau = 2250$. The quasiparticle definition and the Wigner space definition agree very well. The Wigner dispersion is fitted to the relativistic dispersion relation $\sqrt{|\mathbf{p}|^2 + m_{\text{eff}}^2}$ with $m_{\text{eff}} \approx 0.68$.

the initial time bounds declines with evolving time τ. For higher momenta, the decay rate increases as the time τ evolves. Hence, the effect of high amplitudes at large Δt vanishes at sufficiently late times, where the time scale is larger for small momenta. If one considers, for instance, some fixed momentum $|\mathbf{p}^*| < K(t)$ in region (I), then during the time evolution the characteristic momentum $K(t) \sim t^{-\beta}$ moves toward the infrared such that at some later time $t' > t$ one finds $|\mathbf{p}^*| > K(t')$. Since the momentum moved from region (I) into region (II), where the Wigner-space propagators decay exponentially, no boundary effects occur. In that sense, due to the self-similar time evolution it is always possible to wait long enough to overcome the initial-time boundary effect for a given momentum.

3.4.2 Dispersion and effective mass

Motivated by the results of the last section, we may consider a “Wigner” particle distribution function $f(\tau, |\mathbf{p}|)$ obtained from

$$f(\tau, |\mathbf{p}|) + \frac{1}{2} = \int_0^\infty \frac{\mathrm{d}\omega}{\pi}\, \omega\, F(\tau, \omega, |\mathbf{p}|), \tag{3.24}$$

which is a priori different from the “equal-time” definition employed in (3.8). Only in free equilibrium case, that is discussed in Appendix 3.A in more detail, the two definitions are equivalent. However, from the upper panel of Figure 3.12 one observes that both definitions are in good agreement with each other. Small deviations in the high-momentum range can be cured in the limit $a_t \to 0$.

Similarly, we introduced the effective dispersion (3.9) and the Wigner dispersion, see Section 3.4.1. Both definitions for the dispersion relations can be fitted rather well to a relativistic dispersion,

$$\omega(|\mathbf{p}|) = \sqrt{|\mathbf{p}|^2 + m_{\text{eff}}^2}, \tag{3.25}$$

with effective mass m_{eff} that incorporates quantum-statistical fluctuations. Our numerical computations show that the two definitions are in good agreement with each other, which can be seen from the lower graph of Figure 3.12. Although both the dispersion and the effective mass are in general time-dependent, they turn out to be practically constant in time in the scaling regime. Because the extraction of the effective mass from the Wigner dispersion turns out to be numerically more stable than using the equal-time dispersion, the values cited in the text are obtained from the former. By fitting our data to the relativistic dispersion relation (3.25), see also Appendix 3.B.4, we find the following values for the effective mass for different values of the interaction parameter,

$$m_{\text{eff}} = \begin{cases} 0.638 \pm 0.005 & \lambda = 0.01 \\ 0.641 \pm 0.005 & \lambda = 0.10 \\ 0.677 \pm 0.007 & \lambda = 1.00 \\ 0.716 \pm 0.008 & \lambda = 2.00 \end{cases} \tag{3.26}$$

where the error indicates that m_{eff} is not exactly time-independent during the self-similar evolution. The presence of an effective mass explains why the infrared exponents found in Section 3.3 are close to the predictions for a nonrelativistic theory [32]. As can be seen in the upper plot of Figure 3.1, the momenta of the whole infrared regime are much smaller than the effective mass (note the log-scale) and thus effectively nonrelativistic.

3.5 Conclusion

We analyzed the far-from-equilibrium scaling properties of equal-time and unequal-time correlation functions in a scalar quantum field theory. The numerical results are obtained from a fully self-consistent large-N expansion to NLO. Our results for scaling exponents and scaling functions are in agreement within errors with previous weak-coupling estimates for equal-time correlations using effective kinetic theory or classical-statistical field theory. We find these universal results for a wide range of couplings even beyond the weak-coupling regime. Moreover, we have established the self-similar behavior of the strongly momentum-dependent effective coupling.

The computation of the unequal-time spectral and statistical functions allowed us to observe the validity of a generalized fluctuation-dissipation relation in the perturbative regime at high momenta, while we demonstrated that significant violations occur in the nonperturbative infrared. We identified a characteristic deep-infrared regime, where the corresponding distribution function approaches a "plateau". In this regime the spectral function does not decay as a function of relative time, which leads to an enhanced sensitivity to initial times and the absence of positivity for frequencies $\omega > 0$. The statistical function in this regime shows a characteristic peak structure with significant deviations from a Breit-Wigner form.

Our results give unprecedented insights into the nonperturbative nature of collective excitations far from equilibrium. While many features of the system are indeed seen to become universal near a nonthermal fixed point also beyond the weak-coupling regime, unequal-time properties encoded in spectral functions can reveal intriguing properties such as an enhanced sensitivity to initial times. Since our results are based on a large-N expansion, it would be very interesting for future works to also analyze the behavior of weakly-coupled systems with small N using real-time lattice simulations along the lines of [86, 87].

Chapter 4

Thermalization in the quark-meson model

This chapter is based on "*Thermalization and dynamical spectral properties in the quark-meson model*" by L. Shen, J. Berges, J. Pawlowski, A. Rothkopf [88], submitted to Phys. Rev. D, where figures and large parts of the text are taken from. The project was supervised and guided by J. Berges, J. Pawlowski, and A. Rothkopf, who all contributed to writing the text. I carried out the numerical simulations, performed the data analysis, and wrote significant parts of the text. Foundations for this work have been laid during the work on my Master thesis "*Dynamical thermalization in the quark-meson model*" (2017), where in particular a development of the code and an assessment of viable system parameters was carried out. For this project we extended the code used in [64] to include the additional nonvanishing fermionic two-point functions. The source code for this project is publicly accessible via the Zenodo repository under [66].

The aim of this chapter is to gain a deeper understanding of the thermalization process in the quark-meson model, which constitutes a low-energy effective theory of quantum chromodynamics (QCD) with a chiral phase transition manifest in its phase diagram. We investigate the real-time dynamics using two-particle irreducible (2PI) effective action techniques. Our numerical simulation includes the full dynamics of the order parameter of chiral symmetry and spectral properties of quarks and mesons. The latter allows us to trace the available degrees of freedom during the evolution. We show how the model equilibrates in different regions of its phase diagram, where the emergence of Bose-Einstein and Fermi-Dirac statistics confirms that the simulation successfully reaches quantum thermal equilibrium.

This chapter is organized as follows: Section 4.1 outlines the motivation for our work. Subsequently, we briefly review the quark-meson model and give an overview over our nonequilibrium and nonperturbative treatment in Section 4.2. The numerical setup for the time evolution starting from free-field initial conditions quenched to a highly nonequilibrium environment is described. In Section 4.3 we discuss the spectral functions of the bosonic and fermionic degrees of freedom, which provide information about the masses as well as the lifetimes of the dynamical degrees of freedom. We investigate the late-time limit of our simulations, which reveals the dynamical emergence of the fluctuation-dissipation relation and hence allows us to define a thermalization temperature. Finally, Section 4.4 covers the results for the sigma field describing the order parameter of the quark-meson model. We further discuss the behavior of different order parameters in equilibrium which lead to a consistent pseudocritical temperature. In Section 4.5 we conclude with a summary. As a supplement to the main text, information regarding numerical methods can be found in Appendix 4.A.

4.1 Introduction

Recent experimental advances in heavy-ion physics have paved the way for studying strongly interacting matter in extreme conditions. The goal to explore the phase diagram of quantum chromodynamics (QCD) as well as the thermalization of the quark-gluon plasma in heavy-ion collisions (HIC) leads to substantial experimental efforts all over the world. In particular, the quest to discover the conjectured critical point of the QCD phase diagram is a central motivation of modern HIC experiments at collider facilities, such as the Large Hadron Collider (LHC) at CERN and the Relativistic Heavy-Ion Collider (RHIC) at Brookhaven National Laboratory [89, 90]. Ongoing experiments try to reproduce conditions that were present about 10 µs after the beginning of the universe. In the beam energy scan currently executed at RHIC, the phase diagram of QCD is explored over a wide range of temperatures and baryon densities by depositing different amounts of energy in the initial collision volume [91–93]. As the fireball expands and cools, the efficient exchange of energy and momentum among quarks and gluons leads to local thermalization over time [94–96]. The question to answer is: if a critical point exists and some of the volume of the fireball evolves close to it, does the dynamical buildup of long range fluctuations leave any discernible mark on the yields of measurable particles?

Understanding the out-of-equilibrium dynamics of heavy-ion collisions thus remains one of the most pressing theory challenges in heavy-ion physics. So far, genuinely nonperturbative ab-initio calculations of the equilibration process of the quark-gluon plasma and the dynamics close to the phase transition remain out of reach. In order to make progress, we therefore set out to shed light onto pertinent aspects of the physics of dynamical thermalization in heavy-ion collisions by deploying a low-energy effective theory of QCD, the two-flavor quark-meson model. This model incorporates the off-shell dynamics of the lowest mass states in QCD, the pseudoscalar pions and the scalar sigma mode as well as the light up and down quarks. Further degrees of freedom – gluons, heavier quark flavors as well as higher mass hadronic resonances – carry masses $\gtrsim 500\,\mathrm{MeV}$ and are neglected here. This low-energy effective theory reflects the central and physically relevant feature of low-energy QCD: chiral symmetry breaking in vacuum and its restoration at finite temperature and density. At its critical endpoint, the model is expected to lie in the same universality class as QCD and hence constitutes a viable low-energy effective theory to explore dynamical critical phenomena in QCD at finite temperature and density at scales $\lesssim 500\,\mathrm{MeV}$.

In the present work we consider the real-time dynamics of the two-flavor quark-meson model with small current quark masses in a nonexpanding scenario. Progress on the out-of-equilibrium quark-meson model has been made in the context of fermion production [61, 64, 97, 98]. In the presence of an explicit chiral symmetry breaking, the equilibrium chiral transition at finite temperature is a crossover as confirmed for QCD at vanishing and small density, see e.g. [99–101] for recent results. With the help of different initial conditions defined via the initial occupations of sigma and quark fields, we map out the thermalization dynamics for different regions of the phase diagram. This allows, for the first time, to fully study the thermalization dynamics including that of order parameter of chiral symmetry. An extension of the present study to the scenario of an expanding fireball should give access to the freeze-out physics of heavy-ion collisions.

The evolution toward thermal equilibrium is viewed through the lens of the one- and two-point functions of the theory, which are computed with the two-particle irreducible (2PI) approach by means of their quantum equations of motion. These correlation functions not only provide complementary order parameters for the study of chiral symmetry restoration but also give direct access to the spectral properties, including the quasiparticle content of the system. Being genuine nonequilibrium quantities, they map out the whole time evolution of the system including the physics of the crossover transition in the late-time limit.

4.2 The quark-meson model

QCD evolves from a theory of dynamical quarks and gluons at large momentum scales, the fundamental degrees of freedom, to a theory of dynamical hadrons at low momentum scales. This transition of the dynamical degrees of freedom is related to the mass gaps of the respective fields. It is by now well understood that the gluon degrees of freedom start to decouple at about 1 GeV, that is above the chiral symmetry breaking scale k_χ of about 400 MeV. Most of the hadron resonances are too heavy for taking part in the offshell dynamics and we are left with the up, down and to some extend the strange quarks, as well as the pions and the scalar sigma mode, for details see [102, 103]. Indeed, low-energy effective theories emerge naturally at low momentum scales from first principle QCD, and their systematic embedding leads us to the quark-meson model. While its quantitative validity has been proven for momentum scales k with $k \lesssim 300\,\mathrm{MeV}$ [104], it reproduces qualitative QCD features up to $k \lesssim 700\,\mathrm{MeV}$. It is this natural QCD embedding as well as its robust QCD-type chiral properties that has triggered a plethora of works with the quark-meson model on the QCD phase structure with functional methods, see e.g. [63, 105–109]. More recently also real-time correlation functions in equilibrium have been investigated, see e.g. [110–120].

(Pre-)Thermalization has been studied in the $O(N = 4)$ symmetric scalar model coupled to fermions using a $1/N$ expansion to next-to-leading order of the 2PI effective action in [5, 61]. The model was studied extensively in [64, 97] in the context of inflaton dynamics to describe nonequilibrium instabilities with fermion production from inflaton decay. In [98] the model was investigated for highly occupied bosonic fields, where the predictions were shown to agree well with lattice simulation results in the classical-statistical regime. Further results for spectral functions in and out of equilibrium with 2PI effective action techniques can be found in [65], and with classical-statistical simulations in [86, 121] for scalar theories and in [19] for Yang-Mills theory.

In this work we build on these results and investigate the nonequilibrium evolution of the two-flavor quark-meson model introduced in Section 2.4. The quasiparticle excitation spectrum of the quark-meson model is encoded in the spectral functions of the respective fields. Putting together results from Sections 2.3 and 2.4, we recapitulate that the spectral functions of mesons and quarks are defined as the expectation values of the commutator and anticommutator,

$$\begin{aligned} \rho^{\phi}_{ab}(x,y) &= \; i \; \langle [\varphi_a(x), \varphi_b(y)] \rangle \; , \\ \rho^{\psi}_{AB}(x,y) &= \; i \; \langle \{\psi_A(x), \bar{\psi}_B(y)\} \rangle \; , \end{aligned} \tag{4.1}$$

where $a, b = 1, \dots, N$ denote field space and $A, B = 1, \dots, 4$ Dirac spinor indices. Fermion flavor indices are omitted and the operator nature of the quantum fields is implied.

We consider spatially homogeneous and isotropic systems with parity and CP invariance such that only the scalar, vector, vector-zero and tensor components ρ_S, ρ_0, ρ_V, and ρ_T, as introduced in (2.111), have to be considered. The relevant contributions to the quark spectral function are the scalar, vector-zero and vector components, where the vector-zero component represents the quark excitations of the system [118, 122]. For chiral symmetric theories with $m_\psi = 0$ the scalar and tensor components vanish. The spectral functions also encode the equal-time commutation and anticommutation relations of the quantum theory, implying that

$$i\partial_t \rho^\phi(t,t',|\mathbf{p}|)\Big|_{t=t'} = 1\,, \qquad\qquad \rho_0(t,t,|\mathbf{p}|) = i\,, \tag{4.2}$$

while all other fermion components vanish at equal time.

In addition to the spectral functions we also consider the so-called *statistical functions.* These are the anticommutator and commutator expectation values

$$\begin{aligned} F^\phi(x,y) &= \frac{1}{2}\left\langle\{\varphi(x),\varphi(y)\}\right\rangle - \phi(x)\phi(y)\,, \\ F^\psi(x,y) &= \frac{1}{2}\left\langle[\psi(x),\bar{\psi}(y)]\right\rangle\,, \end{aligned} \tag{4.3}$$

where field space, Dirac and flavor indices are suppressed. The statistical functions carry information about the particle density of the system, i.e. the occupation of the available modes in the system. Together, the spectral and statistical functions fully describe the time-ordered connected two-point correlation functions.

The nonequilibrium dynamics of the spectral and statistical functions is studied using the evolution equations derived from the 2PI effective action. Quantum fluctuations are taken into account at NLO in $1/N$, with $N = 4$ being the number of scalar fields, and at NLO in the Yukawa coupling g, see Sections 2.3.4 and 2.4.4 for details. We iteratively solve the equations of motion without further approximations.

4.2.1 Initial conditions

The derivation of the nonequilibrium 2PI effective action and the equations of motions following from it rely on the assumption of a Gaussian initial state. This corresponds to a system initially exhibiting the characteristics of a noninteracting theory. However, higher order correlation functions build up during the subsequent time evolution. While this appears at first sight to correspond to a very limited choice of initial conditions, it still allows for a wide variety of different configurations through which we can determine for instance the energy density $\varepsilon_{\text{init}}$ at the beginning of our computation. In particular, the Gaussian initial state represents a genuine nonequilibrium state in the fully interacting nonequilibrium system, in which the time evolution takes place.

We allow for spontaneous symmetry breaking by using a negative mesonic bare mass squared $m^2 < 0$ in the classical potential of the system. Since the initial state is determined by a free theory with $m^2 = m^2_{\text{init}} > 0$, the sign flip of m^2 leads to a quench of the classical potential from positive to negative curvature in the first time step. At initial time, the classical potential is minimal at vanishing field expectation value while the minimum at $t > 0$ becomes nonzero by taking $m^2 < 0$.

A Gaussian initial state can be fully specified in terms of the one-point and two-point functions. Since the field evolution equation involves second order time derivatives, one has to specify both the sigma field value and its initial time derivative. We denote the former by σ_0 and choose the latter to vanish, i.e.

$$\langle\sigma(t)\rangle\Big|_{t=0} = \sigma_0\,, \qquad\qquad \partial_t\langle\sigma(t)\rangle\Big|_{t=0} = 0\,. \tag{4.4}$$

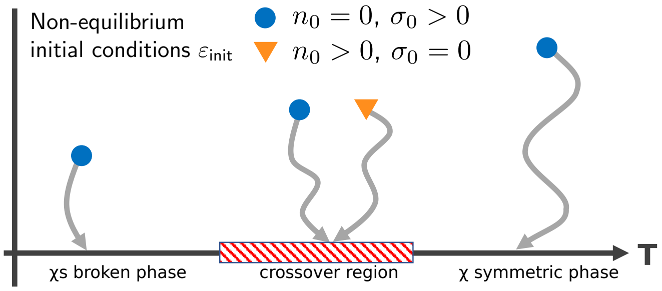

Figure 4.1: Sketch of the setup deployed in this study. We consider the real-time evolution from nonequilibrium initial states characterized by an energy density sourced either through a finite σ field expectation value (blue circle) or a nonzero occupancy of fermionic modes (orange triangle). Depending on the initial energy contained in the system, one of three discernible final states, the chiral broken phase, the crossover regime or the (almost) symmetric phase is approached.

As pointed out above, the presence of the finite bare quark mass m_ψ can cause the field to move away from $\sigma_0 = 0$ due to the backreaction with fluctuations of the theory.

We specify the initial conditions for the two-point functions in terms of the spectral and statistical components. The initial conditions for the bosonic (fermionic) spectral functions are fully determined by the equal-time (anti)commutation relations (4.2). For the remaining statistical functions we employ free-field expressions with a given initial particle number. The bosonic statistical function reads

$$F_i(t, t', |\mathbf{p}|) = \frac{n_i(t, |\mathbf{p}|) + \frac{1}{2}}{\omega_i(t, |\mathbf{p}|)} \cos\left[\omega_i(t, |\mathbf{p}|)(t - t')\right] , \tag{4.5}$$

with $i = \sigma, \pi$. At initial time $t = t' = 0$ the dispersion is set to $\omega_i(0, |\mathbf{p}|) = \sqrt{|\mathbf{p}|^2 + m_{\text{init}}^2}$ with initial mass squared $m_{\text{init}}^2 > 0$ and the particle distribution is given by $n_i(0, |\mathbf{p}|) = 0$. For the fermions the free statistical function can be written as

$$F^\psi(t, t, |\mathbf{p}|) = \frac{-\gamma^i p_i + m_\psi}{\omega_\psi(t, |\mathbf{p}|)} \left(\frac{1}{2} - n_\psi(t, |\mathbf{p}|)\right) , \tag{4.6}$$

where we choose the initial dispersion to be $\omega_\psi(0, |\mathbf{p}|) = \sqrt{|\mathbf{p}|^2 + m_\psi^2}$ and the initial particle distribution to be constant, i.e. $n_\psi(0, |\mathbf{p}|) = n_0$. Details about the numerical implementation of these initial conditions can be found in Appendix 4.A.2.

The energy contained in the initial state via $\varepsilon_{\text{init}}$ determines the temperature at which the system thermalizes. By preparing different initial conditions, we can study the thermalization toward different temperatures and hence phases of the model as sketched in Figure 4.1.

4.2.2 Numerical implementation

As is customary in the context of the 2PI effective action, we discretize the system on the level of the equations of motion. In contrast to the purely bosonic field theory, the explicit form of the fermionic equations allows us to deploy a leap-frog scheme, where the fermionic two-point functions are discretized in a temporally staggered fashion. General information about 2PI simulation methods can be found in Appendix 3.B. Specifications regarding the quark-meson model are summarized in Appendix 4.A.

We choose the parameters of the theory and the ultraviolet (UV) cutoff such that the phenomenology of the low-energy effective theory is reproduced. The numerical time evolution is computed using a spatial grid with $N_x = 200$ lattice points and a lattice spacing of $a_x = 0.2$. The time step size is chosen to be $a_t = 0.05\,a_x$ guaranteeing energy conservation at the level of a few percent for the times analyzed. In the following all dimensionful quantities will be given in units of the pseudocritical temperature T_{pc}, which is obtained according to the procedure described in Section 4.4.2, see Figure 4.18. We find that the pseudocritical temperature has the value $T_{pc} = 1.3\,a_x^{-1}$. The rescaling to dimensionless quantities can be found in Appendix 4.A.3.

Interactions between the macroscopic field, the bosonic and the fermionic propagators lead to an exchange of energy between the different sectors. To observe an efficient energy exchange and equilibration process at computationally accessible times, it is necessary to study large couplings. We choose the quartic self-coupling $\lambda = 90.0$, the Yukawa coupling $g = 5.0$, the bare mass squared $m^2 = -0.0047$ and the bare fermion mass $m_\psi = 0.15$. These parameters not only allow us to observe the equilibration of the system on timescales accessible computationally but also lead to reasonable values for the observables when compared to the phenomenological values known at $T = 0$, where the pion decay constant is $f_\pi \simeq 93.5\,\text{MeV}$, the meson masses are $m_\sigma \simeq 400\,\text{MeV}$ and $m_\pi \simeq 135\,\text{MeV}$, and the constituent quark mass is $m_q = 350\,\text{MeV}$ [123]. The above choices are close to that used in equilibrium computations of the quark-meson model with functional methods and a physical ultraviolet cutoff $\Lambda_{\text{UV}} \approx 1\,\text{GeV}$. Moreover, a large value of the mesonic self-interaction λ is also present in functional QCD computations [103, 124]. There it can be shown that the self-interaction is of subleading relevance for the fluctuation dynamics despite the large size of the coupling. These studies as well as a comparison of the quark-meson model to QCD, see e.g. [104], reveal that a one-to-one correspondence of the low-energy limits of both theories in quantitative approximations to the full dynamics in the quark-meson model either requires a far smaller UV cutoff for the latter or a systematic improvement of the model toward QCD-assisted low-energy effective theories [102, 103]. In the present work we restrict ourselves to studying the qualitative properties of the nonequilibrium dynamics as a first step.

When identifying the sigma field expectation as pion decay constant, we can reproduce $f_\pi < m_\pi < m_q < m_\sigma$ at low temperatures. At the lowest temperatures considered in this work, we find $f_\pi/m_\pi \simeq 0.65$, which is very close to the phenomenologically known value of approximately 0.69, the meson mass ratio $m_\sigma/m_\pi \simeq 1.75$, smaller than the vacuum value of around 2.9 but expected to increase when going to lower temperatures, and $m_q/m_\pi = 1.45$, being on the order of magnitude with zero-temperature value of 2.6. Hence we expect our findings to qualitatively reproduce the QCD dynamics. It is noted, however, that the meson mass ratio $m_\sigma/m_\pi < 2$ leads to another order of the thresholds for scattering processes, and hence respective differences in the spectral functions.

For the bosonic sector, we use vacuum initial conditions, i.e. $n_\phi(t = 0, |\mathbf{p}|) = 0$. The initial mass is fixed at $m^2_{\text{init}} = 0.008$. The fermion initial distribution is chosen to be constant $n_\psi(t = 0, |\mathbf{p}|) = n_0$. We study simulations with fluctuation dominated initial conditions where the fermion number n_0 is varied between 0 and 1 while the initial field value is $\sigma_0 = 0$. Furthermore, the field dominated initial conditions with a nonvanishing field value of $\sigma(t = 0) = \sigma_0$ between 0 and 2.0 with vanishing fermion number $n_0 = 0$ are investigated. Unless otherwise specified, plots are shown for the case $n_0 = 0$ and $\sigma_0 = 0$. For plots showing spectral and statistical functions in frequency space a cubic spline interpolation of the data points is employed.

4.3 Spectral functions

In this section we explore the nonequilibrium evolution of the quark-meson model from the point of view of its quark and meson spectral functions. As these quantities are derived from the two-point correlation functions, they provide insight on the (quasi)particle content of the theory, the dispersion relation of propagating modes and their decay widths, providing insight into the modification of the system due to the presence of a (non)equilibrium medium. Our numerical simulations find clear indications for quasiparticles in both the infrared (IR) and the ultraviolet (UV) momentum range, revealing the presence of additional light propagating fermion modes for temperatures above the pseudocritical temperature.

As discussed in Section 3.4, it is convenient to analyze the spectral functions in the Wigner representation where the Fourier transformed spectral function can be interpreted as the density of states such that its structure provides information about the quasiparticle states of the system. Therefore, the temporal dependence of the unequal-time two-point correlation functions on the two times t and t' is rephrased in terms of Wigner coordinates: the central time $\tau = (t+t')/2$ and the relative time $\Delta t = t - t'$. The dynamics in Δt describes microscopic properties of the system while the evolution in τ describes macroscopic properties governed by nonequilibrium characteristics of the system. In order to study the frequency spectrum of the spectral functions, we apply the Wigner transformation (3.18) to the propagators. For a real and antisymmetric spectral function (as in the bosonic case and for the fermionic scalar, vector and tensor components) as well as for an imaginary and symmetric spectral function (as for the fermionic vector-zero component) the Wigner transform of $\rho(\tau, \Delta t, |\mathbf{p}|)$ is imaginary. Since $\tilde{\rho}(\tau, \omega, |\mathbf{p}|)$ according to its definition in (3.18) is real for all considered bosonic and fermionic components, we omit the tilde in the following to ease notation for the plot labels. Further note that due to symmetry, it is sufficient to present the Wigner transformed spectral functions for positive frequencies ω.

The commutation and anticommutation relations (4.2) can be rephrased in frequency space,

$$\int \frac{\mathrm{d}\omega}{2\pi}\, \omega\, \rho^{\phi}(\tau, \omega, |\mathbf{p}|) = i\,, \qquad\qquad \int \frac{\mathrm{d}\omega}{2\pi}\, \rho_0(\tau, \omega, |\mathbf{p}|) = i\,, \tag{4.7}$$

where they are referred to as *sum rules*. In our numerical computations, the bosonic and fermionic sum rules are satisfied at the level of $\mathcal{O}(10^{-2})$ and $\mathcal{O}(10^{-6})$, respectively.

4.3.1 Establishing thermal equilibrium at late times

Before embarking on a detailed study of the dynamical approach to thermal equilibrium, we first ascertain that our simulations of the quark-meson model reach the unique equilibrium fixed point at late times. We do so by observing the dynamic emergence of the fluctuation-dissipation theorem. One needs to keep in mind that as discussed in [61], the idealized thermal equilibrium state cannot be reached in principle due to the time-reversibility of the evolution equations. The simulation approaches the state more and more closely over time and at some point becomes indistinguishable from it for a given resolution. Hence we expect the computation to approach a steady state.

The fluctuation-dissipation theorem is reflected in a particular property of the spectral and statistical functions in thermal equilibrium: they are not independent of each other. For the bosonic and fermionic two-point functions it can be phrased in four-dimensional Fourier space as

$$F^{\phi}_{\mathrm{eq}}(\omega, \mathbf{p}) = -i\left(\frac{1}{2} + n_{\mathrm{BE}}(\omega)\right)\rho^{\phi}_{\mathrm{eq}}(\omega, \mathbf{p})\,,$$

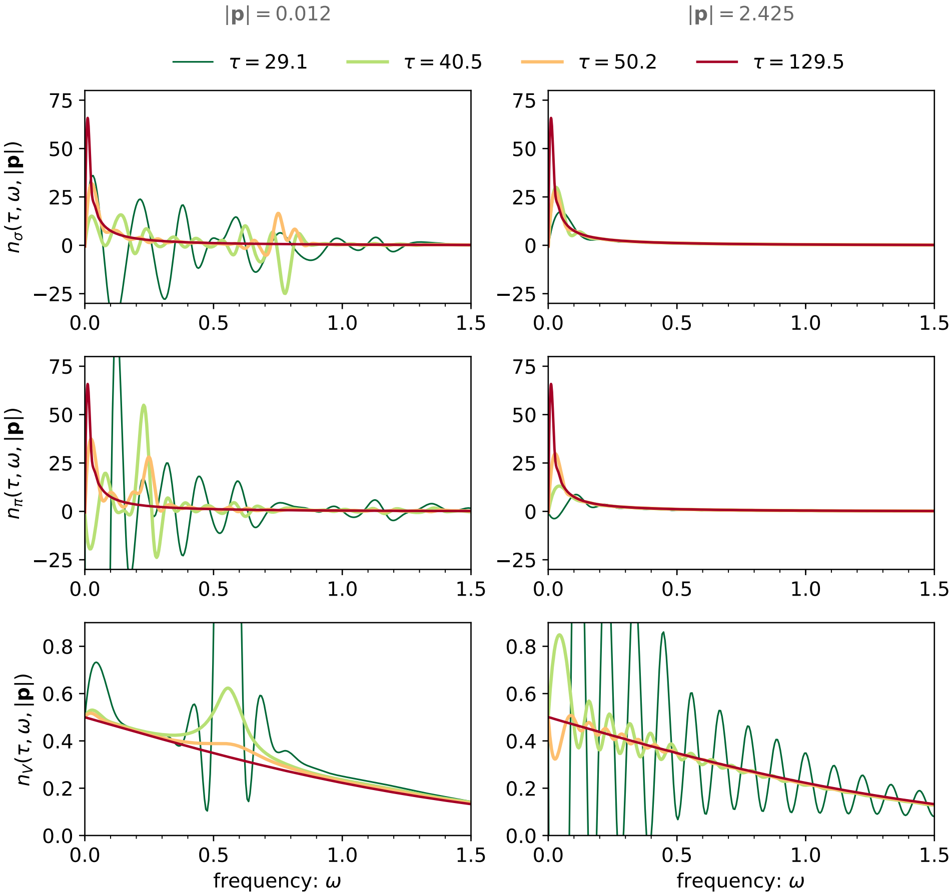

Figure 4.2: We show the time evolution of the effective particle number defined in (4.9) for bosonic and fermionic components (rows) and two different momenta (left and right column). At late times (red curve) the effective partcle number becomes time- and momentum-independent and approaches the shape of a Bose-Einstein and Fermi-Dirac distribution, respectively. The shown data is interpolated using a cubic spline.

$$F^{\psi}_{\text{eq}}(\omega,\mathbf{p}) = +i\left(\frac{1}{2} - n_{\text{FD}}(\omega)\right)\rho^{\psi}_{\text{eq}}(\omega,\mathbf{p})\,, \tag{4.8}$$

with $n_{\text{BE}}(\omega) = (e^{\beta\omega}-1)^{-1}$ being the Bose-Einstein and $n_{\text{FD}}(\omega) = (e^{\beta\omega}+1)^{-1}$ the Fermi-Dirac distribution. In (4.8) the frequency ω is the Fourier conjugate to the relative time $\Delta t = t - t'$ as the time-dependence of F_{eq} and ρ_{eq} can be fully described in terms of Δt due to the time-translation invariance of thermal equilibrium.

Out of equilibrium the independence of F and ρ manifest itself in the fact that the ratio F/ρ in general carries a momentum dependence. The equilibrium relation (4.8) on the other hand allows us to define the generalized particle distribution function [41]

$$n_i(\tau,\omega,|\mathbf{p}|) = i\,\frac{F_i(\tau,\omega,|\mathbf{p}|)}{\rho_i(\tau,\omega,|\mathbf{p}|)} \pm \frac{1}{2}\,, \tag{4.9}$$

with a negative (positive) sign for bosonic (fermionic) components. This kind of distribution function has been studied in the context of nonthermal fixed points in relativistic as well as nonrelativistic scalar field theories [32]. Considering (4.9) the approach of thermal equilibrium in a general nonequilibrium

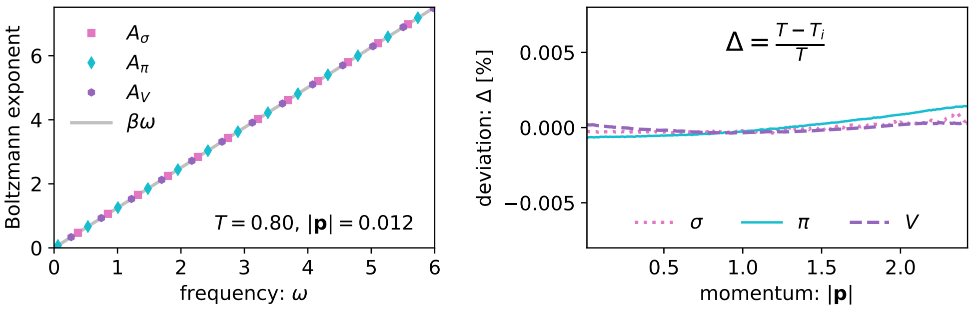

Figure 4.3: *Left:* The generalized Boltzmann exponents defined in (4.10) shown as a function of frequency ω at a given momentum $|\mathbf{p}|$ for bosonic and fermionic components. For better visibility, only every 39th data point is shown. Using a linear fit one can determine the slope β and hence the temperature T for each component. The temperature T indicated in the plot is averaged over all momenta and the three components. *Right:* The relative deviation from the thermalization temperature $\Delta = (T_i - T)/T$ shown for all three components as a function of momentum. The results for the bosonic and fermionic sectors agree very well.

time evolution setup is characterized by $n_i(\tau, \omega, |\mathbf{p}|) \to n_{\mathrm{BE/FD}}(\omega)$.

In Figure 4.2 we show the time evolution of the particle distribution defined in (4.9) for low and high momenta (left and right column). One can see that at late times (red curves) the same shape is approached for small and large momenta, whereas at early times the distribution functions differ from each other. This loss of momentum dependence is required for the thermalization process and reflects the emergence of the fluctuation-dissipation relation in the equilibrium state. From the late-time distributions shown in Figure 4.2 one can already guess that thermal distribution functions are reached.

We also observe that the evolution of the effective particle number is different for fermions and bosons. The bosonic distribution functions n_σ and n_π show strong oscillations along frequencies at low momenta whereas oscillations at high momenta are weak. Since the particle distributions are computed by taking the ratio of the statistical and spectral functions, n_i plotted against ω essentially describes how similar the peaks shapes of F and ρ are. In the high-momentum range we find that the quasiparticle peaks of the bosonic statistical and spectral functions resemble one another from early times on, while in the low-momentum range more time is required for the peak shapes become aligned. In contrast, the quarks show an opposite behavior. Their distributions have much stronger frequency oscillations for large momenta than for small momenta, i.e. it takes longer for the high-momentum modes to approach a thermal distribution.

Putting the pieces together, we can see that a redistribution of the occupancies in fermionic and bosonic degrees of freedom occurs during the nonequilibrium time evolution. While the timescales to converge to thermal distribution functions depend on the particle species and the momentum modes, we find that the distribution functions all become stationary for times $\tau \gtrsim 100$, reflecting the time-translation invariant property of thermal equilibrium.

Although Figure 4.2 already indicates the approach of thermal distribution functions, we still need to prove whether our final state actually fulfils the fluctuation-dissipation theorem. For a quantitative analysis, we compute the *generalized Boltzmann exponents*

$$A_i(\tau, \omega, |\mathbf{p}|) = \ln\left[n_i^{-1}(\tau, \omega, |\mathbf{p}|) \pm 1\right], \tag{4.10}$$

with positive (negative) sign for bosonic (fermionic) components. In thermal equilibrium, the fluctuation-dissipation theorem (4.8) requires these exponents to suffice $A_i(\tau, \omega, |\mathbf{p}|) = \beta\omega$, implying in particular that they become independent of momentum $|\mathbf{p}|$ and time τ, where the latter is fulfilled by our late-time states.

A linear fit of our simulation data for the generalized Boltzmann exponents to $\beta\omega$ yields the thermalization temperature $T_{\mathbf{p}} = \beta_{\mathbf{p}}^{-1}$, which can in general be τ-dependent. An example for such a fit is presented on the left-hand side of Figure 4.3. The plot shows that the Boltzmann exponent of all three components $i = \sigma, \pi, V$ nicely fits to the same line with slope β. We compute the temperature averaged over all momenta to obtain T_i for each component. The system temperature denoted by T is taken to be the mean over all three components.

For every simulation, we compute the temperatures at each momentum $|\mathbf{p}|$ and study the momentum dependence of the obtained temperature $T_{\mathbf{p}}$. As pointed out in [5], thermodynamic relations can become valid before real thermal equilibrium is attained, a phenomenon known as *prethermalization*. Thermal equilibrium is characterized by $T_{\mathbf{p}}$ being equal to some equilibrium temperature for all modes $|\mathbf{p}|$. On the right side of Figure 4.3, the deviations from the mean thermalization temperature T are plotted. As can be seen, the deviations are very small. Hence, the Boltzmann exponents at late times τ become momentum-independent and the late-time states are thermal in the sense that they fulfill the fluctuation-dissipation theorem. The thermalization temperatures for all simulations in this work have been determined at time $\tau = 130$. For the example shown in Figure 4.3 it was checked that the thermalization temperatures found in the time range between $\tau = 100$ and $\tau = 160$ are constant at the level of $\mathcal{O}(10^{-3})$. We verified for all simulations in this work that the temperature has reached a stationary value at time $\tau = 130$.

Having clarified the successful approach to quantum thermal equilibrium in our system, we are now able to study the differences during the out-of-equilibrium evolution leading to the thermal states in detail.

4.3.2 Nonequilibrium evolution of spectral and statistical functions

In this section we study the dynamics of the thermalization process, starting from fluctuation or field dominated initial conditions. We investigate the time evolution of the spectral and statistical functions and consider derived quantities such as particle masses and widths. While the initial conditions strongly influence the nonequilibrium dynamics taking place, the final states are universal and characterized by the initial energy density $\varepsilon_{\text{init}}$ that translates into a unique temperature.

The time evolution leads to the emergence of quasiparticle peaks in the spectral functions of both quark and mesons. The value of the particle mass and its decay width are a consequence of the interactions taking place among the microscopic degrees of freedom. While the initial states correspond to free particles, which would have a spectrum given by a δ-peaks located at the mass parameters of the classical action, the scattering effects included in the nonequilibrium evolution lead to peaks with finite widths in the spectrum.

In Figure 4.4 we present a representative set of fermionic spectral functions from the vector-zero channel, which describes the quark excitation spectrum [55, 122]. The three columns correspond to three different field dominated initial conditions of increasing initial energy density, as sketched by the blue dots in Figure 4.1. The top row shows the Wigner-space spectral function at the lowest available momentum (IR), the bottom row at the highest momentum (UV). We can identify several characteristic properties of these spectral functions from a simple inspection by eye.

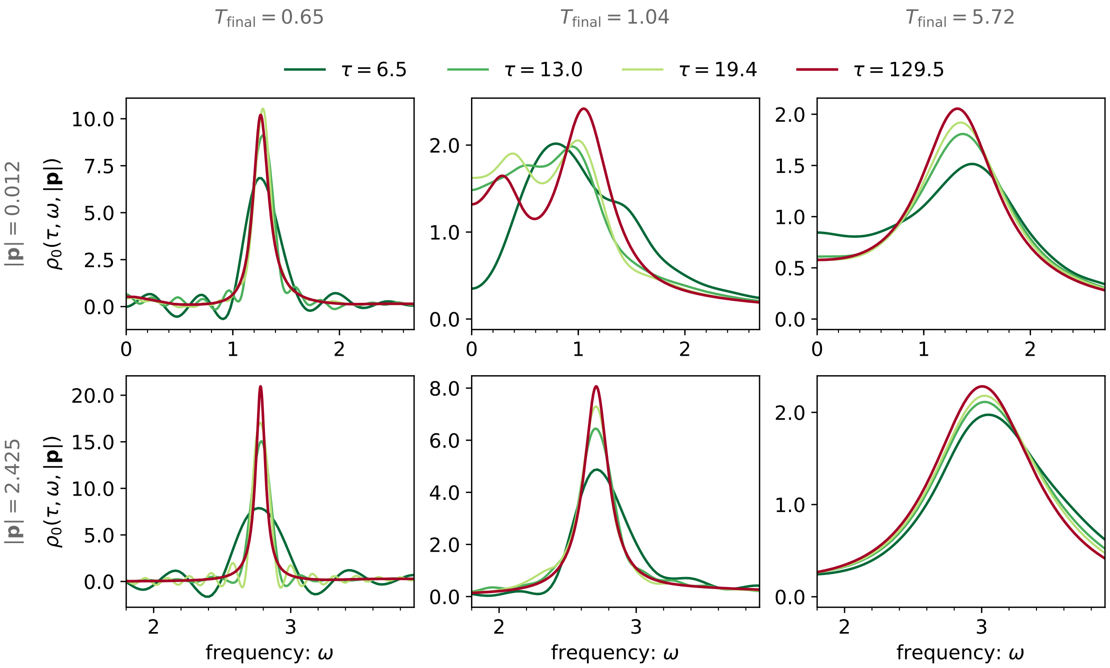

Figure 4.4: A representative selection of spectral functions from the fermion vector-zero channel in the infrared (top row) and the ultraviolet (bottom row) in three different regimes labeled by the temperatures of their final state. Each panel contains four curves indicating different snapshots along the thermalization trajectory. All three simulations employ field dominated initial conditions, i.e. $\sigma_0 > 0$ and $n_0 = 0$.

In the UV a single quasiparticle structure is present at all times and at all energy densities. With increasing energy density in the initial state, corresponding to an increasing final temperature, the position of the peak as well as its width increase. This is consistent with the expectation that a fermion in an energetic medium will be imbued with an in-medium mass (to lowest order in perturbation theory it would be proportional to the temperature). Higher energy densities go hand in hand with an increased chance of scattering between the fermion and the other medium constituents, which also leads to a larger in-medium width. In the UV no qualitative difference exists between the broken, crossover or symmetric phase behavior.

On the other hand, in the IR a clear distinction between the crossover region and all other energy density regimes is visible. While we also find a single quasiparticle structure at low and high initial energy densities, in the crossover region at early times no well-defined peaks are present at all. Instead as times passes two structures emerge. One dominant peak is located where one would expect the usual quasiparticle excitation to reside, another peak sits close to the frequency origin, denoting a significantly lighter additional propagating mode.

In general we find that also for the other fermionic and bosonic spectral functions the approach of the equilibrium state depends on the initial conditions. In the presence of a nonzero initial field value σ_0, the spectral functions evolve differently than in the case where $\sigma_0 = 0$ but the fermion occupation is finite, i.e. when the initial state contains more energy in terms of fermion occupations. As pointed out in Figure 4.4, the most interesting dynamical features can be seen in the low-momentum area, which we therefore focus on during the following analysis.

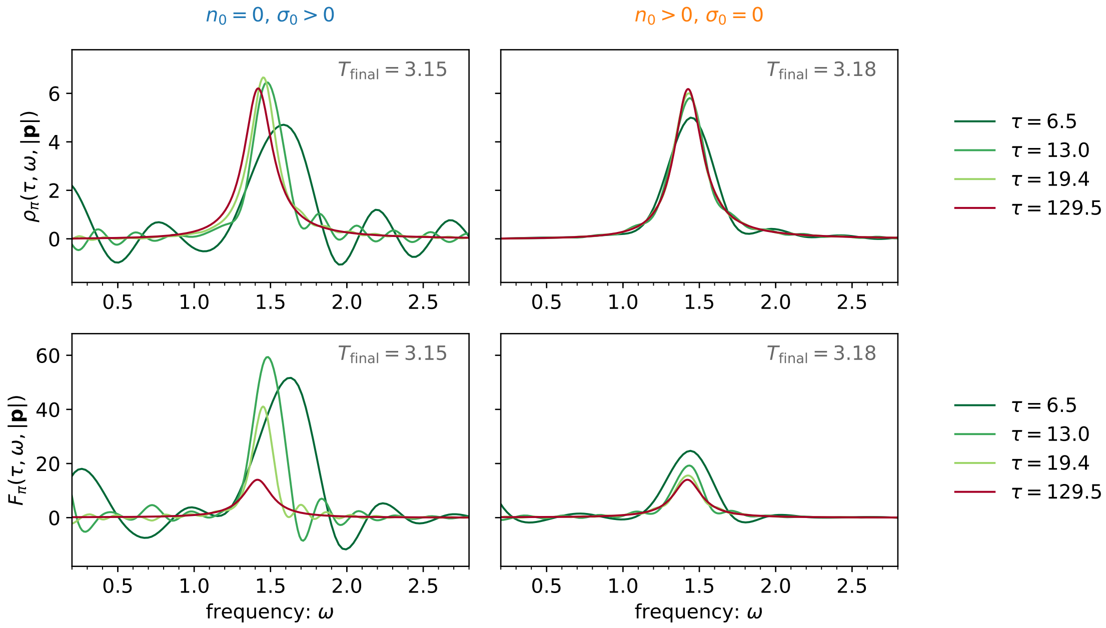

Figure 4.5: Time evolution of the pion spectral and statistical functions shown for two different initial conditions at the smallest available momentum $|\mathbf{p}| = 0.012$. The left column shows a simulation deploying field dominated initial conditions with $\sigma_0 = 1.36$, the right column fluctuation dominated initial conditions with $n_0 = 0.8$. Both simulations lead to thermal states at temperatures where chiral symmetry is restored.

High energy densities

Here, we study the quark-meson model at high enough initial energy densities such that the late-time evolution thermalizes in the high-temperature phase, where chiral symmetry is restored. For our analysis we compare two simulations starting from different initial conditions characterized by almost indistinguishable energy densities. One is dominated by the field $\sigma_0 = 1.36$ and $n_0 = 0$, while the other is dominated by fermion fluctuations $\sigma_0 = 0$ and $n_0 = 0.8$. The final states feature similar thermalization temperatures of $T = 3.15$ and $T = 3.18$, respectively. However, since the initial states vary strongly from each other, the evolution toward thermal equilibrium takes significantly different paths.

For such high initial energy densities, the differences in the time evolution are most apparent in the bosonic sector. This can be studied by looking at the bosonic spectral and statistical functions. Numerical results are shown in Figure 4.5, where only the pion spectral and statistical functions are presented since the behavior of the sigma meson is analogous. The final states of both simulations (red curve) are characterized by the same peak shapes for both spectral and statistical functions. However, the functions at intermediate times exhibit a completely different behavior.

For field dominated initial conditions (left column in Figure 4.5) the peak position of the spectral function moves toward smaller frequencies with time, which means that the mass of the quasiparticle state decreases during the time evolution. In addition, the nonzero initial field leads to large amplitudes in the pion statistical function at early times (lower left plot in Figure 4.5) which corresponds to relatively high occupancies in the bosonic sector compared to the final thermal distribution. These occupancies have to redistribute to other bosonic momentum modes $|\mathbf{p}|$ and the fermionic sector to let

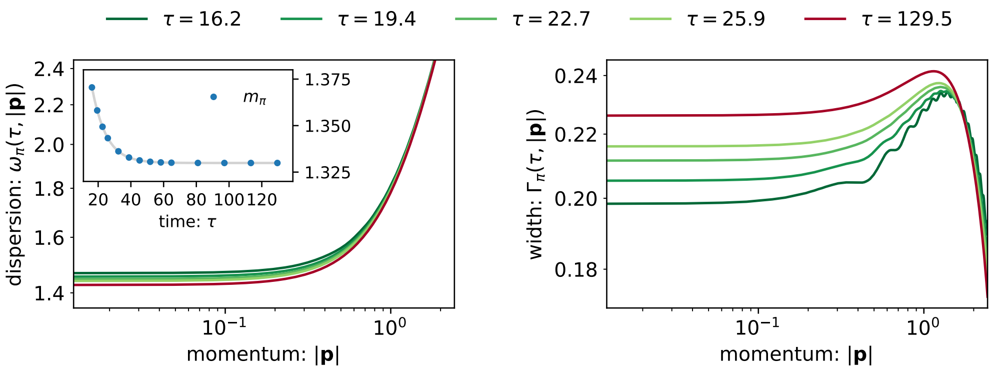

Figure 4.6: Time evolution of the dispersion relation and the momentum-dependent width of the pion. The inset shows the time evolution of pion mass obtained from fits of the dispersion relation to $Z\sqrt{|\mathbf{p}|^2 + m_\pi^2}$ at various times τ, where $Z = 1.07$ is obtained for all times analyzed. The data is shown for field dominated initial conditions with $\sigma_0 = 1.24$ and $n_0 = 0$.

the system equilibrate.

This behavior can be readily understood from the microscopic evolution equations of the system. The finite-valued initial field drives the fluctuations in the bosonic sector because it contributes to the bosonic self-energy at initial time $t = 0$. Since the nonequilibrium time evolution takes into account the full time history since $t = 0$, these initial fluctuations not only play a role at initial time but also at intermediate times. Only at late times, the system looses the memory about the details of the initial state. Since the macroscopic field only couples to the bosons directly but not to the fermions, the energy provided by the initial field is first turned into bosonic fluctuations before being transferred to fermionic modes. As a consequence, the thermalization of an initial state with nonzero initial field value shows rich dynamics in the bosonic spectra.

In contrast, for fluctuation dominated initial conditions (right column in Figure 4.5) one observes a continuous increase of the amplitudes of both spectral and statistical functions until the maximum is reached in the thermal state. If the initial energy density is provided via fermionic fluctuations, the thermal final state is found to be realized already at intermediate times.

The spectral functions can be used to deduce the dispersion relation and lifetimes of the corresponding quasiparticle species. Following [85] we assume for the moment that the spectral function decays exponentially and can be approximated as $\rho(t, t', |\mathbf{p}|) = e^{-\gamma_{\mathbf{p}}|t-t'|}\omega_{\mathbf{p}}^{-1} \sin[\omega_{\mathbf{p}}(t - t')]$ with a dispersion $\omega_{\mathbf{p}}$ and a damping rate $\gamma_{\mathbf{p}}$, which are both allowed to be τ-dependent. The corresponding Wigner transform is given by $\rho(\tau, \omega, |\mathbf{p}|) = \rho_{\mathrm{BW}}(\tau, \omega, |\mathbf{p}|) + \delta\rho(\tau, \omega, |\mathbf{p}|)$ where ρ_{BW} denotes the relativistic Breit-Wigner function

$$\rho_{\mathrm{BW}}(\tau, \omega, |\mathbf{p}|) = \frac{2\omega\Gamma(\tau, |\mathbf{p}|)}{\left[\omega^2 - \omega^2(\tau, |\mathbf{p}|)\right]^2 + \omega^2\Gamma^2(\tau, |\mathbf{p}|)}\,, \tag{4.11}$$

which describes a peak with width $\Gamma(\tau, |\mathbf{p}|) = 2\gamma_{\mathbf{p}}(\tau)$ at position $\omega = \omega(\tau, |\mathbf{p}|)$. The term $\delta\rho \sim \exp(-2\tau\gamma_{\mathbf{p}})$ describes boundary effects due to the finite integration range in (3.18). Since $\delta\rho$ decreases exponentially with $\tau\gamma_{\mathbf{p}}$, this term is negligible for sufficiently large damping ratios and/or sufficiently late times [85]. Otherwise, the frequency-space spectral function suffers under severe noise coming from boundary effects. For all times shown in this work, we find that boundary effects are irrelevant.

We observe that peak shapes of the bosonic spectral functions can be well approximated by the

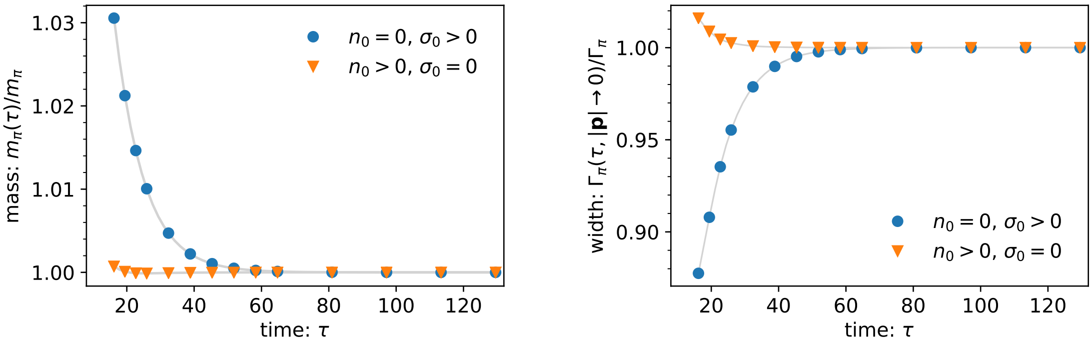

Figure 4.7: Time evolution of the pion mass and the pion width in the limit $|\mathbf{p}| \to 0$. Results are shown for field dominated initial conditions with $\sigma_0 = 1.36$ and $n_0 = 0$ (blue dots) as well as fluctuation dominated initial conditions with $\sigma_0 = 0$ and $n_0 = 0.8$ (orange triangles).

Breit-Wigner function (4.11), see Appendix 4.A.4 for plots. At some given time τ, performing Breit-Wigner fits of the spectral function at all momenta $|\mathbf{p}|$ yields the dispersion relation $\omega(\tau, |\mathbf{p}|)$ and the momentum-dependent width $\Gamma(\tau, |\mathbf{p}|)$. For initial states with high energy densities, such as considered in this section, the spectral and statistical functions exhibit quasiparticle peak structures already at early times (see Figure 4.5). Consequently, it is possible to fit a Breit-Wigner function to the spectral functions at any stage such that the time evolution of the dispersion relation $\omega_i(\tau, |\mathbf{p}|)$ and momentum-dependent width $\Gamma_i(\tau, |\mathbf{p}|)$ for $i = \sigma, \pi$ can be mapped out.

In the left plot of Figure 4.6 we show the dispersion relation of the pion at different times τ encoded in the color scheme. A fit of $\omega(\tau, |\mathbf{p}|)$ to the relativistic dispersion relation $Z\sqrt{|\mathbf{p}|^2 + m^2}$ at various times τ yields the quasiparticle masses $m(\tau)$, which are shown in the inset. In the following, the stationary late-time value is denoted as m. We note that the mass corresponds to the dispersion relation in the limit of vanishing momentum, i.e. $m = \omega(\tau, |\mathbf{p}| \to 0)$. The right plot of Figure 4.6 displays the momentum-dependent width of the pion extracted from the Breit-Wigner fits. We find a plateau in the IR and a maximum in the UV. In analogy to the dispersion, where the quasiparticle mass describes the zero-momentum limit, we can extract the asymptotic value of the width in the limit of vanishing momentum, $\Gamma = \Gamma(\tau, |\mathbf{p}| \to 0)$. Since Γ corresponds to the width of the spectral function that is peaked at the quasiparticle mass, we can be viewed as the width of the quasiparticle. As the right plot in Figure 4.6 indicates, Γ is increasing with time.

We can now work out the differences observed in Figure 4.5 in a quantitative fashion. There is an apparent difference in the approach of the late-time values of the mass m_π and the width Γ_π when comparing the time evolution starting from the two different initial conditions. The results are shown in Figure 4.7, where again only the pion data is shown because the sigma meson behaves accordingly.

For field dominated initial conditions the effective mass of the pion meson decreases during the time evolution, whereas for fluctuation dominated initial conditions it grows, albeit only slightly. This is in accordance to the previous observation of the shifting peak position for field dominated initial conditions. It is important to note that the mass of the quasiparticles is not contained in the initial state, since m_{init} is much smaller than the particle masses of the thermal state, but generated dynamically during the time evolution. The quasiparticle masses build up from the fluctuations contained in the self-energies. Since the nonzero initial field value leads to large bosonic self-energy contributions in the beginning of the time evolution, at early times the masses are larger than in the case of vanishing

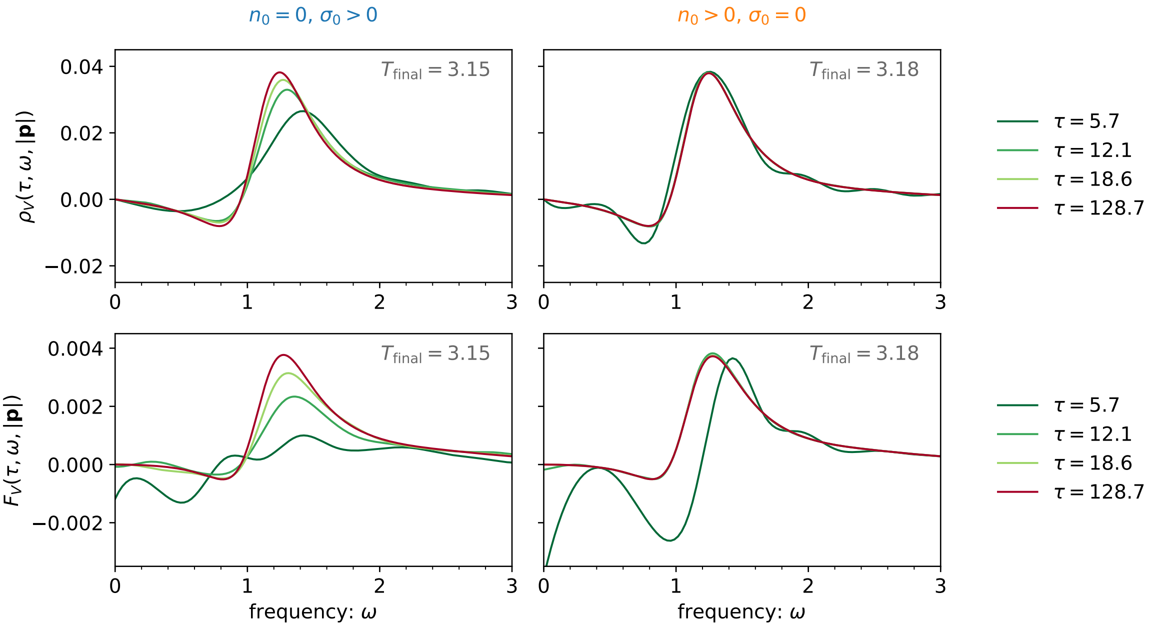

Figure 4.8: Time evolution of the vector component quark spectral and statistical functions shown for the same initial conditions as in Figure 4.5 at momentum $|\mathbf{p}| = 0.016$.

initial field.

The time-dependence of the spectral width shown in the right plot of Figure 4.7 can be understood in terms of the sum rule (4.7) according to which the bosonic spectral functions are normalized. Due to the additional factor of ω in the integrand, which arises from the time-derivative on one of the fields in the boson commutation relation, a larger mass automatically implies smaller widths. Consequently, the behavior of mass and width in the time evolution must be converse to each other.

After discussing the dynamics of the meson spectral and statistical functions at high initial energy densities, we now turn to the quark sector. After decomposing the Dirac structure of fermionic two-point functions and imposing symmetries, we are dealing with four components for the quark spectral and statistical functions, the scalar, vector-zero, vector and tensor components as introduced in (2.111). Of these four components, the vector-zero component contains information about which states can be occupied [55, 122]. Since it is normalized to unity according to the sum rule (4.7), the vector-zero component quark spectral function can be interpreted as the density of states for the quarks.

We note that in a chiral symmetric theory with vanishing fermion bare mass one finds $\rho_S = \rho_P = \rho_T^{\mu\nu} = 0$ since only components in (2.111) that anticommute with γ_5 are allowed. Here, we consider a setup where chiral symmetry restoration takes place. For initial conditions with high energy densities and the corresponding final states in the high-temperature chiral symmetric regime, the quark dynamics can be studied in terms of the vector-zero and vector component.

As was shown in Figure 4.4, for high energy densities there is not much dynamics taking place in the excitation spectrum of the quarks. More insight can be gained by looking at the vector component which is presented in Figure 4.8 for the same field or fluctuation dominated initial conditions as discussed before for the bosons. The interesting case is again the evolution starting from field dominated initial conditions. The corresponding vector spectral function (upper left plot) shows that the peak position moves toward smaller frequencies, just as in the bosonic case. It indicates that the energy of both meson and quark quasiparticles decreases during the time evolution. However, it is important to note that — in contrast to the mesons — the amplitude of the fermion statistical function is increasing during the time evolution. As discussed before, the nonzero initial field leads to strong fluctuations and hence occupancies in the bosonic sector. It takes time for these fluctuations to be transferred to the fermionic sector, which is why we observe that the fermion occupation grows slowly during the time evolution.

For the fluctuation dominated initial conditions we again observe that the spectral and statistical function approach their late-time behavior very quickly. We conclude that the available states and their occupation quickly approach their thermal final state if energy is provided in terms of particles rather than the field in the initial state.

Intermediate energy densities

From Figure 4.4 we can see that the most interesting dynamics is taking place for systems thermalizing in the crossover region. Thus, we aim to study the evolution of the vector-zero quark spectral function for two simulations thermalizing in the cross-over region.

Again we compare two simulations employing field or fluctuation dominated initial conditions, respectively, but in this case we are able to probe initial conditions that lead to the same late-time state. When comparing the late-time field expectation value $\overline{\sigma}$, the mass ratio m_σ/m_π, and the temperature T of the final state of these two simulations, we find that the respective quantities differ by less than 0.5 %. Also, the shape of the spectral and statistical functions in frequency space are the same for both bosonic as well as fermionic components. Quantitatively, we find that $|\rho_1 - \rho_2| / \max(\rho_1)$ is smaller than $\mathcal{O}(10^{-2})$ for all frequencies ω and momenta $|\mathbf{p}|$, where the indices 1 and 2 denote the two simulations compared and $\max(\rho)$ the maximal amplitude of the spectral function ρ. Larger deviations are observed for the vector-zero component statistical function and for the tensor component spectral and statistical functions, where the amplitudes are of order $\mathcal{O}(10^{-7})$ such that numerical inaccuracies come into play. In conclusion, we consider the late-time state of the two simulations to be the same thermal state, universal in the sense that the dependence on the initial conditions is lost. It is characterized solely by a temperature of $T = 1.04$, a mass ratio of $m_\sigma/m_\pi = 1.46$ and a field expectation value of $\overline{\sigma} = 0.33$. As we will see later, this corresponds to a state in the crossover region.

The regime of intermediate energy densities distinguishes itself from high and low energy density initial conditions by showing a double-peak structure in the quark spectral functions. Our findings in a nonperturbative real-time setting corroborate previous observations of such double peak structures with perturbative computations or spectral reconstructions reported e.g. in [122, 125–131].

First, let us consider the vector-zero component describing the excitation spectrum of the quarks. In Figure 4.9 we show the time evolution of both spectral and statistical functions. As before, for fluctuation dominated initial conditions (right column) the system quickly approaches the shape of the late-time two-point functions. However, in the case of field dominated initial conditions, the double-peak structure of the spectral function only emerges at later times. At early times, the spectral function reveals a single broad structure.

We further point out that the statistical function F_0 decays to zero during the time evolution, implying that the fermion occupation is not contained in the vector-zero component but in other components. This agrees well with the effective quasiparticle number that has been employed previously

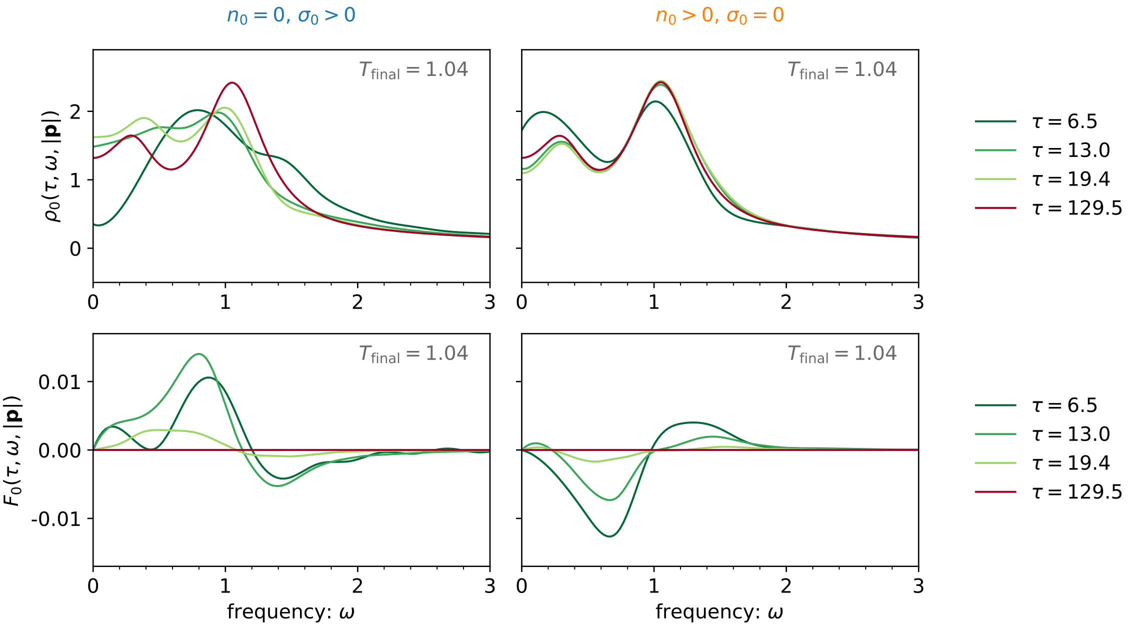

Figure 4.9: Time evolution of the vector-zero component quark spectral and statistical functions shown for two different initial conditions at momentum $|\mathbf{p}| = 0.012$. The left column shows field dominated initial conditions with $\sigma_0 = 0.98$, the right column fluctuation dominated initial conditions with $n_0 = 0.11$. Both lead to the same late-time state with $T = 1.04$.

[55, 97],

$$n_\psi(t, |\mathbf{p}|) = \frac{1}{2} - \frac{|\mathbf{p}| F_V(t, t, |\mathbf{p}|) + M_\psi(t) F_S(t, t, |\mathbf{p}|)}{\sqrt{|\mathbf{p}|^2 + M_\psi^2(t)}} \,, \tag{4.12}$$

with effective mass $M_\psi(t) = m_\psi + h\sigma(t)$. This definition of an effective particle number only provides a good description of the quark content in the system if the occupations in the vector-zero and tensor component are negligible. In our computations we find that F_0 and F_T are of the order $\mathcal{O}(10^{-7})$ and hence irrelevant for the quark particle number.

In order to study the particle content, we take into account the vector component which is shown in Figure 4.10. We can see that the double-peak structure observed in the vector-zero component is also visible in the vector component, in particular in both spectral and statistical functions. From this we learn that the additional light degrees of freedom, provided in the low-frequency peak of the quark spectral density, is actually occupied in terms of the vector component quark statistical function. Hence, for states thermalizing in the crossover temperature regime, there is an additional light mode with finite occupation in the quark sector available to participate in the dynamics.

We further observe that for fixed momentum $|\mathbf{p}|$ the energy of the light mode increases with rising temperature. At sufficiently high temperatures this additional mode reaches energies comparable with the main quasiparticle mode such that the two peaks merge into the single peak persistent in the high-temperature regime.

We conclude this section with a comment on the dynamics found for initial states with low energy-densities. In contrast to the cases of intermediate and high energy densities, we find well-defined

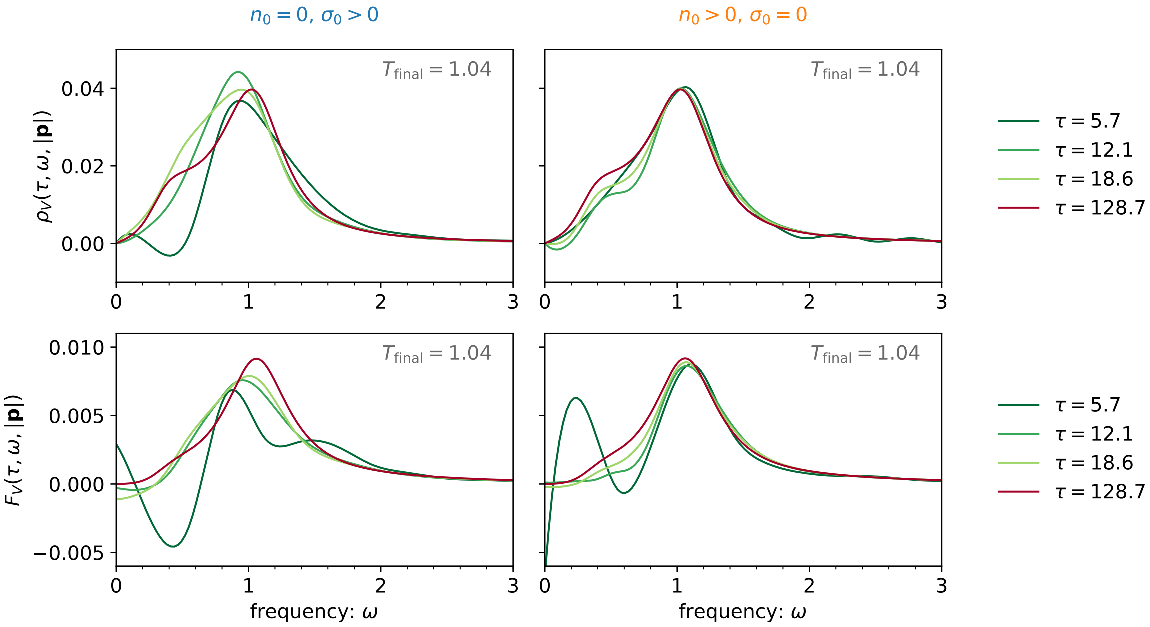

Figure 4.10: Time evolution of the vector component quark spectral and statistical functions shown for two different initial conditions at momentum $|\mathbf{p}| = 0.012$. The left column shows field dominated initial conditions with $\sigma_0 = 0.98$, the right column fluctuation dominated initial conditions with $n_0 = 0.11$. Both lead to the same late-time state with $T = 1.04$.

quasiparticle peaks for both quarks and mesons. The smaller energy density leads to lower thermalization temperatures and a stronger chiral symmetry breaking, reflected by a mass difference between the σ and π mesons. After discussing the nonequilibrium time evolution of the spectral functions, we now turn to the equilibrium properties.

4.3.3 Late-time thermal limit

In this section we discuss the spectral functions of quarks and mesons in the state of quantum thermal equilibrium according to the definition introduced in Section 4.3.1. The properties of spectral functions at different temperatures reflect the crossover transition of the quark-meson model from the chiral broken to the chiral symmetric phase. We find that the shapes of the final states are universal in the sense that they only depend on the temperature and not on the details of the initial state.

Mesons

Information about the different phases of the model can be obtained from the temperature-dependence of the late-time thermal spectral functions of the mesons. We find that the shape of the bosonic spectral functions is described by a Breit-Wigner function for all considered temperatures. Thereby, the width and the position of the Breit-Wigner peak only depend on the temperature but not on the initial conditions chosen.

As discussed in Section 4.3.2, the momentum-dependent width and the dispersion relation are obtained by applying Breit-Wigner fits to the spectral functions. Although the Breit-Wigner function (4.11) has two parameters, the width $\Gamma(\tau, |\mathbf{p}|)$ and the peak position given by $\omega(\tau, |\mathbf{p}|)$, there is only

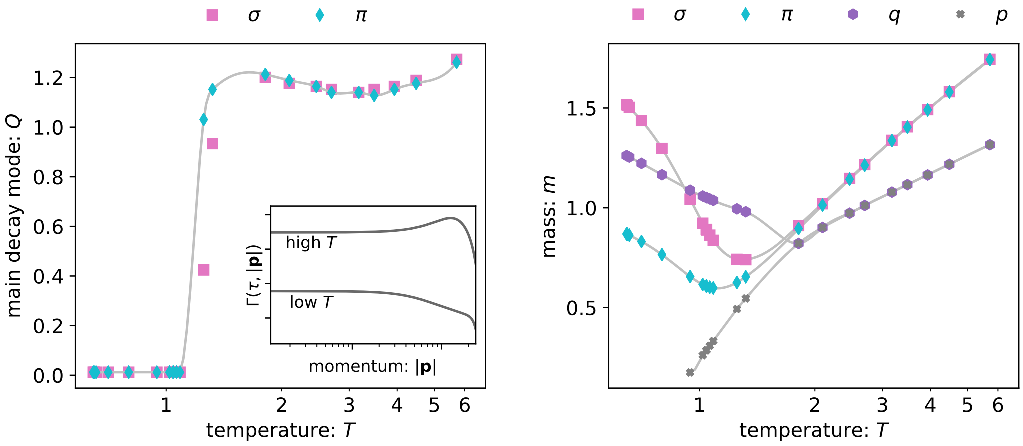

Figure 4.11: *Left:* Temperature-dependence of the characteristic decay momentum Q shown for the σ and π mesons. The inset shows examples for the momentum-dependent width at high and low temperatures. Q corresponds to the momentum at which the width $\Gamma(\tau, |\mathbf{p}|)$ is maximal. *Right:* Temperature-dependence of quasiparticle masses. Restoration of chiral symmetry is reflected in identical masses of the σ and π mesons at high temperatures. The quark q quasiparticle mass is obtained from the dominant peak of the vector-zero component quark spectral function. We also plot the “plasmino” branch p obtained from the quark spectral function. In both plots gray lines show cubic spline interpolations of the data points.

one free parameter since the normalization condition given by the sum rule (4.7) must be satisfied.

In the right plot of Figure 4.6 we already saw that there is a characteristic momentum mode $|\mathbf{p}|$ at which the momentum-dependent width becomes maximal. This corresponds to the momentum at which the decay is strongest and can be considered as the *main decay mode*, in the following denoted by Q. In the left plot of Figure 4.11 we show the main decay mode Q as a function of temperature for both meson species. At low temperatures, the strongest decays are found in the IR, whereas at high temperatures the strongest decays occur in the UV. There is an abrupt change at some critical temperature, above which $Q > 0$ meaning that the momentum-dependent width has a maximum at a nonzero momentum, as shown by the upper line in the inset. Comparing the momentum-dependent width at low T and high T, we can see that the transition from the chiral broken to the chiral symmetric phase is characterized by new decay modes in the UV. Thereby, the main decay mode is suddenly shifted from the IR to the UV.

Another prominent signature for the crossover transition is provided by the quasiparticle masses of the σ and π mesons. The two meson species are distinguishable in the chiral broken phase, where they have different masses, while they become identical in the chiral symmetric phase. When plotting the meson masses as a function of temperature, as shown in the right plot of Figure 4.11, we can nicely visualize the restoration of chiral symmetry, manifest in the quasiparticle masses of σ and π becoming identical (pink and cyan data points). We observe a softening of the masses at intermediate temperatures, i.e. the quasiparticle masses are minimal in the temperature region where the crossover phase transition occurs. Decreasing masses indicate growing correlation lengths. In the limit of a second order phase transition, which is characterized by diverging correlation lengths, the masses would vanish at the transition point. In the high-temperature range, masses grow with rising temperatures. This reflects that the quasiparticle masses can be considered as *thermal masses* in the sense that they contain self-energy contributions and are generated by quantum fluctuations, which increase with temperature.

We further note that one could also study the temperature dependence of the width $\Gamma = \Gamma(\tau, |\mathbf{p}| \rightarrow$

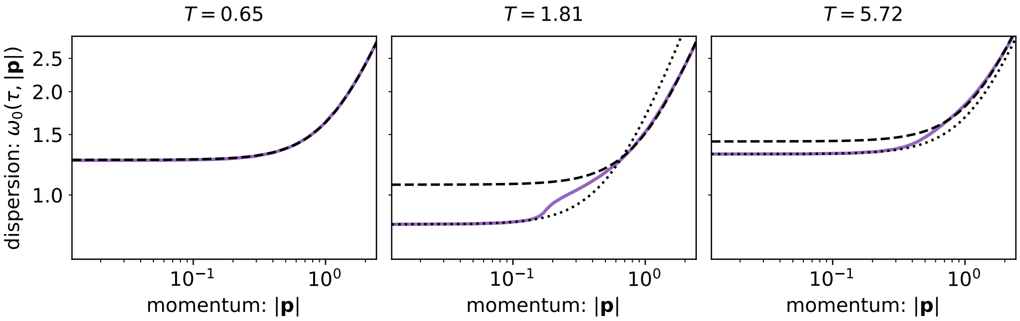

Figure 4.12: The dispersion relation of the vector-zero quark spectral function shown for three different temperatures. At low temperature a fit to the relativistic dispersion relation $Z\sqrt{|\mathbf{p}|^2 + m_q^2}$ is shown by the black dashed line. For higher temperatures the behavior at small and large momenta differs as the additional low-frequency peak and the main peak merge into one peak. We perform separate fits at low and high momenta, shown by the dashed and dotted black lines.

0) instead of $m = \omega(\tau, |\mathbf{p}| \to 0)$. However, the information is equivalent due to the normalization of the spectral functions, as pointed out above. Consequently, the behavior of Γ is converse to the behavior of m and not presented here explicitly. The with Γ is small at low temperatures, strongly grows toward intermediate temperatures where it reaches a maximum value in the crossover temperature regime, and then decays slowly when going to higher temperatures.

Quarks

We now consider the thermal spectral functions for the quark sector. Several aspects of the different components invite discussion. Let us begin with a recap of the findings shown in the vector-zero component of the quark spectral function. As presented in Figure 4.4 the spectral density has different shapes at low, intermediate and high temperatures. In particular, the intermediate temperature range of the crossover transition is characterized by a double-peak structure, with an additional light mode that we refer to as the *plasmino* mode. The temperature-dependence of the fermionic quasiparticle masses is depicted in Figure 4.11. The mass of the low-frequency plasmino mode (denoted by p) grows continuously with rising T until it merges with the main peak (denoted by q), forming the wide quasiparticle peak found for initial states with large energy densities. For related studies with perturbative computations or spectral reconstructions see e.g. [122, 125–131]. Although the double-peak structure is only visible in the low-momentum regime, it can be studied by considering the dispersion relation obtained from the vector-zero quark spectral function.

For temperatures below some critical temperature in the crossover regime, the vector-zero spectral function reveals the shape of a nonrelativistic Breit-Wigner function, also known as the Lorentz function,

$$\rho_{\mathrm{L}}(\tau, \omega, |\mathbf{p}|) = \frac{A\,\Gamma(\tau, |\mathbf{p}|)}{\left[\omega - \omega(\tau, |\mathbf{p}|)\right]^2 + \Gamma^2(\tau, |\mathbf{p}|)}\,, \tag{4.13}$$

where A is a normalization constant, $\Gamma(\tau, |\mathbf{p}|)$ the width and $\omega(\tau, |\mathbf{p}|)$ the dispersion. An example showing the data and the corresponding fit to a Lorentz function is provided in Appendix 4.A.4. When temperature is increased, the vector-zero quark spectral function ceases to be described in terms of (4.13) as the low-frequency mode arises and grows in amplitude. Due to appearance of the additional

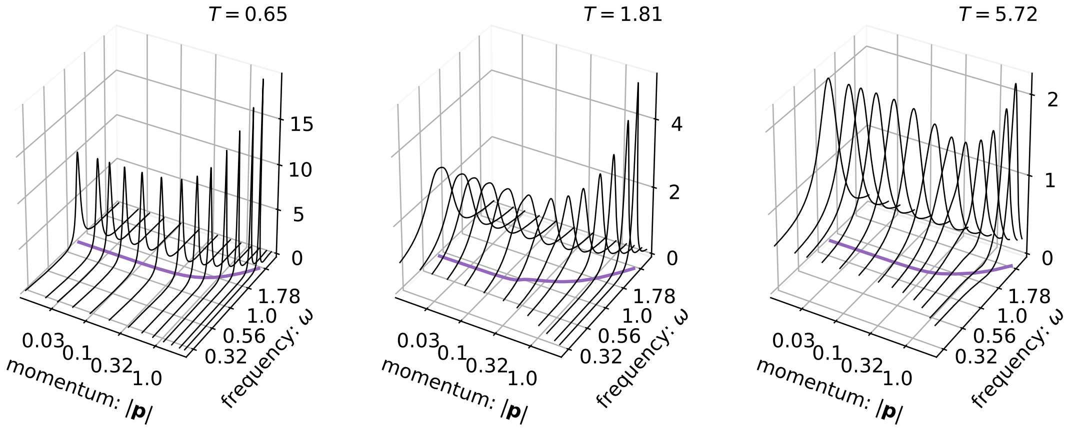

Figure 4.13: The vector-zero quark spectral function as a function of frequency ω shown for a range of spatial momenta $|\mathbf{p}|$. The three plots correspond to the same three temperatures as in Figure 4.12. The purple line indicates peak position of the spectral function in the $|\mathbf{p}|$-ω-plane and is therefore equivalent to the dispersion relation shown in Figure 4.12. The spectral function reveals a narrow quasiparticle peak at low temperatures. As the temperature is increased the light mode interferes with the low-momentum spectral function, leading to a broad peak at small momenta. At high momenta, the quasiparticle-peak remains narrow.

peak, it is not possible to perform a Lorentz fit at all temperatures. As a consequence, we choose to compute the dispersion relation of the quarks by determining the peak position of the main peak of ρ_0. The thus obtained dispersion relations are shown for three temperatures in Figure 4.12.

At low temperatures, where no additional peak is present, the quark dispersion is well-described by a relativistic dispersion relation, see left plot of Figure 4.12. When going to intermediate temperatures, the additional light mode leads to a double-peak structure. As long as the two peaks are distinguishable, one can determine the dispersion relation of the main peak, which yields the same shape as in the low-temperature regime. However, when the main peak and the side peak merge into a single peak, the dispersion relation obtained from the overlap of the two peaks has a dispersion relation of the form shown by the middle plot of Figure 4.12. There is a clearly visible dip in the dispersion, showing that for small momenta the peak position is determined by the light plasmino mode, while for large momenta the peak position is determined by the main quark mode. We can fit the low-momentum and high-momentum areas separately to a relativistic dispersion relation, as shown by the dashed and dotted lines in Figure 4.12. When considering higher temperatures, the position of the dip moves toward larger frequencies and is not visible by eye anymore. However, we find that the dispersion relation cannot be described by the relativistic dispersion relation $Z\sqrt{|\mathbf{p}|^2 + m^2}$ over the whole momentum range but still distinguishes between high-momentum and low-momentum regimes. We conclude that the single peak of ρ_0 at large temperatures is still the result of an overlap of a small low-frequency peak with the main peak. More insight is gained by considering the momentum-dependence of the corresponding spectral functions, which is shown in Figure 4.13. The spectral function $\rho_0(\tau, \omega, |\mathbf{p}|)$ is shown at some late time τ where the system has approached thermal equilibrium. The peak position of the spectral functions corresponds to the dispersion relations shown in Figure 4.12. At low temperatures, we find a single narrow quasiparticle peak. For higher temperatures, however, an additional light mode interferes with the main peak. At intermediate temperatures, where a softening of the mass occurs, the light

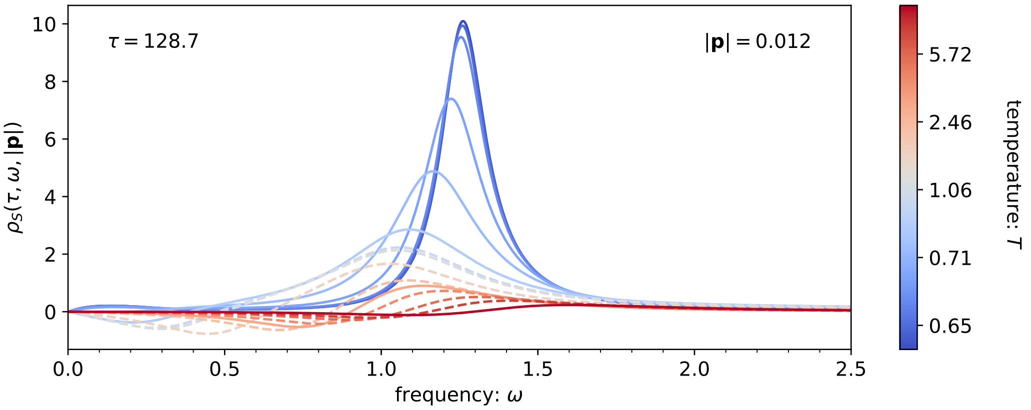

Figure 4.14: The thermalized scalar component of the quark spectral function as a function of frequency shown for different temperatures.

mode and the main peak have comparable frequencies in the infrared. The superposition of the main peak and the light mode leads to a broad peak at small momenta, whereas the peak remains narrow at high momenta. As temperature increases, the light mode is only visible at higher momenta. An example is shown by the right plot in Figure 4.13, where one can see a small enhancement of the spectral function at low frequencies for intermediate momenta. This observation indicates that the quark spectral function harbors additional degrees of freedom at high temperatures, as compared to the low-temperature regime.

From the dispersion relation of the vector-zero quark spectral function, we determine the constituent quark mass by taking the asymptotic value at vanishing momentum, i.e. $m_q = \omega_0(\tau, |\mathbf{p}| \to 0)$. The constituent quark mass behaves analogously to the bosonic masses, meaning that a softening of the mass in the crossover temperature range occurs, see violet data points in the right plot of Figure 4.11. At low temperatures, the constituent quark mass lies between the σ and π masses, which is in qualitative agreement with the particle masses known at $T = 0$. For temperatures below $T \simeq 2$ we find that the pion is the lightest particle in the theory. This supports chiral perturbation theory as an effective theory for QCD where only pion degrees of freedom are considered. On the contrary, at high temperatures the constituent quark mass is smaller than the meson mass. As light modes are easier to excite, they dominate the dynamics in a system. Hence, our observation matches our idea that the chiral symmetric phase is dominated by quark degrees of freedom whereas the chiral broken phase is described by hadronic degrees of freedom, in particular by pions.

Finally, we shortly discuss the scalar component of the quark spectral function. In a chiral symmetric theory with vanishing fermion bare mass, the scalar component of the quark spectral function vanishes, i.e. $\rho_S = 0$. Although chiral symmetry is broken explicitly here, we expect the system to restore chiral symmetry at high temperatures, implying that it approaches the limit where the scalar component of the quark spectral function vanishes. In Figure 4.14 we present the numerically computed scalar component quark spectral function for a range of temperatures, with temperature encoded in the color scheme. The clear quasiparticle peak existing at low temperatures (blue lines) widens and flattens with rising temperature (red lines). The amplitude of the scalar component finally decays to zero, visualizing the predicted restoration of chiral symmetry in the course of the crossover transition. We further note that the peak position of the scalar component spectral function qualitatively shows the same behavior as the vector-zero component. The peak moves toward small frequencies at intermediate temperatures, corresponding to the mass softening, and is shifted toward higher frequencies at low and high temperatures.

4.4 The macroscopic field

In this section, we study the time evolution of the expectation value of the macroscopic field $\langle\sigma(t)\rangle$ for the two kinds of different initial conditions deployed also in the previous section. In addition, we study the model for different fermion bare masses in order to analyze the effects of spontaneous symmetry breaking in the model.

4.4.1 Nonequilibrium time evolution of the field

The classical potential of the sigma field is given by

$$V(\sigma) = \frac{1}{2}m^2\sigma^2 + \frac{\lambda}{4!\,N}\sigma^4\,, \tag{4.14}$$

where the parameter choice of $m^2 < 0$ allows for spontaneous symmetry breaking. Thus, the potential has the shape of a double-well with minima located at $\sigma = \pm\sqrt{-3!\,N\,m^2/\lambda}$. For the parameters employed in this work the minimum is located at $\sigma \approx 0.04$. The time evolution of a classical field in this potential is described by the classical equation of motion

$$\left[\partial_t^2 + m^2 + \frac{\lambda}{6N}\sigma^2(t)\right]\sigma(t) = 0\,, \tag{4.15}$$

where spatial homogeneity and isotropy is assumed. If the initial field value, or the initial field derivative, is nonzero, the field rolls down a potential hill and oscillates until it equilibrates at the minimum of the potential. Here, we go beyond the classical theory and compute the nonequilibrium time evolution including additional quantum fluctuations. As discussed above, we employ an approximation that includes quantum corrections at NLO in $1/N$ and g. The quantum corrections lead to an effective potential and additional terms in the field equation (4.15). The full evolution equations at the given approximation can be found in Sections 2.4.3 and 2.4.4.

Depending on the initial conditions the time evolution of the field shows different properties. Let us first consider field dominated initial conditions, where the initial field is set to a finite value σ_0. The time evolution for the expectation value of the field $\langle\sigma(t)\rangle$ is shown for different σ_0 in the left plot of Figure 4.15. One can see that the field oscillates and eventually reaches a stationary value. In contrast to the classical theory, where the field always reaches the same equilibrium value given by the position of the potential minimum, the field reaches different late-time values. The reason is that the field itself generates quantum fluctuations as it rolls down a potential hill. These dynamically emerging fluctuations again influence the effective potential in which the nonequilibrium time evolution takes place. As the initial field value affects the amount of quantum fluctuations in the system and hence the shape of effective potential, different values of σ_0 lead to different late-time values for $\langle\sigma(t)\rangle$. Before we come to a more detailed discussion of the plots in Figure 4.15, we provide some intuition for the influence of fluctuations on the effective potential.

Quantum fluctuations can be represented as loop corrections of the effective action. The effective potential is obtained when evaluating this effective action at a constant field. For a nonvanishing

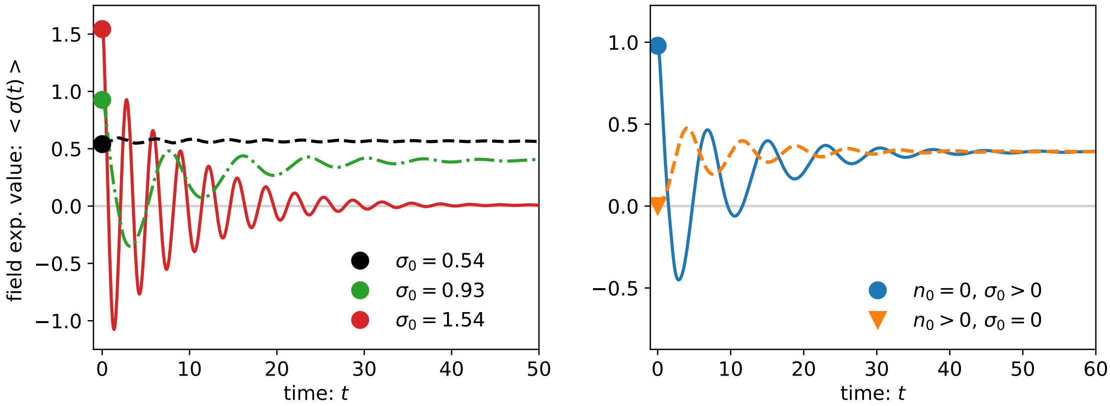

Figure 4.15: *Left:* The time evolution of the field shown for field dominated initial conditions with different initial field values as indicated in the legend. *Right:* The time evolution of the field shown for field dominated initial conditions with $\sigma_0 = 1.98$ (blue) and fluctuation dominated initial conditions with $n_0 = 0.11$ (orange). The same late-time field value $\bar{\sigma} = 0.33$ is approached for both initial states. The grey line in both plots serves as a guide to the eye for $\langle\sigma(t)\rangle = 0$.

fermion bare mass, i.e. $m_\psi \neq 0$, the chiral symmetry breaking tilts the effective potential toward negative values. Thereby, larger m_ψ cause stronger tilts. On the other hand, bosonic fluctuations provide positive contributions, pushing the potential toward a symmetric shape. Together, this leads to a tilted Mexican hat potential with a minimum at some finite field expectation value. The position of the minimum of the effective action can easily be much larger than the position of the minimum of the classical potential.

The influence of these quantum corrections to the effective potential can be visualized by looking at the energy density of the system, which we compute from the energy-momentum tensor. We distinguish classical, bosonic and fermionic contributions to the energy density, with the relevant expressions presented in Section 2.4.4. Quantum fluctuations are taken into account for the fermionic and bosonic parts of the energy density. Hence, the energy density reflects the amount of fluctuations in the system.

In order to study the influence of the initial field, we consider the energy density computed at initial time $\varepsilon_{\text{init}}$. In Figure 4.16 we show the contributions from the field, the bosons and the fermions separately. The blue and pink lines show, how the field and the bosonic energy densities exhibit a positive curvature. In contrast, the fermionic contribution shown in violet leads to a tilt toward negative curvature, which is a consequence of the explicit chiral symmetry breaking. Summing the three parts together, one obtains the total energy density that has a minimum at a nonzero field value, as represented by the gray curve.

It is important to note that the energy density $\varepsilon_{\text{init}}$ computed at time $t = 0$ does not include the quantum fluctuations that are generated dynamically by the field. As the field generates further fluctuations, the effective potential is pushed toward a more symmetric form with its minimum moving toward smaller field expectation values. In order to see this, we also look at the energy density computed at late-times, where the system is thermalized. The result is shown by the black line in Figure 4.16. It can be seen that the energy density indeed becomes steeper and has a minimum at smaller field values. Thus, the energy density provides a useful quantity in order to study the impact of quantum fluctuations on the effective potential, although we emphasize that the energy density and

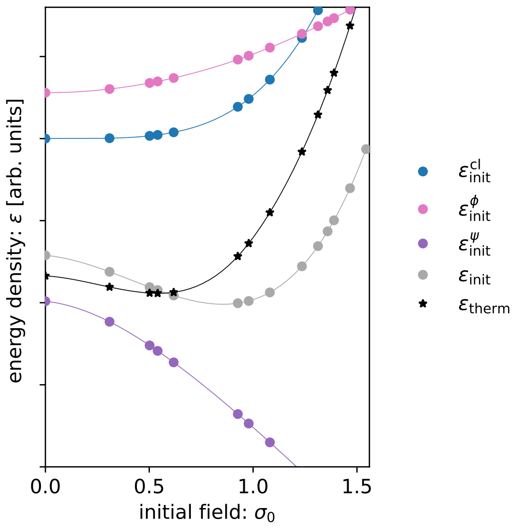

Figure 4.16: The energy density at initial time $\varepsilon_{\mathrm{init}} = \varepsilon(t = 0)$ and at late times $\varepsilon_{\mathrm{th}} = \overline{\varepsilon}$ as a function of the initial field value. We present the classical, bosonic and fermionic contributions to the initial energy density separately. Together, they form a bounded shape with minimum at a nonzero initial field value (gray curve). At late times, the energy density reaches the constant shape shown by $\varepsilon_{\mathrm{therm}}$ in black. The minimum of the energy density at late times corresponds to the maximal field values found.

the effective potential are two different quantities.

Having this qualitative picture of the effective quantum potential in mind, we can understand the behavior of the three curves shown in the left plot of Figure 4.15. If the initial field sits close to the minimum of the effective potential, it barely oscillates and hence almost no additional fluctuations are created dynamically. Accordingly, the shape of the potential does not change with the time evolution such that the position of the minimum stays the same. This is shown by the black line. In contrast, the field can be placed on a point away from the potential minimum. As it starts moving toward the potential minimum, the field dynamically generates fluctuations. These fluctuations change the shape of the potential, thereby altering the position of the minimum. The further away the field is from the potential minimum in the beginning, the more fluctuations are generated and the stronger the potential deforms. As we increase the distance of the initial field from the potential minimum at time $t = 0$, the minimum of the potential at late times moves toward zero. Examples of this behavior are depicted by the green and red curve in the left plot Figure 4.15.

As discussed in the previous section, energy cannot only be provided in terms of a nonzero initial field value (and the fluctuations this field generates), but also in terms of occupancies. Hence, the same late-time field value can be approached for different initial conditions. In the right plot of Figure 4.15 the time evolution of $\langle\sigma(t)\rangle$ is shown for the two simulations discussed in Section 4.3.2. The blue line displays the time evolution of the field starting from field dominated initial conditions, while the orange line shows the time evolution starting from fluctuation dominated initial conditions. For both initial conditions the quantum potential has the same minimum, characterized by a late-time stationary field value of $\overline{\sigma} = 0.33$.

Although we commonly say that initial conditions with the same energy density lead to the same thermal state, there is a caveat. Two initial states thermalizing at the same late-time state usually

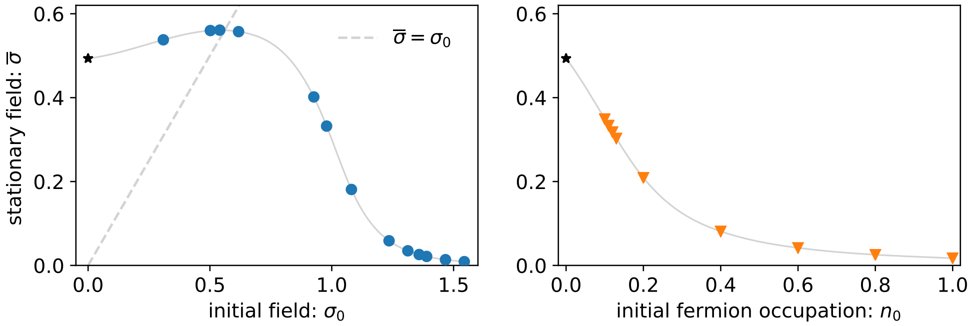

Figure 4.17: The value of the thermalized one-point function for different initial conditions. On the right, the thermal field value $\overline{\sigma}$ is shown for initial conditions with different field values σ_0. The gray dashed line indicates $\overline{\sigma} = \sigma_0$. On the left, the thermal field value is shown for different initial fermion occupation numbers n_0. In both plots, the black star indicates the value obtained for initial conditions with $n_0 = 0$ and $\sigma_0 = 0$. In both plots gray lines show cubic spline interpolations of the data points.

do not have the same energy density at time $t = 0$ because the energy density computed at initial time does not include dynamically generated fluctuations. What one means is that different initial conditions provide the same amount of fluctuations to the system. The way they are provided depends on the initial state and partly they are generated dynamically. However, for the quantum thermal equilibrium state that is approached at late times only the amount of fluctuations introduced to the system is relevant.

4.4.2 Thermal equilibrium

Field expectation value

After discussing the time evolution of the field expectation value we now turn to its late-time properties. We denote the stationary value of the field at late times by $\overline{\sigma}$. As discussed in 4.3.1, at these times the fluctuation-dissipation theorem is satisfied and the system state is considered to be thermal. Thus, we consider $\overline{\sigma}$ to be the thermal field expectation value.

Numerically, the late-time field values $\overline{\sigma}$ are determined by the average of field values over a time range $[t^*, t^* + \Delta t]$ with t^* being a time at which the field is sufficiently stationary. For the results shown in this work we use $t^* = 130$ and $\Delta t = 130$, such that the standard deviation of the mean is $\mathcal{O}(10^{-4})$ to $\mathcal{O}(10^{-11})$ depending on the initial conditions used.

First, let us look at the time evolution of the macroscopic field for different initial field values σ_0. Naively, one might expect that larger field values automatically imply increasing energy densities in the initial state, hence a higher thermalization temperature and smaller field value. However, as the discussion above already pointed out, this is not the case. In the left plot of Figure 4.17 we show how the late-time field value $\overline{\sigma}$ depends on the initial field σ_0. With increasing σ_0, the thermal field $\overline{\sigma}$ first grows and then decays to zero. The maximal value for $\overline{\sigma}$ is expected, when the least amount of fluctuations is generated dynamically, as these fluctuations would push the minimum of the potential and thus $\overline{\sigma}$ toward zero. We indeed find the largest late-time field values for $\sigma_0 \approx \overline{\sigma}$, which in indicated by the gray dashed line in the left plot of Figure 4.17.

Secondly, we consider fluctuation dominated initial conditions where the field value is set to $\sigma_0 = 0$ while the initial fermion occupation is taken to be constant, i.e. $n_\psi(t = 0, |\mathbf{p}|) = n_0$, and varied between

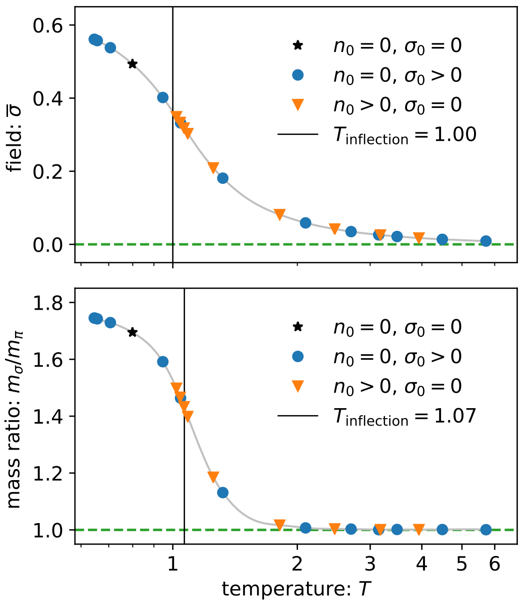

Figure 4.18: Order parameters of the quark-meson model as a function of temperature. In the upper plot, the order parameter is given by the macroscopic field $\overline{\sigma}$ which is the thermalized value of the one-point function. In the lower plot, the order parameter is given by the ratio of the σ-meson and pion masses. The masses are derived from the two-point functions of the corresponding bosonic fields. The gray lines show cubic spline fits to the data points. The inflection points are indicated by the black vertical lines. Since dimensionful quantities are given in units of the pseudocritical temperature T_{pc} defined as the inflection point of the order parameter $\overline{\sigma}$, $T_{\text{inflection}} = 1$ in the upper plot.

zero and one. In the right plot of Figure 4.17 we can see that increasing the fermion occupation number n_0 goes along with smaller thermal field values $\overline{\sigma}$. Thus, for larger n_0 higher temperatures are reached, emphasizing again that larger fermion occupation numbers lead to a rise of the fluctuations that make the effective potential more symmetric.

Crossover phase transition

Our results regarding the thermal state of the system can be summarized in an analysis of the crossover transition between the chiral broken and the chiral symmetric phase of the quark-meson model. When a system becomes thermal, the thermodynamic concept of a phase diagram can be applied. The conjectured phase diagram of the quark-meson model contains important features of the QCD phase diagram. It exhibits a chiral symmetric phase with vanishing field expectation value at high temperature T, as well as a chiral broken phase with nonzero field corresponds at low T.

In order to study the phase transition and the transition temperature, we employ two different order parameters, one deduced from the one-point function and one from the two-point functions. The first one is the field expectation value of the thermalized field $\overline{\sigma}$. It is nonzero in the chirally broken phase and zero in the chirally symmetric phase. Often this field value is identified as the pion decay constant f_π. The second one is the mass ratio m_σ/m_π, where m_σ and m_π are the masses of the σ-meson and the pion, respectively. The masses are determined from the bosonic spectral functions as discussed in Section 4.3.3. In the chiral limit, the mass ratio is expected to go to unity.

Starting from the different initial states analyzed, we find that the system thermalizes at different temperatures. Thereby, the dependence of an order parameter on the temperature provides insight into the nature of the phase transition. In Figure 4.18 we show our numerical results for the temperature-dependence of the two order parameters, $\overline{\sigma}$ in the upper and m_σ/m_π in the lower plot. Every point in the diagram corresponds to a simulation with a different initial state. As indicated in the legend, we consider initial states of various fermion occupations, described by n_0, and initial field values, described by σ_0. It is reassuring to see that the order parameters obtained from field or fluctuation dominated initial conditions align themselves on a single curve, which is characteristic for a smooth crossover transition. This is yet another way of seeing that the thermal states are independent of the details of the initial conditions.

As chiral symmetry is restored with rising temperature, the field value decays to zero while the mass ratio goes down to one. The field expectation value $\overline{\sigma}$ is often considered as a first approximation for the pion decay constant f_π. As can be seen, in the limit $T \to 0$ some value $\overline{\sigma} \simeq \mathcal{O}(1)$ is approached. At the lowest temperature considered we find $\overline{\sigma}/m_\pi \simeq 0.65$, matching the phenomenological value $f_\pi/m_\pi \simeq 0.69$ [123]. Further, we can see from the lower plot in Figure 4.18 that the mass ratio is only $m_\sigma/m_\pi \simeq 1.8$ at the lowest temperatures available, which is smaller than the expectation from the known values of the masses. However, the mass ratio is expected to further increase with decreasing temperature.

We perform a cubic spline fit to the data points and identify the inflection point of the field $\overline{\sigma}$ as the pseudocritical temperature of the crossover T_{pc}. We indicate the inflection point of both the field and the mass ratio in the plots of Figure 4.18. It can be seen that the temperatures deduced from the two different order parameters are comparable with each other. We find that the pseudocritical temperature is of the order of the pion mass. This is in agreement with the expectation of the QCD phase transition being at around 150 MeV for vanishing baryon density.

4.4.3 Spontaneous symmetry breaking

We have seen that the explicit chiral symmetry breaking in the system leads to nonzero field expectation values. Here, we analyze the limit of vanishing explicit symmetry breaking, i.e. $m_\psi \to 0$, with spontaneous symmetry breaking still present.

If the fermion bare mass vanishes, i.e. $m_\psi = 0$, the action of the quark-meson model (2.101) is invariant under chiral $SU_L(2) \times SU_R(2) \sim O(4)$ transformations and therefore symmetric under chiral symmetry. Still, a nonzero field expectation value can break this symmetry spontaneously. For nonzero fermion bare masses, chiral symmetry is explicitly broken and the minimum of the potential is located at some nonzero field value. If the field expectation value stays nonzero for $m_\psi \to 0$, we expect to observe spontaneous symmetry breaking.

We compare simulations with different fermion bare masses m_ψ while all other parameters of the theory are kept fixed. The system is studied for initial conditions with $\sigma_0 = 0.62$ and vanishing fermion and boson occupations, i.e. $n_0 = 0$. In the left plot of Figure 4.19, we show the time evolution of the field expectation value $\langle\sigma(t)\rangle$, for three examples with different fermion bare masses. As before, the field oscillates before it equilibrates to the thermal late-time value $\overline{\sigma}$.

Since the fermion bare mass m_ψ governs the strength of the chiral symmetry breaking and thus the deformation of the potential, increasing fermion bare masses yield larger values for $\overline{\sigma}$. At the same time m_ψ determines the fermion backreaction on the field, i.e. how strong the field is pushed away from its current value. The field only reaches a stationary value, if the backreaction from the fermions

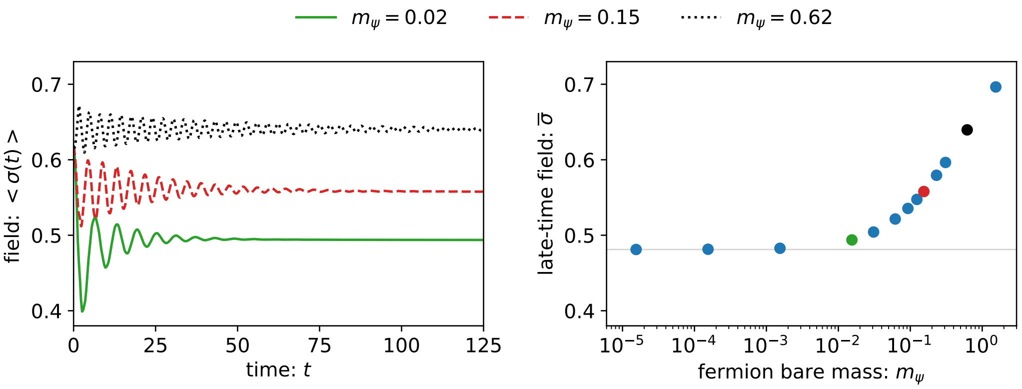

Figure 4.19: Left: The time evolution of the field with initial value $\sigma_0 = 0.62$ shown for three different bare fermion masses m_ψ. The field reaches the stationary value $\overline{\sigma}$ at late times. Right: The asymptotic field value $\overline{\sigma}$ shown for different bare fermion masses m_ψ. The green, red and black data points correspond to the simulations shown in the left plot. The field value decreases with the fermion bare mass and approaches an asymptotic value for $m_\psi \to 0$.

on the field and the bosonic interactions with the field balance out.

Here, fermion bare masses with values from $\mathcal{O}(10^{-4})$ ranging to $\mathcal{O}(1)$ are considered. We find that the field approaches the asymptotic value $\overline{\sigma} = 0.48$ for $m_\psi \to 0$, which is shown in the right plot of Figure 4.19. This analysis shows that our numerical simulations of the quark-meson model reproduce the expected spontaneous symmetry breaking in the limit of vanishing fermion bare mass.

4.5 Conclusion

Motivated by current experimental studies of the QCD phase diagram in heavy-ion collisions, we investigated the dynamical approach of the quark-meson model to thermal equilibrium using a range of different initial conditions dominated by either the sigma field or fermionic fluctuations. The time evolution of one- and two-point functions was computed numerically using closed equations of motion derived from the 2PI effective action at NLO in $1/N$ and the Yukawa coupling g.

We show that our simulations correctly capture the approach of a thermal state, which depends only on the energy density of the initial condition. The crossover phase transition from the chiral broken phase at low temperatures to the chiral symmetric phase at high temperatures is reproduced by the late-time equilibrium states. Thermalization in the chiral broken phase is characterized by a finite field expectation value, a mass difference between the sigma meson and the pions as well as narrow quasiparticle peaks in the spectrum. The restoration of chiral symmetry in the high-temperature regime expresses itself in the field expectation value decreasing to zero, the mass ratio of σ and π mesons going to unity, and the scalar component of the quark spectral functions decaying to zero.

Our investigation focused in detail on the dynamical thermalization revealing differences in the time evolution depending on the initial state employed. We not only studied the time evolution of the field expectation value but also probed the dynamical properties of the two-point functions, expressed in terms of the spectral and statistical functions, which carry information about the available quasiparticle states and their occupation in the system, respectively. For initial states with vanishing initial field but energy supplied by fermion occupation, the spectral and statistical functions of both quarks and mesons approach their late-time thermal shapes already at early times. In contrast, if the energy density is predominantly provided by the nonzero initial field value, the redistribution of energy from the field first to the bosonic sector and subsequently to the fermionic sector leads to high occupancies of the mesons at intermediate stages. This is also reflected by the different behavior found in the time evolution of the quasiparticle masses depending on the initial conditions.

The deployed nonequilibrium setup of the quark-meson model captures important features of the low-energy behavior of QCD. By studying the temperature dependence of the quasiparticle masses, we find that the lightest degrees of freedom are given by the pions at temperatures below and by quarks above the phase transition. This implies that quarks are the relevant degrees of freedom at high temperatures while pions dominate below the critical temperature. Furthermore, we learn from the width that at high temperatures the more energetic high-momentum decay modes are more pronounced than at low temperatures.

The nonvanishing expectation value of the sigma field describes the order parameter of the chiral phase transition. Its dynamics depends on the initial state. If the initial field value is close to the minimum of the effective potential, the field remains almost constant. Otherwise, the field rolls down a potential hill and starts oscillating, thereby dynamically generating fluctuations.

Having shown that the dynamics of the thermalization process reveals interesting features before approaching the final thermal state, we lay the foundation for future investigations of the quark-meson model with nonzero baryon chemical potential. In particular, the possibility of dynamically probing the thermalization of systems surpassing the critical point of the chiral phase transition is of outermost interest.

Chapter 5

Spin-1 Bose-Einstein condensates

In this chapter we present theoretical basics for a spin-1 Bose-Einstein condensate (BEC) in the second quantization formalism, where quantum many-body states are described with the help of field operators. This chapter is based on [132], a review on spinor BECs. We first introduce the model, then discuss the mean-field and subsequently the Bogoliubov approximation, where we mainly follow [132, 133]. Readers who are familiar with spin-1 BECs can move on to Chapter 6.

While a scalar BEC consists of a Bose-condensed cloud of atoms in a single internal state, here we consider a spinor BEC with spin 1 and magnetic sublevels $m = 0, \pm 1$ describing the hyperfine spin states. Compared to a scalar BEC, the additional interactions due to the spin degrees of freedom give rise to rich and interesting quantum phenomena that are absent in scalar BECs. In particular, spinor BECs reveal several phases, where the phase realized depends on the nature of the interactions. Today, there are many experimental platforms where optical and magnetic fields are used to probe and manipulate spinor BECs.

This chapter is organized as follows. In Section 5.1 we present the Hamiltonian of a spin-1 BEC. Section 5.2 deals with the corresponding mean-field theory, from which one can deduce the Gross-Pitaevskii equations and the mean-field phase diagram. In Section 5.3 we discuss the excitation spectrum of the condensate that is obtained from the Bogoliubov approximation.

5.1 The second-quantized Hamiltonian

In this section, we introduce the Hamiltonian of the spin-1 BEC subject to our work. We describe this many-body system in terms of quantum field operators, a formalism known as *canonical* or *second quantization*, where the former term is usually used in the context of quantum field theory and the latter in condensed matter theory. The Hamiltonian presented here is often referred to as the second-quantized Hamiltonian.

We consider a system of N identical spin-f bosons with mass M that interact with each other via s-wave scattering subject to periodic boundary conditions. The field operator of a boson at spatial location $\mathbf{x}$ and time t is denoted by $\hat{\psi}_m(x)$ with $m = -f, -f+1, ..., f$ being the magnetic quantum number. In this thesis, we restrict ourselves to the spin-1 case with $f = 1$ and $m = 0, \pm 1$ in three spatial dimensions, where we use $x = (t, x^1, x^2, x^3)$. The field operators satisfy the equal-time commutation relations

$$[\hat{\psi}_m(t,\mathbf{x}), \hat{\psi}_n(t,\mathbf{y})] = [\hat{\psi}^\dagger_m(t,\mathbf{x}), \hat{\psi}^\dagger_n(t,\mathbf{y})] = 0\,, \tag{5.1a}$$

$$[\hat{\psi}_m(t,\mathbf{x}), \hat{\psi}^\dagger_n(t,\mathbf{y})] = \delta_{mn}\,\delta(\mathbf{x}-\mathbf{y})\,, \tag{5.1b}$$

of a nonrelativistic scalar field theory. We assume that an external magnetic field is applied in the z-direction. The low-energy effective Hamiltonian for this setup can be written as

$$\hat{H} = \hat{H}_{\text{kin}} + \hat{H}_{\text{qZ}} + \hat{H}_{\text{int}}\,, \tag{5.2}$$

where the first term describes the kinetic energy, the second term the quadratic Zeeman shift and the third term the interactions. We do not consider any trapping potential, i.e. the bosonic gas is assumed to be in a uniform system and not subject to any external potential. The nonrelativistic kinetic energy Hamiltonian is given by

$$\hat{H}_{\text{kin}} = \int_{\mathbf{x}} \hat{\psi}^\dagger_m(x) \left(-\frac{\hbar^2\nabla^2}{2M}\right) \hat{\psi}_m(x)\,, \tag{5.3}$$

where the summation over repeated indices $m = 0, \pm 1$ is implied and the shorthand notation $\int_{\mathbf{x}} = \int \mathrm{d}^3x$ is employed. We can expand the field operator in plane waves according to

$$\hat{\psi}_m(\mathbf{x}) = \frac{1}{\sqrt{V}} \sum_{\mathbf{k}} \hat{a}_{\mathbf{k},m} e^{i\mathbf{k}\cdot\mathbf{x}}\,, \tag{5.4}$$

where V is the volume of the system and $\hat{a}_{\mathbf{k},m}$ is the annihilation operator of a spin-1 boson with wave number $\mathbf{k}$ and magnetic quantum number m. The plane waves serve as a complete orthonormal set of basis functions satisfying the orthonormality condition and the completeness relation,

$$\int_{\mathbf{x}} e^{-i\mathbf{k}\mathbf{x}} e^{i\mathbf{k}'\mathbf{x}} = V\delta_{\mathbf{k}\mathbf{k}'}\,, \qquad \frac{1}{V}\sum_{\mathbf{k}} e^{-i\mathbf{k}\mathbf{x}} e^{i\mathbf{k}\mathbf{x}'} = \delta(\mathbf{x}-\mathbf{x}')\,. \tag{5.5}$$

The annihilation and creation operators $\hat{a}_{\mathbf{k},m}, \hat{a}^\dagger_{\mathbf{k},m}$ obey the commutation relations

$$[\hat{a}_{\mathbf{k},m}, \hat{a}_{\mathbf{l},n}] = [\hat{a}^\dagger_{\mathbf{k},m}, \hat{a}^\dagger_{\mathbf{l},n}] = 0\,, \tag{5.6a}$$

$$[\hat{a}_{\mathbf{k},m}, \hat{a}^\dagger_{\mathbf{l},m}] = \delta_{\mathbf{k}\mathbf{l}}\delta_{mn}\,, \tag{5.6b}$$

which ensure that the field operator (5.4) suffices the commutation relations (5.1). Using the annihilation and creation operators, the kinetic part of the Hamiltonian takes the simple form

$$\hat{H}_{\text{kin}} = \sum_{\mathbf{k}} \varepsilon_{\mathbf{k}}\,\hat{n}_{\mathbf{k},m}\,, \qquad \varepsilon_{\mathbf{k}} = \frac{\hbar^2\mathbf{k}^2}{2M}\,, \tag{5.7}$$

where $\hat{n}_{\mathbf{k},m} = \hat{a}^\dagger_{\mathbf{k},m}\hat{a}_{\mathbf{k},m}$ is the number operator and $\varepsilon_{\mathbf{k}}$ the excitation spectrum of the free bosonic excitations.

The external magnetic field applied in the z-direction leads to Zeeman shifts. We do not take into account the linear Zeeman shift since its effect on the dynamics is a spin precession of the two sublevels $m = \pm 1$ around the axis of the magnetic field which can be absorbed into the fields when transforming into the rotating frame of reference. The quadratic Zeeman shift, however, cannot be removed and contributes to the Hamiltonian with

$$\hat{H}_{\mathrm{qZ}} = q \int_{\mathbf{x}} \hat{\psi}^{\dagger}_{m}(x)\, (f_z^2)_{mm'}\, \hat{\psi}_{m'}(x) = q\, m^2 \int_{\mathbf{x}} \hat{\psi}^{\dagger}_{m}(x) \hat{\psi}_{m}(x) = q m^2 \sum_{\mathbf{k}} \hat{a}^{\dagger}_{\mathbf{k},m} \hat{a}_{\mathbf{k},m}\,, \tag{5.8}$$

where q denotes the Zeeman energy and the z-component spin matrix $f^z_{mm'} = m\delta_{mm'}$ is employed for the second equality. The quadratic Zeeman effect shifts the energy of the magnetic sublevels $m = \pm 1$ with respect to the $m = 0$ sublevel in the same direction. If the parameter q is positive (negative), the population of the sublevels $m = \pm 1$ is energetically suppressed (favored).

The last term of the Hamiltonian represents the interacting parts of a spin-1 BEC, which can be written as

$$\hat{H}_{\mathrm{int}} = \frac{1}{2} \int_{\mathbf{x}} \Big[c_0 : \hat{n}^2(x) : + c_1 : \hat{\mathbf{F}}^2(x) : \Big]\,, \tag{5.9}$$

using the scalar product $\hat{\mathbf{F}}^2 = \hat{F}^i \hat{F}^i$ with summation over repeated indices $i = x, y, z$ implied. A detailed derivation of this term can be found in [132]. In (5.9) the coefficients c_0 and c_1 describe the couplings constants for the density-density and spin-spin interactions, respectively. The symbol $: \ldots :$ denotes normal ordering, i.e. all creation operators are placed to the left while all annihilation operators are placed to the right. The interactions are expressed in terms of physical observables, the *number density operator*

$$\hat{n}(t, \mathbf{x}) = \hat{\psi}^{\dagger}_{m}(t, \mathbf{x}) \hat{\psi}_{m}(t, \mathbf{x})\,, \tag{5.10}$$

and the *spin density operator*

$$\hat{F}^i(t, \mathbf{x}) = \hat{\psi}^{\dagger}_{m}(t, \mathbf{x})\; f^i_{mm'}\; \hat{\psi}_{m'}(t, \mathbf{x})\,. \tag{5.11}$$

The latter is defined by the vector of spin-1 matrices $\mathbf{f}_{mm'} = (f^x_{mm'}, f^y_{mm'}, f^z_{mm'})^T$. The spin-1 matrices are the generators of $SU(2)$ and in their three-dimensional irreducible representation they read

$$f^x = \frac{1}{\sqrt{2}} \begin{pmatrix} 0 & 1 & 0 \\ 1 & 0 & 1 \\ 0 & 1 & 0 \end{pmatrix}, \qquad f^y = \frac{i}{\sqrt{2}} \begin{pmatrix} 0 & -1 & 0 \\ 1 & 0 & -1 \\ 0 & 1 & 0 \end{pmatrix}, \qquad f^z = \begin{pmatrix} 1 & 0 & 0 \\ 0 & 0 & 0 \\ 0 & 0 & -1 \end{pmatrix}. \tag{5.12}$$

The density-density interactions are attractive for $c_0 < 0$ and repulsive for $c_0 > 0$. In this thesis, we only consider the case of repulsive density-density interactions typical for present-day ultracold atom experiments. For $c_0 > 0$, a locally nonzero density gives a positive contribution to the energy such that it is energetically favorable for the system to minimize the particle density $\langle \hat{n} \rangle$ and hence the potential energy $c_0 \langle \hat{n}^2 \rangle$.

The spin-spin interaction is ferromagnetic for $c_1 < 0$ or antiferromagnetic for $c_1 > 0$. In the ferromagnetic case, a locally nonzero spin-density gives a negative contribution to the energy. Hence, it becomes energetically favorable for the system to align atomic spins in a way such that $\langle \hat{\mathbf{F}}^2 \rangle$ is maximized and therefore $c_1 \langle \hat{\mathbf{F}}^2 \rangle < 0$ is minimized. In contrast, the antiferromagnetic case energetically favors vanishing local spin densities in order to minimize $c_1 \langle \hat{\mathbf{F}}^2 \rangle > 0$.

Under realistic conditions one finds that the spin-spin interaction is much weaker than the density-density interaction, i.e. $|c_1| \ll c_0$. For example, the coupling ratio is $c_1/c_0 \approx -5 \times 10^{-3}$ for ^{87}Rb $c_1/c_0 \approx 4 \times 10^{-2}$ for ^{23}Na [132].

Using that the total spin of a spin-1 BEC must be 0 or 2, the Hamiltonian can be rephrased in terms of creation and annihilation operators [133],

$$\begin{aligned}\hat{H}_{\text{int}} &= \sum_{\mathbf{k}} (\varepsilon_{\mathbf{k}} + qm^2)\, \hat{a}^{\dagger}_{\mathbf{k},m} \hat{a}_{\mathbf{k},m} \\ &+ \frac{1}{2V} \sum_{\mathbf{k},\mathbf{p},\mathbf{q}} \Big[c_0 \; \hat{a}^{\dagger}_{\mathbf{p},m} \; \hat{a}^{\dagger}_{\mathbf{q},m'} \hat{a}_{\mathbf{p}+\mathbf{k},m} \; \hat{a}_{\mathbf{q}-\mathbf{k},m'} + c_1 \; f^i_{mm'} f^i_{nn'} \hat{a}^{\dagger}_{\mathbf{p},m} \; \hat{a}^{\dagger}_{\mathbf{q},n} \; \hat{a}_{\mathbf{p}+\mathbf{k},m'} \hat{a}_{\mathbf{q}-\mathbf{k},n'} \Big] \,, \qquad (5.13)\end{aligned}$$

where repeated indices m, m', n, n' are summed over the magnetic sublevels $0, \pm 1$ and i is summed over the spatial components x, y, z. We can rewrite (5.9) explicitly in terms of the field operators,

$$\begin{aligned}\hat{H}_{\text{int}} = \int_{\mathbf{x}} \Bigg\{ & \frac{c_0 + c_1}{2} \Big[\hat{\psi}^{\dagger}_1 \hat{\psi}^{\dagger}_1 \hat{\psi}_1 \hat{\psi}_1 + \hat{\psi}^{\dagger}_{-1} \hat{\psi}^{\dagger}_{-1} \hat{\psi}_{-1} \hat{\psi}_{-1} + 2 \hat{\psi}^{\dagger}_0 \hat{\psi}_0 \Big(\hat{\psi}^{\dagger}_1 \hat{\psi}_1 + \hat{\psi}^{\dagger}_{-1} \hat{\psi}_{-1} \Big) \Big] \\ & + (c_0 - c_1) \; \hat{\psi}^{\dagger}_1 \hat{\psi}^{\dagger}_{-1} \hat{\psi}_{-1} \hat{\psi}_1 + \frac{c_0}{2} \; \hat{\psi}^{\dagger}_0 \hat{\psi}^{\dagger}_0 \hat{\psi}_0 \hat{\psi}_0 \\ & + c_1 \Big(\hat{\psi}^{\dagger}_1 \hat{\psi}^{\dagger}_{-1} \hat{\psi}_0 \hat{\psi}_0 + \hat{\psi}^{\dagger}_0 \hat{\psi}^{\dagger}_0 \hat{\psi}_{-1} \hat{\psi}_1 \Big) \Bigg\} \,, \qquad (5.14)\end{aligned}$$

suppressing the spacetime arguments of the field operators to ease notation. The two terms in the last line describe spin-changing collisions whose strength is determined by c_1. Two atoms in the magnetic sublevel $m = 0$ can scatter into one atom in the $m = 1$ and the other atom in the $m = -1$ state, and vice versa. This is expressed by annihilating (creating) two atoms in the $m = 0$ sublevel and creating (annihilating) one atom in the $m = 1$ and one atom in the $m = -1$ sublevel. As a consequence, the initial population balance of the magnetic sublevels can change. In contrast, all other terms preserve the atom population in each mode m. The difference of population in the $m = +1$ and $m = -1$ sublevels is not changed under these spin-changing collisions.

In the special case of $c_1 = -c_0$, all terms in the first line of (5.14) vanish. On the one hand, this implies that no momentum redistribution within the $m = \pm 1$ mode occurs. On the other hand, also spin-preserving collisions between $m = 0$ and $m = \pm 1$ are absent. Besides the spin-changing collisions, only the terms in the second line contribute, i.e. only collisions within the $m = 0$ sublevel and spin-preserving collisions between the sublevels $m = \pm 1$ occur, where the latter is suppressed by a factor of four as compared to the former.

After this discussion of all terms in the Hamiltonian (5.2) describing a spin-1 BEC, we now turn to the mean-field and the Bogoliubov approximation for this system. The aim is to understand the phase diagram and the instabilities of the spin-1 system.

5.2 Mean-field theory

In this section, we present the mean-field approximation of the spin-1 BEC in which one neglects all quantum fluctuations and only considers the mean value of the field. The equations of motion obtained in this scheme are known as the Gross-Pitaevskii equations. In the subsequent section, we discuss the Bogoliubov approximation where quantum fluctuations up to second order are taken into account.

Due to the low particle densities in trapped ultracold atomic gases, the interactions between particles are weak and BECs are very well described by a mean-field theory, which provides a starting point for a qualitative understanding of the behavior of ground states and phases. For a theoretical description one decomposes the quantum field operator into the mean value of the field ψ and its quantum fluctuations $\delta\hat{\psi}$,

$$\hat{\psi}_m(x) = \psi_m(x) + \delta\hat{\psi}_m(x)\,, \tag{5.15}$$

where $\psi_m(x) = \langle\hat{\psi}_m(x)\rangle$ is the expectation value of the field. For large densities and weak interactions, quantum-statistical fluctuations become negligible compared to classical-statistical fluctuations. In these cases, an ultracold quantum many-body system is well described by mean-field theory, where one drops all quantum fluctuations $\delta\hat{\psi}_m$ and simply replaces the field operator by its expectation value,

$$\hat{\psi}_m(x) \rightarrow \psi_m(x)\,, \tag{5.16}$$

where $\psi_m(x)$ is a complex field commonly referred to a the *wave function of the condensate.* The mean-field approximation is valid when dealing with a sufficiently large number of atoms, weak interactions and low system temperatures such that both quantum and thermal fluctuations can be neglected. The wave function is normalized to the total number of atoms in the system,

$$N_{\text{tot}}(t) = \int_{\mathbf{x}} \sum_m |\psi_m(t,\mathbf{x})|^2\,, \tag{5.17}$$

which is conserved in the nonrelativistic theory. In a perfect BEC the number of atoms in the condensate is the same as the number of atoms in the gas.

The equations of motion for the mean-field wave function are obtained by minimizing the energy in the mean-field approximation. Substituting the field operators in the Hamiltonian by their mean-field values, following (5.16), one obtains the *energy functional*

$$E[\psi,\psi^*] = \int_{\mathbf{x}} \left\{ \psi_m^*(x)\left[-\frac{\hbar^2}{2M}\nabla^2 + qm^2\right]\psi_m(x) + \frac{c_0}{2}n^2(x) + \frac{c_1}{2}|\mathbf{F}(x)|^2 \right\}, \tag{5.18}$$

which is a real number since it only depends on the mean fields ψ,ψ^* and not on the field operators $\hat{\psi},\hat{\psi}^\dagger$. The number density operator appearing in the Hamiltonian is replaced by the total number density

$$n(x) = \psi_m^*(x)\psi_m(x) \tag{5.19}$$

and the spin density operator is substituted by the spin density vector

$$F^i(x) = \psi_m^*(x) f^i_{mm'}\psi_{m'}(x)\,, \qquad i = x,y,z\,, \tag{5.20}$$

where the missing hats in contrast to (5.10) and (5.11) distinguish these functions from the operators used in the previous section. The explicit expression for the density-density interaction term can be written as

$$n^2 = |\psi_1|^4 + |\psi_0|^4 + |\psi_{-1}|^4 + 2\Big[|\psi_{-1}|^2|\psi_0|^2 + |\psi_0|^2|\psi_1|^2 + |\psi_1|^2|\psi_{-1}|^2\Big]\,, \tag{5.21}$$

where we suppressed spacetime arguments. Using the representation of the spin-1 matrices (5.12), we obtain the following explicit expressions for the spin density vector (5.20),

$$F^x = \frac{1}{\sqrt{2}}\left[\psi_0^*\left(\psi_1 + \psi_{-1}\right) + \text{c.c.}\right] , \tag{5.22a}$$

$$F^y = \frac{i}{\sqrt{2}}\left[\psi_0^*\left(\psi_1 - \psi_{-1}\right) - \text{c.c.}\right] , \tag{5.22b}$$

$$F^z = |\psi_1|^2 - |\psi_{-1}|^2 , \tag{5.22c}$$

with “c.c.” being the short-hand notation for the complex conjugate of the previous expression. Note that the spin density components F^x, F^y, F^z are real quantities, whereas the *transversal spin*

$$F_\perp = F^x + iF^y = \sqrt{2}\left(\psi_1^*\psi_0 + \psi_0^*\psi_{-1}\right) \tag{5.23}$$

is complex. A nonzero transverse spin corresponds to nonzero field values in the $m = 0$ and $m = \pm 1$ magnetic sublevels [134]. The absolute values of the transversal and longitudinal spins are given by

$$|F_\perp|^2 = F_\perp^* F_\perp = (F^x)^2 + (F^y)^2 \qquad = 2\Big[|\psi_0|^2\left(|\psi_1|^2 + |\psi_{-1}|^2\right) + (\psi_0^*)^2\psi_1\psi_{-1} + \psi_1^*\psi_{-1}^*\psi_0^2\Big] , \tag{5.24a}$$

$$|F^z|^2 = (F^z)^2 \qquad = |\psi_1|^4 - 2|\psi_1|^2|\psi_{-1}|^2 + |\psi_{-1}|^4 , \tag{5.24b}$$

meaning that the absolute value of the total spin is

$$|\mathbf{F}|^2 = F^iF^i = n^2 - |\psi_0|^4 - 4|\psi_1|^2|\psi_{-1}|^2 + 2(\psi_0^*)^2\psi_1\psi_{-1} + 2\psi_1^*\psi_{-1}^*\psi_0^2 = n^2 - |s|^2 , \tag{5.25}$$

where we use the particle number density $n(x) = \psi_m^*(x)\psi_m(x)$ and the complex function $s(x) = \psi_0^2(x) - 2\psi_1(x)\psi_{-1}(x)$, such that

$$|s|^2 = s^*s = |\psi_0|^4 + 4|\psi_1|^2|\psi_{-1}|^2 - 2(\psi_0^*)^2\psi_1\psi_{-1} - 2\psi_1^*\psi_{-1}^*\psi_0^2 \tag{5.26}$$

is the expression determining the spin-changing collisions. In the special case of $c_0 = -c_1$, one can use this definition to rewrite the two interaction terms in the energy functional (5.18) as $E_{\text{int}}[\psi, \psi^*] = \frac{c_0}{2}|s|^2$.

5.2.1 Coupled Gross-Pitaevskii equations

The dynamics of a spin-1 BEC are well described by the equations of motion obtained in the mean-field approximation. These are known as the *Gross-Pitaevskii equations* (GPEs) and have the form of nonlinear Schrödinger equations (NLSEs), where the nonlinear term takes into account interactions between particles. Since interactions of BECs are weak, the GPEs can provide accurate predictions for ultracold atomic gas experiments [135].

The equations of motion of the considered nonrelativistic complex bosonic field theory can be derived from the variational principle

$$i\hbar\partial_t\psi_m(x) = \frac{\delta E[\psi, \psi^*]}{\delta\psi_m^*(x)} , \tag{5.27}$$

where $x = (t, \mathbf{x})$ and $E[\psi, \psi^*]$ is the energy functional obtained in the mean-field theory, see (5.18). The equations of motions can be written as

$$i\hbar\partial_t\psi_m(x) = \left[\left(-\frac{\hbar^2}{2M}\nabla^2 + qm^2 + c_0n(x)\right)\delta_{mm'} + c_1F^i(x)f^i_{mm'}\right]\psi_{m'}(x) , \tag{5.28}$$

where the indices $m, m' = 0, \pm 1$ denote magnetic sublevels. Inserting the expressions for the number and spin densities, we find the following coupled equations for the three field components:

$$i\hbar\partial_t\psi_1 = \left[-\frac{\hbar^2}{2M}\nabla^2 + q + (c_0 + c_1)\left(|\psi_1|^2 + |\psi_0|^2\right) + (c_0 - c_1)|\psi_{-1}|^2\right]\psi_1 + c_1\psi_{-1}^*\psi_0^2\,, \tag{5.29a}$$

$$i\hbar\partial_t\psi_0 = \left[-\frac{\hbar^2}{2M}\nabla^2 + (c_0 + c_1)\left(|\psi_1|^2 + |\psi_{-1}|^2\right) + c_0|\psi_0|^2\right]\psi_0 + 2c_1\psi_0^*\psi_1\psi_{-1}\,, \tag{5.29b}$$

$$i\hbar\partial_t\psi_{-1} = \left[-\frac{\hbar^2}{2M}\nabla^2 + q + (c_0 + c_1)\left(|\psi_{-1}|^2 + |\psi_0|^2\right) + (c_0 - c_1)|\psi_1|^2\right]\psi_{-1} + c_1\psi_1^*\psi_0^2\,. \tag{5.29c}$$

The multi-component GPE (5.28) is the evolution equation describing the mean-field dynamics of a spin-1 BEC. It is equivalent to the coupled equations in (5.29). The (multi-component) GPE is a partial differential equation of first order in time and of second order in space. It is time-reversible meaning that the transformation $t \to -t$ together with $\psi \to \psi^*$ leaves the equation unchanged.

5.2.2 Phase diagram

The spin degrees of freedom of a spinor BEC allow for a variety of interesting states of matter. Knowing the ground states for different system parameters provides a qualitative understanding of the system. The ground states for different parameter regions can be depicted in a phase diagram. The mean-field phase diagram is obtained by finding the mean-field ground states of the system in different parameter regimes. We first determine stationary solutions in the mean-field approximation and then relate them to the parameter region for which these solutions minimize the energy. A recent analysis of the phase diagram can be found in [136].

As ground states are stationary states, we search for stationary solutions of the GPE making the ansatz

$$\psi(t, \mathbf{x}) = \psi(\mathbf{x})e^{-i\mu t/\hbar}\,, \tag{5.30}$$

where μ is the chemical potential. This ansatz is equivalent to a derivation of the GPE by a minimization of the free energy $F = E - \mu N$, where E is the energy functional and N the total particle number. By inserting this ansatz into the multi-component GPE (5.28), we obtain the stationary GPE,

$$\mu\,\psi_m(\mathbf{x}) = \left[\left(-\frac{\hbar^2}{2M}\nabla^2 + qm^2 + c_0 n(\mathbf{x})\right)\delta_{mm'} + c_1 F^i(\mathbf{x}) f^i_{mm'}\right]\psi_{m'}(\mathbf{x})\,. \tag{5.31}$$

Solutions to this equation describe stationary states where all observables are independent of time. The state with minimal energy is considered as the ground state of the system. The mean energy is obtained by inserting the ansatz (5.30) into the energy functional (5.18). It contains a kinetic contribution given by

$$E_{\text{kin}} = \int_{\mathbf{x}} \psi_m^*(\mathbf{x})\left(-\frac{\hbar^2}{2M}\nabla^2\right)\psi_m(\mathbf{x}) \geq 0\,, \tag{5.32}$$

which is minimal for a constant field sufficing $\nabla\psi_m = 0$. Consequently, we are interested in a uniform solution with fixed particle number density n_0, where the wave function takes the form

$$\psi_m = \sqrt{n_0}\,\zeta_m\,, \tag{5.33}$$

with ζ_m being a constant spinor normalized to $\zeta_m^* \zeta_m = 1$. Here, ζ_m describes the order parameter used to distinguish different phases depending on the model parameters. It is convenient to define the *spin per particle*,

$$\mathcal{F}^i \equiv \zeta_m^* f_{mm'}^i \zeta_{m'} , \tag{5.34}$$

which for the above wave function suffices $\mathcal{F}^i = F^i / n_0$. By explicit calculation, one can easily verify that

$$|\boldsymbol{\mathcal{F}}|^2 = \mathcal{F}^i \mathcal{F}^i = 1 - |\zeta_0|^4 - 4|\zeta_1|^2 |\zeta_{-1}|^2 + 2(\zeta_0^*)^2 \zeta_1 \zeta_{-1} + 2\zeta_1^* \zeta_{-1}^* \zeta_0^2 , \tag{5.35}$$

in analogy to (5.25). This allows us to write the *energy per particle* as

$$\varepsilon \equiv \frac{E[\psi, \psi^*]}{n_0} = \sum_{m=0,\pm 1} \left[q m^2 + \frac{n_0}{2} \left(c_0 + c_1 |\boldsymbol{\mathcal{F}}|^2 \right) \right] , \tag{5.36}$$

which contains contributions from the quadratic Zeeman shift, the density-density and the spin-spin interaction. Hereafter, we present the stationary solutions and their energies to subsequently discuss the phase diagram of the spin-1 BEC. The stationary solutions found from the stationary GPE (5.31) are:

- two *ferromagnetic* states

$$\boldsymbol{\zeta}^+ = \begin{pmatrix} e^{i\chi_1} \\ 0 \\ 0 \end{pmatrix} , \qquad \boldsymbol{\zeta}^- = \begin{pmatrix} 0 \\ 0 \\ e^{i\chi_{-1}} \end{pmatrix} , \tag{5.37}$$

  with positive and negative magnetizations in z-direction, i.e. $\mathcal{F}^z = \pm 1$, respectively, no magnetization in the transverse direction $\mathcal{F}_\perp = 0$, $\chi_{\pm 1} \in \mathbb{R}$ describing the phase, and energy $\varepsilon = q + \frac{1}{2} n_0 (c_0 + c_1)$,

- one *antiferromagnetic* state

$$\boldsymbol{\zeta} = \sqrt{\frac{1}{2}} \begin{pmatrix} e^{i\chi_1} \\ 0 \\ e^{i\chi_{-1}} \end{pmatrix} , \tag{5.38}$$

  with no magnetization in any direction, i.e. $\mathcal{F}^i = 0$ for $i = x, y, z$ for vanishing linear Zeeman effect, phases $\chi_{\pm 1} \in \mathbb{R}$, and energy $\varepsilon = q + \frac{1}{2} c_0 n_0$,

- one *polar* state

$$\boldsymbol{\zeta} = \begin{pmatrix} 0 \\ e^{i\chi_0} \\ 0 \end{pmatrix} , \tag{5.39}$$

  with no magnetization in any direction, i.e. $\mathcal{F}^i = 0$ for $i = x, y, z$, phase $\chi_0 \in \mathbb{R}$ and energy $\varepsilon = \frac{1}{2} c_0 n_0$,

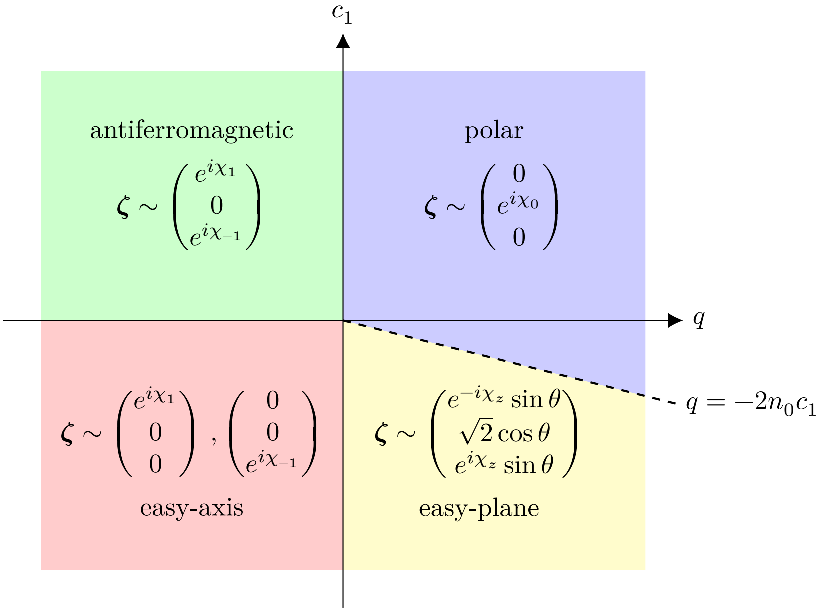

Figure 5.1: Mean-field phase diagram of a spin-1 BEC in the q-c_1-plane for $c_0 > 0$. The ground state wave functions in the respective phases are given by $\psi_m = \sqrt{n_0}\zeta_m$. For the ground state in the easy-plane phase we use $\sin\theta = \sqrt{\frac{1}{2} + \frac{q}{4n_0c_1}}$.

- one state with *broken axisymmetry*

$$\boldsymbol{\zeta} = \frac{1}{2}\, e^{i\chi_0} \begin{pmatrix} e^{-i\chi_z}\sqrt{\frac{2c_1n_0+q}{2c_1n_0}} \\ \sqrt{\frac{2c_1n_0-q}{c_1n_0}} \\ e^{+i\chi_z}\sqrt{\frac{2c_1n_0+q}{2c_1n_0}} \end{pmatrix}, \tag{5.40}$$

only existing for nonnegative arguments in the square roots of all three components, with a phase $\chi_z \in \mathbb{R}$ coming from a spin rotation around the z-axis, energy $\varepsilon = (q + 2c_1n_0)^2/(8c_1n_0) + \frac{1}{2}c_0n_0$, and nonzero transversal spin $\mathcal{F}_\perp = e^{i\chi_z}\sqrt{(2n_0c_1)^2 - q^2}/(2n_0|c_1|)$ while $\mathcal{F}^z = 0$ for vanishing linear Zeeman effect.

As we consider repulsive density-density interactions, c_0 is positive and the remaining parameter space is spanned by q and c_1. The ground state for a given set of parameters $\{q, c_1\}$ is the stationary state among the states (5.37)–(5.40) that minimizes the energy per particle. This is depicted by the mean-field phase diagram in Figure 5.1, where the ground states are assigned to different regions in the q-c_1-plane.

For a discussion of the various ground states, we look at the energy per particle given by (5.36). For an antiferromagnetic spin-spin interaction with $c_1 > 0$, it is energetically favorable to minimize the spin per particle $|\boldsymbol{\mathcal{F}}|$. This is achieved by the polar state (5.39) and the antiferromagnetic state (5.38) since the magnetization vanishes for both. A particle population of the magnetic sublevels $m = \pm 1$ decreases (increases) the energy for negative (positive) q. Hence, the antiferromagnetic (polar) state with(out) particle population in the $m = \pm 1$ sublevels is the ground state for $q < 0$ ($q > 0$). The corresponding phases are called the antiferromagnetic phase ($c_1 > 0$, $q < 0$, green patch in Figure 5.1) and the polar phase ($c_1 > 0$, $q > 0$, blue patch in Figure 5.1). They are separated by a first order

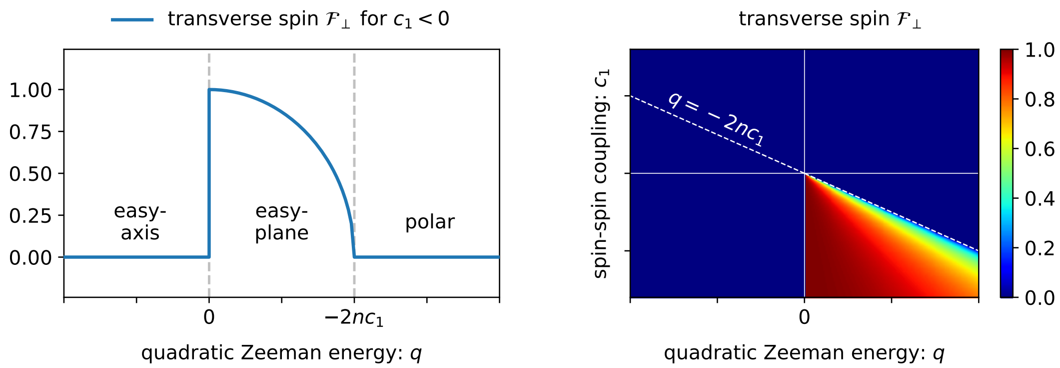

Figure 5.2: The transversal spin per particle $\mathcal{F}_\perp$ shown as a function of q for $c_1 < 0$ (left side) and in the q-c_1-plane encoded in the color scheme (right side). Regions of the easy-axis, easy-plane and polar phase are indicated in the left plot. In the right plot, the dashed line indicates $q = -2nc_1$.

phase transition. In the absence of an external magnetic field, the polar and antiferromagnetic states are degenerate and related to each other by a $\pi/2$-rotation around the x-axis.

If the spin-spin interaction is ferromagnetic with $c_1 < 0$, the system tends maximize its magnetization in order to minimize the energy. As before, for $q < 0$ a population of the magnetic sublevels $m = \pm 1$ is energetically favored. In this case, the ground state is given by one of the ferromagnetic states (5.37). The respective phase is known as the easy-axis phase ($c_1 < 0$, $q < 0$, red patch in Figure 5.1). For vanishing linear Zeeman shift, the two states are degenerate and the sign of the magnetization is spontaneously chosen.

In the case where $c_1 < 0$ and $q > 0$, two effects are acting against each other. The ferromagnetic spin-spin interaction tries to maximize the spin density $|\boldsymbol{\mathcal{F}}|$ against the energy cost of populating the $m = \pm 1$ sublevels due to the Zeeman energy. Comparing the energies of the polar state (5.39) and the state with broken axisymmetry (5.40), one finds that the polar state minimizes the energy for $q > -2n_0c_1$. For $q < -2n_0c_1$, however, the state with broken axisymmetry has the lowest energy. Hence, there is a second order phase transition at $q = -2n_0c_1$ separating the polar phase ($c_1 < 0$, $q > -2n_0c_1$) and the so-called easy-plane phase ($c_1 < 0$, $q < -2n_0c_1$, yellow patch in Figure 5.1), where the state with broken axisymmetry is the ground state. The transverse magnetization $\mathcal{F}_\perp$ changes continuously from zero to a nonzero value across this transition, as shown in Figure 5.2. In contrast, the longitudinal magnetization $\mathcal{F}_z$ stays zero. This gives rise to the name “easy-plane”, pointing out that the transversal spin $F_\perp$ lives in the x-y-plane with a spontaneously chosen azimuthal angle.

In this section, we presented the ground states of the spin-1 BEC in the mean-field approximation. The results were summarized in terms of a phase diagram in the q-c_1-plane, see Figure 5.1. Before we come to the discussion of the Bogoliubov approximation, we introduce the relevant scales of the spin-1 system.

5.2.3 Characteristic scales

A characteristic length scale of any Bose gas is defined by the distance ξ at which a typical kinetic energy $\hbar^2/(2M\xi^2)$ balances a typical interaction energy scale. The conventional choice is to use the interaction energies n_0c_0 and n_0c_1, which appear in the energy density (5.36), as the characteristic energy scales of the density-density and spin-spin interactions, respectively. They give rise to two characteristic length scales, the *density healing length* ξ_0 and the *spin healing length* ξ_1,

$$\xi_0 = \frac{\hbar}{\sqrt{2Mn_0|c_0|}}\,, \tag{5.41a}$$

$$\xi_1 = \frac{\hbar}{\sqrt{2Mn_0|c_1|}}\,, \tag{5.41b}$$

where the term *healing length* arises from the fact that it sets the length scale over which the condensates "heals" from local defects. Since a length scale λ can be translated into a momentum scale k by the relation $k = 2\pi/\lambda$, we also define the corresponding characteristic momentum scales,

$$k_{\xi_0} = \frac{2\pi}{\xi_0} = 2\pi\sqrt{2Mn_0|c_0|}\,/\hbar\,, \tag{5.42a}$$

$$k_{\xi_1} = \frac{2\pi}{\xi_1} = 2\pi\sqrt{2Mn_0|c_1|}\,/\hbar\,, \tag{5.42b}$$

which we refer to as the *healing momentum* of the density and the spin, respectively. Furthermore, we define the characteristic time scales

$$\tau_{\xi_0} = \frac{\hbar}{n_0|c_0|}\,, \tag{5.43a}$$

$$\tau_{\xi_1} = \frac{\hbar}{n_0|c_1|}\,, \tag{5.43b}$$

where the latter is commonly referred to as the spin-changing collision time [38].

In realistic experimental systems one typically finds $|c_1| \ll c_0$ such that the characteristic scales of density and spin can differ by several orders of magnitude with $\xi_1 \gg \xi_0$ or $k_{\xi_1} \ll k_{\xi_0}$. However, in the special case of $c \equiv c_0 = -c_1 > 0$ we can define

$$\xi = \frac{\hbar}{\sqrt{2Mn_0c}}\,, \qquad k_\xi = 2\pi\sqrt{2Mn_0c}\,/\hbar\,, \qquad \tau_\xi = \frac{\hbar}{n_0c}\,, \tag{5.44}$$

which become the only relevant scales of the system.

5.3 Bogoliubov theory

In this section we discuss an approximation of the spin-1 Bose gas that is known as *Bogoliubov theory*. In contrast to the mean-field theory, where all quantum fluctuations are neglected, Bogoliubov theory takes into account quantum fluctuations up to second order. Since the Bogoliubov Hamiltonian is diagonalizable, it can be used to find the spectrum of elementary excitations. In the following, we first outline the Bogoliubov approximation for a spin-1 BEC and thereafter present the Bogoliubov theory for the polar phase.

The mean-field ground state is subject to fluctuations which are induced by quantum and thermal fluctuations as well as external perturbations. When these fluctuations are weak, they can be described by Bogoliubov theory. The basic idea is to express the field operator in terms of its mean-field value and small fluctuations, similar to (5.15), and to insert this into the second-quantized Hamiltonian while keeping terms up to second order in the fluctuations.

We split the field operator into one term describing a macroscopically occupied mode, the so-called *condensate* mode, and a term accounting for the quantum and thermal fluctuations of all other modes. This is achieved by writing the mode expansion (5.4) as

$$\hat{\psi}_m(\mathbf{x}) = \frac{1}{\sqrt{V}}\ \hat{a}_{\mathbf{0},m} + \frac{1}{\sqrt{V}} \sum_{\mathbf{k}\neq 0} \hat{a}_{\mathbf{k},m} e^{i\mathbf{k}\cdot\mathbf{x}}\,, \tag{5.45}$$

where $\mathbf{k} = \mathbf{0}$ is the condensate mode. We assume that the total number of atoms is constant and can be decomposed according to

$$N_{\text{tot}} = N_0 + \sum_{\mathbf{k}\neq 0} \langle \hat{a}^\dagger_{\mathbf{k},m} \hat{a}_{\mathbf{k},m} \rangle\ , \tag{5.46}$$

with $N_0 \equiv \langle \hat{a}^\dagger_{\mathbf{0},m} \hat{a}_{\mathbf{0},m} \rangle$ being the occupation number of the condensate mode. In a Bose-Einstein condensed gas, the lowest energy mode ($\mathbf{k} = \mathbf{0}$) is occupied by a macroscopic number of particles such that its occupation number is much larger than the occupation number of all other modes,

$$N_0 \gg \langle \hat{a}^\dagger_{\mathbf{k},m} \hat{a}_{\mathbf{k},m} \rangle \qquad\qquad \forall \mathbf{k} \neq 0\,. \tag{5.47}$$

Since $N_0 = \langle \hat{a}^\dagger_{\mathbf{0},m} \hat{a}_{\mathbf{0},m} \rangle$ is very large as compared to unity, the expression $\hat{a}_{\mathbf{0},m} \hat{a}^\dagger_{\mathbf{0},m} - \hat{a}^\dagger_{\mathbf{0},m} \hat{a}_{\mathbf{0},m} = 1$ is small compared with $\hat{a}_{\mathbf{0},m}$ and $\hat{a}^\dagger_{\mathbf{0},m}$ themselves. This allows us to treat them as ordinary numbers, neglecting their noncommutability [137]. Thus, one can omit the quantum fluctuations of this state and replace its mode operator by a complex number,

$$\hat{a}_{\mathbf{0},m} \to \sqrt{N_0}\ \zeta_m = \left[N_{\text{tot}} - \sum_{\mathbf{k}\neq 0} \langle \hat{a}^\dagger_{\mathbf{k},m} \hat{a}_{\mathbf{k},m} \rangle \right]^{1/2} \zeta_m\,, \tag{5.48}$$

where the normalized spinor ζ_m is a stationary solution of the GPE. Assuming that quantum fluctuations are small, one further neglects all terms in the Hamiltonian that are of higher than quadratic order in $\hat{a}^\dagger_{\mathbf{k},m}$ and $\hat{a}_{\mathbf{k},m}$ for $\mathbf{k} \neq \mathbf{0}$ and arrives at the Bogoliubov Hamiltonian. For a spin-1 BEC it can be written as follows (see [133] for details about the computation):

$$\begin{aligned} \hat{H}_{\text{eff}} = {} & \frac{V}{2} n^2 (c_0 + c_1 \boldsymbol{\mathcal{F}}^2) + q N_{\text{tot}} \langle (f^z)^2 \rangle \\ & + \sum_{\mathbf{k}\neq\mathbf{0}} \Bigg[\Big(\varepsilon_{\mathbf{k}} - n c_1 \boldsymbol{\mathcal{F}}^2 + q m^2 - q \langle (f^z)^2 \rangle \Big) \hat{a}^\dagger_{\mathbf{k},m} \hat{a}_{\mathbf{k},m} + n c_1 \mathcal{F}^i f^i_{mm'} \hat{a}^\dagger_{\mathbf{k},m} \hat{a}_{\mathbf{k},m'} \\ & \qquad + \frac{n c_0}{2} \Big(2 \hat{D}^\dagger_{\mathbf{k}} \hat{D}_{\mathbf{k}} + \hat{D}_{\mathbf{k}} \hat{D}_{-\mathbf{k}} + \hat{D}^\dagger_{\mathbf{k}} \hat{D}^\dagger_{-\mathbf{k}} \Big) + \frac{n c_1}{2} \Big(2 \hat{S}^{i\,\dagger}_{\mathbf{k}} \hat{S}^i_{\mathbf{k}} + \hat{S}^i_{\mathbf{k}} \hat{S}^i_{-\mathbf{k}} + \hat{S}^{i\,\dagger}_{\mathbf{k}} \hat{S}^{i\,\dagger}_{-\mathbf{k}} \Big) \Bigg] \end{aligned} \tag{5.49}$$

where $\langle (f^z)^2 \rangle = \zeta^*_m (f^z)^2_{mm'} \zeta_{m'}$ with normalized spinor ζ_m and

$$\mathcal{F}^i \equiv \zeta^*_m f^i_{mm'} \zeta_{m'}\,, \qquad\qquad \hat{D}_{\mathbf{k}} \equiv \zeta^*_m \hat{a}_{\mathbf{k},m}\,, \qquad\qquad \hat{S}^i_{\mathbf{k}} \equiv \zeta^*_m f^i_{mm'} \hat{a}_{\mathbf{k},m'}\,, \tag{5.50}$$

with $i = x, y, z$. F^i describes the spin per particle, $\hat{D}_{\mathbf{k}}$ and $\hat{S}^i_{\mathbf{k}}$ denote the density and spin fluctuation operators of the condensate, and $n = N_{\text{tot}}/V$ is the total particle number density. The terms proportional to c_0 and c_1 in the third line of (5.49) describe density-density and spin-spin interactions, respectively. The first terms in the round brackets, which are proportional to $\hat{a}^\dagger_{\mathbf{k},m} \hat{a}_{\mathbf{k},m}$, represent the interaction of particle or spin excitations with the condensate; the second and third terms proportional to $(\hat{a}_{\mathbf{k},m} \hat{a}_{-\mathbf{k},m} + \hat{a}^\dagger_{\mathbf{k},m} \hat{a}^\dagger_{-\mathbf{k},m})$ represent the creation or annihilation of particle or spin excitations from the condensate.

The effective Hamiltonian (5.49) can be diagonalized by linear transformations known as the *Bogoliubov transformations.* Thereby, the creation and annihilation operators are expressed as

$$\hat{a}_{\mathbf{k}} = u_{\mathbf{k}}\hat{b}_{\mathbf{k}} + v_{-\mathbf{k}}\hat{b}^{\dagger}_{-\mathbf{k}}\,, \qquad\qquad \hat{a}^{\dagger}_{\mathbf{k}} = u^{*}_{\mathbf{k}}\hat{b}^{\dagger}_{\mathbf{k}} + v^{*}_{-\mathbf{k}}\hat{b}_{-\mathbf{k}}\,, \tag{5.51}$$

where we omit indices for the magnetic quantum number to shorten notation. $u_{\mathbf{k}}$ and $v_{\mathbf{k}}$ are two complex parameters while $\hat{b}_{\mathbf{k}}$ and $\hat{b}^{\dagger}_{\mathbf{k}}$ are operators assumed to obey the bosonic commutation relations with $[\hat{b}_{\mathbf{k}}, \hat{b}^{\dagger}_{\mathbf{k}'}] = \delta_{\mathbf{k}\mathbf{k}'}$ and all others vanishing. The commutation relation poses $|u_{\mathbf{k}}|^2 - |v_{-\mathbf{k}}|^2 = 1$ as a constraint on the two parameters $u_{\mathbf{k}}$ and $v_{\mathbf{k}}$.

Since the Bogoliubov Hamiltonian depends on the spinor ζ_m characterizing different phases, the parameters $u_{\mathbf{k}}$ and $v_{\mathbf{k}}$ also differ from phase to phase. Here, we only present results for a diagonalization in the polar phase ($c_1 > 0$ and $q > 0$, $c_1 < 0$ and $q > -2c_1 n$), where the ground state spinor is given by $\boldsymbol{\zeta} \sim (0,1,0)^T$ and the magnetization vanishes, $\boldsymbol{\mathcal{F}} = 0$. In this case, it is convenient to describe density fluctuations using $\hat{a}_{\mathbf{k},0}$ while introducing the spin fluctuation operators

$$\hat{a}_{\mathbf{k},f_x} \equiv \frac{1}{\sqrt{2}}\left(\hat{a}_{\mathbf{k},1} + \hat{a}_{\mathbf{k},-1}\right)\,, \tag{5.52a}$$

$$\hat{a}_{\mathbf{k},f_y} \equiv \frac{i}{\sqrt{2}}\left(\hat{a}_{\mathbf{k},1} - \hat{a}_{\mathbf{k},-1}\right)\,, \tag{5.52b}$$

to describe fluctuations of the transverse spin. The Bogoliubov Hamiltonian (5.49) for the polar phase then reads

$$\begin{aligned}\hat{H}_{\text{eff,polar}} = \frac{Vn^2c_0}{2} + \sum_{\mathbf{k}\neq 0}\Bigg\{ &\left(\varepsilon_{\mathbf{k}} + nc_0\right)\hat{a}^{\dagger}_{\mathbf{k},0}\hat{a}_{\mathbf{k},0} + \frac{nc_0}{2}\left(\hat{a}^{\dagger}_{\mathbf{k},0}\hat{a}^{\dagger}_{-\mathbf{k},0} + \hat{a}_{\mathbf{k},0}\hat{a}_{-\mathbf{k},0}\right) \\ &+ \left(\varepsilon_{\mathbf{k}} + q + nc_1\right)\hat{a}^{\dagger}_{\mathbf{k},f}\hat{a}_{\mathbf{k},f} + \frac{nc_1}{2}\left(\hat{a}^{\dagger}_{\mathbf{k},f}\hat{a}^{\dagger}_{-\mathbf{k},f} + \hat{a}_{\mathbf{k},f}\hat{a}_{-\mathbf{k},f}\right)\Bigg\}\,,\end{aligned} \tag{5.53}$$

where the summation over $f = f_x, f_y$ is implied and the mode energy is given by $\varepsilon_{\mathbf{k}} = (\hbar\mathbf{k})^2/(2m)$. This effective low-energy Hamiltonian can be diagonalized by Bogoliubov transformations of the form

$$\hat{b}_{\mathbf{k},0} = \sqrt{\frac{\varepsilon_{\mathbf{k}} + nc_0 + \omega_{\mathbf{k},0}}{2\omega_{\mathbf{k},0}}}\,\hat{a}_{\mathbf{k},0} + \sqrt{\frac{\varepsilon_{\mathbf{k}} + nc_0 - \omega_{\mathbf{k},0}}{2\omega_{\mathbf{k},0}}}\,\hat{a}^{\dagger}_{-\mathbf{k},0}\,, \tag{5.54}$$

$$\hat{b}_{\mathbf{k},f} = \sqrt{\frac{\varepsilon_{\mathbf{k}} + q + nc_0 + \omega_{\mathbf{k},\perp}}{2\omega_{\mathbf{k},\perp}}}\,\hat{a}_{\mathbf{k},f} + \sqrt{\frac{\varepsilon_{\mathbf{k}} + q + nc_0 - \omega_{\mathbf{k},\perp}}{2\omega_{\mathbf{k},\perp}}}\,\hat{a}^{\dagger}_{-\mathbf{k},f}\,, \tag{5.55}$$

where the Bogoliubov dispersion relations are given by [137]

$$\omega_{\mathbf{k},0} = \sqrt{\varepsilon_{\mathbf{k}}\left(\varepsilon_{\mathbf{k}} + 2nc_0\right)}\,, \tag{5.56a}$$

$$\omega_{\mathbf{k},\perp} = \sqrt{\left(\varepsilon_{\mathbf{k}} + q\right)\left(\varepsilon_{\mathbf{k}} + q + 2nc_1\right)}\,, \tag{5.56b}$$

with particle number density n, density-density coupling c_0, and spin-spin coupling c_1. The annihilation and creation operators $\hat{b}_{\mathbf{k},f}, \hat{b}^{\dagger}_{\mathbf{k},f}$ with index $f = 0, f_x, f_y$ satisfy canonical commutation relations and

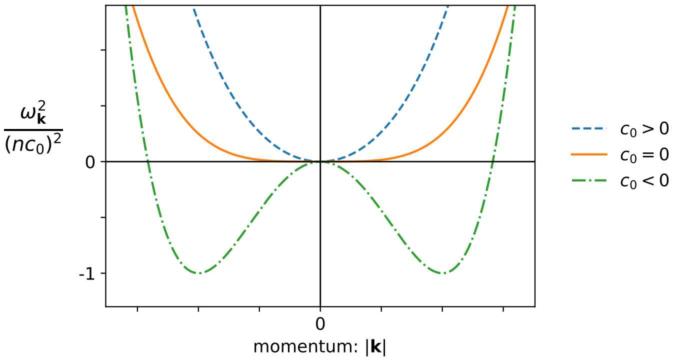

Figure 5.3: The Bogoliubov dispersion squared $\omega_{\mathbf{k},0}^2 = \varepsilon_{\mathbf{k}}(\varepsilon_{\mathbf{k}} + 2nc_0)$ with $\varepsilon_{\mathbf{k}} = (\hbar\mathbf{k})^2/(2m)$ plotted for different parameters c_0, with normalization by $(nc_0)^{-2}$. Unstable modes ($\omega_{\mathbf{k}}^2 < 0$) only appear for repulsive density-density interactions ($c_0 < 0$).

form a new basis. In this basis, the Hamiltonian takes a diagonal form,

$$\hat{H}_{\text{eff,polar}} = E_0 + \sum_{\mathbf{k}\neq 0}\sum_i \omega_{\mathbf{k},i}\hat{b}_{\mathbf{k},i}^\dagger\hat{b}_{\mathbf{k},i}\,, \qquad i = 0, f_x, f_y\,, \tag{5.57}$$

where the ground state energy of the polar phase is given by

$$E_0 = \frac{Vn^2c_0}{2} - \frac{1}{2}\sum_{\mathbf{k}\neq 0}\left[\left(\varepsilon_{\mathbf{k}} + nc_0 - \omega_{\mathbf{k},0}\right) + 2\left(\varepsilon_{\mathbf{k}} + q + nc_1 - \omega_{\mathbf{k},\perp}\right)\right]. \tag{5.58}$$

From the low-energy Hamiltonian (5.57) it becomes clear that the original system of interacting particles can be expressed as a Hamiltonian of noninteracting *quasiparticles*, also referred to as *collective excitations*, with excitation spectrum determined by the dispersion relations (5.56). The Bogoliubov transformation (5.51) describes a real particle $\hat{a}_{\mathbf{k}}$ in terms of a superposition of forward propagating quasiparticles $u_{\mathbf{k}}\hat{b}_{\mathbf{k}}$ and backward propagating quasiparticles $v_{-\mathbf{k}}^*\hat{b}_{-\mathbf{k}}$. The ground state of the interacting system is defined as the vacuum state of these Bogoliubov quasiparticles. In the following, we discuss the excitation spectrum of these quasiparticles in more detail.

5.3.1 Bogoliubov spectrum

The dispersion relations given in (5.56) describe the eigenenergies of the quasiparticle momentum modes. Since the time evolution of these modes is proportional to $e^{-i\omega_{\mathbf{k}}t}$, imaginary eigenenergies, corresponding to $\omega_{\mathbf{k}}^2 < 0$, lead to an exponential growth of the respective modes and therefore to instabilities in the system. The exponential particle production induced by these instabilities is interesting to us because it provides the possibility to create highly occupied far-from-equilibrium states in a BEC.

The density excitations of the system are characterized by the dispersion (5.56a), which is linear for low momenta, $\omega_{\mathbf{k},0} \sim |\mathbf{k}|$, and quadratic for large momenta, $\omega_{\mathbf{k},0} \sim \mathbf{k}^2$. This form of a dispersion relation is known as the Bogoliubov dispersion law. It describes the energies of elementary excitations in the form of collective sound waves.

In Figure 5.3 the dispersion is shown for different couplings c_0. It is gapless in the sense that the minimum value of the dispersion suffices $\omega_{\mathbf{k},\text{min}} \leq 0$. For $c_0 < 0$ the squared dispersion can become negative such that $\omega_{\mathbf{k},0}$ is imaginary and thus unstable for certain momentum modes $\mathbf{k}$. Thereby the

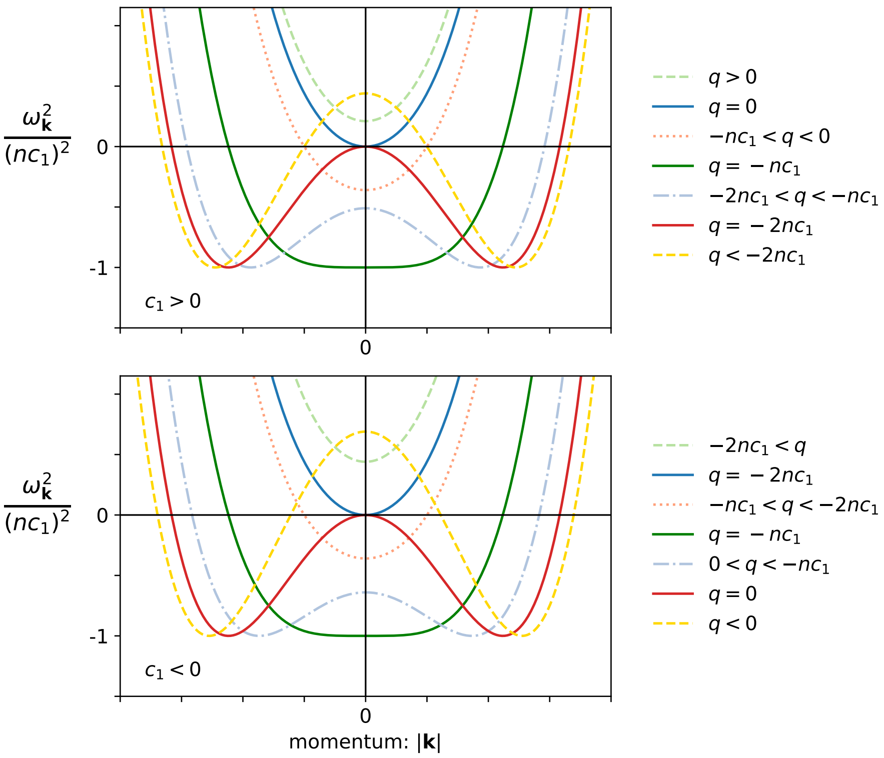

Figure 5.4: The Bogoliubov dispersion squared $\omega_{\mathbf{k},\perp}^2 = (\varepsilon_{\mathbf{k}} + q)(\varepsilon_{\mathbf{k}} + q + 2nc_1)$ with $\varepsilon_{\mathbf{k}} = (\hbar\mathbf{k})^2/(2m)$, normalized by $(nc_1)^{-2}$ such that the minima are at -1. We show the cases $c_1 > 0$ (upper plot) and for $c_1 < 0$ (lower plot) for different Zeeman energies q (decreasing from top to bottom in the line order of the legend). The unstable momentum modes appear for $q < 0$ in the case $c_1 > 0$ (upper plot) and for $q < -2nc_1$ in the case $c_1 < 0$ (lower plot).

minimum value of the dispersion is $\omega_{\mathbf{k},\mathrm{min}} = -n|c_0|$, which determines the maximal growth rate of the unstable modes.

From (5.56b) it follows that the spin fluctuations are characterized by the dispersion squared

$$\omega_{\mathbf{k},\perp}^2 = (\varepsilon_{\mathbf{k}} + q)\,(\varepsilon_{\mathbf{k}} + q + 2nc_1)\,, \tag{5.59}$$

where q is the Zeeman energy, n is the particle number density and c_1 is the spin-spin coupling. Depending on the values of q and nc_1, this dispersion squared has different properties such as a mass gap or unstable modes. Figure 5.4 shows this dispersion relation for different Zeeman energies q, with $c_1 > 0$ in the upper and $c_1 < 0$ in the lower plot. The colors of the lines are chosen such that analogous shapes in the upper and lower plot have the same color. However, we note that they correspond do different values for q.

A mass gap appears if $\omega_{\mathbf{k},\perp}^2$ is strictly positive. This is the case for $q > 0$ and $q > -2nc_1$, as can be seen by the dashed light green line in Figure 5.4. The corresponding mass gap is given by the value of

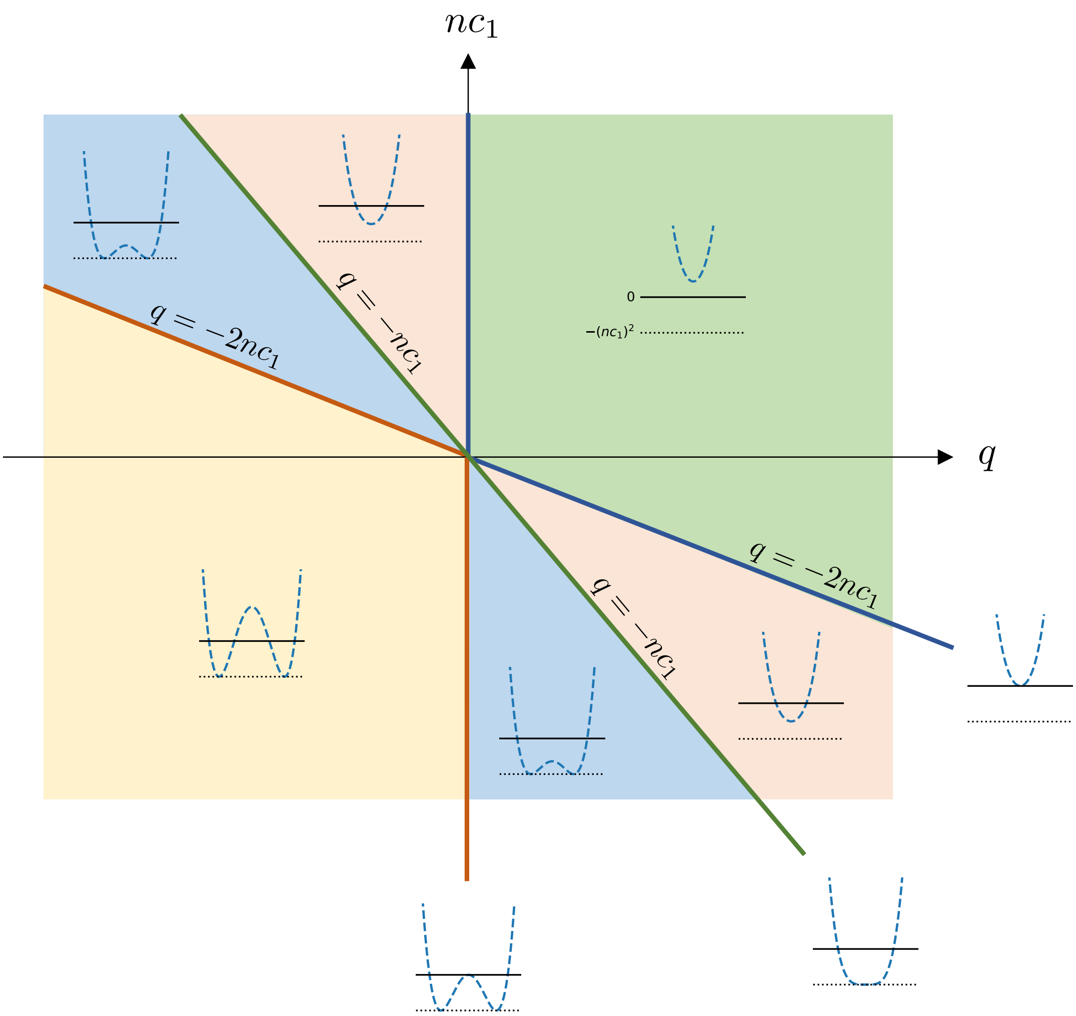

Figure 5.5: The shape of the dispersion squared $(\varepsilon_{\mathbf{k}} + q)(\varepsilon_{\mathbf{k}} + q + 2nc_1)$ with $\varepsilon_{\mathbf{k}} = \mathbf{k}^2/2m$ shown for different regions in the q-c_1-plane. The dispersion squared is represented by the blue dashed line. The full and black lines correspond to the values 0 and the $-(nc_1)^2$, respectively, as sketched in the upper right plot. Unstable modes with $\omega_{\mathbf{k}}^2 < 0$ appear for $q < 0$ and $c_1 > 0$ as well as for $q < -2nc_1$ and $c_1 < 0$. This is visualized by the blue dashed line going below the full black line. For $q < -nc_1$ the dispersion squared has the minimum value $-(nc_1)^2$. In the polar phase (green background), the dispersion has a mass gap, which can be seen by the gap between the black line and the blue dashed line.

the dispersion relation at zero momentum, $\omega_{\mathbf{0},\perp} = \sqrt{q(q+2nc_1)}$. Although the dispersion is positive at zero momentum for $q < 0$ and $q < -2nc_1$, see dashed yellow lines, there is no mass gap because the minimum of the dispersion squared is negative in this parameter regime, $\omega^2_{\mathbf{k},\perp,\mathrm{min}} = -(nc_1)^2 < 0$.

In the following, we discuss the shape of the dispersion squared (5.59) for different parameters q and c_1. Since the dispersion relation is obtained from the ground state of the polar phase, this discussion analyzes the behavior of a polar state set into other phase regions. Figure 5.5 summarizes the behavior of the dispersion in various areas of the q-c_1-plane. One can distinguish three instability regions (shown in yellow, blue, salmon), where (5.59) becomes negative, and one stable region (shown in green), where (5.59) is always positive.

The stable region, where $\omega^2_{\mathbf{k},\perp} > 0$, corresponds to the polar phase. Along the phase boundary to the antiferromagnetic phase, i.e. at $q = 0$ and $c_1 > 0$, the dispersion relation of the spin excitations has the same form as the one of the density excitations, $\omega_{\mathbf{k},\perp} = \sqrt{\varepsilon_{\mathbf{k}}(\varepsilon_{\mathbf{k}} + 2nc_1)}$, which corresponds to the Bogoliubov dispersion law. An analogous form is obtained at the phase boundary to the easy-plane phase, i.e. at $q = -2n_0 c_1$ and $c_1 < 0$, where the dispersion is given by $\omega_{\mathbf{k},\perp} = \sqrt{\varepsilon_{\mathbf{k}}(\varepsilon_{\mathbf{k}} + q)}$.

The dispersion squared is bounded from below. By solving $\mathrm{d}\omega^2_{\mathbf{k}}/\,\mathrm{d}|\mathbf{k}| = 0$, we find the momentum mode $|\mathbf{k}|_{\mathrm{mu}}$ at which the dispersion squared is minimal. This is the momentum mode at which the instability is strongest. For $q > -nc_1$ the dispersion squared describes a simple symmetric bounded potential with minimum located at zero, see green and salmon area in Figure 5.5. For $q < -nc_1$, however, the dispersion squared reveals the shape of a double well with minimum located at a nonzero momentum mode. The *most unstable mode*, the momentum mode for which the dispersion squared is minimal, is found to be

$$k_{\mathrm{mu}} \equiv |\mathbf{k}|_{\mathrm{mu}} = \begin{cases} \sqrt{-2M(q + nc_1)/\hbar^2} & q < -nc_1 \\ 0 & \text{else} \end{cases} , \tag{5.60}$$

where $q = -nc_1$ describes the boundary between symmetric and broken shapes of the dispersion squared, see green line in Figure 5.5. At the most unstable mode, the dispersion squared has its minimal value

$$\omega^2_{\perp,\mathrm{min}} = \begin{cases} -(nc_1)^2 & q < -nc_1 \\ q(q + 2nc_1) & \text{else} \end{cases} , \tag{5.61}$$

which is negative for $-nc_1 < q < 0$ if $c_1 > 0$ and $-nc_1 < q < -2nc_1$ if $c_1 < 0$. In Figure 5.5 this corresponds to the yellow, blue and salmon colored areas.

We further determine the largest momentum mode at which an instability occurs. For the case $nc_1 < 0$ unstable modes are found for $q < -2nc_1$ with the *largest unstable mode*

$$k_{\mathrm{max}} = \sqrt{-2M(2nc_1 + q)/\hbar^2} , \tag{5.62}$$

describing is the largest momentum mode for which $\omega^2_{\mathbf{k}} \leq 0$. In Figure 5.4 the largest unstable mode corresponds to the intersection point of the horizontal black line indicating $\omega^2_{\mathbf{k}} = 0$ and the colored lines showing the normalized dispersion squared.

This concludes our introduction to spin-1 Bose-Einstein condensates. Our analysis in the subsequent chapter builds on the theoretical basics outlined in this chapter, in particular the equations of motion given by the GPE (5.28), the mean-field phase diagram in Figure 5.1 and the presence of unstable modes as summarized in Figure 5.5.

Chapter 6

Far-from-equilibrium dynamics of a spin-1 Bose gas

In this chapter we study the dynamics of a spin-1 Bose gas far from equilibrium. The work on this project was undertaken in collaboration with J. Berges and M. Gärttner, as well as M. Oberthaler and his group, who all provided valuable input in numerous discussions. I carried out the simulations and the data analysis, employing a library in C developed by K. Geier and S. Erne.

This chapter is organized as follows: We begin with an introduction in Section 6.1. A recap of the model is given in Section 6.2, where we also outline the methods used to compute the time evolution. Numerical results for the nonequilibrium time evolution starting from different initial conditions are presented in Section 6.3, where we also discuss the formation of a condensate out of equilibrium. Finally, we conclude in Section 6.4.

Supplemental material to the discussion is provided in three appendices. In Appendix 6.A we present the dimensionless version of the Gross-Pitaevskii equations. Details about the numerical methods can be found in Appendix 6.B. The extraction of scaling exponents is described in Appendix 6.C.

6.1 Introduction

Although the nonequilibrium dynamics of isolated quantum many-body systems has been an object of intensive study for many years, several open questions persist in the field, including the description of the relaxation to thermal equilibrium. The relaxation behavior of quantum systems can reveal properties distinctly different from what is known in classical physics. One particularly interesting phenomenon that is currently attracting interest in both experimental and theoretical investigations is that of *nonthermal fixed points* [30]. It refers to the approach of a regime where the far-from-equilibrium-dynamics of a quantum system becomes self-similar, which is encompassed by the loss of information about the details of the initial condition and microscopic system properties.

One class of far-from-equilibrium initial conditions approaching toward such a nonthermal fixed point comprises initial states with very large occupancies. Overoccupied initial states and universal properties occur in many different physical setups, ranging from the early-universe cosmology [2, 69] over the early stages of heavy-ion collisions [73, 138] to the evolution of ultracold atomic gases [28, 29, 32, 139]. They can relax in self-similar cascades transporting particles toward low momentum

[30, 32, 65] and energy toward high momenta scales [69, 70], where one refers to the former as inverse particle and to the latter as direct energy cascades. The inverse particle cascades associated to infrared nonthermal fixed points can lead to the formation of a Bose condensate out of equilibrium [32, 140–143].

In the vicinity of a nonthermal fixed point, characteristic correlation functions exhibit self-similar scaling in time and space such that their time evolution can be described in terms of universal scaling functions and universal scaling exponents. In the scaling regime, the evolution of a relevant time- and momentum-dependent observable $f(t,k)$ in an isotropic system is fully described by

$$f(t,k) = t^{\alpha} f_S(t^{\beta} k)\,, \tag{6.1}$$

with universal scaling function f_S and universal scaling exponents α and β. In particular, f becomes a function of $t^{\beta}k$ rather than depending on time and momentum independently.

Quantum systems can be grouped into universality classes characterized by the same universal scaling functions and scaling exponents. Access to the properties of one theory in a certain universality class could give important insights about other physical systems that belong to the same universality class [27, 144]. Presently, ultracold atom experiments provide a well-controlled platform to study the nonequilibrium dynamics of isolated quantum systems. The concept of universality far from equilibrium significantly enhances the role of ultracold atom experiments in the investigation of nonequilibrium dynamics since it offers the possibility to use cold-atom setups to simulate important aspects in the dynamics of currently inaccessible systems such as the inflationary early universe. By now, self-similar scaling has been observed experimentally in scalar and spin-1 Bose gases confined in (quasi) one-dimensional trapping geometries [28, 29].

Of particular interest is the study of multi-component spinor Bose gases, where the nonzero spin degree of freedom leads to spin-dependent interactions. Bose-Einstein condensates of atoms with nonzero spin have been the focus of intense experimental [145–148] and theoretical [149–152] studies in recent years. Here we focus on a spin-1 Bose gas in three dimensions that is subject to density-density and strong spin-spin contact interactions.

6.2 Spin-1 Bose gas

We consider a spatially uniform spin-1 Bose gas described by a three-component bosonic spinor field whose components ψ_m correspond to the magnetic sublevels $m = 0, \pm 1$. As introduced in Section 5.1, the Hamiltonian of such a spin-1 Bose gas is given by

$$\hat{H} = \int \mathrm{d}^3x \left[\hat{\psi}^{\dagger}_m(t,\mathbf{x}) \left(-\frac{\hbar^2 \nabla^2}{2M} + q m^2 \right) \hat{\psi}_m(t,\mathbf{x}) + \frac{1}{2} \Big(c_0 :\hat{n}^2(t,\mathbf{x}): + \, c_1 :\hat{\mathbf{F}}^2(t,\mathbf{x}): \Big) \right], \tag{6.2}$$

where the summation over repeated indices m is implied. $\hbar$ denotes the reduced Planck constant, M the particle mass, $:\ :$ normal ordering, and q the quadratic Zeeman energy that is proportional to an external magnetic field along the z-direction. The homogeneous linear Zeeman shift has been absorbed into the definition of the fields. The interactions are expressed in terms of the density operator $\hat{n} = \hat{\psi}^{\dagger}_m \hat{\psi}_m$ and the spin density operator $\hat{\mathbf{F}} = \hat{\psi}^{\dagger}_m \mathbf{f}_{mn} \hat{\psi}_n$, where $\mathbf{f} = (f^x, f^y, f^z)^T$ is the vector of spin matrices, see (5.12). The three field components occupy the same space and are subject to two kinds of contact interactions, spin-independent density interactions and spin-spin interactions, characterized by the couplings c_0 and c_1, respectively.

In realistic experimental setups the spin-spin interactions are much weaker than the density-density interactions, implying that different characteristic length scales are manifest in the system, see Section 5.2.3. This challenges numerical analyses since large lattices are necessary in order to resolve both length scales appropriately. Here, we focus on the spin-spin interactions by assuming that their coupling constant is of the same order as that of density-density interactions. We study repulsive density and ferromagnetic spin interactions, i.e. $c_0 > 0$ and $c_1 < 0$, and work with $c \equiv c_0 = -c_1 > 0$. This enhances the influence of the spin-changing collisions we are interested in and allows us to work with feasible lattice sizes.

The respective interaction energy gives rise to the characteristic length scale of the system, the healing length $\xi = \hbar/\sqrt{2Mn_0c}$, where $n_0 = \langle\hat{n}\rangle$ is the total particle number density of the three magnetic sublevels $m = 0, \pm 1$. Because the density and spin couplings have the same value (up to a sign), the system is characterized by only one length scale and does not distinguish between density and spin healing lengths. We further define the collision time $\tau_\xi = \hbar/(n_0c)$ and the characteristic momentum scale $k_\xi = 2\pi/\xi$. In the following, all lengths, momenta and times are given in units of ξ, k_ξ and τ_ξ.

The Hamiltonian (6.2) is symmetric under $SO(2)_{f_z} \times U(1)_\phi$, meaning that it is invariant under rotations about the z-axis and a global phase ϕ. The global $U(1)_\phi$ gauge symmetry guarantees the conservation of the total particle number. Here we consider vanishing external magnetic fields where no Zeeman effects occur, i.e. $q = 0$. In this case the symmetry group is given by $SO(3)_{\mathbf{f}} \times U(1)_\phi$, where $\mathbf{f}$ denotes the spin degrees of freedom.

The classical equations of motion following from (6.2) are the Gross-Pitaevskii equations (GPEs) presented in (5.28). We deploy a dimensionless formulation of the GPEs that is obtained by expressing lengths in units of $\sqrt{2}\,\xi$ and times in units of τ_ξ. A detailed derivation is provided Appendix 6.A. The nonequilibrium time evolution of the Bose gas is computed using classical-statistical simulation methods based on the truncated Wigner approximation, where the field is evolved in terms of the classical evolution equations while quantum fluctuations are included by adding statistical fluctuations to the initial state. The initial particle occupation receives fluctuations in form of the so-called *Wigner noise* corresponding to an average occupation of half a particle per momentum mode. In this classical-statistical approach, observables are obtained as averages over an ensemble of initial states. Details about the numerical methods are presented in Appendix 6.B.

Numerical computations are carried out on cubic lattices with N_x^3 grid points and side length L. We use N_0 to denote the number of particles in the initial state, excluding the N_W particles included in terms of the Wigner noise. Since we consider large occupation numbers, the total particle number is given by $N_\mathrm{tot} = N_0 + N_\mathrm{W} \approx N_0$. If not stated differently, results are shown for $N_x = 400$, $L = 180$, $N_0 = 10^{10}$ and $N_\mathrm{W} = 9.6 \times 10^7$. For N_0 particles in the initial state, the total particle density is $n_0 = N_0/V \simeq 1715$. Adding Wigner noise to all momentum modes of the lattice, the occupation of one half particle per momentum mode results in an additional particle density of $n_\mathrm{W} = N_\mathrm{W}/3/V \simeq 5.5$ for each magnetic sublevel $m = 0, \pm 1$. Considering such large particle numbers ensures the validity of the classical-statistical approximation. The expectation values are computed using averages of ensembles with ≥ 20 samples for initial states.

Our simulations were carried out on the bwForCluster JUSTUS [153], a high performance computing cluster in the state Baden-Württemberg, with computing times of up to 7 days for a single run. Thereby each single run constituted one sample in the ensemble.

6.3 Far-from-equilibrium dynamics

6.3.1 Overoccupied initial conditions

The self-similar scaling behavior of overoccupied Bose gases has been approached analytically using kinetic theory [32, 76], computed numerically using classical-statistical [32, 36] and 2PI simulation methods [65, 154], and observed experimentally in ultracold atomic gases [28, 29]. In the $U(N)$-symmetric model, which is obtained from the spin-1 Hamiltonian (6.2) by setting $c_1 = q = 0$, one expects scaling exponents $\beta = 0.5$ and $\alpha = d\beta$. This has been shown numerically for the case of $N = 3$, where the exponents $\alpha = 1.62 \pm 0.37$ and $\beta = 0.53 \pm 0.09$ were extracted from classical-statistical simulations [36]. However, it remains an unresolved question how spin-changing collisions influence the self-similar time evolution in the vicinity of a nonthermal fixed point. In this section we examine this issue by studying the time evolution of a spin-1 Bose gas with strong spin-spin interactions.

In order to do so, we analyze the distribution function describing the occupation number of field excitations in the magnetic sublevel m,

$$f_m(t,\mathbf{k}) = \frac{\langle \psi_m^*(t,\mathbf{k})\psi_m(t,\mathbf{k})\rangle}{V}\,, \tag{6.3}$$

where $\langle\cdot\rangle$ denotes the ensemble average, $\psi_m(t,\mathbf{k}) = \int \mathrm{d}^3x\ \psi_m(t,\mathbf{x})e^{-i\mathbf{k}\mathbf{x}}$ is the spatial Fourier transform of the field $\psi_m(t,\mathbf{x})$ and V the volume of the system. The particle density follows as $n_{\mathrm{tot}}(t) = \sum_m \int \mathrm{d}^3k/(2\pi)^3\, f_m(t,\mathbf{k})$, which is a conserved quantity. Since our system is spatially homogeneous and isotropic, the occupation numbers only depend on the radial momentum $k = |\mathbf{k}|$. The angle-averaged distribution function $f_m(t,k)$ is computed by binning the three-dimensional grid data.

We investigate the time evolution of the distribution function (6.3) for two kinds of initial conditions involving overoccupied states. On the one hand, we insert large occupancies into the initial state by hand, using so-called *box initial conditions*. On the other hand, we consider *polar initial conditions* where a parameter quench leads to unusually high occupations due to the exponential growth of unstable momentum modes.

Simulations with box initial conditions employ an initial state with a large occupation number in the infrared momentum regime. The initial particle distribution is described by $f_m(t_0,\mathbf{k}) = A_0\,\Theta(k_q - |\mathbf{k}|)$ in all three magnetic sublevels $m = 0, \pm 1$, with occupancy parameter A_0 and Heaviside step function Θ. We employ $A_0 \simeq 4230$ and $k_q \simeq 0.23$ for numerical computations. In Fourier space the initial field is given by $\psi_m(t_0,\mathbf{k}) = \sqrt{f_m(t_0,\mathbf{k})\,V}\,\exp(i\theta_m(t_0,\mathbf{k}))$ with randomly chosen and thus uncorrelated phase angles $\theta_m(t_0,\mathbf{k})$. This type of initial condition has been widely employed to study self-similar scaling dynamics, see e.g. [32, 62, 65]. It was also used to investigate the $U(3)$ symmetric Bose gas, which corresponds to the special case of $c_1 = 0$ [36, 37]. Experimentally, boxlike initial conditions can be realized by strong cooling quenches [76].

Polar initial conditions are realized by an initial state corresponding to the ground state of the polar phase. We use a field that is described by $\psi_0(t_0,\mathbf{x}) = \sqrt{n_0}\,e^{i\theta(t_0,\mathbf{x})}$ and $\psi_{\pm 1}(t_0,\mathbf{x}) = 0$, where $n_0 = N_0/V \simeq 1715$ is the initial particle density and θ denotes the uncorrelated phase angles. For the homogeneous initial particle density, all particles are contained in the $\mathbf{k} = \mathbf{0}$ momentum mode of the $m = 0$ magnetic sublevel. Computing the time evolution of this initial state in a system with $q = 0$ corresponds to a sudden quench from the polar phase to the boundary of the easy-plane and the easy-axis phase. Since the low-momentum modes of the $m = \pm 1$ sublevels of a polar state are unstable

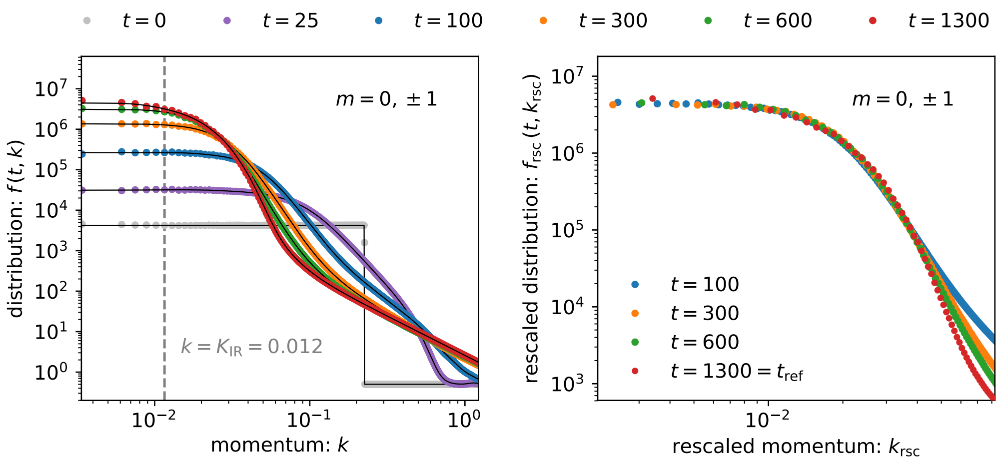

Figure 6.1: *Left*: Time evolution of the distribution function $f(t,k)$ for box initial conditions, where $f(t,k) = \frac{1}{3}\sum_m f_m(t,k)$ is the average over magnetic sublevels $m = 0, \pm 1$. The occupation number evolves self-similarly for times $t \gtrsim 100$. The gray dashed line indicates the momentum K_{IR}, up to which the distribution function shows a plateau.
Right: Rescaled distribution function $f_{\mathrm{rsc}}(t, k_{\mathrm{rsc}}) = (t/t_{\mathrm{ref}})^{-\alpha(t)} f(t,k)$ with rescaled momentum $k_{\mathrm{rsc}} = (t/t_{\mathrm{ref}})^{\beta(t)} k$, using time-dependent scaling exponents $\alpha(t)$ and $\beta(t)$ obtained for reference time $t_{\mathrm{ref}} = 1300$.

in the easy-plane phase (see discussion in Section 5.3.1), this quench leads to an exponential growth of particles in the sublevels $m = \pm 1$. In the presence of spin-changing interactions, occupancies also grow in the $m = 0$ sublevel. In experiments, polar initial states are prepared by transferring all particles to the $m = 0$ sublevel, see e.g. [28].

6.3.2 Nonequilibrium time evolution of distribution functions

This section discusses the nonequilibrium time evolution of the distribution functions $f_m(t,k)$ describing the occupation number of momentum modes k in magnetic sublevel m. We discuss the general pattern of the time evolution, thereby first considering box and subsequently polar initial conditions. An analysis of the distribution function shows that certain universal properties (scaling function f_S) are observed while others are not (exponents α and β).

The left plot in Figure 6.1 shows the numerically computed distribution functions for box initial conditions. The initial occupation number is characterized by a boxlike distribution with a high occupancy at low momenta (gray dots). The distribution quickly takes on the typical shape for inverse particle cascades, where the infrared momentum regime is characterized by a plateau followed by a power law. We observe that the infrared part of the distribution function has a similar shape for times $t \gtrsim 100$, which we investigate more closely below. During the time evolution, the dynamics slows down considerably until the distribution function becomes nearly stationary at late times $t \gtrsim 900$.

In Figure 6.1 we show the distribution function averaged over the three magnetic sublevels $m = 0, \pm 1$, which for vanishing Zeeman energy $q = 0$ are energetically equally favorable. In the presence of spin-changing collisions, two atoms in $m = 0$ can scatter into one atom in $m = \pm 1$ each, and vice versa. It is therefore generally possible that the particle numbers in the $m = 0$ and $m = \pm 1$ sublevels differ. However, for $q = 0$ and equal occupation in each of the magnetic sublevels, the scattering of atoms from $m = 0$ to $m = \pm 1$ and back should have the same probability. For box initial conditions

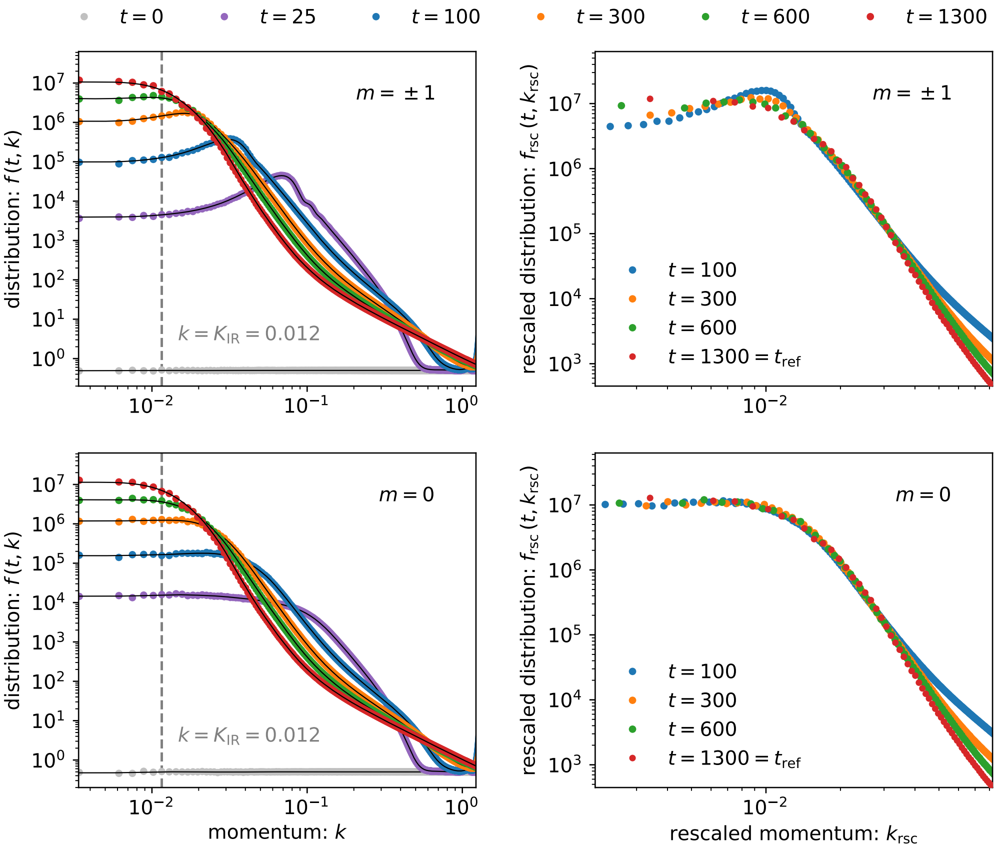

Figure 6.2: *Left column*: Time evolution of the distribution function $f(t,k)$ for polar initial conditions, where in the upper plot $f(t,k) = \frac{1}{2}\left[f_1(t,k) + f_{-1}(t,k)\right]$ is the average over $m = \pm 1$ and in the lower plot $f(t,k) = f_0(t,k)$ describes the magnetic sublevel $m = 0$. For $m = \pm 1$ ($m = 0$), the distribution functions evolves self-similarly for times $t \gtrsim 600$ ($t \gtrsim 100$). The gray dashed line indicates the momentum K_{IR}, up to which the distribution reveals a plateau.
Right column: Rescaled distribution function $f_{\mathrm{rsc}}(t, k_{\mathrm{rsc}}) = (t/t_{\mathrm{ref}})^{-\alpha(t)} f(t,k)$ with rescaled momentum $k_{\mathrm{rsc}} = (t/t_{\mathrm{ref}})^{\beta(t)} k$, using time-dependent scaling exponents $\alpha(t)$ and $\beta(t)$ obtained for reference time $t_{\mathrm{ref}} = 1300$.

with equal initial distribution in all three sublevels, we indeed observe that the particle density in each of the three magnetic sublevels remains constant at the level of $< 3\%$ for the times considered. Hence, it is reasonable to compute the average over the three magnetic sublevels.

In addition to box initial conditions we also study polar initial conditions, for which numerical results are shown in the left column of Figure 6.2. At initial time all particles are contained in the $k = 0$ momentum mode of the $m = 0$ magnetic sublevel. Since the zero mode is not included in the double logarithmic plot, the initial distribution function (gray dots) only shows the Wigner noise corresponding to an occupation of one half particle per momentum mode. The quench to $q = 0$ induces a rapid growth of the particle occupation number in the infrared momentum regime. Subsequently, the dynamics slows down, the occupation numbers approach a shape similar to the case of box initial conditions, and the time evolution becomes almost stationary at late times $t \gtrsim 1200$.

The lower left plot in Figure 6.2 shows that the time evolution of the $m = 0$ magnetic sublevel is similar to the case box initial conditions. For the magnetic sublevels $m = \pm 1$, see the upper left plot

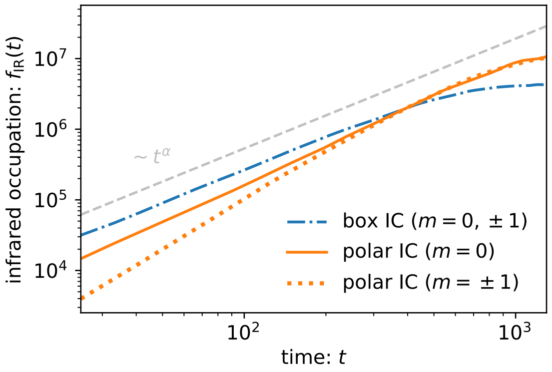

Figure 6.3: Time evolution of the particle occupation number in the infrared plateau region, $f_{\mathrm{IR}}(t)$, for box and polar initial conditions. The infrared occupancy increases faster for polar than for box initial conditions (IC). At early times $t \lesssim 300$, the growth observed for box initial conditions follows $f_{\mathrm{IR}}(t) \sim t^\alpha$, comparable with $\alpha = 1.53$ indicated by the gray dashed line. This holds approximately for polar initial conditions at intermediate times $450 \lesssim t \lesssim 1000$. At late times $t \gtrsim 1000$ the infrared occupation becomes nearly constant.

of Figure 6.2, we find that the distribution function has a clear maximum at early times (purple dots). The reason is that the growth rate is not constant over the range of unstable momentum modes. As discussed in Section 5.3.1, the growth rate is determined by the Bogoliubov dispersion and is maximal at the most unstable momentum mode $k_{\mathrm{mu}} = \sqrt{-2M(q+nc_1)/\hbar^2}$, where M is the particle mass, q the Zeeman energy, n the particle density, c_1 the spin coupling, and $\hbar$ the reduced Planck constant. The distribution function first develops a clear peak at k_{mu}, which then moves toward the infrared. As can be seen from the blue and orange dots in the upper left plot of Figure 6.2, the peak is persistent for a long time such that the distribution function of the $m = \pm 1$ magnetic sublevels needs more time than the $m = 0$ sublevel in order to build up the typical shape of the infrared particle cascade.

A useful quantity to study the slowdown of the dynamics is provided by the occupation number of the plateau in the infrared momentum range. We quantify the occupancy of the plateau by computing the average of the distribution function in the momentum range $\Lambda_{\mathrm{IR}} \leq k \leq K_{\mathrm{IR}}$, where we exclude the $k = 0$ mode. The upper threshold is chosen to be $K_{\mathrm{IR}} = 0.012$ such that the plateau region of the distribution function is well captured, see gray dashed lines in Figures 6.1 and 6.2. The thus obtained infrared occupation $f_{\mathrm{IR}}(t)$ is plotted in Figure 6.3. We find that for both box and polar initial conditions, the infrared occupation undergoes a fast growth at early times, then slows down and becomes nearly constant at late times $t \gtrsim 1000$, indicating that the distribution functions become almost stationary.

In a self-similar scaling regime, where the time evolution is characterized by (6.1), the infrared occupation evolves according to $f_{\mathrm{IR}}(t) \sim t^\alpha$ with some universal scaling exponent α. We find that even before the shape of the distribution function has fully reached its scaling form, the infrared occupancy already reveals a power-law growth in time. We determine the power law by performing linear fits of the infrared occupation over the time range $75 \leq t \leq 525$. Errors are estimated by the largest deviations obtained when altering the time range. We obtain the exponents

$$\begin{aligned} \alpha &= 1.56 \pm 0.05 \text{ for box IC } (\mathrm{m} = 0, \pm 1)\,, \\ \alpha &= 1.77 \pm 0.06 \text{ for polar IC } (\mathrm{m} = 0)\,, \end{aligned} \tag{6.4}$$

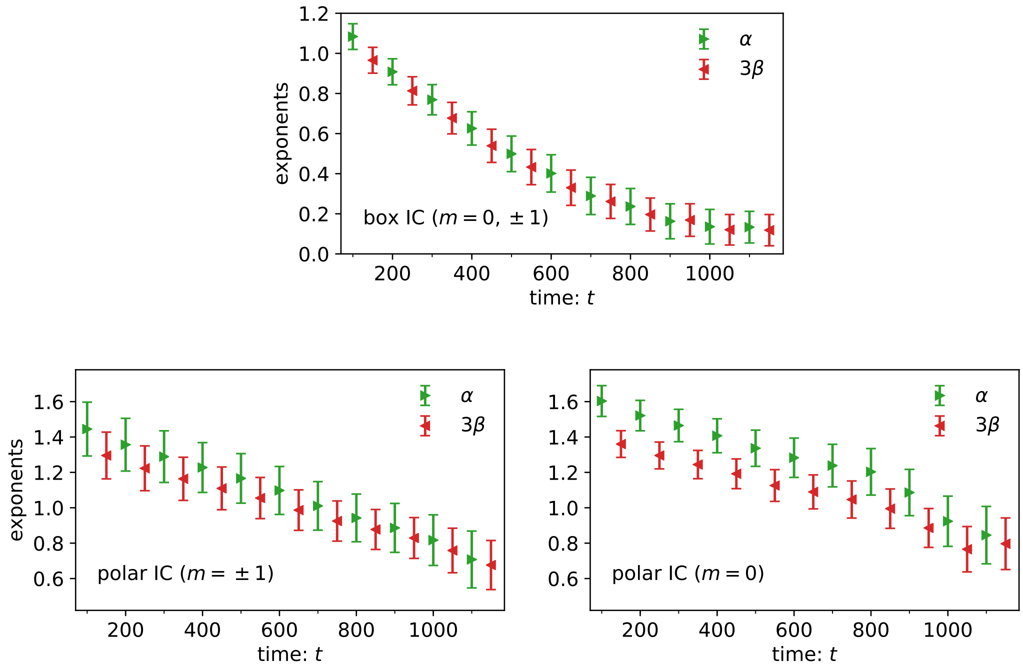

Figure 6.4: Time-dependent scaling exponents $\alpha(t)$ and $\beta(t)$ for box initial conditions (top) and polar initial conditions (bottom row). The presented exponents correspond to the average values obtained for reference times $t_{\text{ref}} = 1300, 1325, 1350$.

$$\alpha = 2.33 \pm 0.07 \text{ for polar IC } (\mathrm{m} = \pm 1)\,.$$

For polar initial conditions the growth rate differs for the magnetic sublevels $m = 0$ and $m = \pm 1$ at early times because a redistribution of particles between the three sublevels occurs. Generally, we find that the power-law growth is stronger than for box initial conditions. At intermediate times in the range $450 \lesssim t \lesssim 1000$, the growth of all sublevels becomes similar and agrees approximately with the exponent α determined for box initial conditions. Finally we note that the exponent α obtained for box initial conditions is comparable to the universal scaling exponent α found for $U(N)$-symmetric Bose gases in three dimensions, where previous studies determined $\alpha = 1.66 \pm 0.12$ for $N = 1$ [32] and $\alpha = 1.62 \pm 0.37$ for $N = 3$ [36].

6.3.3 Postscaling

Recent studies show that systems can establish certain nonequilibrium scaling features while others still deviate from their universal scaling characteristics [23, 37]. The phenomenon of *prescaling* occurs if the distribution function is already governed by the scaling function f_S even before the scaling according to (6.1) emerges. During the stage of prescaling, the time evolution of the distribution function can be described in terms of f_S and time-dependent scaling exponents, which become universal as the system approaches the scaling regime.

In the spin-1 Bose gas we observe that the occupation number distribution function has a similar shape for a wide range of times. However, the discussion of the previous section pointed out that the system does not approach a universal scaling regime characterized by (6.1) but rather quickly leaves the power-law regime. We therefore study the effect of *postscaling* where the time evolution of the

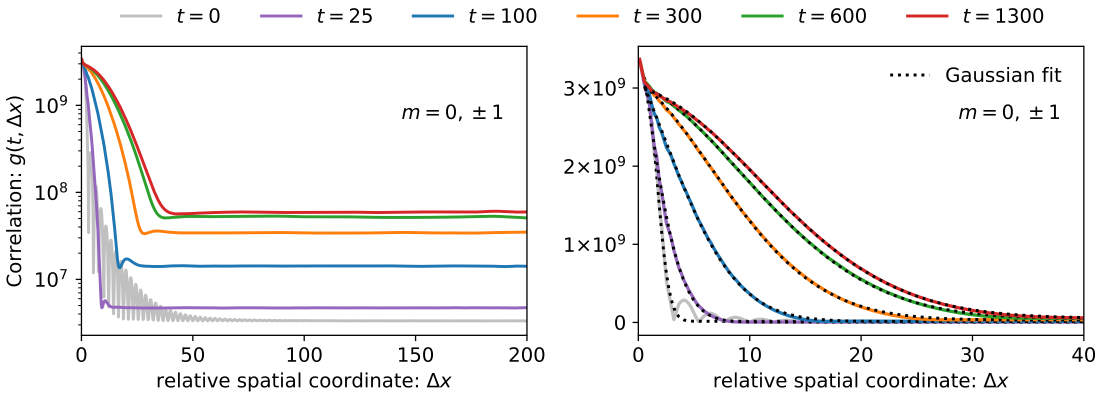

Figure 6.5: Time evolution of the correlation function $g(t, \Delta x)$ for box initial conditions, where $g(t, \Delta) = \frac{1}{2}\sum_m g_m(t, \Delta x)$ is the average over magnetic sublevels $m = 0, \pm 1$. The correlation is normalized such that the total particle number is $N_{\mathrm{tot}} = 3\,g(t, \Delta x = 0) \simeq 10^{10}$. The logarithmic plot on the left-hand side shows the long-range behavior while the linear plot on the right-hand side shows a Gaussian fit to the small-range behavior. The constant long-range correlations indicate the formation of a condensate.

distribution function is governed by a universal scaling function f_S according to

$$f(t, k) = t^{-\alpha(t)} f_S\left(t^{\beta(t)} k\right) , \tag{6.5}$$

with time-dependent scaling exponents $\alpha(t)$ and $\beta(t)$. In this prescription the distributions can be rescaled such that the functions at different times lie on top of each other. The right columns of Figures 6.1 and 6.2 show the rescaled occupation number $f_{\mathrm{rsc}}(t, k) = (t/t_{\mathrm{ref}})^{-\alpha} f(t, k)$, where $k_{\mathrm{rsc}} = (t/t_{\mathrm{ref}})^{\beta} k$ is the rescaled momentum and α, β are time-dependent scaling exponents. For box initial conditions the distribution function reveals the same shape for a wide range of times, while for polar initial conditions good agreement is found for the $m = 0$ sublevel while the $m = \pm 1$ sublevels only become self-similar at late times.

Observing that the dynamics slows down considerably during the evolution, we expect that the exponents $\alpha(t)$ and $\beta(t)$ in (6.5) decrease with time. We determine the time-dependent scaling exponents by comparing the distribution at a time t with the distribution at some reference time t_{ref} at late times, at which the distribution function is almost stationary. We use several reference times t_{ref} in order to extract the exponents at given time t. For details about the extraction of scaling exponents, we refer to Appendix 6.C. Figure 6.4 shows the scaling exponents extracted from our numerical data. As expected, the considerable slow-down of the dynamics and the almost stationary distribution functions at late times are reflected in decreasing values of the scaling exponents. For box initial conditions, we find that the exponents become almost zero at late times. In the case of polar initial conditions, the system needs more time to reach the stationary regime, as can be seen in Figure 6.3, such that the exponents have larger values than in the case of box initial conditions.

6.3.4 Condensation

The approach of a constant infrared occupation at late times is reminiscent of the formation of a condensate far from equilibrium as has been previously observed in relativistic and nonrelativistic scalar field theories [32, 140]. The correlation function describing the occupation number can contain

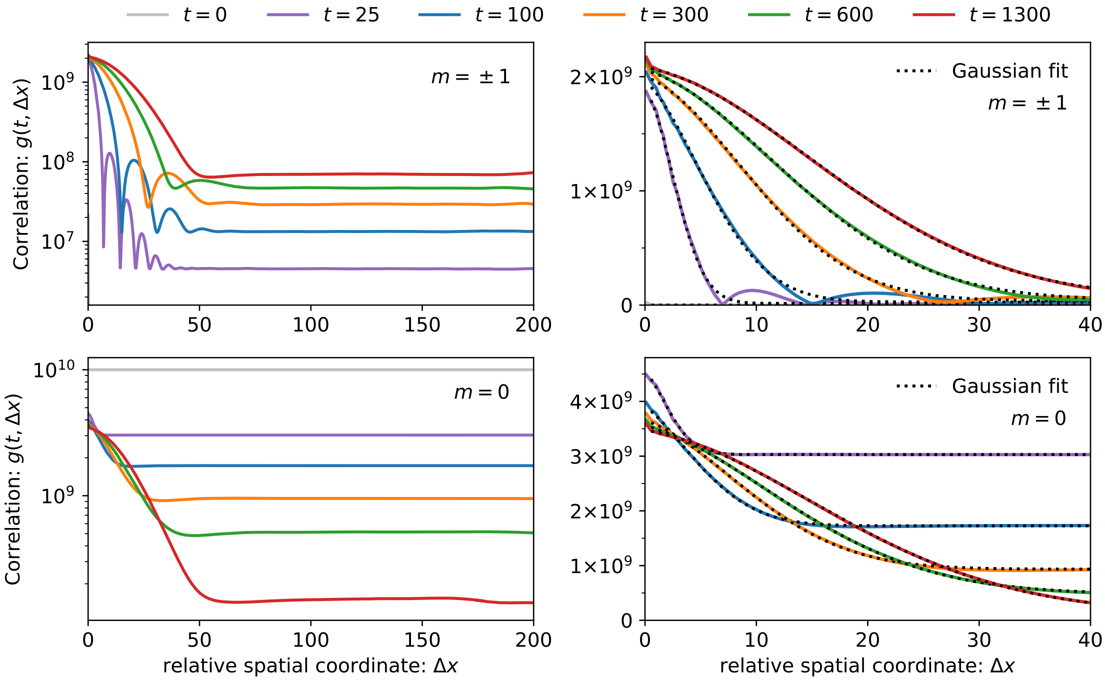

Figure 6.6: Time evolution of the correlation function $g(t,\Delta x)$ for box initial conditions, where $g(t,\Delta) = \frac{1}{2}\sum_m g_m(t,\Delta x)$ is the average over magnetic sublevels $m = 0, \pm 1$. The correlation is normalized such that the total particle number is $N_{\text{tot}} = 3\,g(t,\Delta x = 0) \simeq 10^10$. The logarithmic plot on the left-hand side shows the long-range behavior while the linear plot on the right-hand side shows a Gaussian fit to the small-range behavior. The constant long-range correlations indicate the formation of a condensate.

a condensate fraction that scales proportional to the system size and describes correlations filling the entire volume of the system. Since the condensate fraction is proportional to the volume V of the system, the ratio of condensate fraction and volume becomes independent of V when a condensate is formed [140]. For relativistic and nonrelativistic scalar field theories, it is known that condensation occurs in the nonequilibrium evolution following box initial conditions [32, 140].

Here, we employ a more direct tool to investigate the formation of a condensate far from equilibrium. We study the (dimensionless) correlation function

$$g_m(t,\Delta\mathbf{x}) = V\,\langle\psi_m^*(t',\mathbf{x}-\Delta\mathbf{x})\psi_m(t,\mathbf{x})\rangle\ , \tag{6.6}$$

where $\langle\cdot\rangle$ denotes the ensemble average, $\psi_m(t,\mathbf{x})$ the field component with magnetic sublevel m, and V the volume of the system. In our spatially homogeneous system, the correlation function only depends on the relative spatial coordinate $\Delta\mathbf{x}$ of the fields. The particle number of magnetic sublevel m is obtained from the correlation function at $\Delta\mathbf{x} = \mathbf{0}$, $N_{\text{tot}} = \sum_m g_m(t,\mathbf{0}) = V\sum_m |\psi_m(t,\mathbf{x})|^2$. Numerically, we compute the correlation function by a Fourier transform of the distribution function (6.3) according to $g_m(t,\Delta\mathbf{x}) = V\int \mathrm{d}^3k/(2\pi)^3\, f(t,\mathbf{k})e^{i\mathbf{k}\Delta\mathbf{x}}$. Making use of the isotropy of the system, we calculate the average over the solid angle in three dimensions such that the correlator only depends on the radial distance $\Delta x = |\Delta \mathbf{x}|$.

Bose-Einstein condensation is identified with a constant nonzero limit of g_m when Δx tends to infinity [155], i.e.

$$\lim_{\Delta x \to \infty} g_m(t, \Delta x) = N_C\,, \tag{6.7}$$

where N_C is a constant that determines the condensate fraction. For a nondegenerate ideal atomic gas, the correlation function g_m is a Gaussian function that decays to zero over a distance of the order of the thermal wavelength [156].

We find that the correlation function $g_m(t, \Delta x)$ is described by a Gaussian function at small relative coordinates Δx, while becoming constant at long distances Δx. In Figures 6.5 and 6.6 we plot the correlation functions obtained for box and polar initial conditions, respectively. In the following, we briefly outline the most relevant features of the correlation function at $\Delta x = 0$, for short ranges $\Delta x \lesssim 50$, and for long ranges $\Delta x \gtrsim 50$.

At $\Delta x = 0$ the correlation function (6.6) corresponds to the total number of particles in the magnetic sublevel m, which we denote by N_m. For box initial conditions, the number of particles in each of the three magnetic sublevels is $\frac{1}{3}N_{\mathrm{tot}}$. For polar initial conditions, at initial time all particles are contained in the $m = 0$ magnetic sublevel (gray line in the lower left plot of Figure 6.6) while the magnetic sublevels $m = \pm 1$ only contain particles from the Wigner noise. The initial-time correlation function of the $m = \pm 1$ sublevels is not shown in the upper left plot of Figure 6.6 because it is a few orders of magnitude smaller than the correlation function at later times.

In the short-range regime of $0 < \Delta x \lesssim 50$ we perform a Gaussian fit described by

$$G(\Delta x) = \frac{A}{\sqrt{2\pi\sigma^2}} \exp\left[-\frac{(\Delta x - \mu)^2}{2\sigma^2}\right] + C \tag{6.8}$$

to our numerically computed correlation function. Here A is a normalization constant, σ^2 the variance, μ the central position, and C a constant offset. As can be seen from the plots on the right-hand sides of Figures 6.5 and 6.6, the short-range behavior of the correlation function is well captured by a Gaussian function. This reveals that our system contains a fraction of uncondensed particles, which in momentum space is associated to a thermal tail at large momenta k.

In the long-range regime with $\Delta x \gtrsim 50$, we find that the correlation function is constant. This long-range order behavior indicates the formation of a condensate far from equilibrium. We denote the constant long-range value of the correlation function by $N_{C,m} = g_m(t, \Delta x \gg 1)$ such that the ratio $N_{m,C}/N_m$, with N_m being the total particle number in magnetic sublevel m, determines the fraction of condensed particles in sublevel m of the system. For box initial conditions we find that the inverse particle cascade leads to a growth of the condensate fraction with time until it reaches a constant fraction of about 1.8% at late times. The polar initial state with all particles contained in the $k = 0$ momentum mode of the $m = 0$ magnetic sublevel corresponds to a condensate in the $m = 0$ sublevel. Hence, we find a constant correlation function (see gray line in lower left plot of Figure 6.6) with a condensate fraction of 100%. As particles are redistributed between the magnetic sublevels, the condensate fraction in the $m = 0$ sublevel decreases while it increases in the $m = \pm 1$ sublevels. At late times, the condensate fractions are about 4.1% and 3.2% for $m = 0$ and $m = \pm 1$, respectively.

6.4 Conclusion

In this chapter we investigated the self-similar scaling properties and the formation of a condensate in a spin-1 Bose gas. Employing classical-statistical simulation methods, we studied the far-from equilibrium time evolution starting from different overoccupied initial states.

We find that the system transiently passes a regime where the occupation number in the infrared momentum range grows with t^{α}, where the constant exponent α is comparable to the universal scaling exponents found in scalar Bose gases. Since the shape of the distribution function is still changing in this regime, we conclude that the system does not approach the scaling regime characterized by universal self-similar scaling. Nevertheless, the distribution function is self-similar for a wide range of times and momenta, and its time evolution can be described by a universal scaling function, however, with time-dependent scaling exponents. As opposed to the phenomenon of prescaling, here we observe that certain universal scaling properties are realized after the system has left the regime of the power-law scaling with t^{α} and refer to this as postscaling. Our observations show that the spin-1 Bose gas with strong ferromagnetic spin-spin interactions evolves differently than $U(N)$-symmetric Bose gases, where overoccupied initial conditions lead to the approach of a scaling regime associated to nonthermal fixed points.

The interactions in our system lead to a quick buildup of long-range correlations and hence the formation of a condensate far from equilibrium. This phenomenon has previously been observed in relativistic and nonrelativistic scalar field theories, where it was studied in momentum space. Here we investigate the correlation function in coordinate space, which also provides access to the fraction of condensed particles in the system. While we observe nonthermal condensation in the field correlation function for both box and polar initial conditions, future investigations should also take into account spin correlation functions.

Finally, we emphasize that we consider the special case where density and ferromagnetic spin interactions have the same coupling strength. For this case the quick formation of a nonthermal condensate seems to prevent the establishment of self-similar scaling and hence the approach of a nonthermal fixed point. It remains an open question to clarify and possibly quantify the influence of spin-dependent interactions on the path that nonequilibrium time evolution takes. In particular, our analysis suggests that the spin interactions enhance the emergence of long-range correlations, thus leading to fast condensation.

Chapter 7

Conclusion

In this thesis we investigated the relaxation dynamics of various isolated quantum systems driven out of equilibrium. The nonequilibrium dynamics of these systems along with the approach to nonthermal fixed points or thermal equilibrium were studied by means of numerical simulations. We conclude with a summary of our work and an outlook on prospective research in this field.

7.1 Summary

The analyses in this thesis concern three different physical systems, the relativistic scalar field theory, the quark-meson model, and the spin-1 Bose gas, for which theoretical background is provided in Chapters 2 and 5. The results of this thesis contribute to theoretical investigations of quantum field theory out of equilibrium in terms of real-time simulations of nonequilibrium dynamics. We probe important observables, like distribution functions or excitation spectra, out of equilibrium by computing the time evolution of fields and correlations. Chapters 3 and 6 are concerned with the far-from-equilibrium dynamics in the vicinity of a nonthermal fixed point while Chapter 4 studies the approach to thermal equilibrium.

In Chapter 3 we numerically compute the time evolution of a relativistic N-component scalar field theory using evolution equations obtained from the two-particle irreducible (2PI) effective action at next-to-leading order (NLO) in an expansion in $1/N$, which allows us to consider couplings beyond the weak-coupling regime. We determine the universal scaling exponents characterizing the self-similar time evolution of the particle distribution and the effective four-vertex, for which we find values $\alpha = 1.6 \pm 0.08\,, \beta = 0.59 \pm 0.02$ and $\alpha_\lambda = -2.01 \pm 0.42\,, \beta_\lambda = 0.67 \pm 0.02$ (for coupling $\lambda = 1.0$), respectively. The scaling exponents are comparable for a wide range of couplings, even for nonperturbative couplings beyond the range of validity of classical-statistical simulations. Phenomenologically, extreme conditions beyond the limit of weak interactions arise in the context of heavy-ion collisions, where the relevant gauge coupling is expected to be neither particularly small nor large at early times. Our results may be helpful in understanding dynamical aspects of gauge theories far from equilibrium since universality between highly occupied scalar and gauge field dynamics has been observed for weak couplings [27]. In addition, we compute the frequency spectrum of spectral and statistical functions by taking into account unequal-time two-point correlation functions. We observe that strong violations of the fluctuation-dissipation relation occur in the nonperturbative infrared momentum range. This manifests that the system is not thermal in the scaling regime, and challenges effective kinetic descriptions based on the fluctuation-dissipation relation.

Chapter 4 is concerned with the thermalization process of the quark-meson model. Our numerical simulations based on 2PI effective action techniques not only include the dynamics of the order parameter of chiral symmetry but also the spectral functions of quarks and mesons. We show that the system thermalizes into different regions of its phase diagram, where the approach of thermal states is characterized by the emergence of the fluctuation-dissipation relation and an effective memory loss about the details of the initial state. The properties of the intermediate stages, however, depend on the initial conditions and involve different trajectories for the redistribution of energy and particles. We recover the crossover transition from the phase with broken chiral symmetry to the phase with restored chiral symmetry in terms of order parameters deduced from the one-point and two-point correlation functions of the system.

In Chapter 6 the time evolution of a spin-1 Bose gas is studied using classical-statistical simulations. For the considered case of strong spin-spin interactions, the system quickly approaches a regime where the occupation numbers become almost stationary. During the time evolution, the system reveals certain scaling properties but does not converge to the proper scaling regime, where relevant observables are solely characterized by universal scaling functions and universal scaling exponents. Instead we find that the distribution functions can be described by universal scaling functions with time-dependent scaling exponents reflecting the deceleration of the dynamics. The slowdown of the evolution is accompanied by the emergence of long-range correlations indicating the formation of a condensate out of equilibrium.

7.2 Outlook

Although substantial progress has been made in the recent years, understanding the relaxation dynamics of isolated quantum systems still poses a challenge for theory. The analysis of effective theories and the concept of universality provide the opportunity to study systems which may be otherwise out of reach. Our theoretical work employing numerical simulations contributes to the understanding of dynamical properties in active fields of research like ultracold atomic gases or heavy-ion collisions. In the following, we outline open questions and prospective research activities in these fields.

Our analysis of the relativistic scalar field theory invites for further exploration of the far-from-equilibrium dynamics at nonthermal fixed points. On the one hand, our results for scalar fields could contribute to the understanding of dynamical aspects of gauge theories far from equilibrium. Thereby an important task for the future is to investigate whether the universality between highly occupied scalar and gauge field theories, which so far is known for weak couplings [27], also holds beyond the weak-coupling limit. On the other hand, direct comparisons to the dynamics of ultracold atomic gases out of equilibrium are possible as the relativistic scalar field theory behaves nonrelativistically in the infrared momentum range. Knowing that relativistic and nonrelativistic scalar field theories belong to the same universality class, one may carry our results over to nonrelativistic systems.

Our work on relativistic scalar fields shows that unequal-time spectral and statistical functions contain additional information about the system. Similar conclusions are drawn in investigations using classical-statistical simulations [87]. Hence, one is strongly encouraged to also study unequal-time correlation functions in other systems. While spectral functions have been investigated in scalar Bose gases using classical-statistical simulations [86], similar studies on spinor Bose gases are still pending. Computing statistical and spectral functions in classical-statistical simulations of spinor Bose gases is an important next step to improve our understanding of ongoing ultracold atom experiments. It sheds light on open questions regarding the fluctuation-dissipation theorem as well as the excitation spectrum of such systems. These prospective investigations are accompanied by theoretical and experimental efforts in the development of measurement protocols for unequal-time correlation functions [157, 158].

Furthermore, our analysis on the relativistic scalar field theory also constitutes one of the first works accessing the (effective) four-vertex in a quantum field theory out of equilibrium. The results in [75] and our findings show a strong suppression of the vertex function in the strongly-correlated infrared regime. Future studies on four-point functions possibly open new pathways to the dynamical properties of a system and provide new opportunities for the description of out-of-equilibrium dynamics in quantum field theories.

Utilizing effective field theories, our work on the quark-meson model touches two of the most pressing topics in ongoing heavy-ion programs: the thermalization process of the quark-gluon plasma and the phase diagram of quantum chromodynamics (QCD). Our analysis at zero baryon chemical potential traces the relaxation trajectories with final states along the crossover transition between chiral symmetric and broken regimes of the quark-meson model. However, our work constitutes only a first step. The particularly promising feature of the quark-meson model is that – in contrast to other approaches like lattice QCD – it can be extended to nonzero baryon chemical potential by adding a term $\bar{\psi}\mu\gamma_0\psi$ to the action, with chemical potential μ and gamma matrix γ_0. Hence, it is possible to study dynamical properties at the critical end point in the phase diagram of the quark-meson model, which may provide important insight about the conjectured critical point in the QCD phase diagram.

Our observations regarding the time evolution of the spin-1 Bose gas motivate for further theoretical and experimental studies. The numerical results obtained for the distribution function suggest that the system quickly builds up a condensate. In the future, simulations with different system sizes can shed light on whether and how condensation takes place. Further simulations could also take into account different strengths for the spin-spin interaction. Our analysis of ferromagnetic spin-spin interactions characterized by a coupling strength $c_1 = -c_0$, with c_0 being the coupling constant of repulsive density-density interactions, shows that the time evolution quickly slows down without approaching a transient self-similar scaling regime. Future theoretical efforts may show whether and how the phenomenon of dynamical scaling depends on interaction strengths. One is particularly interested in scenarios with realistic experimental coupling ratios c_0/c_1. At the same time, upcoming experiments exploit Feshbach resonances to control the interaction between atoms in ultracold quantum gases and may provide further insight.

Future work also involves the development and employment of other simulation methods. One is interested in methods that can deal with couplings beyond the weak-coupling limit, which may allow for the exploration of new interesting regimes. Furthermore, it is desirable to study the approach to quantum thermal equilibrium, which cannot be simulated using classical-statistical methods.

Appendix to Chapter 3

3.A The free scalar field theory

In this appendix we discuss the 2PI formalism for the *free*, i.e. noninteracting and therefore exactly solvable, relativistic scalar field theory in homogeneous and isotropic space. We consider the $O(N)$-symmetric theory (2.49) with coupling λ set to zero, i.e. the classical action

$$S[\varphi] = \int_x \left[\frac{1}{2}\partial^\mu \varphi_a(x) \partial_\mu \varphi_a(x) - \frac{1}{2} m^2 \varphi_a(x) \varphi_a(x) \right] , \tag{3.27}$$

with field index $a = 1, \ldots, N$ and bare mass m. We focus on the 2PI approach and refer to standard textbooks, e.g. [44], for a general discussion of scalar quantum fields.

3.A.1 Free-field solutions

Since the self-energies are zero for vanishing coupling, the equations of motion for the one-point and two-point functions can be obtained from the exact 2PI evolution equations (2.77) by setting the right-hand sides to zero. Consequently, the time evolution of the macroscopic field as well as the spectral and statistical functions is governed by simple harmonic oscillator equations,

$$\left(\partial_t^2 + m^2\right) \phi(t) = 0 \,, \tag{3.28a}$$

$$\left(\partial_t^2 + \omega_{\mathbf{p}}^2\right) F(t,t',|\mathbf{p}|) = 0 \,, \tag{3.28b}$$

$$\left(\partial_t^2 + \omega_{\mathbf{p}}^2\right) \rho(t,t',|\mathbf{p}|) = 0 \,, \tag{3.28c}$$

with $\omega_{\mathbf{p}} = \sqrt{\mathbf{p}^2 + m^2}$. We omit the indices $\perp$ and $\parallel$ of F and ρ since there is no coupling between the longitudinal and transverse sectors for vanishing self-energies.

The field equation can be solved by $\phi(t) = \phi_0 \cos(mt) + \dot{\phi}_0 \sin(mt)$ where the constants $\phi_0 = \phi(t=0)$ and $\dot{\phi}_0 = \partial_t \phi(t)\big|_{t=0}$ depend on the initial conditions. The solutions for the spectral and statistical functions can be written down as linear combinations of $\sin\left[\omega_{\mathbf{p}}(t-t')\right]$ and $\cos\left[\omega_{\mathbf{p}}(t-t')\right]$. Since the statistical (spectral) function is (anti)symmetric upon exchange of t and t', it can only contain the cosine (sine) contribution.

While the solution of the free spectral function is fully determined by the symmetry and the normalization condition posed by the bosonic commutation relations (2.70), the solution of the statistical function can be written such that it corresponds to the thermal propagator. Then the free-field solutions for the statistical and spectral functions are given by [59, 85]

$$F(t,t',|\mathbf{p}|) = \frac{f_{\mathbf{p}} + \frac{1}{2}}{\omega_{\mathbf{p}}} \cos\left[\omega_{\mathbf{p}}(t-t')\right] \,, \tag{3.29a}$$

$$\rho(t, t', |\mathbf{p}|) = \frac{1}{\omega_{\mathbf{p}}} \ \sin\left[\omega_{\mathbf{p}}(t - t')\right] \ , \tag{3.29b}$$

with dispersion relation $\omega_{\mathbf{p}}$ and particle distribution $f_{\mathbf{p}}$. In thermal equilibrium, two-point functions are time-translation invariant, i.e. they only depend on the relative time $\Delta t = t - t'$, and can be Fourier transformed with respect to Δt. The corresponding expressions in frequency space read

$$F(\omega, |\mathbf{p}|) = \pi \ \frac{f_{\mathbf{p}} + \frac{1}{2}}{\omega_{\mathbf{p}}} \left[\delta(\omega - \omega_{\mathbf{p}}) + \delta(\omega + \omega_{\mathbf{p}})\right] \ , \tag{3.30a}$$

$$\rho(\omega, |\mathbf{p}|) = \pi \ \frac{i}{\omega_{\mathbf{p}}} \left[\delta(\omega - \omega_{\mathbf{p}}) - \delta(\omega + \omega_{\mathbf{p}})\right] = i \ \underbrace{2\pi \, \mathrm{sgn}(\omega) \delta(\omega^2 - \omega_{\mathbf{p}}^2)}_{\tilde{\rho}(\omega, \mathbf{p})} , \tag{3.30b}$$

where we define the real spectral function $\tilde{\rho}(\omega, |\mathbf{p}|)$ in analogy to (3.18b) by using the identity

$$\delta(x^2 - a^2) = \frac{1}{2|a|} \left[\delta(x - a) + \delta(x + a)\right] \ . \tag{3.31}$$

From (3.30) we see that in the free theory the spectral and statistical functions are both determined by δ-peaks in frequency space, which manifest the on-shell relation $\omega = \pm\omega_{\mathbf{p}}$. These peaks are interpreted as bound states corresponding to well-defined particles with dispersion relation $\omega_{\mathbf{p}} = \sqrt{\mathbf{p}^2 + m^2}$. We note that the peaks obtain a finite width in the interacting theory. For exponentially decaying correlation functions, the frequency-space propagators have the shape of a relativistic Breit-Wigner function.

The frequency-space solutions (3.30) suffice the fluctuation-dissipation relation (3.21) for a thermal distribution function, i.e. $f_{\mathbf{p}} = f_{\mathrm{BE}}(\omega = \omega_{\mathbf{p}})$ with f_{BE} being the Bose-Einstein distribution. This follows straightforward noting that the Bose-Einstein distribution fulfills

$$f_{\mathrm{BE}}(\omega) + \frac{1}{2} = -\Big[f_{\mathrm{BE}}(-\omega) + \frac{1}{2}\Big] \, , \tag{3.32}$$

which can be easily proven by inserting the expression $f_{\mathrm{BE}}(\omega) = (e^{\beta\omega} - 1)^{-1}$ explicitly.

3.A.2 Particle distribution

In the free theory, the field can be expanded in terms of creation and annihilation operators that describe particles as field excitations created from the vacuum, the state of lowest energy. This interpretation of field excitations as particles allows us to define a particle number distribution. There exist different definitions that agree with each other in the free theory but not necessarily in the interacting case. In the following, we outline equal-time and unequal-time definitions for the free scalar field. Thereby we emphasize that particle number is not conserved in any relativistic quantum field theory, since the relativistic dispersion relation $\omega_{\mathbf{p}}^2 = \mathbf{p}^2 + m^2$ implies that energy can be converted into particles and vice versa.

Using the free-field solution (3.29a) one can define a distribution function $f(t, |\mathbf{p}|)$ and a dispersion $\omega(t, |\mathbf{p}|)$ according to [32]

$$F(t, t, |\mathbf{p}|) \equiv \frac{f(t, |\mathbf{p}|) + \frac{1}{2}}{\omega(t, |\mathbf{p}|)} \, . \tag{3.33}$$

This expression allows us to identify the definitions of the equal-time distribution function (3.8) and the equal-time dispersion relation (3.9) employed in the main text,

$$f(t,|\mathbf{p}|) + \frac{1}{2} = \sqrt{F(t,t',|\mathbf{p}|)\partial_t\partial_{t'}F(t,t',|\mathbf{p}|)}\,\Big|_{t=t'}\,,$$

$$\omega(t,|\mathbf{p}|) = \sqrt{\frac{\partial_t\partial_{t'}F(t,t',|\mathbf{p}|)}{F(t,t',|\mathbf{p}|)}}\,\Bigg|_{t=t'}\,,$$

where one recovers $f(t,|\mathbf{p}|) = f_\mathbf{p}$ and $\omega(t,|\mathbf{p}|) = \omega_\mathbf{p}$ in the free theory. Out of equilibrium, these equal-time definitions can provide an extremely useful quasiparticle interpretation [32, 41, 60].

Another useful definition of a particle distribution originates from kinetic theory where the general dependence of a two-point function on the two coordinates (x, y) is phrased in terms of the center-of-mass coordinate $X = (x + y)/2$ and the relative coordinate $s = x - y$, the latter being equivalent to the Fourier mode p. We define the distribution function $f(X, p)$ by the relation

$$F(X,p) = -i\Big(f(X,p) + \frac{1}{2}\Big)\rho(X,p)\,, \tag{3.34}$$

which in thermal translation invariant theories reduces to the fluctuation-dissipation theorem (3.21). Using the symmetry properties $F(X, p) = F(X, -p)$ and $\rho(X, p) = -\rho(X, -p)$ we obtain the relation

$$f(X,p) + \frac{1}{2} = -\Big[f(X,-p) + \frac{1}{2}\Big]\,, \tag{3.35}$$

a generalized version of (3.32). In the free theory, where the dependence on the central coordinate is absent, we can do the replacement $F(X, p) \to F(p) = F(\omega, \mathbf{p})$ and proceed accordingly for ρ. Motivated by the free-field solution of F in frequency space (3.30a), we define the particle distribution $f(\mathbf{p})$ by the relation

$$f(\mathbf{p}) + \frac{1}{2} \equiv \int_0^\infty \frac{\mathrm{d}\omega}{2\pi}\, 2\,\omega\, F(\omega,\mathbf{p})\,, \tag{3.36}$$

where the ω in the integrand arises from the factor of $1/\omega$ in (3.33), which originates from the second-order time derivative in the relativistic theory. This definition complies with the free equilibrium case as can be shown by the following short computation,

$$\begin{aligned}
f(\mathbf{p}) + \frac{1}{2} &= \int_{-\infty}^\infty \frac{\mathrm{d}\omega}{2\pi}\,\omega\,\pi\,\frac{f_\mathrm{BE}(\omega)+\frac{1}{2}}{\omega_\mathbf{p}}\,\left[\delta(\omega-\omega_\mathbf{p}) + \delta(\omega+\omega_\mathbf{p})\right] \\
&= \frac{1}{2}\left[(+\omega_\mathbf{p})\frac{f_\mathrm{BE}(\omega_\mathbf{p})+\frac{1}{2}}{\omega_\mathbf{p}} + (-\omega_\mathbf{p})\frac{f_\mathrm{BE}(-\omega_\mathbf{p})+\frac{1}{2}}{\omega_\mathbf{p}}\right] \\
&= f_\mathrm{BE}(\omega_\mathbf{p}) + \frac{1}{2}\,,
\end{aligned} \tag{3.37}$$

where we used (3.32) to obtain the last equality. Definition (3.36) can be generalized to nonequilibrium interacting setups by including the time-dependence of the statistical function [31, 32],

$$f(t=\tau,\mathbf{p}) + \frac{1}{2} = \int_0^\infty \frac{\mathrm{d}\omega}{2\pi}\, 2\omega\, F(\tau,\omega,\mathbf{p})\,, \tag{3.38}$$

where $\tau = X^0 = (t + t')/2$ denotes the central time.

3.A.3 Mode energy

In this section we briefly outline the mode energy distribution for the free scalar field theory. We consider the case of a vanishing macroscopic field, where the $O(N)$ symmetry allows for rotations such that the propagators become diagonal in field space and the statistical propagator can be written as $F_{ab} = F\delta_{ab}$ with $F_{aa} = NF$.

For this setup, the mode energy density (2.99) derived from the energy-momentum tensor reduces to

$$\varepsilon^{\phi}(t, |\mathbf{p}|) = \frac{1}{2} N \left[\partial_t \partial_{t'} F(t, t', |\mathbf{p}|) \Big|_{t=t'} + \omega_{\mathbf{p}}^2 F(t, t, |\mathbf{p}|) \right] , \tag{3.39}$$

where again $\omega_{\mathbf{p}} = \sqrt{\mathbf{p}^2 + m^2}$. If we insert the free-field statistical function (3.29a) into this expression, we find $\varepsilon^{\phi}(t, |\mathbf{p}|) = N\omega_{\mathbf{p}}^2 F(t, t, |\mathbf{p}|) = N\omega_{\mathbf{p}}(f_{\mathbf{p}} + \frac{1}{2})$, which in accordance to (3.12) can be written as

$$\varepsilon^{\phi}(t, |\mathbf{p}|) = N \left[f(t, |\mathbf{p}|) + \frac{1}{2} \right] \omega(t, |\mathbf{p}|) \, . \tag{3.40}$$

This relation holds in the free equilibrium situation with $f(t, \mathbf{p}) = f_{\mathbf{p}}$ and $\omega(t, \mathbf{p}) = \omega_{\mathbf{p}}$. It allows us to define the equal-time quasiparticle energy density

$$\frac{\varepsilon(t)}{N} \equiv \int_{\mathbf{p}} \left[f(t, |\mathbf{p}|) + \frac{1}{2} \right] \omega(t, |\mathbf{p}|) \, , \tag{3.41}$$

where the quantum half can be neglected if occupancies are large.

3.A.4 Wigner transformation

For the free-field statistical and spectral functions (3.29) it is possible to compute the Wigner transforms (3.18) analytically. One obtains

$$F(\tau, \omega, \mathbf{p}) = \frac{f_{\mathbf{p}} + \frac{1}{2}}{\omega_{\mathbf{p}}} \left[\frac{\sin\left[(\omega - \omega_{\mathbf{p}})2\tau\right]}{\omega - \omega_{\mathbf{p}}} + \frac{\sin\left[(\omega + \omega_{\mathbf{p}})2\tau\right]}{\omega + \omega_{\mathbf{p}}} \right] , \tag{3.42a}$$

$$\tilde{\rho}(\tau, \omega, \mathbf{p}) = \frac{1}{\omega_{\mathbf{p}}} \left[\frac{\sin\left[(\omega - \omega_{\mathbf{p}})2\tau\right]}{\omega - \omega_{\mathbf{p}}} - \frac{\sin\left[(\omega + \omega_{\mathbf{p}})2\tau\right]}{\omega + \omega_{\mathbf{p}}} \right] . \tag{3.42b}$$

For finite τ, the Wigner space two-point functions are rapidly oscillating in ω with an envelope peaked around $\omega = \pm\omega_{\mathbf{p}}$. In the limit $\tau \to \infty$ the Wigner transforms (3.42) approach the δ-functions given in (3.30), which follows straightforwardly from

$$\lim_{\varepsilon \to 0} \frac{\sin\left[(x - a)\varepsilon^{-1}\right]}{x} = \pi \, \delta(x - a) \, . \tag{3.43}$$

For completeness, we provide the explicit calculation of the Wigner transforms,

$$\begin{aligned} F(\tau, \omega, \mathbf{p}) &= \frac{f_{\mathbf{p}} + \frac{1}{2}}{\omega_{\mathbf{p}}} \int_{-2\tau}^{2\tau} \mathrm{d}\Delta t \; e^{i\omega\Delta t} \cos(\omega_{\mathbf{p}}\Delta t) \\ &= \frac{f_{\mathbf{p}} + \frac{1}{2}}{\omega_{\mathbf{p}}} \int_{-2\tau}^{2\tau} \mathrm{d}\Delta t \; \left[\cos(\omega\Delta t)\cos(\omega_{\mathbf{p}}\Delta t) + \underbrace{i \sin(\omega\Delta t)\cos(\omega_{\mathbf{p}}\Delta t)}_{\text{antisymmetric in } \Delta t} \right] \end{aligned}$$

$$\begin{aligned}
&= \frac{f_{\mathbf{p}} + \frac{1}{2}}{2\omega_{\mathbf{p}}} \left[\frac{\sin\left[(\omega - \omega_{\mathbf{p}})\Delta t\right]}{\omega - \omega_{\mathbf{p}}} + \frac{\sin\left[(\omega + \omega_{\mathbf{p}})\Delta t\right]}{\omega + \omega_{\mathbf{p}}} \right]_{-2\tau}^{2\tau} \\
\rho(\tau, \omega, \mathbf{p}) &= \frac{1}{\omega_{\mathbf{p}}} \int_{-2\tau}^{2\tau} \mathrm{d}\Delta t \; e^{i\omega\Delta t} \sin(\omega_{\mathbf{p}}\Delta t) \\
&= \frac{1}{\omega_{\mathbf{p}}} \int_{-2\tau}^{2\tau} \mathrm{d}\Delta t \; \left[\underbrace{\cos(\omega\Delta t)\sin(\omega_{\mathbf{p}}\Delta t)}_{\text{antisymmetric in } s} + i \sin(\omega\Delta t)\sin(\omega_{\mathbf{p}}\Delta t) \right] , \\
&= \frac{i}{2\omega_{\mathbf{p}}} \left[\frac{\sin\left[(\omega - \omega_{\mathbf{p}})\Delta t\right]}{\omega - \omega_{\mathbf{p}}} - \frac{\sin\left[(\omega + \omega_{\mathbf{p}})\Delta t\right]}{\omega + \omega_{\mathbf{p}}} \right]_{-2\tau}^{2\tau} ,
\end{aligned}$$

where it is convenient to employ the integral formulas

$$\int \mathrm{d}x \;\; \sin(ax)\sin(bx) = \frac{\sin\left[(a-b)x\right]}{2(a-b)} - \frac{\sin\left[(a+b)x\right]}{2(a+b)} ,$$

$$\int \mathrm{d}x \;\; \cos(ax)\cos(bx) = \frac{\sin\left[(a-b)x\right]}{2(a-b)} + \frac{\sin\left[(a+b)x\right]}{2(a+b)} .$$

The numerical implementation of the Wigner transformation and analytical calculations for exponentially decaying functions can be found in Appendix 3.D.

3.B Numerical methods

In general, the evolution equations (2.77) with approximations considered in Section 2.3.4 cannot be solved analytically without additional approximations. The method of choice is to discretize the equations and solve them numerically. We emphasize here that, in contrast to lattice simulation approaches, we do not discretize the action but solve the analytically derived equations of motion in a discretized version. In the case of fermions, this approach avoids the problem of fermion doublers [159]. While the equations of motions presented in Section 2.3.3 are valid in arbitrary spatial dimensions d, we have to specify the spatial dimensionality for our numerical computations and use $d = 3$.

This appendix contains detailed information about the numerical methods employed for the analysis in Chapter 3. We outline the discretization methods and the numerical stability of our parameters. Moreover, the numerical implementation of initial conditions, the rescaling to dimensionless quantities, and the extraction of the effective mass are described.

3.B.1 Discretization

In this appendix we provide details about the numerical discretization underlying our computations. Thereby we first discuss the spatial and subsequently the temporal discretization. Since we do not discretize the action but rather solve the evolution equations on a discretized lattice, we can choose a grid reflecting the imposed symmetries.

The dynamical variables of our theory are the one- and two-point functions, which are objects with a dependence on up to two temporal and one spatial coordinate. For computational convenience they are stored in the momentum space representation. Due to the assumption of spatially homogeneous and isotropic systems, the one-point function only depends on one time-like coordinate while the two-point functions depend on two time-like coordinates and one spatial argument.

Spatial discretization

Due to the assumption of spatial homogeneity and isotropy, the spatial coordinate of two-point functions of the form $G(x, y)$ effectively reduces to $|\mathbf{x} - \mathbf{y}|$ or, equivalently, $|\mathbf{p}|$. Since the angular part of the Fourier transformation can be computed analytically, the spatial domain can be discretized on a linear grid with N_x lattice points containing the discrete values of the absolute spatial argument $|\mathbf{x}|$ or $|\mathbf{p}|$. This significantly reduces the amount of memory needed because we only have to store N_x data points instead of N_x^3 values required by a cubic lattice.

In the case of an isotropic system, the Fourier transformation from momentum space to coordinate space can be computed as

$$\begin{aligned} f(|\mathbf{x}|) &= \int \frac{\mathrm{d}^3 p}{(2\pi)^3}\, f(|\mathbf{p}|) e^{i\mathbf{p}\mathbf{x}} \\ &= \frac{1}{(2\pi)^3} \int_0^{2\pi} \mathrm{d}\varphi \int_0^{\pi} \mathrm{d}\theta \int_0^{\infty} \mathrm{d}|\mathbf{p}|\; |\mathbf{p}|^2 \sin(\theta) f(|\mathbf{p}|) e^{i\mathbf{p}\mathbf{x}} \\ &= \frac{2\pi}{(2\pi)^3} \int_0^{\infty} \mathrm{d}|\mathbf{p}|\; \frac{|\mathbf{p}|}{|\mathbf{x}|}\; f(|\mathbf{p}|) \int_0^{\pi} \mathrm{d}\theta\; |\mathbf{p}||\mathbf{x}| \sin(\theta) e^{i|\mathbf{p}||\mathbf{x}|\cos(\theta)} \\ &= \frac{1}{2\pi^2 |\mathbf{x}|} \int_0^{\infty} \mathrm{d}|\mathbf{p}|\; |\mathbf{p}|\; \sin(|\mathbf{p}||\mathbf{x}|)\; f(|\mathbf{p}|), \end{aligned} \tag{3.44}$$

where we explicitly performed the solid angle integration. Analogously, one obtains

$$f(|\mathbf{p}|) = \frac{4\pi}{|\mathbf{p}|} \int_0^{\infty} \mathrm{d}|\mathbf{x}|\; |\mathbf{x}| f(|\mathbf{x}|) \sin(|\mathbf{x}||\mathbf{p}|) \tag{3.45}$$

for the transformation from coordinate space to momentum space. From (3.44) and (3.45) it follows that one only needs to compute sine transforms, for which much faster algorithms exist as compared to normal Fourier transforms.

In our numerical routines we discretize the momenta and coordinates according to

$$|\mathbf{p}| \;\to\; |\mathbf{p}|_i = \frac{\pi}{a_x N_x}(i+1)\,, \qquad \mathrm{d}|\mathbf{p}| \to \frac{\pi}{a_x N_x}\,, \tag{3.46a}$$

$$|\mathbf{x}| \;\to\; |\mathbf{x}|_i = a_x (i + 1/2)\,, \qquad \mathrm{d}|\mathbf{x}| \to a_x\,, \tag{3.46b}$$

where a_x is the spatial grid spacing, N_x the number of grid points and $i = 0, ..., N_x - 1$ the grid index. The starting points of the discrete momenta and coordinates are chosen such that the fastest one-dimensional Fourier transform routines of the FFTW library can be applied [160, 161]. The chosen discretization introduces an infrared cutoff at $\Lambda_{\mathrm{IR}} = \pi/(N_x a_x)$ as well as an ultraviolet cutoff at $\Lambda_{\mathrm{UV}} = \pi/a_x$. Using (3.46) the discretized versions of the Fourier transformations (3.44) and (3.45) read

$$f(|\mathbf{x}|_j) = \frac{1}{2(j+1/2) a_x^3 N_x^2} \sum_{i=0}^{N_x - 1} (i+1) f(|\mathbf{p}|_i)\; \sin\left(\frac{\pi}{N_x}(i+1)(j+1/2)\right)\,, \tag{3.47}$$

$$f(|\mathbf{p}|_j) = \frac{4 a_x^3 N_x}{(j+1)} \sum_{i=0}^{N_x - 1} (i+1/2) f(|\mathbf{x}|_i)\; \sin\left(\frac{\pi}{N_x}(j+1)(i+1/2)\right)\,, \tag{3.48}$$

where $j = 0, \dots, N_x - 1$.

Numerically, the discrete sine transform corresponds to the real-odd discrete Fourier transform (RODFT). Accordingly, there exists the discrete cosine transform for the real-even discrete Fourier transform. In our computations, the sine transforms are computed using the FFTW library, which includes the RODFT10 and RODFT01 transforms defined as [161],

$$Y_k = 2\sum_{j=0}^{N-1} X_j \sin\left(\frac{\pi}{N}(j+\tfrac{1}{2})(k+1)\right) , \tag{3.49a}$$

$$Y_k = (-1)^k X_{n-1} + 2\sum_{j=0}^{N-2} X_j \sin\left(\frac{\pi}{N}(j+1)(k+\tfrac{1}{2})\right) , \tag{3.49b}$$

where X is the purely real input array of length N having odd symmetry and Y the purely imaginary output array of length N having also odd symmetry.

The discretization in spatial direction allows for parallel computing, which is implemented by the *Message Passing Interface* (MPI) [162]. To accelerate the computation, we distribute the spatial array to several processes (so-called *client* processes) by splitting the array into pieces such that every process computes the time evolution for a certain range of momenta. Thereby each process stores the full time dependence for the given spatial lattice points. With all time dependence available every process is able to compute the memory integrals in the equations of motion (see Section 2.3.3) for the given range of spatial momenta. However, for momentum integrations as they appear in Fourier transformations and loop integrals the whole momentum range is necessary and therefore all pieces of $|\mathbf{p}|$ or $|\mathbf{x}-\mathbf{y}|$ need to be combined on one process (the so-called *master* process) for these tasks.

Temporal discretization

The 2PI evolution equations presented in Section 2.3.3 are causal and therefore explicit in time, meaning that only explicitly known quantities at earlier times influence the time evolution to quantities at later times.

We discretize in the two temporal directions t and t' using N_t time steps of size a_t in both temporal directions, such that

$$t \to t_i = i\,a_t\,, \qquad\qquad t' \to t'_i = i\,a_t\,, \tag{3.50}$$

with $i = 1, ..., N_t$ and $t_{\max} = a_t N_t$. Since the statistical (spectral) function is (anti)symmetric in the exchange of t and t', it is sufficient to store times $t' \leq t$, knowing that times $t' > t$ can be obtained by symmetry.

For the analysis of the two-point correlation functions we employ the central time $\tau = (t+t')/2$ and the relative time $\Delta t = t - t'$. Using the above discretization, the temporal grid spacing in relative time is $a_{\Delta t} = 2a_t$ while the number of lattice points in the relative time direction is the same, i.e. $N_{\Delta t} = N_t$. Hence, the relative time Δt is discretized according to

$$\Delta t \to \Delta t_i = i a_{\Delta t}\,, \qquad\qquad i = -\frac{N_{\Delta t}}{2}, ..., \frac{N_{\Delta t}}{2}\,, \tag{3.51}$$

where i is (half) integer for $N_{\Delta t}$ being even (odd) such that $\Delta t \in [-t_{\max}, t_{\max}]$. The Fourier modes corresponding to the relative time are given by the frequencies

$$\omega_i = \frac{2\pi}{N_{\Delta t} a_{\Delta t}}\, i\,, \qquad\qquad i = -\frac{N_{\Delta t}}{2}, \dots, \frac{N_{\Delta t}}{2}\,, \tag{3.52}$$

which means that the frequency range is given by $[-\pi/a_{\Delta t}, \pi/a_{\Delta t}]$. Only frequencies below the frequency cutoff $\omega_{\max} = \pi/a_{\Delta t} = \pi/(2a_t)$ are available on the temporal lattice, implying that the smallest relative time resolved on the lattice is $\Delta t_{\min} = 2\pi/\omega_{\max} = 4\,a_t$. We note that the ratio between frequency cutoff and spatial momentum cutoff is given by

$$\frac{\omega_{\max}}{\Lambda_{\mathrm{UV}}} = \frac{1}{2}\frac{a_x}{a_t}\,, \tag{3.53}$$

where the ratio a_x/a_t depends on the physical parameters and is usually much larger than 1 in order to obtain numerical convergence, cf. Courant-Friedrichs-Lewy stability condition [163]. Thereby the ratio a_x/a_t needed for a convergent solution depends on the physical parameters chosen to describe the specific system. Generally, one finds $\omega_{\max} > \Lambda_{\mathrm{UV}}$ and requires that characteristic momentum scales of the system are sufficiently smaller than the cutoff Λ_{UV}.

After discussing the temporal grid, we now come to the discretization of the evolution equations for the two-point functions and the macroscopic field. The evolution equations have the form of *integro-differential equations* in time which involve both integrals and derivatives with respect to time arguments. Using the trapezoidal rule for integration and the Euler method for derivatives, we discretize according to

$$\int_t^{t'} \mathrm{d}t\; f(t) \to a_t \left[\frac{1}{2} f(t_i) + \sum_{l=i+1}^{j-1} f(t_l) + \frac{1}{2} f(t_j)\right]\,, \tag{3.54}$$

$$\frac{\partial^2}{\partial t^2} f(t) \to \frac{f(t_{i+1}) - 2f(t_i) + f(t_{i-1})}{a_t^2}\,, \tag{3.55}$$

with discrete times as introduced in (3.50). We emphasize that the evolution equations are causal in the sense that only explicitly known quantities at earlier times determine the time evolution of the unknown quantities at later times. This becomes clear when looking at the discretized version of the evolution equations, for instance

$$\begin{aligned}\rho(t_{i+1}, t_j) = {} & 2\rho(t_i, t_j) - \rho(t_{i-1}, t_j) - a_t^2 \left[|\mathbf{p}|^2 + M^2(t_i)\right] \rho(t_i, t_j) \\ & - a_t^3 \left[\frac{1}{2} A(t_i, t_i)\rho(t_i, t_j) + \sum_{l=i+1}^{j-1} A(t_i, t_l)\rho(t_l, t_j) + \frac{1}{2} A(t_i, t_j)\rho(t_j, t_j)\right]\,,\end{aligned} \tag{3.56}$$

omitting the momentum argument for a simpler notation. The right-hand side of the equation only depends on known functions at times $\leq t_i$. Consequently, for given initial conditions we can evolve the propagators and the macroscopic field step by step, going from t_i to t_{i+1} in each time step. Since the evolution equations involve second order time derivatives, specifying initial conditions at times $t_i = 0$ and $t_i = 1$, i.e. at temporal arguments $(t_0, t_0), (t_0, t_1), (t_1, t_0), (t_1, t_1)$ for the two-point functions, enables us to compute the time evolution iteratively for numerical time steps $i, j \geq 2$.

Grid parameters

Simulations with less than 10 000 time steps and a spatial grid with 500 grid points were carried out on the bwUniCluster [153], a high performance computing cluster in the state Baden-Württemberg. Long simulations with up to 15 000 time steps were computed on the bwForCluster JUSTUS [153], a high-performance computing resource intended for jobs with high memory needs.

The long simulations were computed on 26 nodes with two processes each, taking about 90 h computing time. A total job required 2.5 TB of memory corresponding to 50 GB per process.

3.B.2 Initial conditions

The nonequilibrium 2PI evolution equations of Section 2.3.3 require the specification of Gaussian initial conditions. This is equivalent to the specification of initial values for the one-point and two-point correlation functions, which we outline in the following.

In spatially homogeneous systems, the macroscopic field only depends on time such that the initial condition for the one-point function is fully determined by the field and its time derivative at initial time, i.e. $\phi(t_0)$ and $\partial_t \phi(t)\big|_{t=t_0}$. If both are zero at t_0, the field expectation value remains zero at all times due to the $O(N)$ symmetry.

The spectral function defined in (2.65b) obeys the equal-time commutation relations (2.70), which fully determine its initial conditions. Using the forward derivative[1] these relations yield the following initial condition at discrete times,

$$\rho(t_0, t_0, |\mathbf{p}|) = 0\,, \tag{3.58a}$$

$$\rho(t_1, t_0, |\mathbf{p}|) = a_t\,, \tag{3.58b}$$

$$\rho(t_1, t_1, |\mathbf{p}|) = 0\,. \tag{3.58c}$$

Here and in the following, we do not state the (t_0, t_1)-component explicitly as it can be obtained by symmetry.

For the statistical two-point functions we employ the free-field expression (3.29a) with a given initial particle occupation number distribution. The discretized time evolution of the first time step can be calculated using the forward derivative such that one obtains the initial conditions

$$F(t_0, t_0, |\mathbf{p}|) = \frac{f_\mathbf{p} + \frac{1}{2}}{\omega_\mathbf{p}}, \tag{3.59a}$$

$$F(t_1, t_0, |\mathbf{p}|) = F(t_0, t_0, |\mathbf{p}|), \tag{3.59b}$$

$$F(t_1, t_1, |\mathbf{p}|) = F(t_0, t_0, |\mathbf{p}|)\Big(a_t^2 \omega_\mathbf{p}^2 + 1\Big)\,, \tag{3.59c}$$

with initial distribution $f_\mathbf{p}$ and initial dispersion $\omega_\mathbf{p}$. In our analysis, we specify $f_\mathbf{p}$ by the boxlike distribution (3.5) and deploy $\omega_\mathbf{p} = \sqrt{\mathbf{p}^2 + m_\text{init}^2}$ with a vanishing initial mass $m_\text{init}^2 \to 0^+$.

---

[1] With forward derivative we mean the numerical approximation of the derivative by taking the forward difference,

$$\frac{\mathrm{d}}{\mathrm{d}t} f(t) = \frac{f(t+dt) - f(t)}{dt}\,. \tag{3.57}$$

dimensionful quantity	mass dimension	dimensionless quantity
t	-1	$t\,Q$
$\lvert\mathbf{x}\rvert$	-1	$\lvert\mathbf{x}\rvert\,Q$
ω	$+1$	ω/Q
$\lvert\mathbf{p}\rvert$	$+1$	$\lvert\mathbf{p}\rvert\,/Q$
m^2	$+2$	$m^2\,/Q^2$
λ	0	λ
$\phi(t,\mathbf{x})$	$+1$	$\phi(t,\mathbf{x})/Q$
$G(t,t',\mathbf{x}-\mathbf{y})$	$+2$	$G(t,t',\mathbf{x}-\mathbf{y})\,/Q^2$
$G(t,t',\mathbf{p})$	-1	$G(t,t',\mathbf{p})\,Q$
$G(\tau,\omega,\mathbf{p})$	-2	$G(\tau,\omega,\mathbf{p})\,Q^2$
$\Pi(t,t',\mathbf{x}-\mathbf{y})$	$+4$	$\Pi(t,t',\mathbf{x}-\mathbf{y})/Q^4$
$\Pi(t,t',\mathbf{p})$	$+1$	$\Pi(t,t',\mathbf{p})/Q$
$\Pi(\tau,\omega,\mathbf{p})$	0	$\Pi(\tau,\omega,\mathbf{p})$
$f(t,\mathbf{p})$	0	$f(t,\mathbf{p})$
$\lambda_{\text{eff}}(t,\mathbf{p})$	0	$\lambda_{\text{eff}}(t,\mathbf{p})$
$\omega(t,\mathbf{p})$	$+1$	$\omega(t,\mathbf{p})\,/Q$
$\varepsilon(t)=E(t)/V$	$+4$	$\varepsilon(t)\,/Q^4$
$\varepsilon(t,\mathbf{p})$	$+1$	$\varepsilon(t,\mathbf{p})/Q$

Table 3.1: Mass dimensions of dimensionful physical quantities and the corresponding dimensionless expressions using Q as an (energy/momentum) unit of mass dimension -1. All quantities are given in the notation deployed in the main text.

3.B.3 Mass dimensions

For the interpretation of our numerical results we rescale all physical quantities such that they become dimensionless. This purpose can be achieved, for instance, by using a unit with mass dimension -1, e.g. the lattice spacing or a characteristic time of the system, or a unit with mass dimension $+1$, e.g. some relevant energy or momentum scale.

In coordinate space the bosonic two-point function $G(x,y)$ has mass dimension 2. Performing a spatial Fourier transformation,

$$G(t,t',\mathbf{p}) = \int_{\mathbf{x}-\mathbf{y}} G(t,t',\mathbf{x}-\mathbf{y})e^{i\mathbf{p}(\mathbf{x}-\mathbf{y})}\,,$$

decreases the mass dimension by three such that the boson propagator in spatial momentum space, $G(t,t',\mathbf{p})$, has mass dimensions -1. The Wigner transformation further decreases the mass dimension by one since Δt has mass dimension -1 while ω is of mass dimension 1. Thus, the Fourier Wigner space propagator $G(\tau,\omega,\mathbf{p})$ has mass dimension -2. This agrees with the sum rule (3.19).

Table 3.1 contains a list of physical quantities appearing in computations of the relativistic scalar field theory discussed in Chapter 3 based on the 2PI effective action approach. As stated in the main text, the numerical results presented in Chapters 3 are given in terms of the initial characteristic momentum scale Q_0, which has mass dimension +1.

3.B.4 Extracting the effective mass

The effective mass is obtained from the dispersion relation. We use the Wigner dispersion rather than the equal-time quasiparticle dispersion because its numerical stability in the infrared is better. Since the spectral function does not have a clear peak at small momenta $|\mathbf{p}|$, we deploy the dispersion relation deduced from the statistical function $F(\tau, \omega, |\mathbf{p}|)$ and fit it to

$$\omega(\tau, \mathbf{p}) = \sqrt{\mathbf{p}^2 + m_{\text{eff}}^2(\tau)}\,, \tag{3.60}$$

which yields the τ-dependent effective mass. We find that the effective mass is almost stationary and only decreases very slowly with time. Hence, we can estimate the error of the effective mass in terms of the the difference to an earlier time. The effective masses presented in (3.26) correspond to values obtained from the latest available time $\tau_{\text{max}} = 2250$. The error is extracted as

$$\Delta m_{\text{eff}} = m_{\text{eff}}(\tau_{\text{max}} - \Delta\tau) - m_{\text{eff}}(\tau_{\text{max}})\,, \tag{3.61}$$

where a time difference of $\Delta\tau = 2400$ is employed.

3.B.5 Numerical stability

In this appendix we show that the grid parameters chosen for our analysis ensure that the simulations are insensitive to infrared (IR) and ultraviolet (UV) cutoffs as well as changes in the time step size.

Insensitivity to IR and UV cutoffs

In the following, possible effects of the spatial grid spacing and the volume on the distribution function are studied. We also take into account the influence of these parameter on the numerical stability of the conserved quantities in the system. The results are shown for the coupling $\lambda = 1.0$ and vanishing bare mass squared $m^2 = 0.0$. We consider times up to $t = 1200$ at which the distribution is described by the typical shape of the scaling function.

In order to study the UV cutoff dependence, we consider a constant box size $L = N_x a_x$ where N_x is the number of grid points and a_x the grid spacing. We compare three sets of parameters with grid spacings that lead to UV cutoffs between $\Lambda_{\text{UV}} = 3.4$ and $\Lambda_{\text{UV}} = 5.2$. Thereby, numerical convergence is retained by keeping the ratio of the spatial and temporal grid spacing fixed at $a_x/a_t = 2.5$.
For the analysis of the IR cutoff, the grid spacing is kept fixed at $a_s = 0.75$ while the grid size is varied by choosing different numbers of grid points. This leads to IR cutoffs $\Lambda_{\text{UV}} = \pi/(N_x a_x)$ in the range from 0.005 to 0.014.

In Figure 3.1 we show that the distribution function is basically independent of changes of the IR or the UV cutoff. Minor deviations occur in the high momentum regime when changing the UV cutoff, but this does not affect the low-momentum regime that is of interest for this work. We find

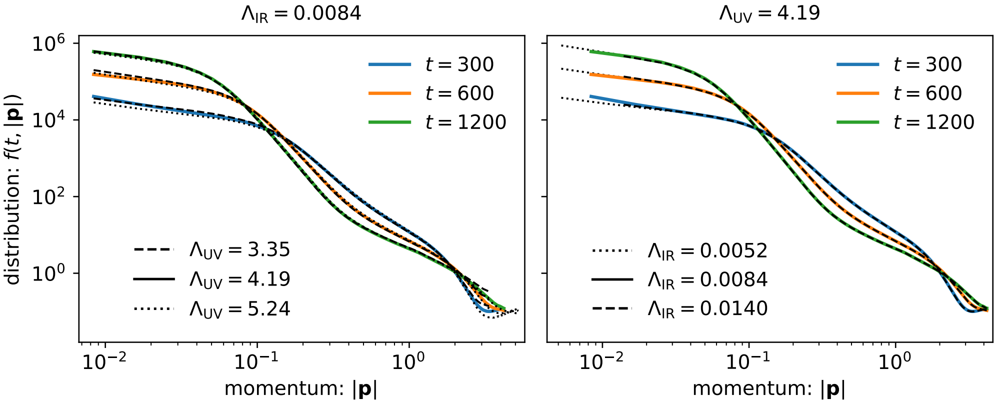

Figure 3.1: Particle distribution function for different UV cutoffs (left) and IR cutoffs (right) shown for three different times. The distribution is insensitive to cutoffs changes.

good agreement between the distributions computed on grids with different volumes, implying that the numerical implementation is insensitive to the size of the spatial grid.

In a second step, we study the behavior of the energy density for different UV and IR cutoffs, see Figure 3.2. The bump in the beginning of the time evolution is a consequence of the quench occurring in the first time step. The quench violates conservation laws explicitly while the time evolution itself respects energy conservation.

Since the analysis of the UV cutoff dependence is carried out at constant ratio a_x/a_t, the time step size is varied in order to study different UV cutoffs. As a direct consequence, the level at which energy conservation holds numerically improves for simulations with larger UV cutoffs due to the smaller time step sizes deployed. However, in all three simulations the energy loss is less than $1\,\%$ for the times shown.

As the grid parameters a_x and a_t as well as the bare parameters m^2 and λ are kept fixed for the IR cutoff tests, the precision of the energy conservation should not change much. This is reproduced numerically and shown in the lower plot of Figure 3.2.

Finally, let us consider the total particle density that is obtained by integrating over all modes of the particle distribution function,

$$n(t) = \int \frac{\mathrm{d}^3 p}{(2\pi)^3}\, f(t, |\mathbf{p}|)\,, \tag{3.62}$$

which is not necessarily constant in a relativistic quantum field theory. However, particle number changing processes are expected to be suppressed. We find that the total particle density is almost constant, as shown in Figure 3.3. The increase at early times stems from the quench at initial time. One observes that particle number changing processes lead to a slow decay of the total particle density. However, for the times analyzed the particle density only decreases by a few percent.

From this analysis we conclude that IR and UV cutoff effects are sufficiently weak for our chosen set of grid parameters. This implies that the results presented in the main part of this chapter are

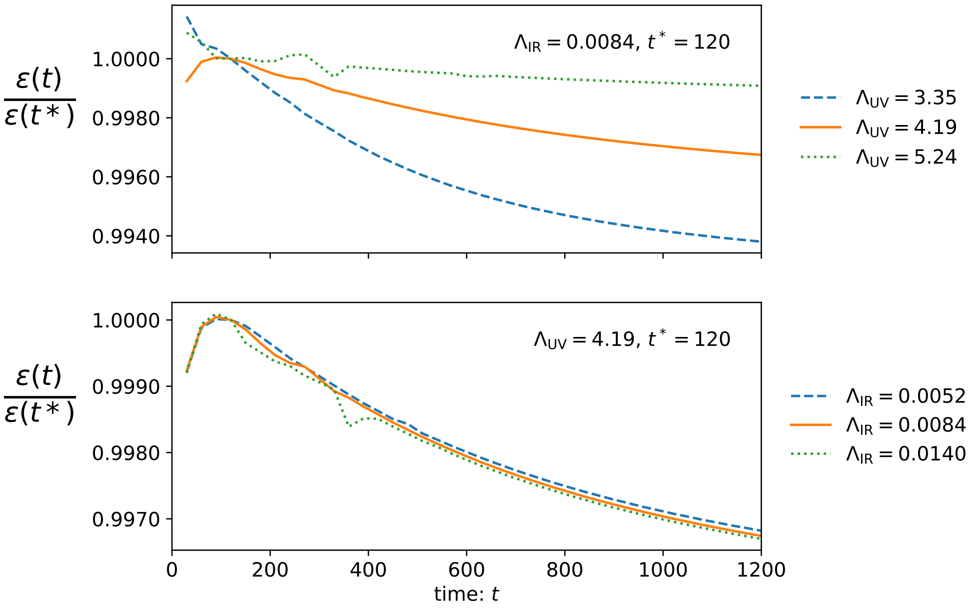

Figure 3.2: The energy density $\varepsilon(t)$ for different UV cutoffs (top) and IR cutoffs (bottom), normalized by $\varepsilon(t^*)$ with t^* given in the plots for better visualization. The conservation of energy holds at the level of 1 % for the times shown. Because the ratio a_x/a_t is kept fixed for the different UV cutoffs, the decrease of a_t with decreasing Λ_{UV} leads to better results for the energy conservation.

insensitive to the spatial discretization.

Insensitivity to the temporal discretization

As pointed out above, the numerical stability depends on the ratio a_x/a_t. The numerical time evolution becomes more exact and more stable with a smaller time step size a_t. Here we check that our choice for the time step size does not influence our results for the particle distribution function. Figure 3.4 shows that an increase of the time step size up to $a_t = 0.375$ does not affect the shape of the particle distribution function. We find that the simulations with $a_t = 0.300$ and $a_t = 0.375$ both agree with the results employing the smaller time step $a_t = 0.24$.

However, too large time step sizes lead to unstable numerical computations, which is reflected in the violation of energy conservation in form of a diverging energy density. In Figure 3.5 we show the energy conservation for the time step sizes analyzed above. We find that although energy is showing a diverging behavior for $a_t = 0.375$ (green dotted line), the energy conservation still holds at the level of 2 % for the times shown. This explains that the distribution function still has the same shape as for the smaller time steps. As expected, smaller time steps yield better results in terms of energy conservation.

Furthermore, we also investigate how the Wigner distribution function and the dispersion relation depend on the time step size. In Section 3.4.2 the agreement between the equal-time definition and the Wigner space definition was shown. Now we consider these quantities for different time step sizes a_t. From Figure 3.6 we learn that the agreement between the two definitions improves as the time step size is decreased. However, deviations between the two definitions only occur in the UV such that the analysis of the IR is insensitive to small changes of the time step size.

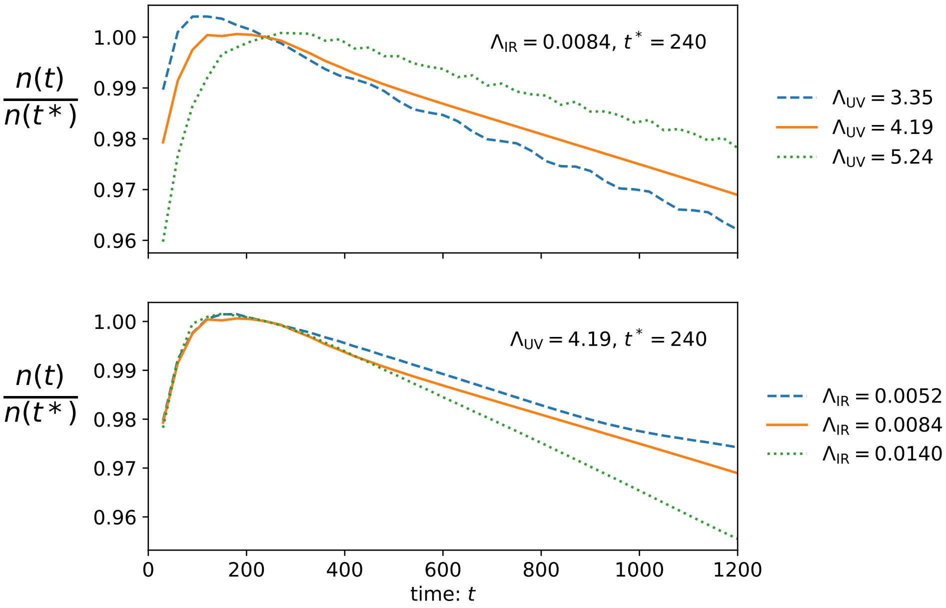

Figure 3.3: The quasiparticle number obtained from the integrated particle distribution for different UV cutoffs (top) and IR cutoffs (bottom).

In order to approach late times, it is our aim to choose a time step as large as possible. Since the results for $a_t = 0.24$ and $a_t = 0.30$ agree very well with each other, both in terms of the energy density as well as the quasiparticle number, we choose to employ $a_t = 0.3$ for the analysis presented in the main text.

3.C Extracting scaling exponents of the self-similar time evolution

In this appendix, we present the fitting procedure employed to determine the scaling exponents α and β from the numerical data. Our method is similar to the approach put forward in [32, 74, 80].

In the self-similar scaling regime, the particle distribution is characterized by the scaling behavior $f(t, \mathbf{p}) = s^{\alpha/\beta} f(s^{-\beta} t, s\mathbf{p})$ with some scale factor s. For notational convenience we write $\mathbf{p} = |\mathbf{p}|$ in this appendix. To compare the numerically computed distribution function at same reference time t_{ref} with the distribution function at some earlier time t_i, we chose the scale factor as $s = (t_i/t_{\mathrm{ref}})^{\beta}$. Hence, the time evolution is described by

$$f(t_i, \mathbf{p}) = \left(\tfrac{t_i}{t_{\mathrm{ref}}}\right)^{\alpha} \underbrace{f\left(t_{\mathrm{ref}}, \left(\tfrac{t_i}{t_{\mathrm{ref}}}\right)^{\beta} \mathbf{p}\right)}_{= f_S(\xi)}, \tag{3.63}$$

where the scaling function f_S only depends on $\xi \equiv (t/t_{\mathrm{ref}})^{\beta}\, \mathbf{p}$, and not on t and $\mathbf{p}$ independently. In case of perfect self-similar scaling behavior, the scaling function is time-independent. For the

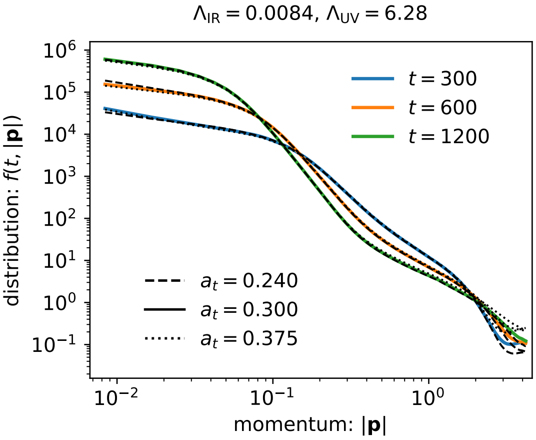

Figure 3.4: Particle distribution function for numerical simulations with different time step sizes a_t.

numerical data, however, the scaling function depends on the time of comparison t_i. Thus, we can only approximate the scaling function by a time-dependent rescaled function, which we define as

$$f_{\mathrm{rsc}}\left(t_i, \left(\tfrac{t_i}{t_{\mathrm{ref}}}\right)^{\beta} \mathbf{p}\right) \equiv \left(\tfrac{t_i}{t_{\mathrm{ref}}}\right)^{-\alpha} f(t_i, \mathbf{p})\,. \tag{3.64}$$

Here, the left-hand side depends on the rescaled momentum $\mathbf{p}_{i,\mathrm{rsc}} = \left(\tfrac{t_i}{t_{\mathrm{ref}}}\right)^{\beta} \mathbf{p}$ and, as the scaling is not perfect, on the time t_i. Equivalently, one can write

$$f_{\mathrm{rsc}}(t_i, \mathbf{p}_{i,\mathrm{rsc}}) = \left(\tfrac{t_i}{t_{\mathrm{ref}}}\right)^{-\alpha} f\left(t_i, \left(\tfrac{t_j}{t_{\mathrm{ref}}}\right)^{-\beta} \mathbf{p}_{i,\mathrm{rsc}}\right) \tag{3.65}$$

in order to compare the distribution at a reference time t_{ref} and with distributions at earlier times t_i with $i = 1, \dots, n$ and $t_i < t_{i+1}$. At the reference time t_{ref}, we have $\mathbf{p}_{\mathrm{ref,rsc}} = \mathbf{p}$ and $f_{\mathrm{rsc}}(t_{\mathrm{ref}}, \mathbf{p}_{\mathrm{ref,rsc}}) = f(t_{\mathrm{ref}}, \mathbf{p})$. For the correct set of scaling exponents, a perfectly self-similar time evolution implies

$$f\left(t_{\mathrm{ref}}, \mathbf{p}\right) = f_{\mathrm{rsc}}\left(t_i, \mathbf{p}_{i,\mathrm{rsc}}\right) \tag{3.66}$$

for all times t_i and t_{ref} within the scaling regime. In the literature, different numerical methods have been employed in order to determine the set of exponents α and β [32, 74, 80]. The general procedure is to define some cost function quantifying deviations from a perfect self-similar scaling behavior and determining exponents by minimizing these deviations.

In our scaling analysis, we minimize the quantity

$$\chi^2(\alpha, \beta) = \frac{1}{n} \sum_{j=0}^{n} \int \mathrm{d} \log \mathbf{p} \left[\Delta_i(\mathbf{p})\right]^2 , \tag{3.67}$$

with deviations specified by

$$\Delta_i(\mathbf{p}) = \log f_{\mathrm{rsc}}(t_{\mathrm{ref}}, \mathbf{p}) - \log f_{\mathrm{rsc}}(t_j, \mathbf{p})\,, \tag{3.68}$$

where the integration over $\log \mathbf{p}$ increases the sensitivity at low momenta. We checked that our results

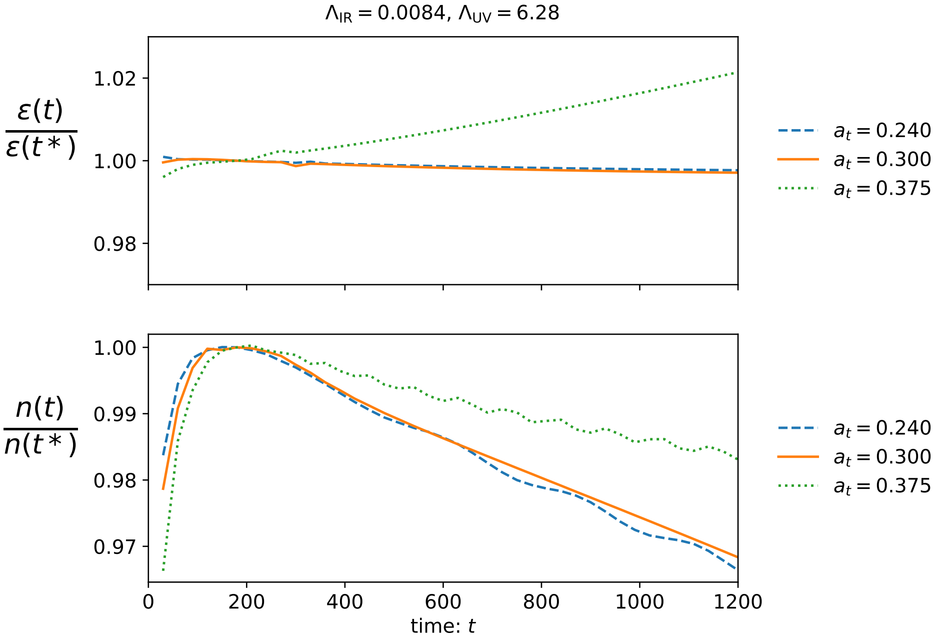

Figure 3.5: Energy density and quasiparticle number (normalized) as a function of time, shown for different time step sizes a_t.

are in good agreement with results using the method in [32], where

$$\Delta_i(\mathbf{p}) = \frac{f_{\mathrm{rsc}}(t_{\mathrm{ref}}, \mathbf{p}) - f_{\mathrm{rsc}}(t_j, \mathbf{p})}{f_{\mathrm{rsc}}(t_{\mathrm{ref}}, \mathbf{p})} \tag{3.69}$$

is used to determine the deviations.

For the χ^2 defined in (3.67), we find that the exponents obtained in the fitting routine are insensitive to the number of comparisons n, which in our analysis is chosen to be $n = 4$. We further have to specify the time window of the comparisons as well as the momentum range to be integrated over. The time window of the comparisons is $\Delta t_{\mathrm{fit}} = t_{\mathrm{ref}} - t_1$ (using our convention of $t_i < t_{i+1}$). The value Δt_{fit} depends on the speed of the dynamics in the analyzed scaling regime. For the times considered in our simulations, we use $\Delta t_{\mathrm{fit}} = 720$. If going to far later times, one would have to increase the time window as the dynamics slows down.

Since the momentum range of the IR plateau decreases with later times, it is convenient to compare the distribution at some t_{ref} with earlier times (at which the plateau momentum region is larger). The distribution at the reference time is then used in order to choose an appropriate momentum range for the comparison of rescaled functions. For the reference time, we determine the characteristic particle cascade momentum K and the momentum scale Q separating the IR and the high-momentum regime. The values of K and Q are determined by the local maximum and minimum of the auxiliary function $|\mathbf{p}|^3 f(t, |\mathbf{p}|)$ as shown in Figure 3.7.

In order to capture as much as possible of the infrared plateau region, the lower bound of the fit range is chosen to be close to the infrared momentum cutoff Λ. We exclude only a small fraction x of the momentum range $[\Lambda, K]$, where we measure x on the logarithmic momentum axis. The upper bound of the fit range should be as large as possible without running into the high-momentum power-

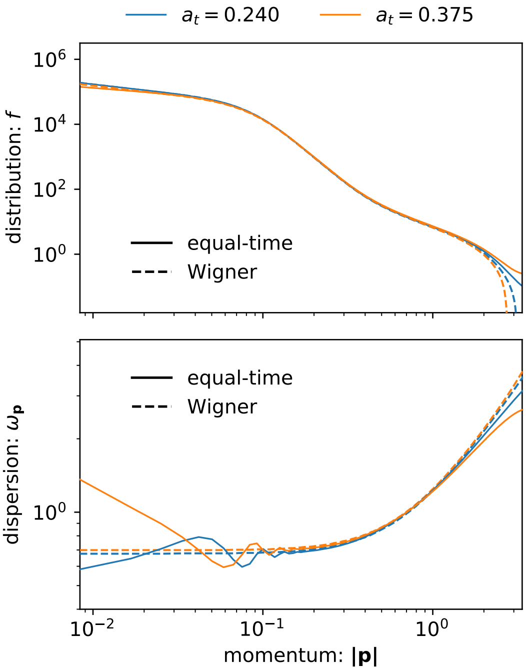

Figure 3.6: The distribution function f and the dispersion relation $\omega_\mathbf{p}$ shown at time $t = \tau = 600$ for different time step sizes a_t. The quasiparticle definition is shown by full, the Wigner space definition by dashed lines. The IR behavior is insensitive to changes in the time step size. Differences occur in the UV but can be removed by decreasing the time step size.

law cascade. Therefore, we take into account a large fraction y of the momentum range between K and Q, on a logarithmic momentum axis, such that we are sure to include the relevant momenta but avoid the nonlinear smoothing out when approaching Q. To summarize, the momentum range for the comparison is given by $[p_\mathrm{min}, p_\mathrm{max}]$ with

$$\ln(p_\mathrm{min}) = \ln(\Lambda) + x\Big(\ln(K) - \ln(\Lambda)\Big), \qquad \ln(p_\mathrm{max}) = \ln(K) + y\Big(\ln(Q) - \ln(K)\Big),$$

which can be written as

$$p_\mathrm{min} = \Lambda^{1-x}K^x, \qquad p_\mathrm{max} = K^{1-y}Q^y, \tag{3.70}$$

where Λ denotes the infrared momentum cutoff, i.e. the smallest momentum numerically available.

The results of the numerical scaling analysis naturally depend on the choice of values for x and y. A physical result is obtained for reasonably large y and sufficiently small x. We analyze the dependence of the exponents α and β as well as their errors $\Delta\alpha$ and $\Delta\beta$ on the parameters x and y. The contour plots in Figure 3.8 show the dependence of the values for the scaling exponents on x and y with the red dot at $(x, y) = (0.05, 0.92)$ marking the point used to determine the exponents presented in the main text of this chapter. The values of α in the blue regions of $y \lesssim 0.952$ agree within $< 0.5\%$; the values of β in the whole blue region corresponding to $y \gtrsim 0.855$ agree within $< 0.5\%$. The errors decrease toward small y, which reflects the fact that the likelihood of perfect scaling grows if the compared momentum range decreases.

In order to compute the difference $\Delta_i(\mathbf{p})$, the discrete data is interpolated such that the discrete momenta of the compared functions coincide. The interpolation is carried out using a cubic interpola-

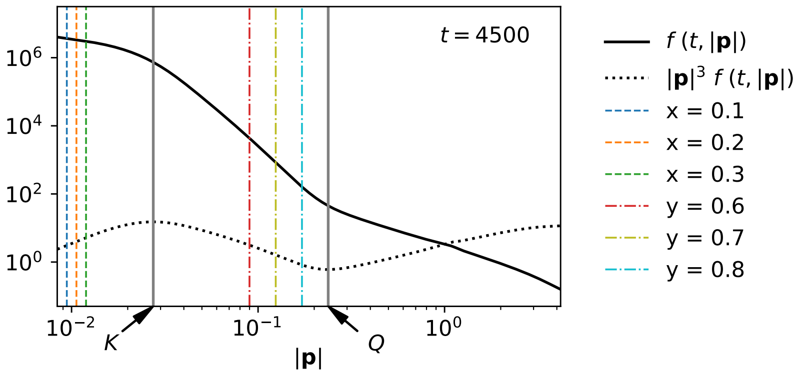

Figure 3.7: Visualization of the momentum range used for comparing rescaled distribution functions. Different values for x and y according to (3.70) are shown. The local maxima and minima of the function $|\mathbf{p}|^3 f(t, |\mathbf{p}|)$ are used in order to determine the characteristic momenta K and Q.

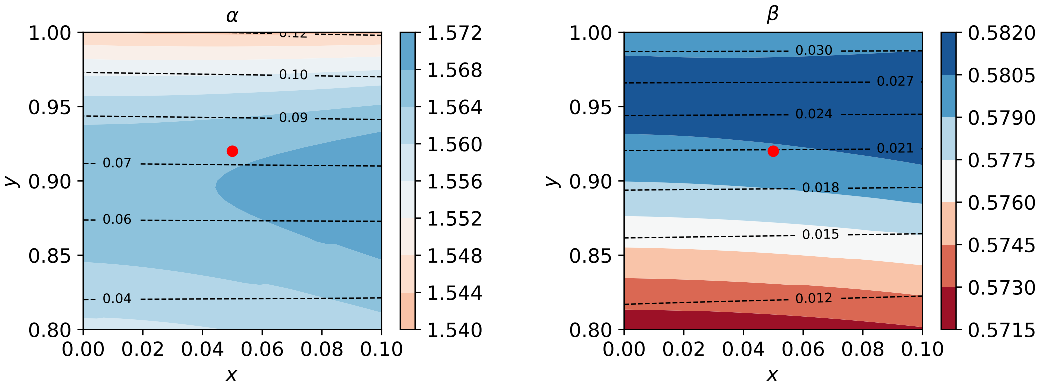

Figure 3.8: Scaling exponents α (left) and β (right) with values encoded in the color scheme, shown for different x and y as defined in (3.70). The dashed lines represent errors of the exponents as contour lines in the x-y-plane. The red dot indicates the point $(x, y) = (0.05, 0.92)$ employed for the scaling analysis in the main text. These plots correspond to $t_{\text{ref}} = 4500$ and $t_{\text{win}} = 720$. The exponents are not equal to the asymptotic values, which are obtained from late-time averages.

tion method provided by the Python SciPy library (`scipy.interpolate.interp1d`) [164]. We also use the SciPy library (`scipy.optimize.minimize`) to minimize χ^2 at different reference times t_{ref}. This yields values $\bar{\alpha}$ and $\bar{\beta}$ for which χ^2 is minimal. In Figure 3.9 we show the values for $\chi^2_{\text{min}} = \chi^2(\bar{\alpha}, \bar{\beta})$ as a function of the reference time. We see that χ^2_{min} decreases in time, reflecting that the system reaches the scaling regime.

The error for the obtained values $\bar{\alpha}$ and $\bar{\beta}$ is estimated by the likelihood functions

$$W(\alpha) = \frac{1}{\mathcal{N}_\alpha} \exp\left[-\frac{\chi^2(\alpha, \bar{\beta})}{2\chi^2(\bar{\alpha}, \bar{\beta})}\right], \qquad W(\beta) = \frac{1}{\mathcal{N}_\beta} \exp\left[-\frac{\chi^2(\bar{\alpha}, \beta)}{2\chi^2(\bar{\alpha}, \bar{\beta})}\right], \tag{3.71}$$

where the normalization constants $\mathcal{N}_{\alpha,\beta}$ are chosen such that $\int \mathrm{d}\alpha\ W(\alpha) = \int \mathrm{d}\beta\ W(\beta) = 1$. By approximating W with a Gaussian distribution, the errors of the exponents can be estimated by the standard deviation σ of the Gaussian function, which we refer to as *fit errors*. Plots of the scaling exponents α in the main text show $\bar{\alpha} \pm \sigma_\alpha$ as data points with error bars, and equivalently for other exponents. Our numerical computations show that α and β as well as $\Delta\alpha_{\text{fit}} = \sigma_\alpha$ and $\Delta\beta_{\text{fit}} = \sigma_\beta$

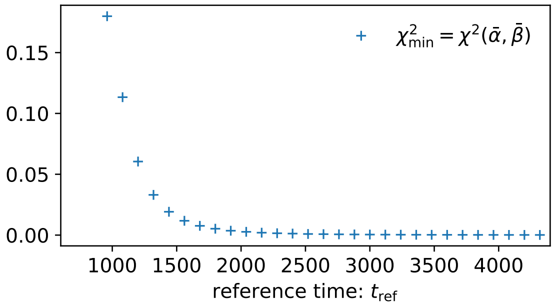

Figure 3.9: $\chi^2_{\rm min}$, the minimum value found for $\chi^2(\alpha, \beta)$, at different reference times $t_{\rm ref}$. $\chi^2_{\rm min}$ approaches a constant small value as the system reaches the scaling regime.

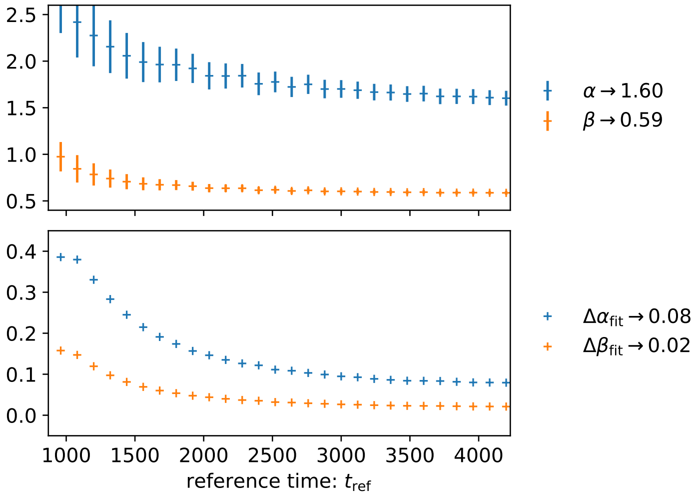

Figure 3.10: The scaling exponents α and β as well as the corresponding fit errors as a function of the reference time $t_{\rm ref}$. The error bars of α and β in the upper plot are exactly the fit errors shown in the lower plot. The asymptotic values are given in the legend. The coupling is $\lambda = 1$.

approach constant values, as shown in Figure 3.10.

The asymptotic values of the exponents are determined by averaging over the values obtained at late reference times. We compute the mean over a time window $\Delta t_{\rm av} \geq 600$ and use the corresponding standard deviation to quantify fluctuations, which we denote by the statistical errors $\Delta\alpha_{\rm stat}$ and $\Delta\beta_{\rm stat}$. For the asymptotic values of the exponents, we provide the error

$$\Delta\alpha = \sqrt{(\Delta\alpha_{\rm fit})^2 + (\Delta\alpha_{\rm stat})^2}\,, \tag{3.72}$$

and accordingly for the other exponents β and α_λ.

3.D The Wigner transformation

In this appendix we present the methods used in order to compute the Wigner transformed spectral and statistical functions according to the definition in (3.18). We discuss consequences of the finite integration range present in initial value problems.

In order to compute the Wigner transform $f(\omega)$ of a temporal signal $f(t)$, we need to numerically evaluate integrals of the form

$$f(\omega) = \int_{-2\tau}^{2\tau} \mathrm{d}t \; e^{i\omega t} f(t) \,, \tag{3.73}$$

where we use t instead of Δt here for notational convenience. The frequency ω is the Fourier mode corresponding to t. The finite integration bounds reflect the initial time bounds present in initial value problems, where an initial state is specified at some initial time t_0. Since the causal time evolution occurs for times later than t_0, one finds $\tau \geq 0$ and $-2\tau \leq t \leq 2\tau$ for $t_0 = 0$.

We are interested in signals oscillating with a given frequency ν that are enveloped by some function $g(t)$ which can be written as

$$f_\pm(t) = g(t) \; \frac{1}{2}(e^{i\nu t} \pm e^{-i\nu t}) \,, \tag{3.74}$$

where the relative sign determines whether the signal is symmetric or antisymmetric. In the following, we present the methods that we employ in order to compute (3.73) for such signals.

3.D.1 Numerical methods

If $g(t)$ decays sufficiently strong, i.e. if it becomes sufficiently small at the boundaries $\pm 2\tau$, effects from the finite integration boundaries are negligible. In this case, the Wigner transform can be computed using a discrete Fourier transformation (DFT),

$$f(\omega_m) = \sum_{n=0}^{N_t - 1} f(t_n) e^{i2\pi mn/N_t} \,, \tag{3.75}$$

where N_t denotes the number of data points, while ω_m and t_m are the discretized frequency and time, respectively, with $m = 0, \ldots, N_t - 1$. In our simulations, the DFT is implemented using the FFTW library [160].

For an exponentially decaying envelope, which is described by $g(t) \sim \exp(-\gamma|t|)$ with some decay constant γ, the DFT can be compared to the analytically calculated Wigner transform with finite as well as infinite integration boundaries, see Appendix 3.D.2 below. For the parameters relevant in our simulations, we confirmed that the DFT of the exponentially decaying Wigner functions appearing in the high momentum regime yields accurate results. In addition, we checked the applicability of the DFT for other momentum ranges by comparing the decaying behavior of the propagator functions with exponential decays. Thus, for the analysis shown in the main text we use the DFT to compute the Wigner transform of the statistical function in all momentum ranges and the spectral function for medium or high momenta.

In general, the finite integration boundaries in (3.73) lead to oscillations of the Wigner transform $f(\omega)$. These are particularly relevant if the envelope function $g(t)$ increases toward larger $|t|$. In this case, we determine the envelope $g(t)$ by a polynomial fit and the oscillation frequency ν using the Lomb-Scargle periodogram implemented in the Python SciPy library. We can then analytically compute the Wigner transformation of (3.74) for the relevant parameters. This method is employed for computing the spectral function at small momenta. However, when comparing the Wigner transform at different spatial momenta $|\mathbf{p}|$ as in Figure 3.7, we employ the DFT for both F and ρ.

3.D.2 Exponentially damped signals

In this appendix, we present the analytical computation of the Wigner transform for exponentially damped oscillations. We consider functions of the form

$$f_\rho(t) = e^{-\gamma|t|}\sin(\omega_\mathbf{p} t)\,, \tag{3.76a}$$

$$f_F(t) = e^{-\gamma|t|}\cos(\omega_\mathbf{p} t)\,, \tag{3.76b}$$

with a damping constant γ. These functions decay sufficiently strong within the time bounds $|t| \leq 2\tau$ if γ or τ is large. Computing the Fourier transform of these signals analytically yields

$$f_\rho(\omega) = \int_{-\infty}^{+\infty} \mathrm{d}t\; e^{i\omega t} e^{-\gamma|t|}\sin(\omega_\mathbf{p} t) = i\,\frac{4\,\gamma\,\omega\,\omega_\mathbf{p}}{(\omega^2-\omega_\mathbf{p}^2)^2 + 2(\omega^2+\omega_\mathbf{p}^2)\gamma^2+\gamma^4}\,, \tag{3.77a}$$

$$f_F(\omega) = \int_{-\infty}^{+\infty} \mathrm{d}t\; e^{i\omega t} e^{-\gamma|t|}\cos(\omega_\mathbf{p} t) = \frac{2\,\gamma\left(\gamma^2+\omega^2+\omega_\mathbf{p}^2\right)}{(\omega^2-\omega_\mathbf{p}^2)^2 + 2(\omega^2+\omega_\mathbf{p}^2)\gamma^2+\gamma^4}\,, \tag{3.77b}$$

from which it becomes clear that the damping constant γ describes the width of the spectra. At order $\mathcal{O}(\gamma^2)$ these expressions are equivalent to (3.23). It is also possible to compute the Wigner transform of these signals analytically. The result can be written in a similar form to (3.77),

$$f_\rho(\omega) = \int_{-2\tau}^{+2\tau} \mathrm{d}t\; e^{i\omega t} e^{-\gamma|t|}\sin(\omega_\mathbf{p} t) = i\,\frac{4\,\gamma\,\omega\,\omega_\mathbf{p}\;\left[1+h_\rho(\omega)\right]}{(\omega^2-\omega_\mathbf{p}^2)^2 + 2(\omega^2+\omega_\mathbf{p}^2)\gamma^2+\gamma^4}\,, \tag{3.78a}$$

$$f_F(\omega) = \int_{-2\tau}^{+2\tau} \mathrm{d}t\; e^{i\omega t} e^{-\gamma|t|}\cos(\omega_\mathbf{p} t) = \frac{2\,\gamma\left(\gamma^2+\omega^2+\omega_\mathbf{p}^2\right)\;\left[1+h_F(\omega)\right]}{(\omega^2-\omega_\mathbf{p}^2)^2 + 2(\omega^2+\omega_\mathbf{p}^2)\gamma^2+\gamma^4}\,, \tag{3.78b}$$

where the difference is phrased in terms of the functions

$$\begin{aligned} h_\rho(\omega) = -e^{-2\tau\gamma}\Bigg\{&\cos(2\tau\omega)\;\Big[\cos(2\tau\omega_\mathbf{p}) + \frac{(\omega^2-\omega_\mathbf{p}^2+\gamma^2)}{2\gamma\omega_\mathbf{p}}\sin(2\tau\omega_\mathbf{p})\Big] \\ &+\sin(2\tau\omega)\Big[\frac{(\gamma^2+\omega^2+\omega_\mathbf{p}^2)}{2\omega\omega_\mathbf{p}}\sin(2\tau\omega_\mathbf{p}) - \frac{(\omega^2-\omega_\mathbf{p}^2-\gamma^2)}{2\gamma\omega}\cos(2\tau\omega_\mathbf{p})\Big]\Bigg\}\,, \end{aligned} \tag{3.79a}$$

$$\begin{aligned} h_F(\omega) = -e^{-2\tau\gamma}\Bigg\{&\cos(2\tau\omega)\;\Big[\cos(2\tau\omega_\mathbf{p}) + \frac{\omega_\mathbf{p}(\omega^2-\omega_\mathbf{p}^2-\gamma^2)}{\gamma\left(\gamma^2+\omega^2+\omega_\mathbf{p}^2\right)}\sin(2\tau\omega_\mathbf{p})\Big] \\ &+\sin(2\tau\omega)\Big[\frac{2\omega\omega_\mathbf{p}}{\left(\gamma^2+\omega^2+\omega_\mathbf{p}^2\right)}\sin(2\tau\omega_\mathbf{p}) - \frac{\omega\left(\omega^2-\omega_\mathbf{p}^2+\gamma^2\right)}{\gamma\left(\omega^2+\omega_\mathbf{p}^2+\gamma^2\right)}\cos(2\tau\omega_\mathbf{p})\Big]\Bigg\}\,. \end{aligned} \tag{3.79b}$$

Since the functions h_ρ and h_F decay exponentially with time τ, they are negligible at sufficiently late times. Furthermore, they contain terms $\sin(2\tau\omega)$ and $\cos(2\tau\omega)$ such that they oscillate in ω with a frequency determined by τ. The larger the integration range is, the higher the oscillation frequency becomes.

We note that the on-shell expressions for (3.79) are equal at order $\mathcal{O}(\gamma^2)$,

$$g_\rho(\omega = \omega_{\mathbf{p}}) = g_F(\omega = \omega_{\mathbf{p}}) = -e^{-2\tau\gamma}\,, \tag{3.80}$$

such that $f_F(\omega)$ is proportional to $f_\rho(\omega)$ as required by the fluctuation-dissipation theorem. In the limit $\tau \to \infty$ the standard relativistic Breit-Wigner function is recovered.

3.D.3 Phase shift in discretized Wigner transformations

In our numerical simulations we compute the Wigner transformation using the discrete Fourier transform (DFT). The FFTW library contains implementations of the one-dimensional DFT equivalent to (3.75). In the Wigner transform, however, the integration range is centered around zero such that we would like to compute a DFT of the form

$$f(\omega_m) = \sum_{n=-N_t/2}^{N_t/2-1} f(t_n)\, e^{i2\pi mn/N_t}\,. \tag{3.81}$$

where as before ω_m and t_m denote the discretized frequency and time, respectively, with $m = 0, ..., N_t - 1$, where N_t is the number of data points. A simple index shift yields the DFT

$$f(\omega_m) = \sum_{n=0}^{N_t-1} \tilde{f}_n\, e^{i2\pi m\left(n-\frac{N_t}{2}\right)/N_t}\,, \qquad \tilde{f}_n = f\left(t_{n-N_t/2}\right)\,, \tag{3.82}$$

where $\tilde{f}_n$ is the array that stores the function values at discretized times in the interval $[-2\tau, 2\tau]$ as elements numbered from 0 to $N_t - 1$. As a consequence, one has to take into account a phase shift of $\exp(-i\pi m)$ in order to determine $f(\omega_m)$,

$$f(\omega_m) = e^{-i\pi m}\tilde{f}_m \qquad \tilde{f}_m = \sum_{n=0}^{N_t-1} \tilde{f}_n\, e^{i2\pi mn/N_t}\,, \tag{3.83}$$

where $\tilde{f}_m$ is obtained by the DFT implemented in the FFTW library. In our numerical implementation we compute both real and imaginary components of $f(\omega_m)$ from products of the real and imaginary components of $\tilde{f}_m$ and the phase factor.

3.E Four-vertices at NLO in the large-N expansion

In this appendix, we analyze the scaling properties of the self-energy contributions at NLO in the large-N expansion. We consider the symmetric theory with vanishing field expectation value where the two-point functions can be taken as diagonal in field space, i.e. $G_{ab} = G\,\delta_{ab}$ with $a, b = 1, \ldots, N$ where N is the number of field components. We derive an expression for the effective four-vertex function λ_{eff} and its scaling behavior. In the course of the derivation, we present the scaling behavior of the self-energy summation functions I_F and I_ρ, (2.92), as well as the one-loop self-energy contributions Π_F and Π_ρ, (2.93).

3.E.1 The effective four-vertex

In the vertex-resummed kinetic theory, one replaces the coupling constant λ by an effective coupling λ_{eff} that takes into account vertex corrections in the non-perturbative regime.

In spatially translation invariant setups, a Fourier transformation of the one-loop self-energy functions (2.93) with respect to the relative coordinate $x-y$ yields

$$\Pi_F(\tau,p) = \frac{\lambda}{6}\int_q \Big[F(\tau,p-q)\,F(\tau,q) - \frac{1}{4}\rho(\tau,p-q)\,\rho(\tau,q)\Big]\,, \tag{3.84a}$$

$$\Pi_\rho(\tau,p) = \frac{\lambda}{3}\int_q F(\tau,p-q)\rho(\tau,q)\,, \tag{3.84b}$$

where $p=(\omega,\mathbf{p})$ is the Fourier mode corresponding to $x-y$ and $\tau=(x^0+y^0)/2$ is the central time. It is convenient to define the momentum-dependent effective coupling

$$\lambda_{\text{eff}}(\tau,p) = \frac{\lambda}{[1+\Pi_R(\tau,p)]\,[1+\Pi_A(\tau,p)]} = \frac{\lambda}{|1+\Pi_R(\tau,p)|^2}\,, \tag{3.85}$$

where Π_R and Π_A are the Fourier transformed retarded and advanced one-loop functions,

$$\Pi_R(x,y) = \quad \theta(x^0-y^0)\Pi_\rho(x,y)\,, \tag{3.86a}$$

$$\Pi_A(x,y) = -\theta(y^0-x^0)\Pi_\rho(x,y) = \Pi_R^*(x,y)\,, \tag{3.86b}$$

which are related to each other, cf. (2.62). The quantum corrections contained in the summation functions I_F and I_ρ, (2.92), can be expressed in terms of the effective coupling times the one-loop term [31–33],

$$\lambda\; I_F(p) = \lambda_{\text{eff}}(\tau,p)\,\Pi_F(\tau,p)\,, \tag{3.87a}$$

$$\lambda\; I_\rho(p) = \lambda_{\text{eff}}(\tau,p)\,\Pi_\rho(\tau,p)\,, \tag{3.87b}$$

which corresponds to (3.15). This allows us to write the self-energies in terms of the effective coupling as [31–33]

$$C(\tau,p) = -\frac{1}{3N}\int_q \lambda_{\text{eff}}(\tau,p-q)\Big[\Pi_F(\tau,p-q)F(\tau,q) - \frac{1}{4}\Pi_\rho(\tau,p-q)\rho(\tau,q)\Big]\,, \tag{3.88a}$$

$$A(\tau,p) = -\frac{1}{3N}\int_q \lambda_{\text{eff}}(\tau,p-q)\Big[\Pi_F(\tau,p-q)\rho(\tau,q) + \Pi_\rho(\tau,p-q)F(\tau,q)\Big]\,, \tag{3.88b}$$

where C and A denote the symmetric and antisymmetric components of the self-energy Σ. The effective coupling incorporates vertex corrections resulting from the resummation of loop diagrams at NLO.

3.E.2 Scaling properties

In this appendix we derive the scaling relation (3.17), i.e. we deduce the scaling properties of the effective vertex in the low-momentum regime. The scaling behavior of the effective vertex can be derived from the scaling properties of the distribution function f, as pointed out in the main text, or from the scaling properties of the spectral and statistical functions. The latter approach is discussed here. We first show the relation between the scaling properties of f and the statistical function F, and then present the scaling properties for the one-loop function and the effective vertex.

In our analysis we are interested in the highly occupied infrared momentum regime, where the particle transport toward low momentum scales occurs via a self-similar cascade. Thereby, the self-similar time evolution of the distribution function is described by a time-independent scaling function and scaling exponents according to (3.10). The analysis in Section 3.3.1 shows that the low-momentum regime of the relativistic scalar field theory behaves nonrelativistically and is described by the scaling exponents of a nonrelativistic scalar field theory. Consequently, we choose the following scaling ansatz for the statistical and spectral functions [32, 33],

$$F\left(\tau,\omega,\mathbf{p}\right) = s^{z+\alpha/\beta}\; F\left(s^{-1/\beta}\tau, s^{z}\omega, s\mathbf{p}\right), \tag{3.89a}$$

$$\rho\left(\tau,\omega,\mathbf{p}\right) = s^{2}\; \rho\left(s^{-1/\beta}\tau, s^{z}\omega, s\mathbf{p}\right), \tag{3.89b}$$

where an occupation number exponent is defined in terms of α and β, and a dynamical scaling exponent z is considered. The dynamical scaling exponent z appears in spatially isotropic settings where only the spatial momenta are related by rotational symmetry whereas frequencies may scale differently. The dispersion is assumed to scale with the dynamical scaling exponent according to $\omega_{\mathbf{p}} = s^{-z}\omega_{s\mathbf{p}}$, from which one obtains $z = 2$ in the nonrelativistic limit where $\omega_{\mathbf{p}} = \mathbf{p}^2/(2m)$.

We can show that the scaling ansatz (3.89a) is equivalent to the scaling property (3.10) by using the following definition of a particle distribution function in a nonrelativistic scalar field theory [32],

$$f(\tau,\mathbf{p}) = \int \frac{\mathrm{d}\omega}{2\pi}\;\; F(\tau,\omega,\mathbf{p})\,, \tag{3.90}$$

neglecting the quantum half here due to the high occupancies considered. This differs from the definition in (3.24) by a factor of ω since the nonrelativistic theory does not involve a second-order time derivative. The scaling behavior for f corresponding to the scaling ansatz (3.89a) follows as

$$\begin{aligned} f(\tau,\mathbf{p}) &= \int \frac{\mathrm{d}\omega}{2\pi}\;\; F(\tau,\omega,\mathbf{p}) \\ &= \int \frac{\mathrm{d}\omega}{2\pi}\;\; s^{z+\alpha/\beta}F(s^{-1/\beta}\tau, s^{z}\omega, s\mathbf{p}) \\ &= \int \frac{\mathrm{d}\omega\; s^{-z}}{2\pi}\;\; s^{z+\alpha/\beta}F(s^{-1/\beta}\tau, \omega, s\mathbf{p}) \\ &= s^{\alpha/\beta}\int \frac{\mathrm{d}\omega}{2\pi}\;\; F(s^{-1/\beta}\tau, \omega, s\mathbf{p}) \\ &= s^{\alpha/\beta} f(s^{-1/\beta}\tau, s\mathbf{p}) \end{aligned}$$

where the dynamical scaling exponent z cancels out. For $\tau = t$ one finds (3.10).

In order to compute the scaling properties of effective coupling λ_{eff}, we determine the scaling behavior of the following one-loop self-energy terms,

$$\Pi_F(\tau,p) = \frac{\lambda}{6}\int_q F(\tau,p-q)\,F(\tau,q)\,, \tag{3.91a}$$

$$\Pi_\rho(\tau,p) = \frac{\lambda}{3}\int_q F(\tau,p-q)\,\rho(\tau,q)\,, \tag{3.91b}$$

$$\Pi_R(\tau,p) = \frac{\lambda}{3}\int_q F(\tau,p-q)\,G_R(\tau,q)\,, \tag{3.91c}$$

where we neglected the ρ^2-term in (3.91a) because large occupancies are considered. This approximation corresponds to the classical-statistical field theory limit of the underlying quantum theory, which is obtained by neglecting the quantum vertex only appearing in the quantum theory. In this approximation, we recover the fact that the leading-order infrared behavior of the scaling solutions is the same for the quantum and classical theory [33].

Here, we compute the scaling behavior of the one-loop functions (3.91) from the scaling properties of F, ρ and G_R. Since the retarded Greens function is directly related to the spectral function, it has the same scaling properties and it is sufficient to present the calculations for Π_F and Π_ρ. Alternatively, one can express (3.91) in terms of the distribution function $f(t, \mathbf{p})$ and the dispersion $\omega_{\mathbf{p}}$ in order to compute the scaling properties.

The scaling behavior of Π_F and Π_R can be computed by inserting the scaling ansatz (3.89) into (3.91),

$$\begin{aligned}
\Pi_F(\tau, p) &= \frac{\lambda}{6} \int_q F(\tau, p-q)\, F(\tau, q) \\
&= \frac{\lambda}{6} \int_q s^{z+\alpha/\beta} F\left(s^{-1/\beta}\tau, s^z(p^0 - q^0), s(\mathbf{p}-\mathbf{q})\right) s^{z+\alpha/\beta} F(s^{-1/\beta}\tau, s^z q^0, s\mathbf{q}) \\
&= s^{2z+2\alpha/\beta-z-d}\ \frac{\lambda}{6} \int_q F\left(s^{-1/\beta}\tau, s^z p^0 - q^0, s\mathbf{p}-\mathbf{q}\right) F(s^{-1/\beta}\tau, q^0, \mathbf{q}) \\
&= s^{z+2\alpha/\beta-d}\ \Pi_F(s^{-1/\beta}\tau, s^z\omega, s\mathbf{p})\,,
\end{aligned}$$

$$\begin{aligned}
\Pi_\rho(\tau, p) &= \frac{\lambda}{3} \int_q F(\tau, p-q)\, \rho(\tau, q) \\
&= \frac{\lambda}{3} \int_q s^{z+\alpha/\beta} F\left(s^{-1/\beta}\tau, s^z(p^0 - q^0), s(\mathbf{p}-\mathbf{q})\right) s^2 \rho(s^{-1/\beta}\tau, s^z q^0, s\mathbf{q}) \\
&= s^{z+\alpha/\beta+2-z-d}\ \frac{\lambda}{3} \int_q F\left(s^{-1/\beta}\tau, s^z p^0 - q^0, s\mathbf{p}-\mathbf{q}\right) \rho(s^{-1/\beta}\tau, q^0, \mathbf{q}) \\
&= s^{2+\alpha/\beta-d}\ \Pi_\rho(s^{-1/\beta}\tau, s^z\omega, s\mathbf{p})\,,
\end{aligned}$$

where we performed the shifts $(q^0, \mathbf{q}) \to (s^{-z}q^0, s^{-1}\mathbf{q})$ and $\mathrm{d}q^0\,\mathrm{d}^d q \to \mathrm{d}q^0\,\mathrm{d}^d q\, s^{-z-d}$ to obtain the third equality in both calculations. The scaling properties of Π_R and Π_A are derived analogously. Using $z = 2$, $s = \tau^\beta$ and $\omega = \omega_{\mathbf{p}}$, we find

$$\Pi_F(\tau, \omega_{\mathbf{p}}, \mathbf{p}) = \tau^{(2-d)\beta+2\alpha} \Pi_F\left(1, \omega_{\tau^\beta \mathbf{p}}, \tau^\beta \mathbf{p}\right)\,, \tag{3.92}$$

$$\Pi_R(\tau, \omega_{\mathbf{p}}, \mathbf{p}) = \tau^{(2-d)\beta+\ \alpha} \Pi_R(1, \omega_{\tau^\beta \mathbf{p}}, \tau^\beta \mathbf{p})\,, \tag{3.93}$$

implying that $\tau^{(2-d)\beta+2\alpha}\Pi_F(\tau, \omega_{\mathbf{p}}, \mathbf{p})$ only depends on $\tau^\beta \mathbf{p}$, and analogously for Π_ρ.

For high occupancies, the statistical function and hence the one-loop contributions are very large such that the effective vertex (3.85) can be approximated as

$$\lambda_{\text{eff}}(\tau, p) \approx \frac{\lambda}{\Pi_R(\tau, p)\Pi_A(\tau, p)}\,, \tag{3.94}$$

for which one infers the self-similar scaling behavior of the effective coupling,

$$\lambda_{\text{eff}}(\tau, \omega, \mathbf{p}) = \tau^{-2(2\beta-d\beta+\alpha)} \lambda_{\text{eff}}(1, \omega_{\tau^\beta \mathbf{p}}, \tau^\beta \mathbf{p})\,, \tag{3.95}$$

which we investigate in Section 3.3.3. It describes the scaling behavior of the effective vertex in the nonrelativistic regime for the case of large occupancies.

Appendix to Chapter 4

4.A Numerical methods

A detailed description of the numerical methods for the computation of 2PI evolution equations considering the case of a relativistic scalar field theory is provided in Appendix 3.B. Here we discuss the aspects that arise in the quark-meson model due to the appearance of quark fields in addition to the scalar fields. Moreover, the fitting of spectra to Breit-Wigner functions is shown.

4.A.1 Discretization

In contrast to the relativistic scalar field theory, the evolution equations of the quark sector involve first-order time derivatives. These are discretized according to the Euler method,

$$\frac{\partial}{\partial t} f(t) \to \frac{f(t_{i+1}) - f(t_{i-1})}{2a_t}\,, \tag{4.16}$$

where t_i are discrete times and a_t is the time step size. In this discretization one obtains discretized evolution equations of the form

$$\begin{aligned} \rho_T(t_{i+1},t_j) = \rho_T(t_{i-1},t_j) &+ 2\ a_t \left[|\mathbf{p}|\rho_S(t_i,t_j) - M_\psi(t_i)\rho_V(t_i,t_j)\right] \\ &- 4\ a_t^2 \left[\frac{1}{2}A_S(t_i,t_i)\rho_S(t_i,t_j) + \sum_{l=i+1}^{j-1} A_S(t_i,t_l)\rho_S(t_l,t_j) + \frac{1}{2}A_S(t_i,t_j)\rho_S(t_j,t_j) + \ \ldots\right]\,, \end{aligned} \tag{4.17}$$

where we suppress spatial arguments to shorten notation. The structure of the fermionic equations is reminiscent of the form of classical canonical equations. In this analogy, the scalar and vector components play the role of the canonical coordinate while the vector-zero and tensor components are analogous to the canonical momentum, or vice versa. If one leaves the memory integrals out of account, one can directly see from (2.114) and (2.115) that derivatives of scalar and vector components only depend on vector-zero and tensor components, and vice versa. Hence, it is natural to apply a "leapfrog" algorithm to the fermions, where one stores each component either at even $t-t'$ or odd $t-t'$. In our analysis, the scalar and the vector component are discretized at even $t-t'$, while the vector-zero and the tensor component are discretized at odd $t-t'$. Consider for instance the discretized fermionic evolution equation given in (4.17), where for even time argument (t_i,t_j) of the scalar and the vector two-point function the time argument $(t_{i\pm1},t_j)$ of the tensor component is automatically odd. This generalization of the "leapfrog" prescription of temporally inhomogeneous two-point functions implies that the discretization in time direction is coarser for the fermionic quantities than for the bosonic ones. In the numerical realization we use a two-dimensional time grid of size $N_t \times N_t$ with spacing a_t to store two fermionic two-point functions, one at even and one at odd grid points. The formulas for the fermionic self-energies suggest to pair the scalar-like components S and 0 as well as the vector-like components V and T. In integrations, the twice as large time step is compensated by explicitly including a factor of two.

4.A.2 Initial Conditions

Computing the time evolution iteratively requires to specify initial conditions at the numerical time steps t_0 and t_1. While the initial quark spectral function is determined by the fermionic anticommutation relations, the initial quark statistical function is chosen to comply with the free-field expression (4.6), which in terms of Lorentz components reads

$$F_S(t_0,t_0,|\mathbf{p}|) = \frac{m_\psi}{\omega_\psi(t_0,|\mathbf{p}|)}\left(\frac{1}{2} - n_\psi(t_0,|\mathbf{p}|)\right)\,, \tag{4.18a}$$

$$F_0(t_0,t_0,|\mathbf{p}|) = 0\,, \tag{4.18b}$$

$$F_V(t_0,t_0,|\mathbf{p}|) = \frac{|\mathbf{p}|}{\omega_\psi(t_0,|\mathbf{p}|)}\left(\frac{1}{2} - n_\psi(t_0,|\mathbf{p}|)\right)\,, \tag{4.18c}$$

$$F_T(t_0,t_0,|\mathbf{p}|) = 0\,, \tag{4.18d}$$

where m_ψ is the fermion bare mass, ω_ψ the quark dispersion relation and n_ψ the quark distribution function. The initial conditions at (t_1,t_0) and (t_1,t_1) are obtained by applying the forward derivative to free evolution equation,

$$F_S(t_0,t_0,|\mathbf{p}|) = \frac{m_\psi}{\omega_\psi(t_0,|\mathbf{p}|)}\left(\frac{1}{2} - n_\psi(0,|\mathbf{p}|)\right), \tag{4.19a}$$

$$F_S(t_1,t_1,|\mathbf{p}|) = F_S(t_0,t_0,|\mathbf{p}|)\Big(1 + a_t^2\omega_\psi^2(t_0,|\mathbf{p}|)\Big), \tag{4.19b}$$

$$F_0(t_1,t_0,|\mathbf{p}|) = -i\ a_t\ \omega_\psi(t_0,|\mathbf{p}|)\left(\frac{1}{2} - n_\psi(t_0,|\mathbf{p}|)\right), \tag{4.19c}$$

$$F_V(t_0,t_0,|\mathbf{p}|) = \frac{|\mathbf{p}|}{\omega_\psi(t_0,|\mathbf{p}|)}\left(\frac{1}{2} - n_\psi(t_0,|\mathbf{p}|)\right), \tag{4.19d}$$

$$F_V(t_1,t_1,|\mathbf{p}|) = F_V(t_0,t_0,|\mathbf{p}|)\Big(1 + a_t^2\omega_\psi^2(t_0,|\mathbf{p}|)\Big), \tag{4.19e}$$

$$F_T(t_1,t_0,|\mathbf{p}|) = 0. \tag{4.19f}$$

Because the numerical stability of the simulations is improved by only using terms up to a_t, we implement (4.19) with $F_S(0,0,|\mathbf{p}|) = F_S(1,1,|\mathbf{p}|)$ and $F_V(0,0,|\mathbf{p}|) = F_V(1,1,|\mathbf{p}|)$.

4.A.3 Mass dimensions

All quantities in the main text of Chapter 4 are given in terms of dimensionless quantities. Table 3.1 contains a lists of quantities that appear in the 2PI formulation of a scalar field theory. The additional quantities arising computations of the quark-meson model are shown in Table 4.2. In Chapter 4 we use the energy unit $Q = T_{pc}$, with T_{pc} being the pseudocritical temperature of the crossover transition, to rescale physical quantities to dimensionless quantities.

dimensionful quantity	mass dimension	dimensionless quantity
T	$+1$	T/Q
β	-1	$\beta\, Q$
$\Gamma(t,\lvert\mathbf{p}\rvert)$	$+1$	$\Gamma(t,\lvert\mathbf{p}\rvert)/Q$
m_ψ	$+1$	m_ψ/Q
g	0	g
$\psi(t,\mathbf{x})$	$+\frac{3}{2}$	$\psi(t,\mathbf{x})/Q^{3/2}$
$\Delta(t,t',\mathbf{x}-\mathbf{y})$	$+3$	$\Delta(t,t',\mathbf{x}-\mathbf{y})/Q^3$
$\Delta(t,t',\mathbf{p})$	0	$\Delta(t,t',\mathbf{p})$
$\Delta(\tau,\omega,\mathbf{p})$	-1	$\Delta(\tau,\omega,\mathbf{p})\, Q$

Table 4.2: Mass dimensions of dimensionful physical quantities and the corresponding dimensionless expressions using Q as an (energy/momentum) unit of mass dimension -1. All quantities are given in the notation deployed in the main text.

4.A.4 Extracting dispersion relations

As discussed in the main text, the spectral functions of both mesons and quarks reveal clear quasiparticle peak structures. In this appendix we provide a few details about the numerical procedure used to extract the dispersion relations from these spectral functions.

We find that the peaks of the meson spectral functions are well described by the relativistic Breit-Wigner function (4.11), which is the case for all considered temperatures and momenta. Hence, the dispersion relation of the mesons is obtained from Breit-Wigner fits to the data, for which an example is provided in the left plot of Figure 4.11.

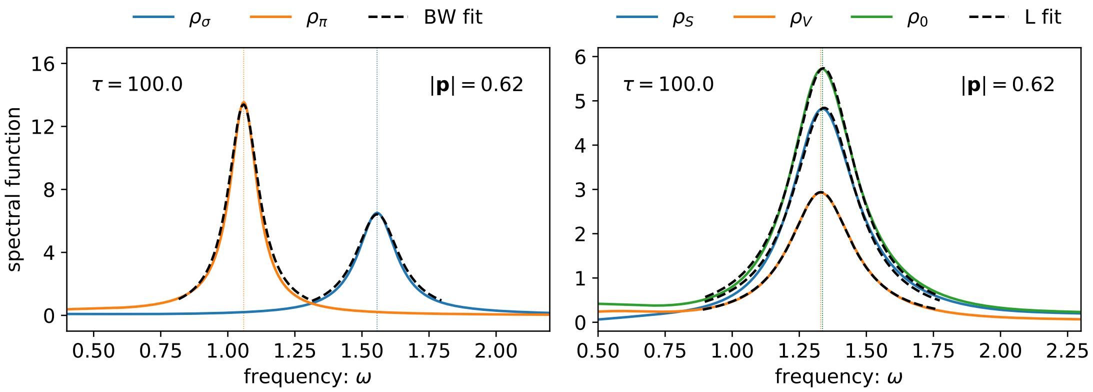

Figure 4.11: The sigma and pion spectral functions (left) and the scalar, vector and vector-zero components of the quark spectral function (right), shown for given momentum $|\mathbf{p}|$ and central time τ. Fits to the relativistic Breit-Wigner function (left) and the Lorentz function (right) are indicated by black dashed lines. Vertical lines mark the peak positions of the spectral functions.

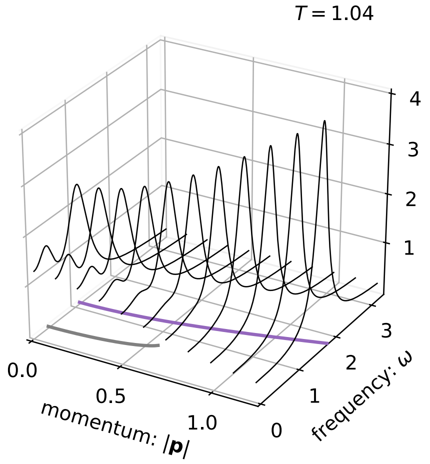

Figure 4.12: The vector-zero quark spectral function as a function of frequency ω shown for a range of spatial momenta $|\mathbf{p}|$. This plots corresponds to a final state in the crossover region where a double-peak structure appears in the low-momentum regime. The purple and gray lines indicate the peak positions of the main and side peaks in the ω-$|\mathbf{p}|$-plane.

In contrast, quark spectral functions may be characterized by the Lorentz function (4.13) with an example shown in the right plot of Figure 4.11. However, the quark spectral functions can not always be described by a Lorentz curve. As discussed in the main text, and shown in Figure 4.4, the vector-zero quark spectral function reveals a double-peak structure for certain temperatures and momenta. Hence, we choose to determine the quark dispersions by using the peak positions rather than Lorentz fits. Relevant for the excitation spectrum is the vector-zero component of the quark spectral function [118, 122]. We determine the peak positions by finding the local maxima of $\rho_0(\tau, \omega, |\mathbf{p}|)$ for different momenta $|\mathbf{p}|$, where a cubic spline interpolation of the spectral function improves accuracy. The position of the main peak yields the quark dispersion $\omega_0(\tau, |\mathbf{p}|)$, while an additional “plasmino” dispersion $\omega_p(\tau, |\mathbf{p}|)$ is found for states revealing a side peak at low momenta. In Figure 4.12 we show an example of a vector-zero quark spectral function with a double-peak structure in the low-momentum regime. The dispersion relations deduced from the two peaks are marked by the purple and gray lines in the ω-$|\mathbf{p}|$-plane.

The obtained dispersion relations give rise to physical masses that correspond to the asymptotic values at vanishing momentum, i.e. $m = \omega(\tau, |\mathbf{p}| \to 0)$. The σ and π meson masses are obtained by fitting the respective dispersion relations to $Z\sqrt{|\mathbf{p}|^2 + m^2}$. For the plasmino and quark masses, we simply use the values of the dispersion relations $\omega_p(\tau, |\mathbf{p}|)$ and $\omega_0(\tau, |\mathbf{p}|)$ at the smallest available momentum.

Appendix to Chapter 6

6.A Dimensionless equations of motion

In this appendix we derive a dimensionless version of the (multi-component)mean-field or Gross–Pitaevskii equation (GPE) for a spin-1 Bose gas given in (5.28). The dimensionless GPE and the units introduced in this section form the basis for all numerical computations of the time evolution.

For the discussion in this appendix, we use $x = (t, \mathbf{x})$ to denote the dimensionful spacetime coordinate and introduce $\tilde{x} = (\tilde{t}, \tilde{\mathbf{x}})$ as the corresponding dimensionless quantity. The dimensionful quantities can be expressed in terms of a length unit a_x and a time unit a_t by writing $\mathbf{x} = \tilde{\mathbf{x}}\, a_x$ and $t = \tilde{t}\, a_t$. We relate the time and length units to each other using $a_t = M a_x^2/\hbar$, which means that we set the time unit a_t equal to the period of a quantum harmonic oscillator with oscillation length a_x. The time unit a_t corresponds to an energy unit $a_\omega \equiv \hbar a_t^{-1} = \hbar^2/(M a_x^2)$.

We proceed to rewrite all terms appearing in the GPE in terms of dimensionless quantities. For that we note that the derivative operators can be converted by the relations $\partial_t = a_t^{-1}\partial_{\tilde{t}}$ and $\partial_x = a_x^{-1}\partial_{\tilde{x}}$. Since $n(\tilde{x}) = \psi_m^\dagger(\tilde{x})\psi_m(\tilde{x})$ describes the particle density of dimension a_x^{-3}, we define the dimensionless field $\tilde{\psi}$ by the relation $\psi_m = \tilde{\psi}_m a_x^{-3/2}$. This ensures that $\tilde{n}$ and $\tilde{F}$ defined as $n = \tilde{n}\, a_x^{-3}$ and $F = \tilde{F} a_x^{-3}$ are the dimensionless particle and spin densities, respectively. Thus, the GPE (5.28) can be rephrased as

$$i\partial_{\tilde{t}}\tilde{\psi}_m(\tilde{x}) = \left[\left(-\frac{1}{2}\tilde{\nabla}^2 + \tilde{q}\, m^2 + \tilde{c}_0\tilde{n}(\tilde{x})\right)\delta_{mm'} + \tilde{c}_1\tilde{F}^i(\tilde{x}) f^i_{mm'}\right]\tilde{\psi}_{m'}(\tilde{x})\,, \tag{6.9}$$

where the dimensionless parameters are given by

$$\tilde{q} = q\,\frac{a_t}{\hbar} = q\,\frac{M a_x^2}{\hbar^2}\,, \qquad \tilde{c}_0 = c_0\,\frac{a_t}{\hbar a_x^3} = c_0\,\frac{M}{\hbar^2 a_x}\,, \qquad \tilde{c}_1 = c_1\,\frac{a_t}{\hbar a_x^3} = c_1\,\frac{M}{\hbar^2 a_x}\,, \tag{6.10}$$

in $d = 3$ dimensions. Equivalently, one can write $q = \tilde{q}\, a_\omega$ and $n_0 c_i = \tilde{n}_0 \tilde{c}_i\, a_\omega$ with the energy unit a_ω defined above. When considering the SI units of the dimensionful parameters,

$$[q] = [nc_0] = [nc_1] = \frac{\mathrm{kg\,m^2}}{\mathrm{s^2}}\,, \qquad [c_0] = [c_1] = \frac{\mathrm{kg\,m^5}}{\mathrm{s^2}}\,, \tag{6.11}$$

one can revise that both q and nc_0 are energy scales, implying that the ratio $q/(n|c_i|) = \tilde{q}/(\tilde{n}|\tilde{c}_i|)$ is dimensionless.

Using the definitions in (6.10) one can also express the characteristic scales of the system in terms of dimensionless parameters and the corresponding unit. For the healing lengths, healing momenta and time scales discussed in Section 5.2.3 we obtain

$$\xi_i = \frac{\hbar}{\sqrt{2Mn_0|c_i|}} = \tilde{\xi}_i\, a_x\,, \qquad \tilde{\xi}_i = \frac{1}{\sqrt{2\tilde{n}_0|\tilde{c}_i|}}\,, \tag{6.12}$$

$$k_{\xi_i} = \frac{2\pi}{\hbar}\sqrt{2Mn_0|c_i|} = \tilde{k}_{\xi_i} a_x^{-1}\,, \qquad \tilde{k}_{\xi_i} = 2\pi\sqrt{2\tilde{n}_0|\tilde{c}_i|} = \frac{2\pi}{\tilde{\xi}_i}\,, \tag{6.13}$$

$$\tau_{\xi_i} = \frac{\hbar}{n_0|c_0|} = \tilde{\tau}_\xi\, a_t\,, \qquad \tilde{\tau}_{\xi_i} = \frac{1}{\tilde{n}_0|\tilde{c}_i|} \tag{6.14}$$

with index $i = 0, 1$ labeling density and spin, respectively, and $\tilde{n}_0 = n_0 a_x^3$. Analogous relations hold for the excitation spectrum of free particles, the most unstable mode, and the largest unstable mode,

$$\varepsilon_{\mathbf{k}} = (\hbar\mathbf{k})^2/(2M) = \tilde{\varepsilon}_{\tilde{\mathbf{k}}}\, a_\omega\,, \qquad \tilde{\varepsilon}_{\tilde{\mathbf{k}}} = \tilde{\mathbf{k}}^2/2\,, \tag{6.15}$$

$$k_{\mathrm{mu}} = \sqrt{-2M(n_0c_1+q)/\hbar^2} = \tilde{k}_{\mathrm{mu}} a_x^{-1}\,, \qquad \tilde{k}_{\mathrm{mu}} = \sqrt{-2(\tilde{n}_0\tilde{c}_1+\tilde{q})}\,, \tag{6.16}$$

$$k_{\max} = \sqrt{-2M(2n_0c_1+q)/\hbar^2}\,, = \tilde{k}_{\max} a_x^{-1}\,, \qquad \tilde{k}_{\max} = \sqrt{-2(2\tilde{n}_0\tilde{c}_1+\tilde{q})}\,, \tag{6.17}$$

where we use $|\mathbf{k}| = |\tilde{\mathbf{k}}|\, a_x^{-1}$ to express momenta in terms of length scales.

The discussions of the mean-field phase diagram and the Bogoliubov excitation spectrum in Sections 5.2 and 5.3 can be directly carried over to dimensionless quantities. Heuristically, the dimensionless relations are obtained from the dimensionful ones by setting $M = \hbar = 1$ and adding a tilde to all dimensionful quantities. For instance, the phase transition at $q = -2n_0c_1$ is determined by $\tilde{q} = -2\tilde{n}_0\tilde{c}_1$.

Units defined by the healing length

For numerical computations of the dimensionless GPE (6.9) one needs to specify the three parameters $\tilde{q}$, $\tilde{c}_0$ and $\tilde{c}_1$. The values of these parameters depend on the given choice for the length unit a_x. It is convenient to employ a convention of units where the healing length is proportional to the length unit. We choose a formulation in which the length unit a_x is defined by the density healing length ξ_0 according to $a_x = \sqrt{2}\,\xi_0$. This implies that the length, time and energy units are given by

$$a_x = \frac{\hbar}{\sqrt{Mn_0|c_0|}}\,, \qquad a_t = \frac{\hbar}{n_0|c_0|}\,, \qquad a_\omega = n|c_0|\,, \tag{6.18}$$

where $n_0 = N_0/V$ is the particle density of the condensed particles in the system, which in a perfect BEC corresponds to the total particle density. For our computations we set N_0 to be the number of particles excluding the quantum half added to the initial state in form of statistical fluctuations. By writing $\xi_0 = \tilde{\xi}_0 a_x$ and $\xi_1 = \tilde{\xi}_1 a_x$ we find the dimensionless healing lengths to be given by

$$\tilde{\xi}_0 = \frac{1}{\sqrt{2}} \approx 0.7\,, \qquad \tilde{\xi}_1 = \frac{1}{\sqrt{2}}\sqrt{\frac{|c_0|}{|c_1|}}\,, \tag{6.19}$$

where the spin healing length only depends on the dimensionless coupling ratio $c_0/c_1 = \tilde{c}_0/\tilde{c}_1$. Analogously, one finds the dimensionless momentum and time scales

$$\tilde{k}_{\xi_i} = \frac{2\pi}{\tilde{\xi}_i} = \sqrt{8}\,\pi\sqrt{\frac{|\tilde{c}_i|}{|\tilde{c}_0|}}\,, \tilde{\tau}_{\xi_i} = \frac{|c_0|}{|c_i|}\,, \tag{6.20}$$

with $i = 0, 1$ for the density and the spin, respectively. We note that the values for the density-related quantities are $\tilde{k}_{\xi_0} \approx 8.89$ and $\tau_{\xi_0} = 1$ while the spin-related quantities only depend on the coupling ratio c_0/c_1. For the specific choice in (6.18), the dimensionless parameters are given by

$$\tilde{q} = \frac{q}{n_0|c_0|}\,, \qquad \tilde{c}_0 = \frac{c_0}{|c_0|}\frac{1}{\tilde{n}_0}\,, \qquad \tilde{c}_1 = \frac{c_1}{|c_0|}\frac{1}{\tilde{n}_0}\,, \tag{6.21}$$

implying $\tilde{n}_0\tilde{c}_0 = \mathrm{sgn}(c_0)$. This particular convention of units is characterized by the property $\tilde{n}_0|\tilde{c}_0| = 1$, which shows itself in a simplification of the expressions for the characteristic scales.

As a side remark, we also provide the relevant equations for a conversion to other units. This may come into play when comparing numerical simulations using different units. Assume that one set of dimensionless parameters $(\tilde{q}, \tilde{c}_0, \tilde{c}_1)$ is obtained for the length unit a_x while another set of dimensionless parameters $(\tilde{q}', \tilde{c}_0', \tilde{c}_1')$ is based on the length unit a_x'. The parameters can be related to each other by

$$\tilde{q}' = \tilde{q}\left(\frac{a_x}{a_x'}\right)^{-2}, \qquad \tilde{c}_0' = \tilde{c}_0\left(\frac{a_x}{a_x'}\right), \qquad \tilde{c}_1' = \tilde{c}_1\left(\frac{a_x}{a_x'}\right), \tag{6.22}$$

while other dimensionless quantities are converted according to

$$\tilde{n}' = \tilde{n}\left(\frac{a_x}{a_x'}\right)^{-3}, \qquad \tilde{\tau}_{\xi_i}' = \tilde{\tau}_{\xi_i}\left(\frac{a_x}{a_x'}\right)^{2}, \qquad \tilde{\xi}_i' = \tilde{\xi}_i\left(\frac{a_x}{a_x'}\right), \qquad \tilde{k}_{\xi_i}' = \tilde{k}_{\xi_i}\left(\frac{a_x}{a_x'}\right)^{-1}, \tag{6.23}$$

where again $i = 0, 1$ for density and spin, respectively.

Dimensionless GPE with rescaled field

In the dimensionless GPE (6.9) it is possible to scale out one of the coupling dependencies, for instance one can rescale the field in a way such that the density-density coupling is set to one. In order to do so, we perform a rescaling of the field according to

$$\tilde{\psi}_m(\tilde{x}) \to \bar{\psi}_m(\tilde{x}) = \frac{1}{\sqrt{\tilde{n}_0}}\,\tilde{\psi}_m(\tilde{x})\,, \tag{6.24}$$

where $\bar{\psi}_m(\tilde{x})$ is the rescaled dimensionless field. As a consequence, we obtain the rescaled dimensionless particle density $\bar{n}_m(\tilde{x}) = \tilde{n}_0^{-1}\,\tilde{n}(\tilde{x})$ and the rescaled dimensionless spin density $\bar{F}_m(\tilde{x}) = \tilde{n}_0^{-1}\,\tilde{F}(\tilde{x})$. Inserting the rescaled field into (6.9) yields a dimensionless GPE of the form

$$i\partial_{\tilde{t}}\bar{\psi}_m(\tilde{x}) = \left[\left(-\frac{1}{2}\tilde{\nabla}^2 + \bar{q}\,m^2 + \bar{c}_0\,\bar{n}\,(\tilde{x})\right)\delta_{mm'} + \bar{c}_1\,\bar{F}^i(\tilde{x})f^i_{mm'}\right]\bar{\psi}_{m'}(\tilde{x})\,, \tag{6.25}$$

with parameters are given by

$$\bar{q} = \tilde{q} = \frac{q}{n_0|c_0|}\,, \qquad \bar{c}_0 = \tilde{c}_0\tilde{n}_0 = 1\,, \qquad \bar{c}_1 = \tilde{c}_1\tilde{n}_0 = \frac{c_1}{|c_0|}\,, \tag{6.26}$$

where $\tilde{q}$, $\tilde{c}_0$ and $\tilde{c}_1$ are the dimensionless parameters in (6.21). In this formulation the density coupling parameter is absorbed into the field such that only $\bar{q}$ and $\bar{c}_1$ need to be specified. The relevant dimensionless time, length and momentum scales become

$$\tilde{\tau}_{\xi_i} = \frac{1}{|\bar{c}_i|} \qquad \tilde{\xi}_i = \frac{1}{\sqrt{2|\bar{c}_i|}} \qquad \tilde{k}_{\xi_i} = 2\pi\sqrt{2|\bar{c}_i|}\,, \tag{6.27}$$

where the tilde indicates the dimensionless scales introduced above. In this convention, the most unstable momentum is given by $\tilde{k}_{\mathrm{mu}} = \sqrt{-2(\bar{q}+\bar{c}_1)}$ and the largest unstable momentum by $\tilde{k}_{\mathrm{max}} = \sqrt{-2(\bar{q}+2\bar{c}_1)}$.

In our simulations, the time evolution is carried out in the convention using the healing length as length unit and performing a field rescaling to set the density coupling to unity. The input parameters for the simulations are therefore provided in terms of the Zeeman energy $\bar{q}$ and spin-coupling $\bar{c}_1$. The computation of observables, however, is performed without field rescaling such that it yields the dimensionless particle and spin densities $\tilde{n}(\tilde{x})$ and $\tilde{F}(\tilde{x})$.

6.B Numerical methods

This appendix provides an overview over the methods used to numerically compute the time evolution of a spin-1 Bose gas. Our computations are based on *classical-statistical* simulations of the multi-component GPE (5.28). We solve the dimensionless GPE (6.9) on a cubic lattice using a *time splitting Fourier pseudospectral* (TSFP) method. In the following, we first summarize key aspects of the classical-statistical approximation, then briefly outline the TSFP method and finally describe the employed discretization.

6.B.1 The classical-statistical approximation

In the classical-statistical approximation, also known as the truncated Wigner approximation (TWA), a quantum field theory is mapped onto a classical-statistical field theory [165–167]. In regimes where the quantum theory is generally expected to be well-described by the corresponding classical theory, this method provides an accurate description of the full quantum dynamics. Since this is the case for weak couplings and large occupancies, we can use the TWA to study the far-from-equilibrium dynamics of a spin-1 BEC with overoccupied initial conditions as it is discussed in Chapter 6.

In the following, we outline the procedure and the validity of classical-statistical simulations. For a derivation of the TWA from the full generating functional we refer to [168]. A derivation based on the so-called Wigner representation of quantum dynamics can be found e.g. in [165, 167].

In classical-statistical simulations, fields are evolved according to their classical equations of motion and observables are computed by averaging functions of these fields over an ensemble of initial conditions. This means that the quantum theory is simulated by a classical random process where quantum corrections appear only through the initial conditions and the ensemble average. Quantum fluctuations are mimicked by adding appropriate classical-statistical fluctuations, also referred to as *truncated Wigner noise*, to the initial state. For each realization in an ensemble of initial conditions, the field is evolved using the GPE. Observables are computed by taking the average over all realizations of the given ensemble [167].

In our numerical computations, Wigner noise is included in the form of uncorrelated Gaussian white noise corresponding to an average occupation of one half per momentum mode. We add random Gaussian distributions centered around $\sqrt{n_{\mathrm{W}}}\,\exp(i\theta_{\mathbf{k}})$ to the initial state at time t_0, with $n_{\mathrm{W}} = 0.5$ representing the occupation of the quantum half and $\theta_{\mathbf{k}}$ being a random phase angle.

By making the TWA, simulations of ultracold Bose gas dynamics reduce to computing the time evolution of the classical field for many initial states [166]. Hence, the TWA constitutes an immense reduction in complexity as compared to the full many-body quantum problem. Applications of the TWA range from cosmology [169–171], quantum field theory [172, 173], and heavy-ion collisions [73, 174, 175] to quantum optics and ultracold quantum gases [165, 166].

The range of validity and the limitations of classical-statistical simulations can be obtained by direct comparisons of the nonequilibrium classical and quantum time evolution for the same initial conditions. For relativistic and nonrelativistic scalar field theories, analyses employing 2PI effective action techniques and kinetic frameworks can be found in [172, 173, 176].

Firstly, we note that the TWA only provides an accurate description of the quantum dynamics if the characteristic occupation numbers are large enough. In the path integral formalism one finds that the TWA consists in neglecting terms that are only present in the quantum theory while keeping terms from the classical theory. This can be stated in form of a "classicality" condition requiring sufficiently large occupancies [168]. Usually, this limits the application of the TWA to not too late times. At too late times all classical-statistical descriptions break down since typical occupancies become of order one, which is the case for thermal equilibrium, and genuine quantum processes dominate. Hence, the approach of quantum thermal equilibrium cannot be captured by classical-statisticl simulations [168].

Secondly, classical-statistical simulations are restricted to sufficiently weak couplings. The reason is that the coupling controls the relative size of the occupation number per mode as compared to the quantum half. Since the quantum half has to be subject to an ultraviolet cutoff regulating the Rayleigh-Jeans divergence present in classical theories, the TWA breaks down for larger couplings where the cutoff dependence becomes sizable [177]. If the coupling is too large, the exchange between high and low momentum modes is not sufficiently suppressed such that the quantum half can decay. Since this does not reflect the correct behavior of a quantum theory, it restricts the validity of classical-statistical simulations.

To stay in the range of validity of the classical-statistical approximation, we have to ensure that couplings are small and occupations are large, with respect to the characteristic scales of the system. Since the far-from-equilibrium dynamics studied in Chapter 6 is dominated by the highly occupied infrared momentum range, it poses a regime that can be accurately captured by classical-statistical simulations.

6.B.2 The time splitting Fourier pseudospectral method

The time splitting Fourier pseudospectral (TSFP) method is an explicit numerical method to solve nonlinear partial differential equations like the nonlinear Schrödinger equation. It can be efficiently implemented using fast Fourier transforms. The TSFP method respects periodic boundary conditions and conserves properties of continuous partial differential equations, for instance time reversibility, time-transverse invariance, the dispersion relation of plane wave solutions and the total particle number [178].

The core idea of the TSFP method is to split the original partial differential equation into subproblems that can be solved exactly or whose exact solution can be approximated in an appropriate way. Thereby a *Fourier pseudospectral* method is used to discretize the subproblem involving the spatial derivative. The solutions of the subproblems are subsequently combined by means of a *time splitting* scheme that approximates the solution of the original problem to a desired order in time.

Here, we work with a two-way splitting of the spin-1 evolution equation following [179]. Since both subsystems can be solved exactly in time, this splitting yields a symplectic integrator of the spin-1

GPE. The solutions of the subsystems are combined using the optimized fourth order time splitting scheme put forward by [180]. For a detailed description of the method and our implementation of the spin-1 BEC we refer to [181].

6.B.3 Lattice discretization

Simulations are performed on a three dimensional cubic lattice with periodic boundary conditions and volume $V = L^3$, where $L = L_x = L_y = L_z$ is the (dimensionful) side length of the lattice. For a_x being the length unit of our system, we can write $L = \tilde{L}\, a_x$ with $\tilde{L}$ being the dimensionless side length of the cubic lattice, also referred to as the numerical side length. The dimensionless volume then follows as $\tilde{V} = \tilde{L}^3$.

The resolution of the simulation is determined by the number of lattice points used in order to discretize the side length $\tilde{L}$. On our cubic grid we consider the same number of grid points N for each lattice side such that $\tilde{L} = N\tilde{a}$ with $\tilde{a}$ being the dimensionless lattice spacing. The spatial extend in each direction $i = x, y, z$ is described by the discrete coordinates

$$\tilde{\mathbf{x}} = \begin{pmatrix} \tilde{x} \\ \tilde{y} \\ \tilde{z} \end{pmatrix} \to \tilde{\mathbf{x}}_{\mathbf{n}} = \tilde{a} \begin{pmatrix} n_x \\ n_y \\ n_z \end{pmatrix}, \qquad n_i = -\frac{N}{2}, ..., \frac{N}{2} - 1\,, \tag{6.28}$$

with spatial extend $-\tilde{L}/2 \leq \tilde{x}_{i,n} < \tilde{L}/2$ in each direction $i = x, y, z$. We assume that our lattice respects periodic boundary conditions such that we can apply discrete Fourier transforms. The Fourier momenta corresponding to the spatial discretization, which are also referred to as *lattice momenta*, take the form

$$\tilde{\mathbf{p}} = \begin{pmatrix} \tilde{p}_x \\ \tilde{p}_y \\ \tilde{p}_z \end{pmatrix} \to \tilde{\mathbf{p}}_n = \frac{2\pi}{\tilde{L}} \begin{pmatrix} n_x \\ n_y \\ n_z \end{pmatrix}, \qquad n_i = -\frac{N}{2}, ..., \frac{N}{2} - 1\,, \tag{6.29}$$

such that the smallest nonzero momentum in one direction is $\tilde{p}_{i,\min} = 2\pi/\tilde{L}$ with $i = x, y, z$, while the largest momentum in one direction is $\tilde{p}_{i,\max} = \pi/\tilde{a}$. Considering $-\pi/\tilde{a} \leq \tilde{p}_{i,n} < \pi/\tilde{a}$ one finds that the total momentum range in one direction is $2\pi/\tilde{a}$, which corresponds to the length scale $\tilde{a}$. For the three-dimensional cubic lattice, we obtain the lattice momentum cutoffs

$$\tilde{\Lambda}_{\mathrm{IR}} = |\tilde{p}_{i,\min}| = \frac{2\pi}{\tilde{L}}\,, \tag{6.30a}$$

$$\tilde{\Lambda}_{\mathrm{UV}} = \sqrt{\tilde{p}_{i,\max}\,\tilde{p}_{i,\max}} = \frac{\sqrt{3}\pi}{\tilde{a}} = \frac{\sqrt{3}\pi N}{\tilde{L}}\,, \tag{6.30b}$$

where we consider any of the three directions $i = x, y, z$ in the former and sum over $i = x, y, z$ in the latter case. The infrared (IR) momentum cutoff describes the smallest momentum interval on the grid, while the ultraviolet (UV) cutoff describes the largest absolute momentum value on our cubic grid. The UV cutoff momentum corresponds to the wavelength $\lambda_{\min} = 2\pi/\Lambda_{\mathrm{UV}} \approx 1.15\,\tilde{a}$, which is the smallest wavelength that can be resolved on the grid.

The spatial discretization is closely connected to the numerical stability of the TSFP method. Numerical instabilities intrinsic to splitting algorithms can be avoided by choosing sufficiently small time steps Δt, which should suffice [182]

$$\Delta t \lesssim \frac{2\pi}{\left(\tilde{\Lambda}_{\mathrm{UV}}\right)^2} = \frac{2\tilde{L}}{3\pi N^2}\,, \tag{6.31}$$

with $\tilde{\Lambda}_{\mathrm{UV}}$ being the largest momentum on the discrete grid. In general, one wants to employ time steps as large as possible without encountering inaccuracies or instabilities in order to reduce the required computing capacity. For our simulations, we compare various Δt and use the largest time step for which the distribution functions is in good agreement with simulations employing smaller time step sizes.

6.C Extracting scaling exponents of the self-similar time evolution

In this appendix we describe the fitting procedure deployed to determine the time-dependent scaling exponents $\alpha(t)$ and $\beta(t)$ for the occupation number distribution functions of the spin-1 Bose gas. The method is adapted from the procedure described in Appendix 3.C.

Considering (3.64) and the associated discussion, we numerically approximate the scaling function by

$$f_{\mathrm{rsc}}(t,k_{\mathrm{rsc}}) = \left(\tfrac{t}{t_{\mathrm{ref}}}\right)^{-\alpha} f\,(t,k)\;, \qquad\qquad k_{\mathrm{rsc}} = \left(\tfrac{t}{t_{\mathrm{ref}}}\right)^{-\beta} k\,, \tag{6.32}$$

where f is the distribution function and k_{rsc} is the rescaled momentum. This relation allows for a comparison of the distribution function at a time t with the distribution function at some reference time t_{ref}. Deviations from a perfect scaling behavior are quantified by (3.67), which we minimize using optimization routines provided by the Python SciPy library. Errors are estimated as described in Appendix 3.C.

The computation of the deviations requires an interpolation of the numerically computed distribution functions. We smooth and interpolate our data using a cubic spline provided by the Python SciPy library. In order to analyze the infrared scaling behavior, we take into account all momenta for which $f(t_{\mathrm{ref}},k)$ is larger than a constant threshold f_{thresh} which is chosen such that only the inverse particle cascade is included. The results in the main text are computed for $f_{\mathrm{thresh}} = 10^4$.

Since the dynamics of the spin-1 Bose gas slows down during the time evolution, it is convenient to use the distribution functions at late times as reference. We compare the distribution function at a time t to several reference times t_{ref}, at which the system is nearly stationary. The exponents presented in the main text are obtained from the average over the reference times $t_{\mathrm{ref}} = 1300, 1325, 1350$. Since a proper comparison is only possible for sufficiently large time windows $\Delta t = t_{\mathrm{ref}} - t$, we only present results for $t \lesssim 1200$.

List of publications

Parts of this dissertation have been or will be published in the following preprints and peer-reviewed articles:

- L. Shen and J. Berges, "Spectral, statistical and vertex functions in scalar quantum field theory far from equilibrium", Phys. Rev. D **101**, 056009 (2020).
- L. Shen, J. Berges, J. Pawlowski, and A. Rothkopf, "Thermalization and dynamical spectral properties in the quark-meson model", (2020), arXiv:`2003.03270 [hep-ph]` (submitted to Phys. Rev. D).

Bibliography

[1] D. I. Podolsky, G. N. Felder, L. Kofman, and M. Peloso, “Equation of state and beginning of thermalization after preheating”, Phys. Rev. D **73**, 023501 (2006).

[2] L. Kofman, A. D. Linde, and A. A. Starobinsky, “Reheating after inflation”, Phys. Rev. Lett. **73**, 3195 (1994).

[3] A. Arrizabalaga, J. Smit, and A. Tranberg, “Equilibration in ϕ^4 theory in 3+1 dimensions”, Phys. Rev. D **72**, 025014 (2005).

[4] M. A. Amin, M. P. Hertzberg, D. I. Kaiser, and J. Karouby, “Nonperturbative Dynamics Of Reheating After Inflation: A Review”, Int. J. Mod. Phys. D **24**, 1530003 (2014).

[5] J. Berges, S. Borsanyi, and C. Wetterich, “Prethermalization”, Phys. Rev. Lett. **93**, 142002 (2004).

[6] U. W. Heinz, and P. F. Kolb, “Early thermalization at RHIC”, Nucl. Phys. A **702**, 269 (2002).

[7] P. Braun-Munzinger, V. Koch, T. Schäfer, and J. Stachel, “Properties of hot and dense matter from relativistic heavy ion collisions”, Phys. Rept. **621**, 76 (2016).

[8] C. Kollath, A. M. Läuchli, and E. Altman, “Quench dynamics and nonequilibrium phase diagram of the Bose-Hubbard model”, Phys. Rev. Lett. **98**, 180601 (2007).

[9] M. Moeckel, and S. Kehrein, “Crossover from adiabatic to sudden interaction quenches in the Hubbard model: prethermalization and non-equilibrium dynamics”, New J. Phys. **12**, 055016 (2010).

[10] R. Barnett, A. Polkovnikov, and M. Vengalattore, “Prethermalization in quenched spinor condensates”, Phys. Rev. A **84**, 023606 (2011).

[11] R. Nandkishore, and D. A. Huse, “Many body localization and thermalization in quantum statistical mechanics”, Annu. Rev. Condens. Matter Phys. **6**, 15 (2015).

[12] J. Eisert, M. Friesdorf, and C. Gogolin, “Quantum many-body systems out of equilibrium”, Nat. Phys. **11**, 124 (2015).

[13] T. Mori, T. Ikeda, E. Kaminishi, and M. Ueda, “Thermalization and prethermalization in isolated quantum systems: a theoretical overview”, J. Phys. B **51**, 112001 (2018).

[14] I. Bloch, J. Dalibard, and S. Nascimbene, “Quantum simulations with ultracold quantum gases”, Nat. Phys. **8**, 267 (2012).

[15] A. Polkovnikov, K. Sengupta, A. Silva, and M. Vengalattore, “Nonequilibrium dynamics of closed interacting quantum systems”, Rev. Mod. Phys. **83**, 863 (2011).

[16] W. Busza, K. Rajagopal, and W. van der Schee, “Heavy Ion Collisions: The Big Picture, and the Big Questions”, Annu. Rev. Nucl. Part. Sci. **68**, 339 (2018).

[17] C. Ratti, “Lattice QCD and heavy ion collisions: a review of recent progress”, Rept. Prog. Phys. **81**, 084301 (2018).

[18] N. Tanji, and J. Berges, “Nonequilibrium quark production in the expanding QCD plasma”, Nucl. Phys. A **982**, 243 (2019).

[19] K. Boguslavski, A. Kurkela, T. Lappi, and J. Peuron, “Spectral function for overoccupied gluodynamics from real-time lattice simulations”, Phys. Rev. D **98**, 014006 (2018).

[20] A. Kurkela, A. Mazeliauskas, J.-F. Paquet, S. Schlichting, and D. Teaney, “Matching the Nonequilibrium Initial Stage of Heavy Ion Collisions to Hydrodynamics with QCD Kinetic Theory”, Phys. Rev. Lett. **122**, 122302 (2019).

[21] N. Mueller, “Out-of-equilibrium dynamics of topological an anomalous effects from chiral kinetic theory”, PoS Quark Confinement and the Hadron Spectrum **336**, 277 (2019).

[22] G. Giacalone, A. Mazeliauskas, and S. Schlichting, “Hydrodynamic attractors, initial state energy and particle production in relativistic nuclear collisions”, Phys. Rev. Lett. **123**, 262301 (2019).

[23] A. Mazeliauskas, and J. Berges, “Prescaling and far-from-equilibrium hydrodynamics in the quark-gluon plasma”, Phys. Rev. Lett. **122**, 122301 (2019).

[24] W. Ketterle, D. Durfee, and D. Stamper-Kurn, “Making, probing and understanding Bose-Einstein condensates”, Proceedings of the Int. School of Phys. “Enrico Fermi” **140**, 67 (1999).

[25] R. Grimm, M. Weidemüller, and Y. B. Ovchinnikov, “Optical Dipole Traps for Neutral Atoms”, Adv. At. Mol. Opt. Phys. **42**, 95 (2000).

[26] T. Langen, R. Geiger, and J. Schmiedmayer, “Ultracold atoms out of equilibrium”, Annu. Rev. Condens. Matter Phys. **6**, 201 (2015).

[27] J. Berges, K. Boguslavski, S. Schlichting, and R. Venugopalan, “Universality far from equilibrium: From superfluid Bose gases to heavy-ion collisions”, Phys. Rev. Lett. **114**, 061601 (2015).

[28] M. Prüfer, P. Kunkel, H. Strobel, S. Lannig, D. Linnemann, C.-M. Schmied, J. Berges, T. Gasenzer, and M. K. Oberthaler, “Observation of universal dynamics in a spinor Bose gas far from equilibrium”, Nature **563**, 217 (2018).

[29] S. Erne, R. Bücker, T. Gasenzer, J. Berges, and J. Schmiedmayer, “Universal dynamics in an isolated one-dimensional Bose gas far from equilibrium”, Nature **563**, 225 (2018).

[30] J. Berges, A. Rothkopf, and J. Schmidt, “Nonthermal fixed points: effective weak coupling for strongly correlated systems far from equilibrium”, Phys. Rev. Lett. **101**, 041603 (2008).

[31] J. Berges, and D. Sexty, “Strong versus weak wave-turbulence in relativistic field theory”, Phys. Rev. D **83**, 085004 (2011).

[32] A. Piñeiro Orioli, K. Boguslavski, and J. Berges, “Universal self-similar dynamics of relativistic and nonrelativistic field theories near nonthermal fixed points”, Phys. Rev. D **92**, 025041 (2015).

[33] J. Berges, and G. Hoffmeister, “Nonthermal fixed points and the functional renormalization group”, Nucl. Phys. B **813**, 383 (2009).

[34] M. Karl, B. Nowak, and T. Gasenzer, “Tuning universality far from equilibrium”, Scientific reports **3**, 2394 (2013).

[35] B. Nowak, J. Schole, and T. Gasenzer, “Universal dynamics on the way to thermalization”, New J. Phys. **16**, 093052 (2014).

[36] A. N. Mikheev, C.-M. Schmied, and T. Gasenzer, “Low-energy effective theory of nonthermal fixed points in a multicomponent Bose gas”, Phys. Rev. A **99**, 063622 (2019).

[37] C.-M. Schmied, A. N. Mikheev, and T. Gasenzer, “Prescaling in a far-from-equilibrium Bose gas”, Phys. Rev. Lett. **122**, 170404 (2019).

[38] C.-M. Schmied, M. Prüfer, M. K. Oberthaler, and T. Gasenzer, “Bidirectional universal dynamics in a spinor Bose gas close to a nonthermal fixed point”, Phys. Rev. A **99**, 033611 (2019).

[39] T. Giamarchi, A. J. Millis, O. Parcollet, H. Saleur, and L. F. Cugliandolo, *Strongly Interacting Quantum Systems out of Equilibrium: Lecture Notes of the Les Houches Summer School*, Vol. 99 (Oxford University Press, 2012).

[40] J. Rammer, *Quantum field theory of non-equilibrium states* (Cambridge University Press, 2007).

[41] J. Berges, “Introduction to nonequilibrium quantum field theory”, AIP Conf. Proc. **739**, 3 (2004).

[42] A. Kamenev, *Field theory of non-equilibrium systems* (Cambridge University Press, 2011).

[43] E. A. Calzetta, and B.-L. B. Hu, *Nonequilibrium quantum field theory*, Cambridge Monographs on Mathematical Physics (Cambridge University Press, 2008).

[44] M. E. Peskin, and D. V. Schroeder, *An introduction to quantum field theory* (Westview, 1995).

[45] S. Weinberg, *The quantum theory of fields* (Cambridge university press, 1995).

[46] M. Srednicki, *Quantum field theory* (Cambridge University Press, 2007).

[47] A. Andreassen, W. Frost, and M. D. Schwartz, “Consistent use of effective potentials”, Phys. Rev. D **91**, 016009 (2015).

[48] S. Borsanyi, “Nonequilibrium field theory from the 2PI effective action”, PoS Johns Hopkins Workshop **22**, 004 (2006).

[49] A. Arrizabalaga, and U. Reinosa, “Finite-temperature φ^4 theory from the 2PI effective action: Two-loop truncation”, Eur. Phys. J. A **31**, 754 (2007).

[50] J. M. Cornwall, R. Jackiw, and E. Tomboulis, “Effective action for composite operators”, Phys. Rev. D **10**, 2428 (1974).

[51] E. Calzetta, and B.-L. Hu, “Nonequilibrium quantum fields: Closed-time-path effective action, Wigner function, and Boltzmann equation”, Phys. Rev. D **37**, 2878 (1988).

[52] M. Gell-Mann, and F. Low, “Bound states in quantum field theory”, Phys. Rev. **84** (1951) `10.1103/PhysRev.84.350`.

[53] J. Schwinger, “Brownian motion of a quantum oscillator”, J. Math. Phys. **2**, 407 (1961).

[54] L. V. Keldysh, et al., “Diagram technique for nonequilibrium processes”, Sov. Phys. JETP **20** (1965).

[55] J. Pruschke, “Nonequilibrium Fermion Production in Quantum Field Theory”, Dissertation (Technische Universität, Darmstadt, June 2010), `http://tuprints.ulb.tu-darmstadt.de/2209/`.

[56] K. B. Petersen, M. S. Pedersen, et al., “The matrix cookbook”, Technical University of Denmark **7** (2008).

[57] J.-P. Blaizot, and E. Iancu, “The quark–gluon plasma: collective dynamics and hard thermal loops”, Phys. Rept. **359**, 355 (2002).

[58] G. Aarts, D. Ahrensmeier, R. Baier, J. Berges, and J. Serreau, “Far-from-equilibrium dynamics with broken symmetries from the $1/N$ expansion of the 2PI effective action”, Phys. Rev. D **66**, 045008 (2002).

[59] G. Aarts, and J. Smit, “Classical approximation for time dependent quantum field theory: Diagrammatic analysis for hot scalar fields”, Nucl. Phys. B **511**, 451 (1998).

[60] J. Berges, “Controlled nonperturbative dynamics of quantum fields out-of-equilibrium”, Nucl. Phys. A **699**, 847 (2002).

[61] J. Berges, S. Borsanyi, and J. Serreau, “Thermalization of fermionic quantum fields”, Nucl. Phys. B **660**, 51 (2003).

[62] J. Berges, and B. Wallisch, “Nonthermal fixed points in quantum field theory beyond the weak-coupling limit”, Phys. Rev. D **95**, 036016 (2017).

[63] J. Berges, D.-U. Jungnickel, and C. Wetterich, “The Chiral phase transition at high baryon density from nonperturbative flow equations”, Eur. Phys. J. C **13**, 323 (2000).

[64] J. Berges, J. Pruschke, and A. Rothkopf, “Instability-induced fermion production in quantum field theory”, Phys. Rev. D **80**, 023522 (2009).

[65] L. Shen, and J. Berges, “Spectral, statistical and vertex functions in scalar quantum field theory far from equilibrium”, Phys. Rev. D **101**, 056009 (2020).

[66] L. Shen, and A. Rothkopf, *Solver for 2PI evolution equations at NLO in large N*, Mar. 2020.

[67] B. A. Bassett, S. Tsujikawa, and D. Wands, “Inflation dynamics and reheating”, Rev. Mod. Phys. **78**, 537 (2006).

[68] J. H. Traschen, and R. H. Brandenberger, “Particle Production During Out-of-equilibrium Phase Transitions”, Phys. Rev. D **42**, 2491 (1990).

[69] R. Micha, and I. I. Tkachev, “Relativistic turbulence: A Long way from preheating to equilibrium”, Phys. Rev. Lett. **90**, 121301 (2003).

[70] R. Micha, and I. I. Tkachev, “Turbulent thermalization”, Phys. Rev. D **70**, 043538 (2004).

[71] S. Schlichting, “Turbulent thermalization of weakly coupled non-abelian plasmas”, Phys. Rev. D **86**, 065008 (2012).

[72] A. Kurkela, and G. D. Moore, “UV Cascade in Classical Yang-Mills Theory”, Phys. Rev. D **86**, 056008 (2012).

[73] J. Berges, K. Boguslavski, S. Schlichting, and R. Venugopalan, “Turbulent thermalization process in heavy-ion collisions at ultrarelativistic energies”, Phys. Rev. D **89**, 074011 (2014).

[74] J. Berges, K. Boguslavski, S. Schlichting, and R. Venugopalan, “Universal attractor in a highly occupied non-Abelian plasma”, Phys. Rev. D **89**, 114007 (2014).

[75] M. Prüfer, T. V. Zache, P. Kunkel, S. Lannig, A. Bonnin, H. Strobel, J. Berges, and M. K. Oberthaler, “Experimental extraction of the quantum effective action for a non-equilibrium many-body system”, (2019), arXiv:`1909.05120 [cond-mat.quant-gas]`.

[76] I. Chantesana, A. Piñeiro Orioli, and T. Gasenzer, “Kinetic theory of nonthermal fixed points in a Bose gas”, Phys. Rev. A **99**, 043620 (2019).

[77] R. Walz, K. Boguslavski, and J. Berges, “Large-N kinetic theory for highly occupied systems”, Phys. Rev. D **97**, 116011 (2018).

[78] S. Bhattacharyya, J. F. Rodriguez-Nieva, and E. Demler, “Universal dynamics far from equilibrium in Heisenberg ferromagnets”, (2019), arXiv:`1908.00554 [cond-mat.stat-mech]`.

[79] G. D. Moore, “Condensates in Relativistic Scalar Theories”, Phys. Rev. D **93**, 065043 (2016).

[80] M. Karl, and T. Gasenzer, “Strongly anomalous non-thermal fixed point in a quenched two-dimensional Bose gas”, New J. Phys. **19**, 093014 (2017).

[81] M. Mace, S. Schlichting, and R. Venugopalan, “Off-equilibrium sphaleron transitions in the Glasma”, Phys. Rev. D **93**, 074036 (2016).

[82] J. Berges, M. Mace, and S. Schlichting, “Universal self-similar scaling of spatial Wilson loops out of equilibrium”, Phys. Rev. Lett. **118**, 192005 (2017).

[83] J. Deng, S. Schlichting, R. Venugopalan, and Q. Wang, “Off-equilibrium infrared structure of self-interacting scalar fields: Universal scaling, Vortex-antivortex superfluid dynamics and Bose-Einstein condensation”, Phys. Rev. A **97**, 053606 (2018).

[84] J. Berges, K. Boguslavski, M. Mace, and J. M. Pawlowski, “Gauge-invariant condensation in the nonequilibrium quark-gluon plasma”, (2019), arXiv:`1909.06147 [hep-ph]`.

[85] G. Aarts, and J. Berges, “Nonequilibrium time evolution of the spectral function in quantum field theory”, Phys. Rev. D **64**, 105010 (2001).

[86] A. Piñeiro Orioli, and J. Berges, “Breaking the fluctuation-dissipation relation by universal transport processes”, Phys. Rev. Lett. **122**, 150401 (2019).

[87] K. Boguslavski, and A. Piñeiro Orioli, “Unraveling the nature of universal dynamics in $O(N)$ theories”, (2019), arXiv:`1911.04506 [hep-ph]`.

[88] L. Shen, J. Berges, J. Pawlowski, and A. Rothkopf, “Thermalization and dynamical spectral properties in the quark-meson model”, (2020), arXiv:`2003.03270 [hep-ph]`.

[89] M. A. Stephanov, K. Rajagopal, and E. V. Shuryak, “Event-by-event fluctuations in heavy ion collisions and the QCD critical point”, Phys. Rev. D **60**, 114028 (1999).

[90] X. Luo, and N. Xu, “Search for the QCD Critical Point with Fluctuations of Conserved Quantities in Relativistic Heavy-Ion Collisions at RHIC: An Overview”, Nucl. Sci. Tech. **28**, 112 (2017).

[91] B. Mohanty, “STAR experiment results from the beam energy scan program at RHIC”, J. Phys. G **38**, 124023 (2011).

[92] M. Aggarwal, et al., “An Experimental Exploration of the QCD Phase Diagram: The Search for the Critical Point and the Onset of De-confinement”, (2010), arXiv:`1007.2613 [nucl-ex]`.

[93] T. Nonaka, “Studying the QCD Phase Diagram in RHIC-BES at STAR”, JPS Conf. Proc. **26**, 024007 (2019).

[94] P. B. Arnold, “Quark-Gluon Plasmas and Thermalization”, Int. J. Mod. Phys. E **16**, 2555 (2007).

[95] P. B. Arnold, J. Lenaghan, G. D. Moore, and L. G. Yaffe, “Apparent thermalization due to plasma instabilities in quark-gluon plasma”, Phys. Rev. Lett. **94**, 072302 (2005).

[96] U. W. Heinz, “Thermalization at RHIC”, AIP Conf. Proc. **739**, 163 (2004).

[97] J. Berges, D. Gelfand, and J. Pruschke, “Quantum theory of fermion production after inflation”, Phys. Rev. Lett. **107**, 061301 (2011).

[98] J. Berges, D. Gelfand, and D. Sexty, “Amplified Fermion Production from Overpopulated Bose Fields”, Phys. Rev. D **89**, 025001 (2014).

[99] C. Bonati, M. D’Elia, F. Negro, F. Sanfilippo, and K. Zambello, “Curvature of the pseudocritical line in QCD: Taylor expansion matches analytic continuation”, Phys. Rev. D **98**, 054510 (2018).

[100] S. Borsanyi, Z. Fodor, J. N. Guenther, S. K. Katz, K. K. Szabo, A. Pasztor, I. Portillo, and C. Ratti, “Higher order fluctuations and correlations of conserved charges from lattice QCD”, JHEP **10**, 205 (2018).

[101] H. T. Ding, et al., “Chiral Phase Transition Temperature in (2+1)-Flavor QCD”, Phys. Rev. Lett. **123**, 062002 (2019).

[102] J. M. Pawlowski, “Equation of state and phase diagram of strongly interacting matter”, Nucl. Phys. A **931**, 113 (2014).

[103] W.-j. Fu, J. M. Pawlowski, and F. Rennecke, “The QCD phase structure at finite temperature and density”, Phys. Rev. D **101**, 054032 (2020).

[104] R. Alkofer, A. Maas, W. A. Mian, M. Mitter, J. Paris-Lopez, J. M. Pawlowski, and N. Wink, “Bound state properties from the functional renormalization group”, Phys. Rev. D **99**, 054029 (2019).

[105] B.-J. Schaefer, and J. Wambach, “The Phase diagram of the quark meson model”, Nucl. Phys. A **757**, 479 (2005).

[106] V. Skokov, B. Stokic, B. Friman, and K. Redlich, “Meson fluctuations and thermodynamics of the Polyakov loop extended quark-meson model”, Phys. Rev. C **82**, 015206 (2010).

[107] T. K. Herbst, J. M. Pawlowski, and B.-J. Schaefer, “The phase structure of the Polyakov–quark–meson model beyond mean field”, Phys. Lett. B **696**, 58 (2011).

[108] K. Kamikado, T. Kunihiro, K. Morita, and A. Ohnishi, “Functional Renormalization Group Study of Phonon Mode Effects on Chiral Critical Point”, PTEP **2013**, 053D01 (2013).

[109] W.-j. Fu, J. M. Pawlowski, F. Rennecke, and B.-J. Schaefer, “Baryon number fluctuations at finite temperature and density”, Phys. Rev. D **94**, 116020 (2016).

[110] S. Floerchinger, “Analytic Continuation of Functional Renormalization Group Equations”, JHEP **05**, 021 (2012).

[111] R.-A. Tripolt, N. Strodthoff, L. von Smekal, and J. Wambach, “Spectral Functions for the Quark-Meson Model Phase Diagram from the Functional Renormalization Group”, Phys. Rev. D **89**, 034010 (2014).

[112] J. M. Pawlowski, and N. Strodthoff, “Real time correlation functions and the functional renormalization group”, Phys. Rev. D **92**, 094009 (2015).

[113] C. Jung, F. Rennecke, R.-A. Tripolt, L. von Smekal, and J. Wambach, “In-Medium Spectral Functions of Vector- and Axial-Vector Mesons from the Functional Renormalization Group”, Phys. Rev. D **95**, 036020 (2017).

[114] T. Yokota, T. Kunihiro, and K. Morita, “Functional renormalization group analysis of the soft mode at the QCD critical point”, PTEP **2016**, 073D01 (2016).

[115] J. M. Pawlowski, N. Strodthoff, and N. Wink, “Finite temperature spectral functions in the O(N)-model”, Phys. Rev. D **98**, 074008 (2018).

[116] T. Yokota, T. Kunihiro, and K. Morita, "Tachyonic instability of the scalar mode prior to the QCD critical point based on the functional renormalization-group method in the two-flavor case", Phys. Rev. D **96**, 074028 (2017).

[117] Z. Wang, and P. Zhuang, "Meson spectral functions at finite temperature and isospin density with the functional renormalization group", Phys. Rev. D **96**, 014006 (2017).

[118] R.-A. Tripolt, J. Weyrich, L. von Smekal, and J. Wambach, "Fermionic spectral functions with the Functional Renormalization Group", Phys. Rev. D **98**, 094002 (2018).

[119] Z. Wang, and L. He, "Fermion spectral function in hot strongly interacting matter from the functional renormalization group", Phys. Rev. D **98**, 094031 (2018).

[120] C. Jung, and L. von Smekal, "Fluctuating vector mesons in analytically continued functional RG flow equations", Phys. Rev. D **100**, 116009 (2019).

[121] S. Schlichting, D. Smith, and L. von Smekal, "Spectral functions and critical dynamics of the $O(4)$ model from classical-statistical lattice simulations", Nucl. Phys. B **950**, 114868 (2020).

[122] M. Kitazawa, T. Kunihiro, and Y. Nemoto, "Novel Collective Excitations and Quasi-particle Picture of Quarks Coupled with a Massive Boson at Finite Temperature", Prog. Theor. Phys. **117**, 103 (2007).

[123] M. Tanabashi, K. Hagiwara, K. Hikasa, K. Nakamura, Y. Sumino, F. Takahashi, J. Tanaka, K. Agashe, G. Aielli, C. Amsler, et al., "Review of Particle Physics", Phys. Rev. D **98**, 030001 (2018).

[124] A. K. Cyrol, M. Mitter, J. M. Pawlowski, and N. Strodthoff, "Nonperturbative quark, gluon, and meson correlators of unquenched QCD", Phys. Rev. D **97**, 054006 (2018).

[125] M. Kitazawa, T. Kunihiro, and Y. Nemoto, "Quark spectrum above but near critical temperature of chiral transition", Phys. Lett. B **633**, 269 (2006).

[126] M. Kitazawa, T. Kunihiro, K. Mitsutani, and Y. Nemoto, "Spectral properties of massless and massive quarks coupled with massive boson at finite temperature", Phys. Rev. D **77**, 045034 (2008).

[127] F. Karsch, and M. Kitazawa, "Quark propagator at finite temperature and finite momentum in quenched lattice QCD", Phys. Rev. D **80**, 056001 (2009).

[128] J. A. Mueller, C. S. Fischer, and D. Nickel, "Quark spectral properties above T_c from Dyson-Schwinger equations", Eur. Phys. J. C **70**, 1037 (2010).

[129] S.-x. Qin, L. Chang, Y.-x. Liu, and C. D. Roberts, "Quark spectral density and a strongly-coupled QGP", Phys. Rev. D **84**, 014017 (2011).

[130] S.-x. Qin, and D. H. Rischke, "Quark Spectral Function and Deconfinement at Nonzero Temperature", Phys. Rev. D **88**, 056007 (2013).

[131] C. S. Fischer, J. M. Pawlowski, A. Rothkopf, and C. A. Welzbacher, "Bayesian analysis of quark spectral properties from the Dyson-Schwinger equation", Phys. Rev. D **98**, 014009 (2018).

[132] Y. Kawaguchi, and M. Ueda, "Spinor Bose-Einstein condensates", Phys. Rept. **520**, 256 (2012).

[133] S. Uchino, M. Kobayashi, and M. Ueda, "Bogoliubov Theory and Lee-Huang-Yang Correction in Spin-1 and Spin-2 Bose-Einstein Condensates in the Presence of the Quadratic Zeeman Effect", Phys. Rev. A **81**, 063632 (2010).

[134] C. Frapolli, T. Zibold, A. Invernizzi, K. Jiménez-García, J. Dalibard, and F. Gerbier, “Stepwise Bose-Einstein Condensation in a Spinor Gas”, Phys. Rev. Lett. **119**, 050404 (2017).

[135] J. Rogel-Salazar, “The Gross–Pitaevskii equation and Bose–Einstein condensates”, Eur. J. Phys. **34**, 247 (2013).

[136] C.-M. Schmied, T. Gasenzer, M. Oberthaler, and P. Kevrekidis, “Stability analysis of ground states in a one-dimensional trapped spin-1 Bose gas”, Comm. Nonlinear Sci. Numer. **83**, 105050 (2020).

[137] N. N. Bogolyubov, “On the theory of superfluidity”, J. Phys.(USSR) **11** (1947).

[138] R. Baier, A. H. Mueller, D. Schiff, and D. Son, “‘Bottom up’ thermalization in heavy ion collisions”, Phys. Lett. B **502**, 51 (2001).

[139] M. Schmidt, S. Erne, B. Nowak, D. Sexty, and T. Gasenzer, “Non-thermal fixed points and solitons in a one-dimensional Bose gas”, New J. Phys. **14**, 075005 (2012).

[140] J. Berges, and D. Sexty, “Bose condensation far from equilibrium”, Phys. Rev. Lett. **108**, 161601 (2012).

[141] J. Berges, and J. Jaeckel, “Far from equilibrium dynamics of Bose-Einstein condensation for Axion Dark Matter”, Phys. Rev. D **91**, 025020 (2015).

[142] B. Nowak, and T. Gasenzer, “Universal dynamics on the way to thermalization”, New J. Phys. **16**, 093052 (2014).

[143] N. G. Berloff, and B. V. Svistunov, “Scenario of strongly nonequilibrated Bose-Einstein condensation”, Phys. Rev. A **66**, 013603 (2002).

[144] J. Schmiedmayer, and J. Berges, “Cold Atom Cosmology”, Science **341**, 1188 (2013).

[145] A. Görlitz, T. Gustavson, A. Leanhardt, R. Löw, A. Chikkatur, S. Gupta, S. Inouye, D. Pritchard, and W. Ketterle, “Sodium Bose-Einstein condensates in the F= 2 state in a large-volume optical trap”, Phys. Rev. Lett. **90**, 090401 (2003).

[146] D. Hall, M. Matthews, C. Wieman, and E. A. Cornell, “Measurements of relative phase in two-component Bose-Einstein condensates”, Phys. Rev. Lett. **81**, 1543 (1998).

[147] L. Sadler, J. Higbie, S. Leslie, M. Vengalattore, and D. Stamper-Kurn, “Spontaneous symmetry breaking in a quenched ferromagnetic spinor Bose–Einstein condensate”, Nature **443**, 312 (2006).

[148] Z. Hadzibabic, P. Krüger, M. Cheneau, B. Battelier, and J. Dalibard, “Berezinskii–Kosterlitz–Thouless crossover in a trapped atomic gas”, Nature **441**, 1118 (2006).

[149] T.-L. Ho, “Spinor Bose Condensates in Optical Traps”, Phys. Rev. Lett. **81**, 742 (1998).

[150] T. Ohmi, and K. Machida, “Bose-Einstein condensation with internal degrees of freedom in alkali atom gases”, Journal of the Physical Society of Japan **67**, 1822 (1998).

[151] E. Demler, and F. Zhou, “Spinor bosonic atoms in optical lattices: Symmetry breaking and fractionalization”, Phys. Rev. Lett. **88**, 163001 (2002).

[152] J. Mur-Petit, M. Guilleumas, A. Polls, A. Sanpera, M. Lewenstein, K. Bongs, and K. Sengstock, “Dynamics of F= 1 Rb 87 condensates at finite temperatures”, Phys. Rev. A **73**, 013629 (2006).

[153] *Baden Württemberg’s HPC*, `www.bwhpc-c5.de`.

[154] C. Scheppach, J. Berges, and T. Gasenzer, “Matter Wave Turbulence: Beyond Kinetic Scaling”, Phys. Rev. A **81**, 033611 (2010).

[155] O. Penrose, and L. Onsager, “Bose-Einstein condensation and liquid helium”, Phys. Rev. **104**, 576 (1956).

[156] M. Naraschewski, and R. Glauber, “Spatial coherence and density correlations of trapped Bose gases”, Phys. Rev. A **59**, 4595 (1999).

[157] P. Uhrich, S. Castrignano, H. Uys, and M. Kastner, “Noninvasive measurement of dynamic correlation functions”, Phys. Rev. A **96**, 022127 (2017).

[158] P. Uhrich, C. Gross, and M. Kastner, “Probing unitary two-time correlations in a neutral atom quantum simulator”, Quantum Science and Technology **4**, 024005 (2019).

[159] I. Montvay, and G. Münster, *Quantum Fields on a Lattice*, Cambridge Monographs on Mathematical Physics (Cambridge University Press, 1994).

[160] *FFTW*, `www.fftw.org`.

[161] M. Frigo, and S. G. Johnson, “FFTW for version 3.3.8”, (2018).

[162] *MPI Forum*, `www.mpi-forum.org`.

[163] W. H. Press, S. A. Teukolsky, W. T. Vetterling, and B. P. Flannery, *Numerical recipes 3rd edition: The art of scientific computing* (Cambridge university press, 2007).

[164] E. Jones, T. Oliphant, P. Peterson, et al., *SciPy: open source scientific tools for Python*, `www.scipy.org`, 2001.

[165] A. Polkovnikov, “Phase Space Representation of Quantum Dynamics”, Annals of Physics **325**, 1790 (2010).

[166] P. Blakie, A. Bradley, M. Davis, R. Ballagh, and C. Gardiner, “Dynamics and statistical mechanics of ultra-cold Bose gases using c-field techniques”, Adv. Phys. **57**, 363 (2008).

[167] A. Norrie, R. Ballagh, and C. Gardiner, “Quantum turbulence and correlations in Bose-Einstein condensate collisions”, Phys. Rev. A **73**, 043617 (2006).

[168] J. Berges, “Nonequilibrium Quantum Fields: From Cold Atoms to Cosmology”, arXiv:`1503.02907 [hep-ph]`.

[169] S. Khlebnikov, and I. Tkachev, “Classical decay of inflaton”, Phys. Rev. Lett. **77**, 219 (1996).

[170] T. P. Billam, R. Gregory, F. Michel, and I. G. Moss, “Simulating seeded vacuum decay in a cold atom system”, Phys. Rev. D **100**, 065016 (2019).

[171] B. Opanchuk, R. Polkinghorne, O. Fialko, J. Brand, and P. D. Drummond, “Quantum simulations of the early universe”, Annalen der Physik **525**, 866 (2013).

[172] G. Aarts, and J. Berges, “Classical aspects of quantum fields far from equilibrium”, Phys. Rev. Lett. **88**, 041603 (2002).

[173] J. Berges, and T. Gasenzer, “Quantum versus classical statistical dynamics of an ultracold Bose gas”, Phys. Rev. A **76**, 033604 (2007).

[174] J. Berges, S. Scheffler, and D. Sexty, “Bottom-up isotropization in classical-statistical lattice gauge theory”, Phys. Rev. D **77**, 034504 (2008).

[175] J. Berges, D. Gelfand, S. Scheffler, and D. Sexty, “Simulating plasma instabilities in $SU(3)$ gauge theory”, Phys. Lett. B **677**, 210 (2009).

[176] S. Jeon, “Boltzmann equation in classical and quantum field theory”, Phys. Rev. C **72**, 014907 (2005).

[177] J. Berges, K. Boguslavski, S. Schlichting, and R. Venugopalan, “Basin of attraction for turbulent thermalization and the range of validity of classical-statistical simulations”, JHEP **05**, 054 (2014).

[178] X. Antoine, W. Bao, and C. Besse, “Computational methods for the dynamics of the nonlinear Schrödinger/Gross–Pitaevskii equations”, Comput. Phys. Commun. **184**, 2621 (2013).

[179] L. Symes, R. McLachlan, and P. Blakie, “Efficient and accurate methods for solving the time-dependent spin-1 Gross-Pitaevskii equation”, Phys. Rev. E **93**, 053309 (2016).

[180] S. Blanes, and P. C. Moan, “Practical symplectic partitioned Runge–Kutta and Runge–Kutta–Nyström methods”, J. Comput. Appl. Math. **142**, 313 (2002).

[181] K. Geier, “Dynamics of Vector Solitons in Spinor Bose-Einstein Condensates”, Master thesis (Heidelberg University, 2017).

[182] S. A. Chin, “Higher-order splitting algorithms for solving the nonlinear Schrödinger equation and their instabilities”, Phys. Rev. E **76**, 056708 (2007).

Acknowledgments

Finally, I want to express my thanks to all the people who have contributed to this thesis and supported me during my doctorate. You helped me incredibly during this time and brought me one step further in my life. Irrespective of whether you are explicitly mentioned here or not, I highly appreciate your support.

First of all I thank my supervisor Jürgen Berges as well as my co-supervisors Alexander Rothkopf and Jan Pawlowski for their guidance during the last four years. I am very grateful that I received Jürgen's constant support and the possibility to work on different projects. His peaceful nature and his dedication to physics impressed me again and again. Jan's optimism plus his omnipresent smile and Alexander's enthusiasm for the research we are doing have been an important source of motivation for me. Furthermore, I would like to thank Martin Gärttner for opening new pathways for me and providing me with the opportunity to become part of SynQS. This has been an enriching experience.

I want to thank Thomas Gasenzer for many interesting discussions and in particular for the pleasant collaboration on Theo III. I learned a lot from you during this time.

I thank Tina for handling all kinds of organizational issues very efficiently and providing relevant information quickly. My time at the ITP would have been much harder without you. I very much enjoyed working with you. Furthermore, I also thank Dagmar and Christiane for their help with administrative and organizational issues in and around KIP.

I want to thank past and present members in Jürgen's group: Niklas (thanks for your confidence in me), Oscar (always there for funny but also serious conversations), Robert (I could always talk about problems with you), Torsten (thank you for answering many questions and for building raw black hats with me), Aleksandr (great office mate), Daniel S. (always motivated and enthusiastic), Gregor (interesting questions and discussions, as well as thought-through answers), Benjamin (thanks for your time in Amsterdam and your continuing interest in my work), Alexander L. (in particular for your support in Stavanger), Michael (for helpful discussions and bringing in good mood), Aleksas, Alexander S., Asier, Daniel K., Dustin, Erekle, Frederick, Ignacio, Kirill, Jan, Malo, Naoto, Niels, Roland, Savvas. When finalizing the work on this thesis, our virtual coffee breaks via Skype were a pleasant diversion.

Many thanks also go to the extended SynQS team for providing such a great working environment. In addition to interesting discussions and seminars I appreciated our group activities, such as the weekly breakfast (in real or virtually), a lot. I would like to mention Celia, who supported me with her experience regarding research and university, and Maurus, who taught me basic workshop skills and accompanied me in the Faculty Council.

Moreover, I would like to thank my examination committee, the Heidelberg Graduate School for Physics, the Graduate Academy, the DFG Collaborative Research Center IsoQuant, the state of Baden-Württemberg through bwHPC, and the people involved for their support.

Zuletzt möchte ich meinen Freunden und meiner Familie danken. Eure Unterstützung während meines Studiums und meiner Promotion hat mir sehr geholfen und diesen Weg überhaupt erst ermöglicht. Ohne Ann-Christin wären die vielen Jahre in Heidelberg nicht so schön gewesen. Mein besonderer Dank gilt Felix – danke, dass du immer für mich da bist.